MERLIN Validation & Application of AAR Problems

ANALYSES OF THE RILEM TC-259 BENCHMARK PROBLEMS FOR
AAR MODEL VALIDATION
& OTHERS

BY

VICTOR SAOUMA

MOHAMMAD AMIN HARIRI-ARDEBILI
THE UNIVERSITY OF COLORADO, BOULDER
X-ELASTICA
BOULDER, OCTOBER 2019

PREFACE

This report details the validation of the Merlin finite element code (Saouma, Červenka, and Reich, 2010) with the benchmark problems defined by the RILEM TC-259 Committee (*Prognosis of deterioration and loss of serviceability in structures affected by alkali-silica reactions.*

In addition, this report contains simulation of reinforced concrete panels extracted from nuclear containment vessel performed by the authors through a contract from the Oak Ridge National Laboratory (Saouma, Hariri-Ardebili, and Le Pape, 2015; Saouma, V.E. and Hariri-Ardebili, M.A. and Puatatsananon, W. and Le Pape, Y., 2014).

All analyses were executed with the finite element code Merlin (Saouma, Červenka, and Reich, 2010). Used is the AAR expansion model developed by Saouma and Perotti (2006) and validated in (Saouma, 2013), is to the best of the authors knowledge, the most widely adopted one by other researchers. A non-comprehensive list of implementation includes:

1. Rodriguez et al. (2011) implemented the model in Abaqus and analyzed an arch dam.
2. El Mohandes and Vecchio (2013) in the Vector3 program and the analysis of reactive shear walls.
3. Mirzabozorg (2013) in Iran for the analysis of Amir-Kabir arch dam in the NSAD-DRI code.
4. Pan et al. (2013) from Tsinghua University for the analysis of Kariba dam.
5. Huang and Spencer (2016) and Huang, Spencer, and Cai (2015) implemented this AAR model in the fully coupled Grizzly/Moose program.
6. Ben-Ftima, Sadouki, and Bruhwiler (2016) Polytechnic of Montreal, and Swiss Federal Institute of Technology, as a model in Abaqus for the analysis of a hydraulic structure.
7. Thonstad et al. (2021) implemented in LS-Dyna by NIST.

MERLIN AAR Problems

Contents

MERLIN AAR Problems

List of Figures

MERLIN AAR Problems

MERLIN AAR Problems

MERLIN AAR Problems

MERLIN AAR Problems

List of Tables

MERLIN AAR Problems

Part I

Proposed AAR Model

Chapter 1

Finite Element Model Description

The AAR model of the author is an uncoupled one, that is the constitutive model is in no way affected by the AAR which itself is considered to be an initial strain (akin of temperature), which grafts itself on the mechanical one.

This section will describe first the AAR model yielding to the expression of the AAR strain tensor which is accounted for. Then the nonlinear continuum based constitutive model is described next. This model can be activated whenever the AAR induced strain (or others) may either crack the concrete or initiate its ascent in the nonlinear compressive branch. Finally, the nonlinear discrete interface element is described. Though not directly affected by chemically induced volumetric strain, its presence is of paramount importance to model slot (often cut to relieve stresses) closure due to AAR.

1.1 AAR Model

1.1.1 Premises

Two different aspects of mathematical modeling of AAR in concrete may be distinguished: 1) The kinetics of the chemical reactions and diffusion processes involved, and 2) The mechanics of fracture that affects volume expansion and causes loss of strength, with possible disintegration of the material (Bažant, Zi, and Meyer, 2000).

The proposed model (Saouma and Perotti, 2006), (Saouma, 2013) is driven by the following considerations:

1. AAR is a volumetric expansion, and as such can not be addressed individually along a principal direction without due regard to what may occur along the other two orthogonal ones.
2. Kinetics component is taken from the work of (Larive, 1998; Ulm et al., 2000).
3. AAR is sufficiently influenced by temperature to account its temporal variation in an analysis.
4. AAR expansion is constrained by compression, and is redirected in other less constrained principal directions.This will be accomplished by assigning "weights" to each of the three principal directions.
5. Relatively high compressive or tensile stresses inhibit AAR expansion due to the formation of micro or macro cracks which absorb the expanding gel.
6. High compressive hydrostatic stresses slow down the reaction.
7. Triaxial compressive state of stress reduces but does not eliminate expansion.

8. Accompanying AAR expansion is a reduction in tensile strength and elastic modulus.

1.1.2   Expansion Curve

One of the most extensive and rigorous investigation of AAR has been conducted by (Larive, 1998) who tested more than 600 specimens with various mixes, ambiental and mechanical conditions. Not only did the author conduct this extensive experimental investigation, but a numerical model has also been proposed for the time expansion of the concrete. In particular, a thermodynamical based model for the expansion evolution is developed, and then calibrated with the experimental data, Figure 1.1.
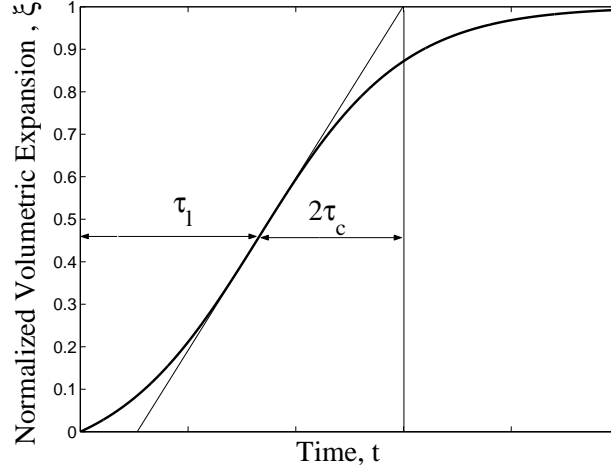
Figure 1.1: Normalized Expansion Curve ($\xi(t) = \varepsilon_{F,Vol}^{AAR}(t)/\varepsilon_{AAR}^{\infty}$)

$$\xi(t,\theta) = \frac{1 - e^{-\frac{t}{\tau_c(\theta)}}}{1 + e^{-\frac{(t-\tau_l(\theta))}{\tau_c(\theta)}}} \qquad (1.1)$$

where τ_l and τ_c are the latency and characteristic times respectively. The first corresponds to the inflexion point, and the second is defined in terms of the inter-subsection of the tangent at τ_L with the asymptotic unit value of ξ. In a subsequent work, (Ulm et al., 2000) have shown the thermal dependency of those two coefficients:

$$\begin{array}{rcl} \tau_l(\theta) & = & \tau_l(\theta_0)\exp\left[U_l\left(\frac{1}{\theta} - \frac{1}{\theta_0}\right)\right] \\ \tau_c(\theta) & = & \tau_c(\theta_0)\exp\left[U_c\left(\frac{1}{\theta} - \frac{1}{\theta_0}\right)\right] \end{array} \qquad (1.2)$$

expressed in terms of the absolute temperature ($\theta^o K = 273 + T^o C$) and the corresponding activation energies. U_l and U_c are the activation energies minimum energy required to trigger the reaction for the latency and characteristic times respectively, and were determined (for Larive's test) to be

$$\begin{array}{rcl} U_l & = & 9,400 \pm 500K \end{array} \qquad (1.3)$$

$$\begin{array}{rcl} U_c & = & 5,400 \pm 500K \end{array} \qquad (1.4)$$

To the best of the authors knowledge, the only other tests for these values were performed by (Scrivener, 2005) who obtained values within 20% of Larive's, and dependency on types of aggregates and alkali content of the cement has not been investigated. Hence, in the absence of other tests, those values can be reasonably

considered as representative of dam concrete also. The temperature dependence is highlighted by Figure 1.2 where the expansion curve determined in the laboratory at 38^oC is compared with the corresponding one at a dam average temperature of 7^oC.
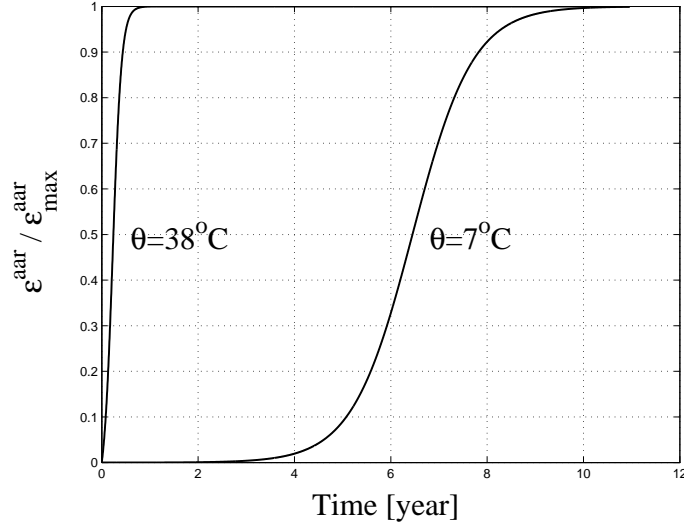
Figure 1.2: Effect of Temperature on AAR Expansion

1.1.3 Volumetric Expansion

Hence, the general (uncoupled) equation for the incremental free volumetric AAR strain is given by

$$\dot{\varepsilon}_V^{AAR}(t) = \Gamma_t(f_t'|w_c, \sigma_I|COD_{max})\Gamma_c(\overline{\sigma}, f_c')g(h)\dot{\xi}(t, \theta) \left. \varepsilon^\infty \right|_{\theta=\theta_0} \tag{1.5}$$

where COD is the crack opening displacement, $\xi(t, \theta)$ is a sigmoid curve expressing the volumetric expansion in time as a function of temperature and is given by Eq. 1.1, ε^∞ is the laboratory determined (or predicted) maximum free volumetric expansion at the reference temperature θ_0, Figure 1.1.

The retardation effect of the hydrostatic compressive stress manifests itself through τ_l. Hence, Eq. 1.2 is expanded as follows

$$\tau_l(\theta, \theta_0, I_\sigma, f_c') = f(I_\sigma, f_c')\tau_l(\theta_0) \exp\left[U_l\left(\frac{1}{\theta} - \frac{1}{\theta_0}\right)\right] \tag{1.6}$$

where

$$f(I_\sigma, f_c') = \begin{cases} 1 & \text{if } I_\sigma \geq 0. \\ 1 + \alpha\frac{I_\sigma}{3f_c'} & \text{if } I_\sigma < 0. \end{cases} \tag{1.7}$$

and I_σ is the first invariant of the stress tensor, and f_c' the compressive strength. Based on a careful analysis of (Multon, 2004), it was determined that $\alpha = 4/3$. It should be noted, that the stress dependency (through I_σ) of the kinetic parameter τ_l makes the model a truly coupled one between the chemical and mechanical phases. Coupling with the thermal component, is a loose one (hence a thermal analysis can be separately run), $0 < g(h) \leq 1$ is a reduction function to account for humidity given by

$$g(h) = h^m \tag{1.8}$$

MERLIN AAR Problems

where h is the relative humidity (Capra and Bournazel, 1998). However, one can reasonably assume that (contrarily to bridges) inside a dam $g(h) = 1$ for all temperatures.

$\Gamma_t(f'_t|w_c, \sigma_I|COD_{max})$ accounts for AAR reduction due to tensile cracking (in which case gel is absorbed by macro-cracks), Figure 1.3.
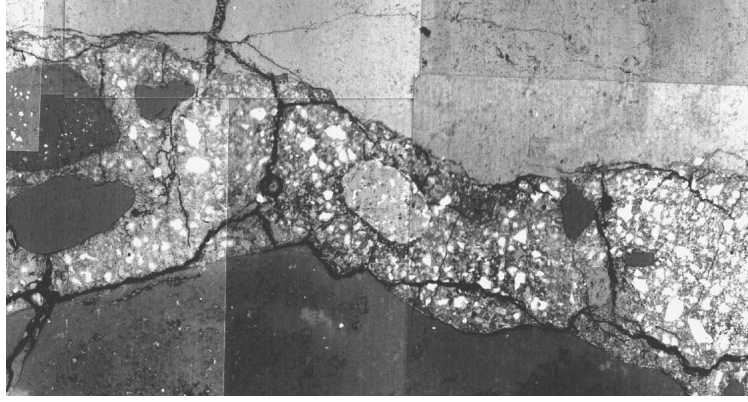
Figure 1.3: Stress Induced Cracks with Potential Gel Absorption (Scrivener, 2003)

A hyperbolic decay, with a non-zero residual value is adopted, Figure 1.4:
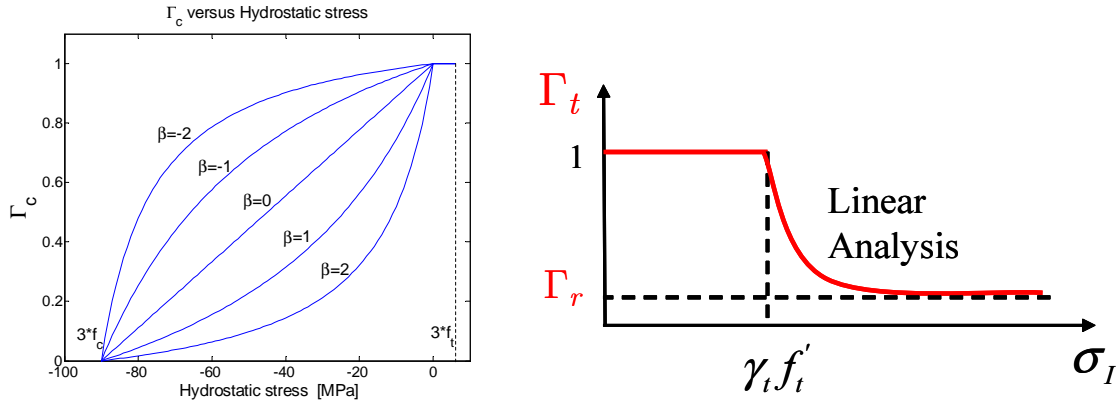
Figure 1.4: Graphical Representation of Γ_c and Γ_t

$$\text{Smeared Crack} \begin{cases} \text{No } \Gamma_t = \begin{cases} 1 & \text{if } \sigma_I \leq \gamma_t f'_t \\ \Gamma_r + (1 - \Gamma_r)\gamma_t \frac{f'_t}{\sigma_I} & \text{if } \gamma_t f'_t < \sigma_I \end{cases} \\ \text{Yes } \Gamma_t = \begin{cases} 1 & \text{if } \text{COD}_{max} \leq \gamma_t w_c \\ \Gamma_r + (1 - \Gamma_r)\gamma_t \frac{w_c}{\text{COD}_{max}} & \text{if } \gamma_t w_c < \text{COD}_{max} \end{cases} \end{cases} \quad (1.9)$$

where γ_t is the fraction of the tensile strength beyond which gel is absorbed by the crack, Γ_r is a residual AAR retention factor for AAR under tension. If an elastic model is used, then f'_t is the the tensile strength, σ_I the maximum principal tensile stress. On the other hand, if a smeared crack model is adopted, then COD_{max} is the maximum crack opening displacement at the current Gauss point, and w_c the maximum crack opening displacement in the tensile softening curve (Whitman et al., 1988).

Concrete pores being seldom interconnected, and the gel viscosity relatively high, gel absorption by the

MERLIN AAR Problems

pores is not explicitly accounted for. Furthermore, gel absorption by the pores is accounted for by the kinetic equation through the latency time which depends on concrete porosity. The higher the porosity, the larger the latency time.

Γ_c in turns accounts for the reduction in AAR volumetric expansion under compressive stresses (in which case gel is absorbed by diffused micro-cracks) (Multon, 2004):

$$\Gamma_c = \begin{cases} 1 & \text{if} \quad \overline{\sigma} \leq 0. \quad \text{Tension} \\ 1 - \frac{e^{\beta \overline{\sigma}}}{1+(e^{\beta}-1.)\overline{\sigma}} & \text{if} \quad \overline{\sigma} > 0. \quad \text{Compression} \end{cases} \tag{1.10}$$

$$\overline{\sigma} = \frac{\sigma_I + \sigma_{II} + \sigma_{III}}{3f_c'} \tag{1.11}$$

Whereas this expression will also reduce expansion under uniaxial or biaxial confinement, Figure 1.4, these conditions are more directly accounted for below through the assignment of weights.

1.1.4 AAR Strain Redistribution

The third major premise of the model, is that the volumetric AAR strain must be redistributed to the three principal directions according to their relative propensity for expansion on the basis of a weight which is a function of the respective stresses. Whereas the determination of the weight is relatively straightforward for triaxial AAR expansion under uniaxial confinement (for which some experimental data is available), it is more problematic for biaxially or triaxially confined concrete.

Given principal stress vector defined by $\sigma_k, \sigma_l, \sigma_m$, we need to assign a weight to each of those three principal directions. These weights will control AAR volumetric expansion distribution. For instance, with reference to Figure 1.5, we consider three scenarios.
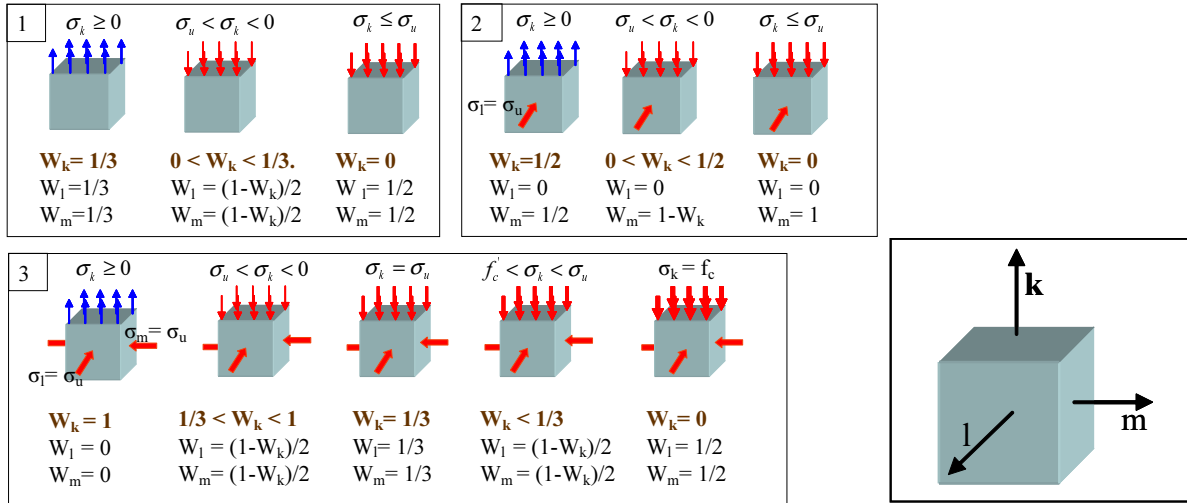
Figure 1.5: Weight of Volumetric AAR Redistribution in Selected Cases

Uniaxial State of stress, where we distinguish the following three cases:

1. In the first case, we have uniaxial tension, and hence, the volumetric AAR strain is equally redistributed in all three directions.

2. Under a compressive stress greater than the limiting one (σ_u), the weight in the corresponding

(k) direction should be less than one third. The remaining AAR has to be equally redistributed in the other two directions.

3. If the compressive stress is lower than σ_u, than AAR expansion in the corresponding direction is prevented (weight equal zero), and thus the other two weights must be equal to one half.

Biaxial state of stress in which we have a compressive stress equal to σ_u in one of the three principal directions. In this case, the corresponding weight will always be equal to zero. As to the possible three combinations:

1. Tension in one direction, equal weights of one half.

2. Compression greater than σ_u in one direction, then the corresponding weight must be less than one half, and the remaining weight is assigned to the third direction.

3. Compression less to σ_u, then the corresponding weight is again zero, and a unit weight is assigned to the third direction.

Triaxial state of stress in which we have σ_u acting on two of the three principle directions. We identify the following five cases:

1. Tension along direction k, then all the expansion is along k.

2. Compressive stress greater than σ_u, then we have a triaxial state of compressive stress, and the corresponding weight will be between one and one third. The remaining complement of the weight is equally distributed in the other two directions.

3. Compression equal to σ_u, hence we have a perfect triaxial state of compressive stress. In this case we have equal weights of one third. It should be noted that the overall expansion is reduced through Γ_c.

4. Compression less than σ_u but greater than the compressive strength. In this case, the weight along k should be less than one third, and the remaining equally distributed along the other two directions.

5. Compression equal to the compressive strength. In this case, the corresponding weight is reduced to zero, and the other two weights are equal to one half each.

Based on the preceding discussion, we generalize this weight allocation scheme along direction k as follows

1. Given σ_k, identify the quadrant encompassing σ_l and σ_m, Figure 1.6[1]. Weight will be determined through a bilinear interpolation for those four neighboring nodes.

2. Determine the weights of the neighboring nodes from Table 1.1 through proper linear interpolation of σ_k.

3. Compute the weight from:

$$W_k(\sigma_k, \sigma_l, \sigma_m) = \sum\nolimits_{i=1}^{4} N_i(\sigma_l, \sigma_m) W_i(\sigma_k) \tag{1.12}$$

---

[1]Since compressive stresses are quite low compared to the compressive strength, we ignore the strength gained through the biaxiality or triaxiality of the stress tensor (Kupfer and Gerstle, 1973). Furthermore, the strength gain is only about 14% for equibiaxial compressive stresses (CEB, 1983)

MERLIN AAR Problems
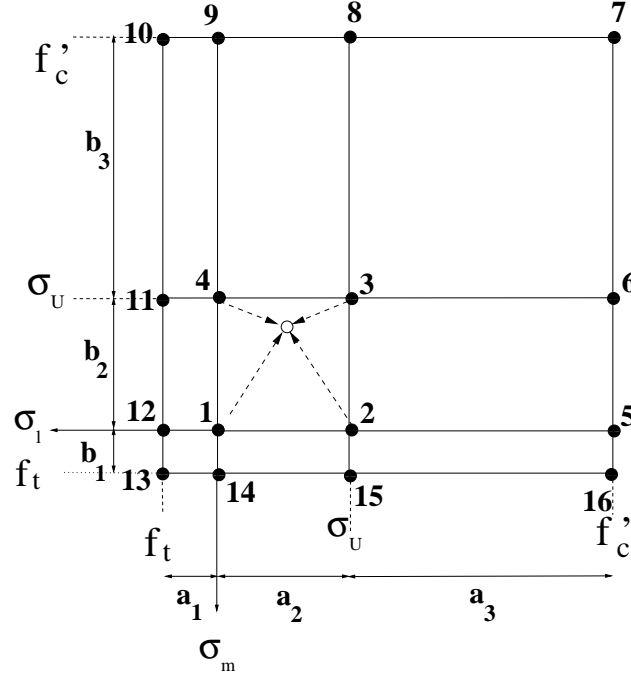
Figure 1.6: Weight Regions

Node			Weights		
No.	σ_l	σ_m	$\sigma_k \geq 0$	$\sigma_k = \sigma_u$	$\sigma_k = f_c'$
1	0.	0.	1/3	0.	0.
2	σ_u	0.	1/2	0.	0.
3	σ_u	σ_u	1.	1/3	0.
4	0.	σ_u	1/2	0.	0.
5	f_c'	0.	1/2	0.	0.
6	f_c'	σ_u	1.	1/2	0.
7	f_c'	f_c'	1.	1.	1/3
8	σ_u	f_c'	1.	1/2	0.
9	0.	f_c'	1/2	0.	0.
10	f_t'	f_c'	1/2	0.	0.
11	f_t'	σ_u	1/2	0.	0.
12	f_t'	0.	1/3	0.	0.
13	f_t'	f_t'	1/3	0.	0.
14	0.	f_t'	1/3	0.	0.
15	σ_u	f_t'	1/2	0.	0.
16	f_c'	f_t'	1/2	0.	0.

Table 1.1: Triaxial Weights

where N_i is the usual two bilinear shape function used in finite element and is given by

$$\mathbf{N}(\sigma_l, \sigma_m) = \frac{1}{ab} \lfloor \ (a - \sigma_l)(b - \sigma_m) \quad \sigma_l(b - \sigma_m) \quad \sigma_l \sigma_m \quad (a - \sigma_l)\sigma_m \ \rfloor \tag{1.13}$$

$$\mathbf{W}(k) = \lfloor \ W_1(\sigma_k) \quad W_2(\sigma_k) \quad W_3(\sigma_k) \quad W_4(\sigma_k) \ \rfloor^t \tag{1.14}$$

$$a = (a_1|a_2|a_3) \qquad b = (b_1|b_2|b_3) \tag{1.15}$$

$$\sigma_l = (\sigma_l|f_c' - \sigma_l) \qquad \sigma_m = (\sigma_m|f_c' - \sigma_m) \tag{1.16}$$

MERLIN AAR Problems

The $i-j$ stress space is decomposed into nine distinct regions, Figure 1.6, where σ_u is the upper (signed) compressive stress below which no AAR expansion can occur along the corresponding direction (except in triaxially loaded cases). Hence, a and b are the dimensions of the quadrant inside which σ_i and σ_j reside.

Weights of the individual nodes are in turn interpolated according to the principal stress component in the third direction σ_k, Table 1.1. It should be noted that those weights are for the most part based on the work of (Larive, 1998) and (Multon, 2004), but in some cases due to lack of sufficient experimental data, based on simple "engineering common sense".

A simple example for weight determination is shown here. Assuming that the principal stresses are given by $\lfloor\ \sigma_l\ \ \sigma_m\ \ \sigma_k\ \rfloor = \lfloor\ -5.0\ \ -8.0\ \ -5.0\ \rfloor$ MPa, and that f_c, f'_t and σ_u are equal to -30.0, 2.0, and -10.0 MPa respectively, we seek to determine W_k.

The stress tensors places us inside the quadrant defined by nodes 1-2-3-4 whose respective weights are equal to: $W_1 = \frac{1}{2}\left(\frac{1}{3}\right) = \frac{1}{6}$, $W_2 = \frac{1}{2}\left(\frac{1}{2}\right) = \frac{1}{4}$, $W_3 = \frac{1}{3} + \frac{1}{2}\left(1.0 - \frac{1}{3}\right) = \frac{2}{3}$, and $W_4 = \frac{1}{2}\left(\frac{1}{2}\right) = \frac{1}{4}$ a and b are both equal to -10 MPa, and the "shape factors" will be $N_1 = \frac{1}{100}\left[(-10+5)(-10+8)\right] = \frac{1}{10}$, $N_2 = \frac{1}{100}\left[-5(-10+8)\right] = \frac{1}{10}$, $N_3 = \frac{1}{100}\left[(-5)(-8)\right] = \frac{4}{10}$, $N_4 = \frac{1}{100}\left[-8(-10+5)\right] = \frac{4}{10}$, and finally $W_k = \frac{1}{10}\times\frac{1}{6} + \frac{1}{10}\times\frac{1}{4} + \frac{4}{10}\times\frac{2}{3} + \frac{4}{10}\times\frac{1}{4} = 0.40833$

Based on the earlier work of Struble and Diamond (1981), in which it was reported that no gel expansion can occur at pressures above 11 MPa (though for a synthetic gel), σ_u is taken as -10 MPa. This value was also confirmed by Larive (1998). f'_t and f'_c are the concrete tensile and compressive strengths respectively.

Individual strain is given by

$$\dot{\varepsilon}_i^{AAR} = W_i\dot{\varepsilon}_V^{AAR} \tag{1.17}$$

and the resulting relative weights are shown in Figure 1.7.

It should be noted that the proposed model will indeed result in an anisotropic AAR expansion. While not explicitly expressed in tensorial form, the anisotropy stems from the different weights assigned to each of the three principal directions.

1.1.5   Degradation

This deterioration being time dependent, the following time dependent nonlinear model is considered, Figure 1.8.

$$
\begin{aligned}
E(t,\theta) &= E_0\left[1 - (1-\beta_E)\,\xi(t,\theta)\right] & (1.18)\\
f'_t(t,\theta) &= f'_{t,0}\left[1 - (1-\beta_f)\,\xi(t,\theta)\right] & (1.19)
\end{aligned}
$$

where E_0 and $f'_{t,0}$ are the original elastic modulus and tensile strength, β_E and β_f are the corresponding residual fractional values when ε_{AAR} tends to ε_{AAR}^∞.

1.2   Nonlinear Continuum Model

Since AAR is likely to cause substantial nonlinear deformation, a nonlinear model for the concrete is essential. Given the diffused nature of the AAR induced damage, AAR is on the one hand a prime candidate for a "smeared" crack model, on the other and major structural cracks are likely to develop (specially in dams)

MERLIN AAR Problems
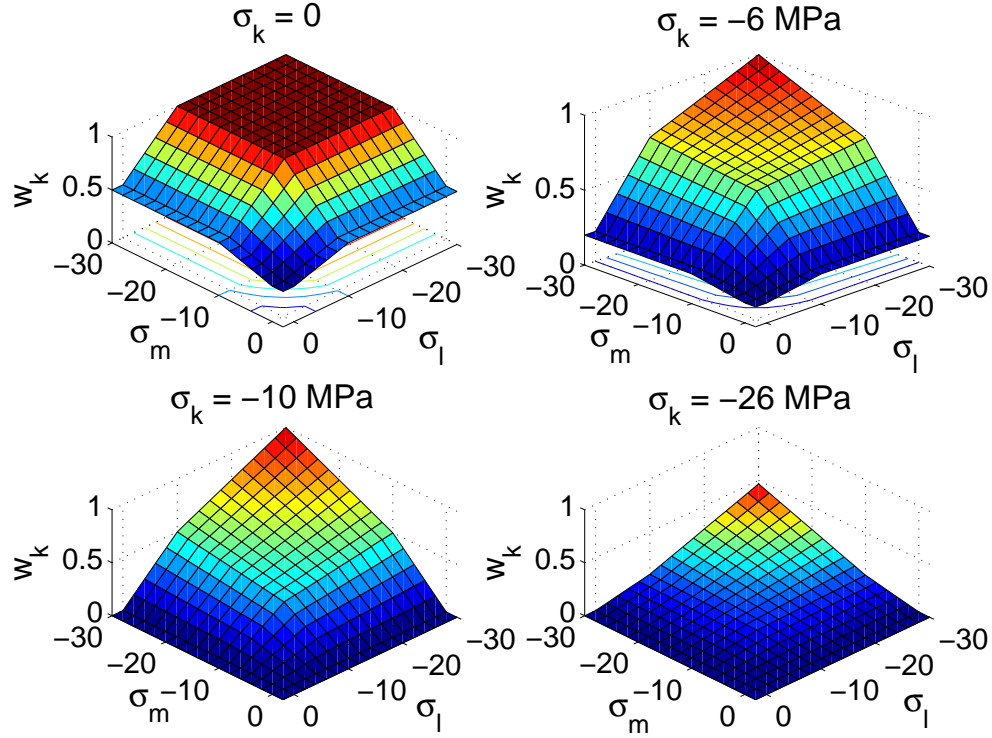
Figure 1.7: Relative Weights
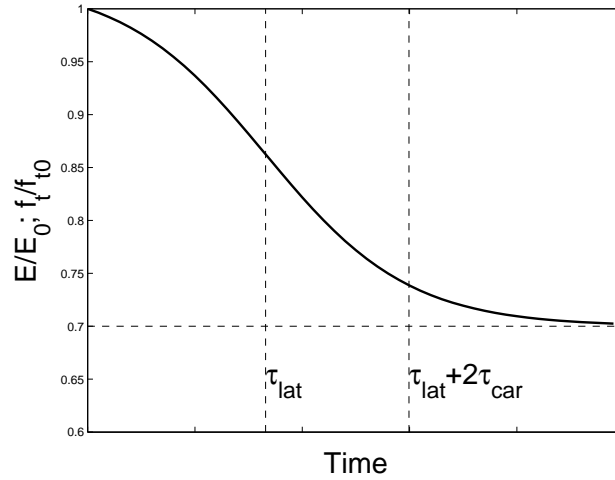
Figure 1.8: Degradation of E and f'_t

for which a "discrete crack" representation is more suitable.

Hence, in the proposed approach, the kinetic model is combined with a nonlinear structural model (uncoupled) which can also combine "smeared" with "discrete" crack for dam analysis.

The structural model, Hansen and Saouma (2003) has three constitutive models concurrently activated. Two for distributed failures implemented in the spirit of plasticity, Červenka and Červenka (1999) and one for localized failure implemented in the spirit of "Fracture Mechanics" (Cervenka, Chandra, and Saouma,

MERLIN AAR Problems

1998).

This fracture-plastic model combines constitutive models for tensile (fracturing) and compressive (plastic) behavior. The fracture model is based on the classical orthotropic smeared crack formulation and crack band model. It employs Rankine failure criterion, exponential (or user defined) softening, and it can be used as rotated or fixed crack model. The hardening/softening plasticity model is based on (Menétrey and Willam, 1995) failure surface. Both models use return mapping algorithm for the integration of constitutive equations. Special attention is given to the development of an algorithm for the combination of the two models. The combined algorithm is based on a recursive substitution, and it allows for the two models to be developed and formulated separately. The algorithm can handle cases when failure surfaces of both models are active, but also when physical changes such as crack closure occur. The model can be used to simulate concrete cracking, crushing under high confinement, and crack closure due to crushing in other material directions.

The method of strain decomposition, as introduced by (Borst, 1986), is used to combine fracture and plasticity models together. Both models are developed within the framework of return mapping algorithm by (Wilkins, 1964). This approach guarantees the solution for all magnitudes of strain increment. From an algorithmic point of view the problem is then transformed into finding an optimal return point on the failure surface. The combined algorithm must determine the separation of strains into plastic and fracturing components, while it must preserve the stress equivalence in both models. The proposed algorithm is based on a recursive iterative scheme. It can be shown that such a recursive algorithm cannot reach convergence in certain cases such as, for instance, softening and dilating materials. For this reason the recursive algorithm is extended by a variation of the relaxation method to stabilize convergence.

1.2.1 Material Model Formulation

The material model formulation is based on the strain decomposition into elastic ε_{ij}^e, plastic ε_{ij}^p and fracturing components ε_{ij}^f (Borst, 1986).

$$\varepsilon_{ij} = \varepsilon_{ij}^e + \varepsilon_{ij}^p + \varepsilon_{ij}^f \tag{1.20}$$

The new stress state is then computed from:

$$\sigma_{ij}^n = \sigma_{ij}^{n-1} + E_{ijkl}(\Delta\varepsilon_{kl} - \Delta\varepsilon_{kl}^p - Delta\varepsilon_{kl}^f \tag{1.21}$$

where the increments of plastic strain $\Delta\varepsilon_{kl}^p$ and fracturing strain $\Delta\varepsilon_{kl}^f$ must be evaluated based on the selected material model.

1.2.2 Rankine-Fracturing Model for Concrete Cracking

Rankine criterion is used for concrete cracking

$$F_i^f = \sigma_{ii}^{\prime t} - f_i^{\prime t} \leq 0 \tag{1.22}$$

where strains and stresses are expressed in material directions. For rotated cracks those correspond to the principal directions, and for the fixed crack model they correspond to the principal ones at the onset of first cracking. Thus, $\sigma_{ii}^{\prime t}$ and $f_{ti}^{\prime}$ are the trial stress and tensile strength in the local material direction i. Prime symbol denotes quantities in the material directions.

MERLIN AAR Problems

Trial stress is determined from the elastic predictor

$$\sigma_{ij}'^{t} = \sigma_{ij}'^{n-1} + E_{ijkl}\Delta\varepsilon_{kl}' \tag{1.23}$$

If Eq. 1.22 is violated (i.e. cracking occurs) then the incremental fracturing strain in direction i can be evaluated under the assumption that the final stress state must satisfy

$$F_i^f = \sigma_{ii}'^{n} - f_{ti}' = \sigma_{ii}'^{t} - E_{iikl}\Delta\varepsilon_{kl}'^{f} - f_{ti}' = 0 \tag{1.24}$$

This equation can be further simplified under the assumption that the increment of fracturing strain is normal to the failure surface, and that always only one failure surface is being checked. Then for surface k the incremental fracturing strain is

$$\Delta\varepsilon_{ij}'^{f} = \Delta\lambda\frac{\partial F_k^f}{\partial\sigma_{ij}} = \Delta\lambda\delta_{ik} \tag{1.25}$$

substituting into Eq. 1.24, the increment of the fracturing multiplier is recovered as

$$\Delta\lambda = \frac{\sigma_{kk}'^{t} - f_{tk}'}{E_{kkkk}} = \frac{\sigma_{kk}'^{t} - f'^{t}(w_k^{max})}{E_{kkkk}} \tag{1.26}$$

where $f'^{t}(w_k^{max})$ is the softening curve in terms of w which is the current crack opening. The softening diagram adopted in this model is the exponential decay function of (Hordijk, 1991). The crack opening w is determined from

$$w_k^{max} = L_t(\hat{\varepsilon}_{kk}'^{f} + \Delta\lambda) \tag{1.27}$$

where $\hat{\varepsilon}_{kk}'^{f}$ is the total fracturing strain in direction k, and L_t is the characteristic dimension of the element as introduced by (Bažant and Oh, 1983), Figure 1.9. L_t is calculated as a size of the element projected into the crack direction, it is a satisfactory solution for low order linear elements.
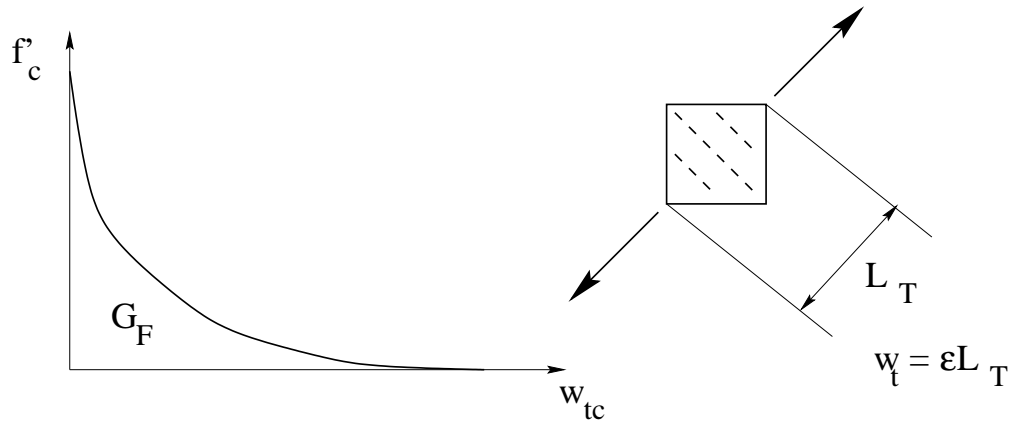
Figure 1.9: Tensile Softening and Characteristic Length, Červenka Consulting, 2019

Eq. 1.26 can be solved by recursive substitution. It can be shown that expanding $f'^{t}(w_k^{max})$ into a Taylor series, that this iteration scheme converges as long as

$$\left|-\frac{\partial f'^{t}(w_k^{max})}{\partial w}\right| < \frac{E_{kkkk}}{L_t} \tag{1.28}$$

MERLIN AAR Problems

This equation is violated for softening materials only when snap-back is observed in the stress-strain relationship, which can occur if large finite elements are used. Since in the standard finite element based method, the strain increment is given, therefore, a snap back on the constitutive level can not be captured. Since in the critical region where snap back occurring on the softening curve will be skipped, then the energy dissipated by the system will be over estimated. Because this is undesirable, finite elements smaller than $L < \frac{E_{kkkk}}{\left| \frac{\partial f'^t(0)}{\partial w} \right|}$ should be used, where $\frac{\partial f'^t(0)}{\partial w}$ is the initial slope of the crack softening curve.

Distinction is made between the total maximum fracturing strain during loading $\hat{\varepsilon}'^f_{kk}$ and the current fracturing strain ε'^f_{ij} which is determined according to (Rots and Blaauwendraad, 1989)

$$
\begin{aligned}
\varepsilon'^f_{kl} &= (E_{ijkl} + E'^f_{ijkl})^{-1} E_{klmn} \varepsilon'_{mm} \qquad (1.29) \\
\sigma'_{ij} &= E'^{cr}_{ijkl} \varepsilon'^f_{kl} \qquad (1.30)
\end{aligned}
$$

where E'^{cr}_{ijkl} is the cracking stiffness in the local material (prime) direction. It is assumed that there is no interaction between normal and shear components thus the crack tensor is given by:

$$
E'^{cr}_{ijkl} = 0 \text{ for } i \neq k \text{ and } j \neq l \qquad (1.31)
$$

The mode I crack stiffness is

$$
E'^{cr}_{iiii} = \frac{f'^t(w_i^{max})}{\hat{\varepsilon}'^f_{ii}} \qquad (1.32)
$$

and mode II and III crack stiffnesses are assumed to be equal to

$$
E'^{cr}_{ijij} = \frac{r_g^{ij} G}{1 - r_g^{ij}} \qquad (1.33)
$$

where $i \neq j$, $r_g^{ij} = \min(r_g^i, r_g^j)$ is the minimum shear retention factors on cracks for the directions i and j and are given by (Kolmar, 1986)

$$
\begin{aligned}
r_g^i &= \frac{-\ln\left(\frac{\varepsilon'_{ii}}{c_1}\right)}{c_2} \qquad (1.34) \\
c_1 &= 7 + 333(\rho - 0.005) \qquad (1.35) \\
c_2 &= 10 - 167(\rho - 0.005) \qquad (1.36)
\end{aligned}
$$

where ρ is the reinforcement ratio assuming that it is below 0.002. G is the elastic shear modulus.

For the special cases before the onset of cracking, when the expressions approach infinity. Large penalty numbers are used for crack stiffness in these cases. The shear retention factor is used only in the case of the fixed crack option.

Finally, the secant constitutive matrix in the material direction is analogous to Eq. 1.29 as presented by (Rots and Blaauwendraad, 1989)

$$
\mathbf{E}'^s = \mathbf{E} - \mathbf{E}(\mathbf{E}'^{cr} + \mathbf{E})^{-1} \mathbf{E} \qquad (1.37)
$$

which should then be transformed to the global coordinate system $\mathbf{E}^s = \Gamma_\varepsilon^T \mathbf{E}'^s \Gamma_\varepsilon$ where Γ_ε is the strain vector transformation matrix (i.e. global to local strain transformation matrix).

MERLIN AAR Problems

1.2.3 Plasticity Model for Concrete Crushing

Starting with the predictor-corrector formula, the stress is determined from

$$\sigma_{ij}^n = \sigma_{ij}^{n-1} + E_{ijkl}(\Delta\varepsilon_{kl} - \Delta\varepsilon_{kl}^p) = \sigma_{ij}^t - E_{ijkl}\Delta\varepsilon_{kl}^p = \sigma_{ij}^t - \sigma_{ij}^p \tag{1.38}$$

where σ_{ij}^t is the total stress, and σ_{ij}^p is determined from the yield function via the return mapping algorithm

$$F^p(\sigma_{ij}^t - \sigma_{ij}^p) = F^p(\sigma_{ij}^t - \Delta\lambda l_{ij}) \tag{1.39}$$

The critical component of this equation is l_{ij} which is the return direction defined by

$$l_{ij} = E_{ijkl}\frac{\partial G^p(\sigma_{kl}^t)}{\partial\sigma_{kl}} \tag{1.40}$$

$$\Rightarrow \Delta\varepsilon_{ij}^p = \Delta\lambda\frac{\partial G^p(\sigma_{ij}^t)}{\partial\sigma_{ij}} \tag{1.41}$$

where $G^p(\sigma_{ij})$ is the plastic potential function whose derivative is evaluated at the predictor stress state σ_{ij}^t to determine the return direction.

The adopted failure surface is the one of Menétrey and Willam (1995) which affords much flexibility in its formulation

$$F_{3p}^P = \left[\sqrt{1.5}\frac{\rho}{f_c'}\right]^2 + m\left[\frac{\rho}{\sqrt{6}f_c'}r(\theta, e) + \frac{\xi}{\sqrt{3}f_c'}\right] - c = 0 \tag{1.42}$$

where

$$m = \sqrt{3}\frac{f_c'^2 - f_t'^2}{f_c'f_t'}\frac{e}{e+1} \tag{1.43}$$

$$r(\theta, e) = \frac{4(1-e^2)\cos^2\theta + (2e-1)^2}{2(1-e^2)\cos\theta + (2e-1)\sqrt{4(1-e^2)\cos^2\theta + 5e^2 - 4e}} \tag{1.44}$$

(ξ, ρ, θ) constitute the Heigh-Westerggard coordinates, f_c' and f_t' are the uniaxial compressive and tensile strength respectively. The curvature of the failure surface is controlled by $e \in \langle 0.5, 1.0 \rangle$ (sharp corner for $e = 0.5$, and circular for $e = 1.0$, Figure 1.10.

The position of the failure surface is not fixed, but rather can move depending on the magnitude of the strain hardening/softening parameter. The strain hardening is based on the equivalent plastic strain which is calculated from $\Delta\varepsilon_{eq}^p = \min(\Delta\varepsilon_{ij}^p)$.

Hardening/softening is controlled by the parameter $c \in \langle 0, 1 \rangle$, which evolved during the yielding/crushing process according to

$$c = \left(\frac{f_c'(\varepsilon_{eq}^p)}{f_c'}\right)^2 \tag{1.45}$$

where $f_c'(\varepsilon_{eq}^p)$ is the hardening/softening law based on uniaxial test, Figure 1.11.

The law shown in Figure 1.11 has an elliptical ascending branch and a linear post-peak softening branch after the peak. The elliptical ascending part depends on strains

$$\sigma = f_{c0} + (f_c - f_{c0}\sqrt{1 - \left(\frac{\varepsilon_c - \varepsilon_{sq}^p}{\varepsilon_c}\right)^2} \tag{1.46}$$

MERLIN AAR Problems
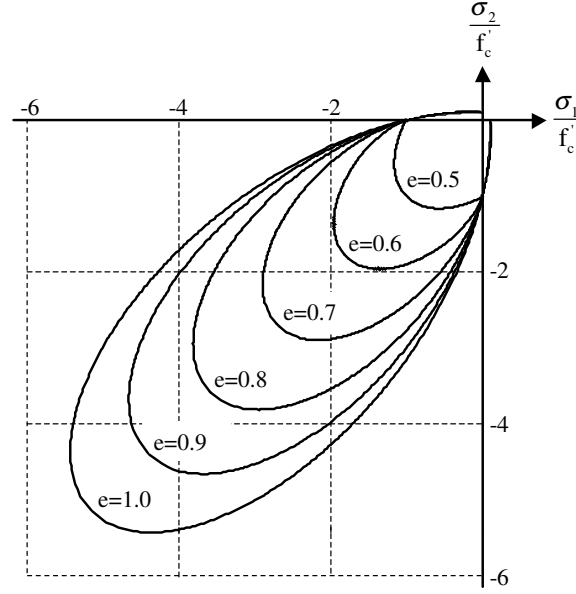
Figure 1.10: Failure Surface

$$w_d = \varepsilon_{eq}^p \, L_c$$
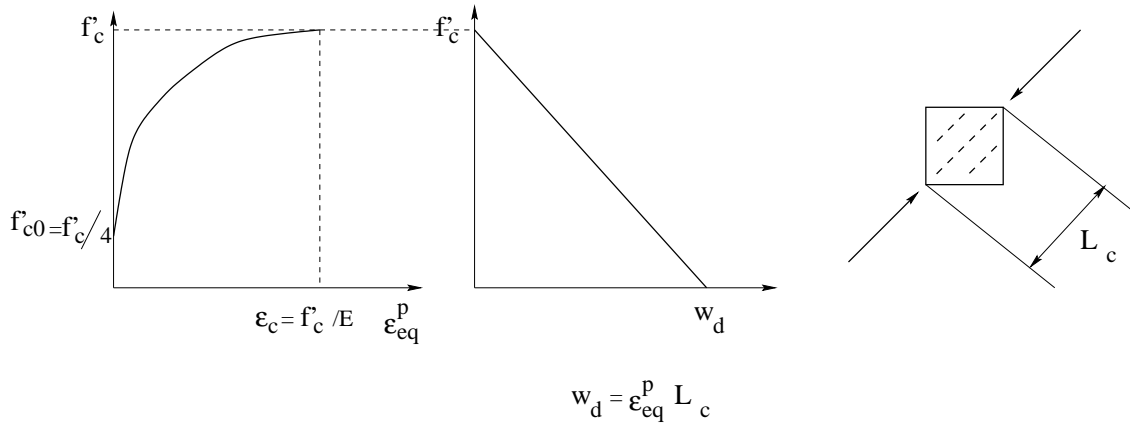
Figure 1.11: Compressive Hardening and Softening, Mier, 1986

while the descending part is based on relative displacements.

In order to introduce mesh objectivity, the descending branch is based on the work of (Mier, 1986) where the equivalent plastic strain is transformed into displacements through the length scale L_c. This parameter is defined in an analogous manner to the crack band parameter in the fracture model, Figure 1.9 and it corresponds to the projection of element size into the direction of minimal principal stresses. The square in Eq. 1.45 is due to the quadratic nature of the Menetrey-Willam surface.

Return direction is given by the following plastic potential

$$G^p(\sigma_{ij}) = \beta \frac{\sqrt{3}}{I_1} + \sqrt{2J_2} \tag{1.47}$$

where β determines the return direction. If $\beta < 0$ material is being compacted during crushing, if $\beta = 0$

MERLIN AAR Problems

material volume is preserved, and if $\beta > 0$ material is dilating. In general the plastic model is non-associated, since the plastic flow is not perpendicular to the failure surface The return mapping algorithm for the plastic model is based on predictor-corrector approach as shown in Figure 1.12.

During the corrector phase of the algorithm the failure surface moves along the hydrostatic axis to simulate hardening and softening. The final failure surface has the apex located at the origin of the Haigh-Westergaard coordinate system. Secant method based Algorithm 1 is used to determine the stress on the surface, which satisfies the yield condition and also the hardening/softening law.
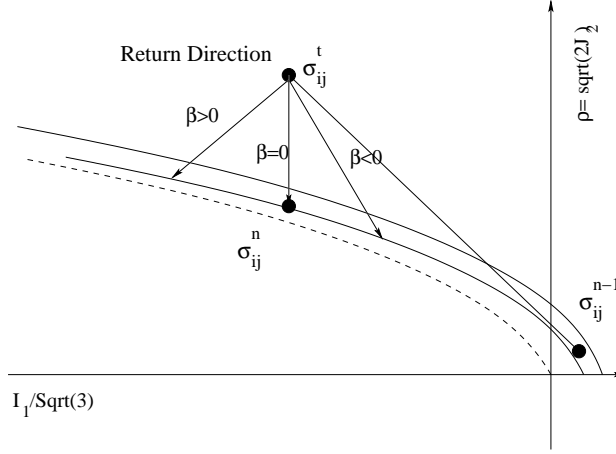
Figure 1.12: Plastic Predictor-Corrector Algorithm (Červenka Consulting, 2019)

Algorithm 1: Input: $\sigma_{ij}^{n-1}, \varepsilon_{ij}^{p^{n-1}}, \Delta\varepsilon_{ij}^{n}$

1. Elastic predictor $\sigma_{ij}^{t} = \sigma_{ij}^{n-1} + E_{ijkl}\Delta\varepsilon_{kl}^{n}$
2. Evaluate failure criterion: $f_A^p = F^p(\sigma_{ij}^t, \varepsilon_{ij}^{p^{n-1}})$, $\Delta\lambda_A = 0$
3. If failure criterion is violated i.e. $f_A^p > 0$
   (a) Evaluate return direction: $m_{ij} = \frac{\partial G^p(\sigma_{ij}^t)}{\partial \sigma_{ij}}$
   (b) Return mapping: $F^p(\sigma_{ij}^t - \Delta\lambda_B E m_{ij}, \varepsilon_{ij}^{p^{n-1}}) = 0 \Rightarrow \Delta\lambda_B$
   (c) Evaluate failure criterion: $f_B^p = F^p(\sigma_{ij}^t - \Delta\lambda_B E m_{ij}, \varepsilon_{ij}^{p^{n-1}}) + \Delta\lambda_B m_{ij}$
   (d) Secant iterations as long as $|\Delta\lambda_A - \Delta\lambda_B| < e$
       i. New plastic multiplier increment: $\Delta\lambda = \Delta\lambda_A - f_A^p \frac{\Delta\lambda_B - \Delta\lambda_A}{f_B^p - f_A^p}$
       ii. New return direction: $m_{ij}^{(i)} = \frac{\partial G^p(\sigma_{ij}^t - \Delta\lambda E m_{ij}^{(i-1)})}{\partial \sigma_{ij}}$
       iii. Evaluate failure criterion: $f^p = F^p(\sigma_{ij}^t - \Delta\lambda E m_{ij}^{(i)}, \varepsilon_{ij}^p + \Delta\lambda m_{ij}^{(i)})$
       iv. New initial values for secant iterations:

$$\begin{aligned} f_B^p < 0 &\Rightarrow f_B^p = f^p, &\Delta\lambda_B = \Delta\lambda \\ f_B^p \geq 0 &\Rightarrow f_A^p = f_B^p, &\Delta\lambda_A = \Delta\lambda_B, \quad f_B^p = f^p, \quad \Delta\lambda_B = \Delta\lambda \end{aligned} \qquad (1.48)$$

   (e) End of secant iteration loop.
4. End of algorithm update stress and plastic strains.

$$\varepsilon_{ij}^{p^n} = \varepsilon_{ij}^{p^{n-1}} + \Delta\lambda_B \ m ij^{(i)} \quad sigma_{ij}^n = \sigma_{ij}^t - \Delta\lambda_B E m_{ij}^{(i)}$$

MERLIN AAR Problems

1.2.4 Combination of Plasticity and Fracture Model

The objective is to combine the above models into a single model such that plasticity is used for concrete crushing and the Rankine fracture model for cracking. This problem can be generally stated as a simultaneous solution of the two following inequalities.

$$F^p(\sigma_{ij}^{n-1} + E_{ijkl}(\Delta\varepsilon_{kl} - \Delta\varepsilon_{kl}^f - \Delta\varepsilon_{kl}^p)) \leq 0 \quad \text{solve for} \quad \Delta\varepsilon_{kl}^p \tag{1.49}$$

$$F^f(\sigma_{ij}^{n-1} + E_{ijkl}(\Delta\varepsilon_{kl} - \Delta\varepsilon_{kl}^p - \Delta\varepsilon_{kl}^f)) \leq 0 \quad \text{solve for} \quad \Delta\varepsilon_{kl}^f \tag{1.50}$$

Each inequality depends on the output from the other one, therefore the following iterative scheme is developed.

Algorithm 2:

1. $F^p(\sigma_{ij}^{n-1} + E_{ijkl}(\Delta\varepsilon_{kl} - \Delta\varepsilon_{kl}^{f^{i-1}} + b\Delta\varepsilon_{kl}^{cor^{(i-1)}} - \Delta\varepsilon_{kl}^{p^{(i)}})) \leq 0$solve for$\Delta\varepsilon_{kl}^{p^{(i)}}$

2. $F^pf(\sigma_{ij}^{n-1} + E_{ijkl}(\Delta\varepsilon_{kl} - \Delta\varepsilon_{kl}^{p^{i-1}} - Delta\varepsilon_{kl}^{f^{(i)}})) \leq 0$solve for$\Delta\varepsilon_{kl}^{f^{(i)}}$

3. $\Delta\varepsilon_{ij}^{cor^{(i)}} = \Delta\varepsilon_{ij}^{f^{(i)}} - \Delta\varepsilon_{ij}^{f^{(i-1)}}$

4. Iterative correction of the strain norm between two subsequent iterations can be expressed as $\|\Delta\varepsilon_{ij}^{cor^{(i)}}\| = (1-b)\alpha^f\alpha^p\|\Delta\varepsilon_{ij}^{cor^{(i-1)}}\|$ where $\alpha^f = \frac{\|\Delta\varepsilon_{ij}^{f^{(i)}} - \Delta\varepsilon_{ij}^{f^{(i-1)}}\|}{\Delta\varepsilon_{ij}^{p^{(i)}}\Delta\varepsilon_{ij}^{p^{(i-1)}}}$ and $\alpha^p = \frac{\|\Delta\varepsilon_{ij}^{p^{(i)}} - \Delta\varepsilon_{ij}^{p^{(i-1)}}\|}{\Delta\varepsilon_{ij}^{f^{(i)}}\Delta\varepsilon_{ij}^{f^{(i-1)}}}$

b is an iteration correction or relaxation factor, which is introduced in order to guarantee convergence. It is to be determined based on the run-time analysis of α^f and α^p, such that the convergence of the iterative scheme can be assured. The parameters α^f and α^p characterize the mapping properties of each model (i.e. plastic and fracture). It is possible to consider each model as an operator, which maps strain increment on the input into a fracture or plastic strain increment on the output. The product of the two mappings must be contractive in order to obtain a convergence. The necessary condition for the convergence is:

$$|(1-b)\alpha^f\alpha^p| < 1 \tag{1.51}$$

If b equals 0, an iterative algorithm based on recursive substitution is obtained. The convergence can be guaranteed only in two cases:

1. One of the models is not activated (i.e. implies α^f or $\alpha^p = 0$
2. There is no softening in either of the two models and dilating material is not used in the plastic part, which for the plastic potential in this work means $\beta < 0$ (Eq. 1.47). This is a sufficient but not necessary condition to ensure that α^f and $\alpha^p < 1$.

It can be shown that the values of α^f and α^p are directly proportional to the softening rate in each model. Since the softening model remains usually constant for a material model and finite element, their values do not change significantly between iterations. It is possible to select the scalar b such that the inequality Eq. 1.51 is satisfied always at the end of each iteration based on the current values of α^f and α^p. There are three possible scenarios, which must be handled, for the appropriate calculation of b:

1. $|alpha^f\alpha^p| \leq \chi$, where χ is related to the requested convergence rate. For linear rate it can be set to $\chi = 1/2$. In this case the convergence is satisfactory and $b = -0$.
2. $\chi < |alpha^f\alpha^p|$, then the convergence would be too slow. In this case b can be estimated as $b = 1 - \frac{|alpha^f\alpha^p|}{\chi}$ in order to increase the convergence rate.
3. $1 \leq |alpha^f\alpha^p|$, then the algorithm is diverging. In this case b should be calculated as $b = 1 - \frac{\chi}{|alpha^f\alpha^p|}$ to stabilize the iterations.

MERLIN AAR Problems

This approach guarantees convergence as long as the parameters does not change drastically between the iterations, which should be satisfied for smooth and correctly formulated models. The rate of convergence depends on material brittleness, dilating parameter β and finite element size. It is advantageous to further stabilize the algorithm by smoothing the parameter b during the iterative process:

$$b = \frac{b^{(i)} + b^{(i-1)}}{2} \tag{1.52}$$

where the superscript i denotes values from two subsequent iterations. This will eliminate problems due to the oscillation of the correction parameter b. Important condition for the convergence of the above Algorithm 2 is that the failure surfaces of the two models are intersecting each other in all possible positions even during the hardening or softening. Additional constraints are used in the iterative algorithm. If the stress state at the end of the first step violates the Rankine criterion, the order of the first two steps in Algorithm 2 is reversed. Also in reality concrete crushing in one direction has an effect on the cracking in other directions. It is assumed that after the plasticity yield criterion is violated, the tensile strength in all material directions is set to zero. On the structural level secant matrix is used in order to achieve a robust convergence during the strain localization process. The proposed algorithm for the combination of plastic and fracture models is graphically shown in Figure 1.13.
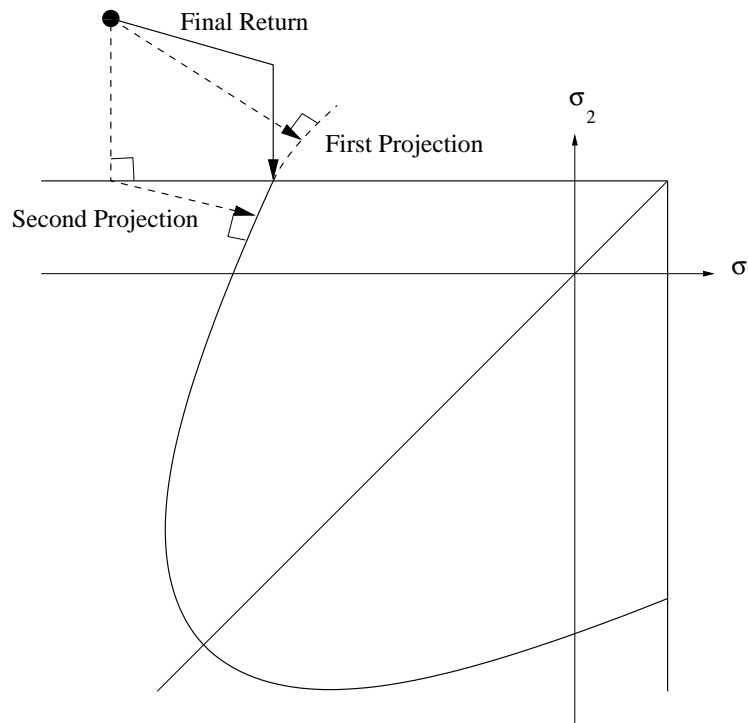
Figure 1.13: Schematic Description of the Iterative Process in 2D (Červenka Consulting, 2019)

When both surfaces are activated, the behavior is quite similar to the multi-surface plasticity. Contrary to the multi-surface plasticity algorithm the proposed method is more general in the sense that it covers all loading regimes including physical changes such as for instance crack closure. Currently, it is developed only for two interacting models, and its extension to multiple models is not straightforward.

MERLIN AAR Problems

1.3   Nonlinear Discrete Joint Element

This subsection discusses the nonlinear modeling of concrete using a discrete crack fracture mechanics based model. It addresses two important issues: mixed mode fracture in homogeneous materials and interface fracture. A new three-dimensional interface crack model is derived. The model is a generalization of classical Hillerborg's fictitious crack model, which can be recovered if shear displacements are set to zero. Several examples are used to validate the applicability of the proposed interface crack model. First, direct shear tests on mortar joints are used to test the model performance in the shear-compression regime. The more complicated combination of shear-tension is investigated using large biaxial tests of concrete-rock interfaces. The applicability to mixed mode cracking in homogeneous concrete is tested using experiments on modified Iosipescu's shear beam and anchor bolt pull-out tests.

1.3.1   Introduction

The assumption of singular stresses at the crack tip is mathematically correct only within the framework of linear elastic fracture mechanics, but physically unrealistic.

In concrete materials, a fracture process zone exists ahead of the crack tip. The most popular model simulating this behavior is Hillerborg's fictitious crack model (FCM), Figure 1.14, (Hillerborg, Modéer, and Petersson, 1976). In a previous work, the classical FCM model was implemented by Reich (1993) for mode I crack propagation, and extended to account for the influence of water pressure inside the crack.

The classical FCM model, defines a relationship between normal crack opening and normal cohesive stresses, and assumes that there are no sliding displacements nor shear stresses along the process zone. This assumption is only partially valid for concrete materials. Based on experimental observations, it is indeed correct that a crack is usually initiated in pure mode I (i.e. opening mode) in concrete, even for mixed mode loading. However, during crack propagation, the crack may curve due to stress redistribution or non-proportional loading, and significant sliding displacements develop along the crack as schematically shown in Figure 1.15.

Therefore, it is desirable to incorporate these shear effects into the proposed crack model. Finally for concrete dams, it is well accepted that the weakest part of the structure is the dam-foundation interface, which is also the location of highest tensile stresses and lowest tensile strength. Given the scope of this work, it is necessary to address this problem.

Hence, the two major objectives of this chapter are:

- Modification of the FCM model to account for shear effects along both the fracture process zone and the true crack.
- Development of an interface model based on fracture mechanics to simulate cracking along rock-concrete interfaces.

The FCM model, within the framework of a discrete crack implementation, can be visualized as an interface between two identical materials. Therefore, we can develop a general model which addresses both objectives.

Interface elements were first proposed by Goodman, Taylor, and Brekke (1968) to model non-linear behavior of rock joints. Since then, numerous interface constitutive models have been proposed for a wide range of applications such as rock-joints Goodman, Taylor, and Brekke (ibid.) masonry structures Lotfi (1992) and concrete fracture Carol, Bažant, and Prat (1992), Feenstra, Borst, and Rots (1991), and Stankowski (1990).

MERLIN AAR Problems
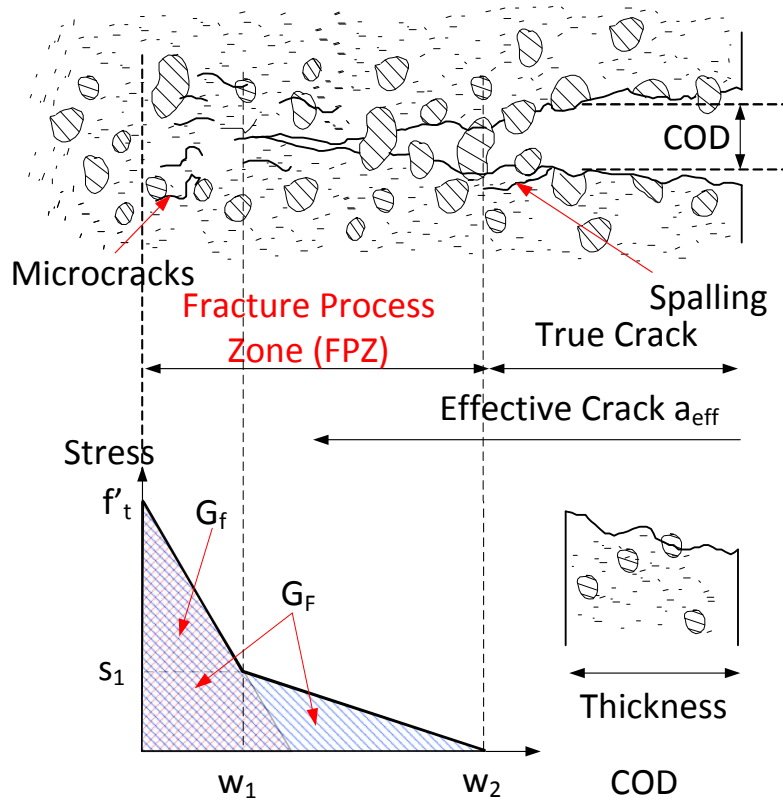
Figure 1.14: Hillerborg's fictitious crack model

In the following section an interface crack model will first be proposed, and then it will be used to simulate cracking both in homogeneous concrete and along a rock-concrete interface. The presented model is a modification of the one first proposed by Carol, Bažant, and Prat (1992).

1.3.2 Interface Crack Model

The objective is to develop a physically sound model, yet simple enough so that all its parameters can be easily derived from laboratory tests. The model should be capable of simulating the behavior of rock-concrete and concrete-concrete interfaces.

Experimental data Saouma et al. (1994) on rock-concrete interfaces show (Figure 1.16) that the decrease in tensile strength is not abrupt, but is rather gradual. This is caused by the presence of the fracture process zone, along which the energy of the system is gradually dissipated.

In the present model, the rock-concrete contact is idealized as an interface between two dissimilar materials with zero thickness. Thus, the objective is to define relationships between normal and tangential stresses with opening and sliding displacements. The notation used in the interface model is illustrated in Figure 1.3.2.

The major premises upon which the model is developed are:
- Shear strength depends on the normal stress.
- Softening is present both in shear and tension.

MERLIN AAR Problems
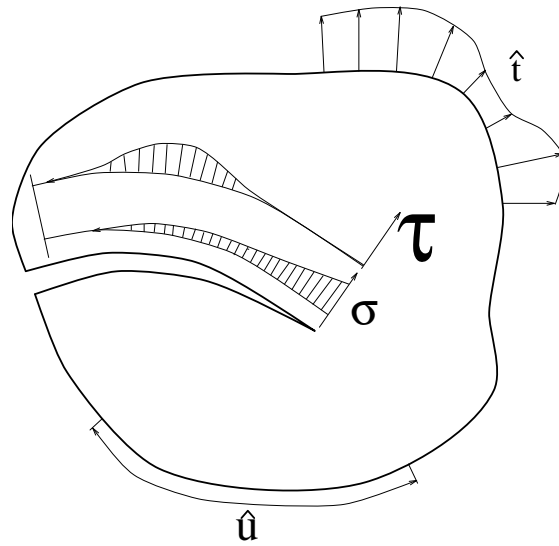
Figure 1.15: Mixed mode crack propagation
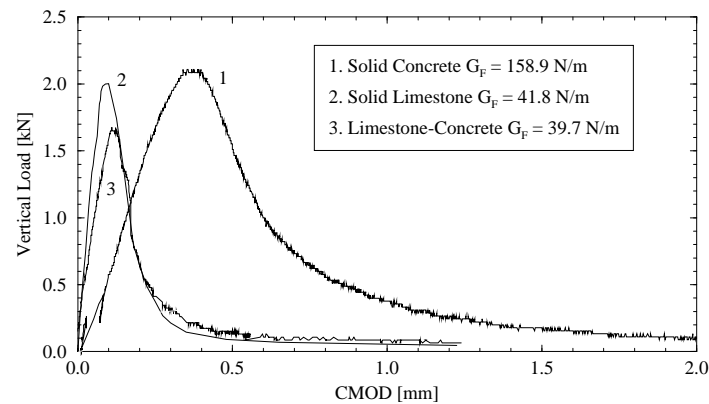
Figure 1.16: Wedge splitting tests for different materials (Saouma et al., 1994)

- There is a residual shear strength due to the friction along the interface, which depends on the compressive normal stress.
- Reduction in strength, i.e. softening, is caused by crack formation.
- There is a zero normal and shear stiffness when the interface is totally destroyed.
- Under compressive normal stresses neither the shear and nor the normal stiffnesses decrease to zero.

MERLIN AAR Problems
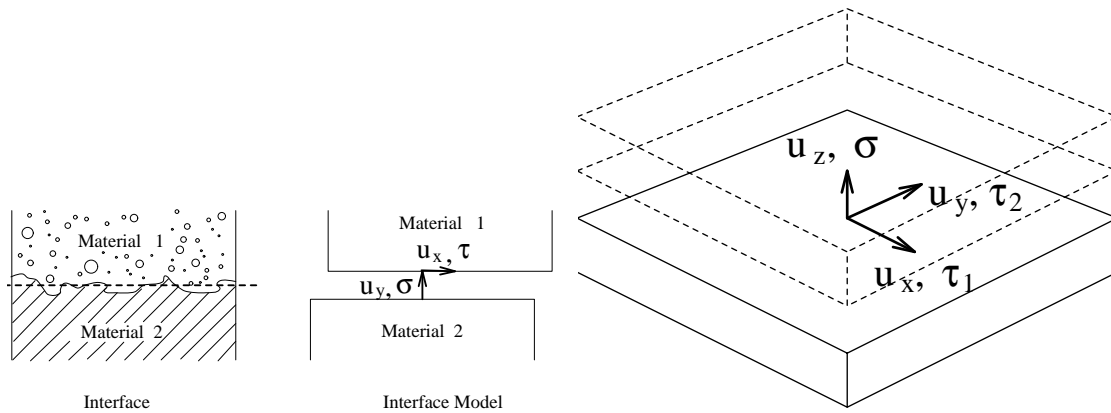
Figure 1.17: Interface idealization and notations

In addition, should a compressive stress be introduced in the normal direction following a full crack opening, two faces of the interface come to contact, and both tangential and normal stiffnesses become nonzero.

- Irreversible relative displacements are caused by broken segments of the interface material and by friction between the two crack surfaces.
- Roughness of the interface causes opening displacements (i.e. dilatancy) when subjected to sliding displacements.
- The dilatancy vanishes with increasing sliding or opening displacements.

Figure 1.18 illustrates the probable character of the fracturing process along an interface.
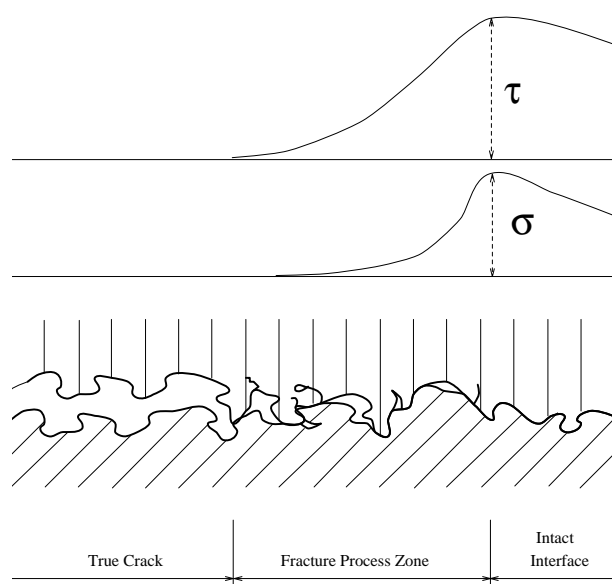
Figure 1.18: Interface fracture

MERLIN AAR Problems

In the proposed model the strength of an interface is described by a failure function:

$$F = (\tau_1^2 + \tau_2^2) - 2\,c\,\tan(\phi_f)(\sigma_t - \sigma) - \tan^2(\phi_f)(\sigma^2 - \sigma_t^2) = 0 \tag{1.53}$$

where:

- c is the cohesion.
- ϕ_f is the angle of friction.
- σ_t is the tensile strength of the interface.
- τ_1 and τ_2 are the two tangential components of the interface traction vector.
- σ is the normal traction component.

The shape of the failure function in two-dimensional case is shown in Figure 1.19, and it corresponds to the failure criteria first proposed by Carol, Bažant, and Prat (1992). The general three-dimensional failure function is obtained by mere rotation around the σ-axis.
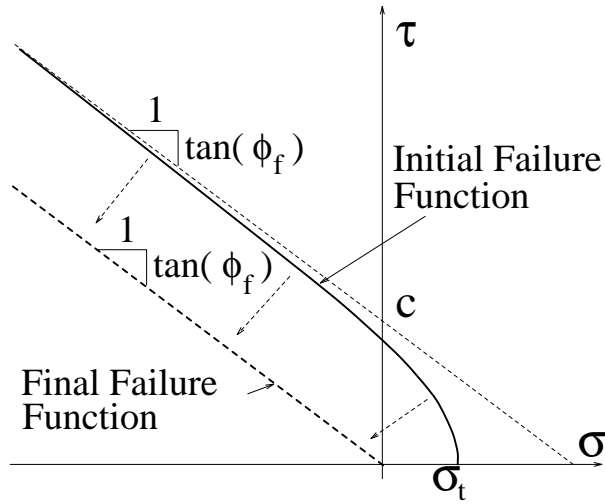
Figure 1.19: Failure function

The evolution of the failure function is based on a softening parameter u^{ieff} which is the norm of the inelastic displacement vector $\boldsymbol{u}^i$. The inelastic displacement vector is obtained by decomposition of the displacement vector $\boldsymbol{u}$ into an elastic part $\boldsymbol{u}^e$ and an inelastic part $\boldsymbol{u}^i$. The inelastic part can subsequently be decomposed into plastic (i.e. irreversible) displacements $\boldsymbol{u}^p$ and fracturing displacements $\boldsymbol{u}^f$. The plastic displacements are assumed to be caused by friction between crack surfaces and the fracturing displacements by the formation of micro-cracks.

$$\begin{aligned} F &= F(c, \sigma_t, \phi_f), \quad c = c(u^{\text{ieff}}), \quad \sigma_t = \sigma_t(u^{\text{ieff}}) \\ \boldsymbol{u} &= \boldsymbol{u}^e + \boldsymbol{u}^i, \quad \boldsymbol{u}^i = \boldsymbol{u}^p + \boldsymbol{u}^f \\ u^{\text{ieff}} &= ||\boldsymbol{u}^i|| = (u_x^{i\,2} + u_y^{i\,2} + u_z^{i\,2})^{1/2} \end{aligned} \tag{1.54}$$

MERLIN AAR Problems

In this work both linear and bilinear relationship are used for $c(u^{\text{ieff}})$ and $\sigma_t(u^{\text{ieff}})$.

$$
\left.
\begin{aligned}
c(u^{\text{ieff}}) &= c_0(1 - \tfrac{u^{\text{ieff}}}{w_c}) && \forall\, u^{\text{ieff}} < w_c \\
c(u^{\text{ieff}}) &= 0 && \forall\, u^{\text{ieff}} \geq w_c \\
w_c &= \tfrac{2G_F^{IIa}}{c_0}
\end{aligned}
\right\} \text{ linear for cohesion}
$$

$$
\left.
\begin{aligned}
c(u^{\text{ieff}}) &= c_0 + u^{\text{ieff}}\tfrac{s_{1c}-c_0}{w_{1c}} && \forall\, u^{\text{ieff}} < w_{1c} \\
c(u^{\text{ieff}}) &= s_c(1 - \tfrac{u^{\text{ieff}}-w_{1c}}{w_c-w_{1c}}) && \forall\, u^{\text{ieff}} \in \langle w_{1c}, w_c\rangle \\
c(u^{\text{ieff}}) &= 0 && \forall\, u^{\text{ieff}} > w_c \\
w_c &= \tfrac{2G_F^{IIa}-c_0 w_{1c}}{s_{1c}}
\end{aligned}
\right\} \text{ bi-linear for cohesion}
$$

(1.55)

$$
\left.
\begin{aligned}
\sigma_t(u^{\text{ieff}}) &= \sigma_{t0}(1 - \tfrac{u^{\text{ieff}}}{w_\sigma}) && \forall\, u^{\text{ieff}} < w_\sigma \\
\sigma_t(u^{\text{ieff}}) &= 0 && \forall\, u^{\text{ieff}} \geq w_{\sigma_t} \\
w_\sigma &= \tfrac{2G_F^{I}}{\sigma_{t0}}
\end{aligned}
\right\} \text{ linear for tensile strength}
$$

$$
\left.
\begin{aligned}
\sigma_t(u^{\text{ieff}}) &= \sigma_{t0} + u^{\text{ieff}}\tfrac{s_{1\sigma}-\sigma_{t0}}{w_{1\sigma}} && \forall\, u^{\text{ieff}} < w_{1\sigma} \\
\sigma_t(u^{\text{ieff}}) &= s_{1\sigma}(1 - \tfrac{u^{\text{ieff}}-w_{1\sigma}}{w_{\sigma_t}-w_{1\sigma}}) && \forall\, u^{\text{ieff}} \in \langle w_{1\sigma}, w_\sigma\rangle \\
\sigma_t(u^{\text{ieff}}) &= 0 && \forall\, u^{\text{ieff}} > w_\sigma \\
w_\sigma &= \tfrac{2G_F^{I}-\sigma_{t0} w_{1\sigma}}{s_{1\sigma}}
\end{aligned}
\right\} \begin{array}{l}\text{bi-linear for} \\ \text{tensile strength}\end{array}
$$

(1.56)

where G_F^I and G_F^{IIa} are mode I and II fracture energies. s_{1c}, w_{1c} and $s_{1\sigma}$, $w_{1\sigma}$ are the coordinates of the breakpoint in the bi-linear softening laws for cohesion and tensile strength respectively. The critical opening and sliding corresponding to zero cohesion and tensile strength are denoted by w_σ and w_c respectively, and they are determined from the condition that the area under the linear or bilinear softening law must be equal to G_F^I and G_F^{IIa} respectively. The significance of these symbols can be best explained through Figure 1.20.
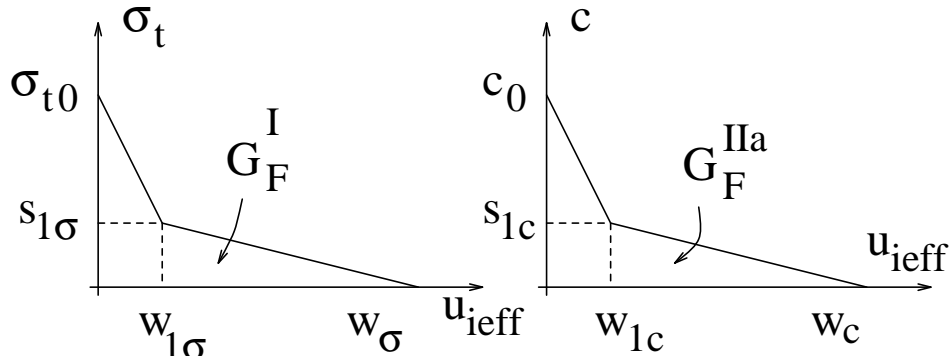
Figure 1.20: Bi-linear softening laws

It should be noted that G_F^{IIa} is not the pure mode II fracture energy (i.e. the area under a τ-u_x curve), but rather is the energy dissipated during a shear test with high confining normal stress. This parameter was first introduced by Carol, Bažant, and Prat (1992) in their micro-plane model. This representation seems to be more favorable to the pure mode II fracture energy G_F^{II}. The determination of G_F^{II} would require

MERLIN AAR Problems

a pure shear test without confinement, which is extremely difficult to perform. Alternatively, a G_F^{IIa} test requires a large normal confinement, and is therefore easier to accomplish. Furthermore, if G_F^{II} is used, the whole shear-compression region of the interface model would be an extrapolation from the observed behavior, whereas the second approach represents an interpolation between the upper bound G_F^{IIa} and the lower bound G_F^I.

The residual shear strength is obtained from the failure function by setting both c and σ_t equal to 0, which corresponds to the final shape of the failure function in Figure 1.19 and is given by:

$$\tau_1^2 + \tau_2^2 = \tan^2(\phi_f)\,\sigma^2 \tag{1.57}$$

Stiffness degradation is modeled through a damage parameter, $D \in \langle 0, 1 \rangle$, which is a relative measure of the fractured surface. Thus, D is related to the secant of the normal stiffness K_{ns} in the uniaxial case:

$$D = \frac{A_f}{A_o} = 1 - \frac{K_{ns}}{K_{no}} \tag{1.58}$$

where K_{no} is the initial normal stiffness of the interface; A_o and A_f are the total interface area and the fractured area respectively.

It is assumed, that the damage parameter D can be determined by converting the mixed mode problem into an equivalent uniaxial one (Figure 1.21). In the equivalent uniaxial problem the normal inelastic displacement is set equal to u^{ieff}. Then, the secant normal stiffness can be determined from:

$$K_{ns} = \frac{\sigma}{u - u^p} = \frac{\sigma_t(u^{\mathrm{ieff}})}{u^e + u^p + u^f - u^p} = \frac{\sigma_t(u^{\mathrm{ieff}})}{\sigma_t(u^{\mathrm{ieff}})/K_{no} + (1-\gamma)u^{\mathrm{ieff}}} \tag{1.59}$$

where γ is the ratio of irreversible inelastic normal displacement to the total value of inelastic displacement. Experimentally, γ can be determined from a pure mode I test through:

$$\gamma = \frac{u_p}{u_i} \tag{1.60}$$

where u^p is the residual displacement after unloading and u^i is the inelastic displacement before unloading, Figure 1.21.
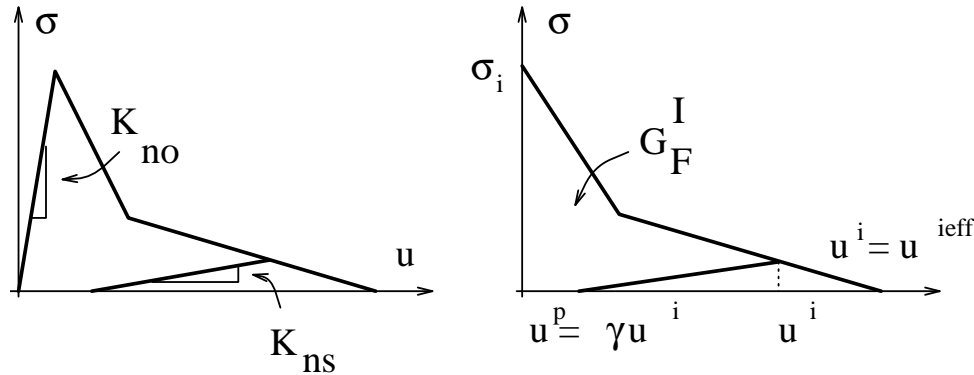
Figure 1.21: Stiffness degradation in the equivalent uniaxial case

MERLIN AAR Problems

For concrete, γ is usually assumed equal to 0.2 Dahlblom and Ottosen (1990) or 0.3 Alvaredo and Whitman (1992). Then, the evolution of the damage parameter D is defined by formula:

$$D = 1 - \frac{\sigma_t(u^{\text{ieff}})}{\sigma_t(u^{\text{ieff}}) + (1-\gamma)u^{\text{ieff}}K_{no}} \tag{1.61}$$

which is obtained by substituting Eq. 1.59 into Eq. 1.58.

The stress-displacement relationship of the interface is expressed as:

$$\boldsymbol{\sigma} = \alpha\mathbf{E}(\boldsymbol{u} - \boldsymbol{u}^p) \tag{1.62}$$

where:

- $\boldsymbol{\sigma}$ is the vector of tangential and normal stress at the interface.

$$\boldsymbol{\sigma} = \{\tau_1, \tau_2, \sigma\}^T \tag{1.63}$$

- α is the integrity parameter defining the relative active area of the interface, and it is related to the damage parameter D.

$$\alpha = 1 - \frac{|\sigma|+\sigma}{2|\sigma|}D \tag{1.64}$$

It should be noted that α can be different from 1 only if the normal stress σ is positive (i.e. the interface is in tension). In other words, the damage parameter D is activated only if the interface is in tension. In compression, the crack is assumed to be closed, and there is full contact between the two crack surface. The activation of D is controlled through the fraction $\frac{|\sigma|+\sigma}{2|\sigma|}$, which is equal to one if σ is positive, and is zero otherwise.

- $\mathbf{E}$ is the elastic stiffness matrix of the interface.

$$\mathbf{E} = \begin{bmatrix} K_{to} & 0 & 0 \\ 0 & K_{to} & 0 \\ 0 & 0 & K_{no} \end{bmatrix} \tag{1.65}$$

It should be noted, that the off-diagonal terms in the elastic stiffness matrix $\mathbf{E}$ of the interface are all equal to zero, which implies that no dilatancy is considered in the elastic range. The dilatancy is introduced later after the failure limit has been reached through the iterative solution process. The dilatancy of the interface is given by dilatancy angle ϕ_d, which is again assumed to be a function of u^{ieff}. In the proposed model, a linear relationship is assumed:

$$\begin{array}{lll} \phi_d(u^{\text{ieff}}) &=& \phi_{d0}\big(1 - \frac{u^{\text{ieff}}}{u_{dil}}\big) \quad \forall u^{\text{ieff}} \leq u_{dil} \\ \phi_d(u^{\text{ieff}}) &=& 0 \qquad\qquad\quad \forall u^{\text{ieff}} > u_{dil} \end{array} \tag{1.66}$$

where u_{dil} is the critical relative displacement after which, the interface does not exhibit the dilatancy effect any more, and ϕ_{d0} is the initial value of the dilatancy angle.

MERLIN AAR Problems

1.4 Dam Analysis Data Preparation

Finally, a typical application to a 2D analysis of an arch gravity dam is presented. Further details of an extensive 2D parametric study, and a 3D practical application will be separately presented (Saouma and Perotti, 2004), Figure 1.22.
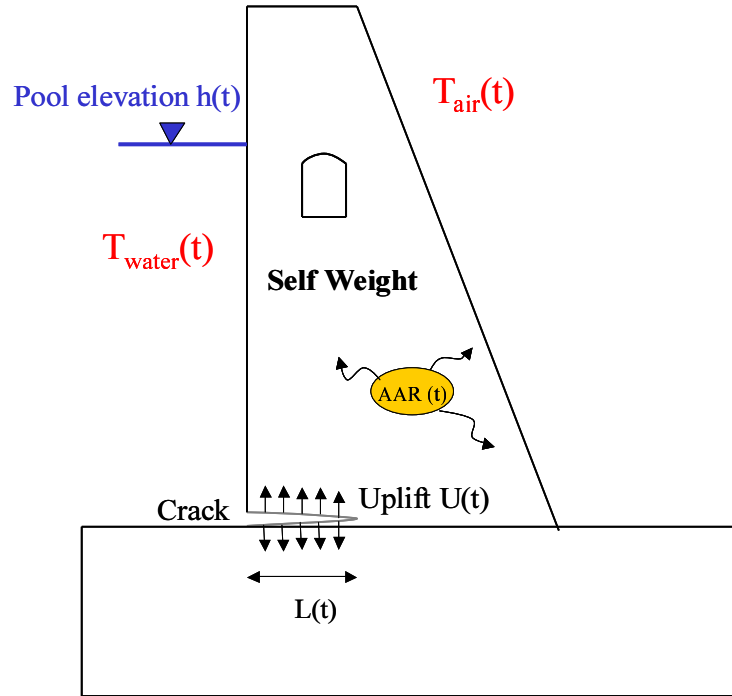
Figure 1.22: Temporal Variation of Load

The comprehensive incremental AAR analysis of a concrete dam is relatively complex, irrespective of the selected AAR model, as data preparation for the load can be cumbersome.

First the seasonal pool elevation variation (for both thermal and stress analysis), and the stress free temperature, T_{ref} (typically either the grouting temperature, or the average yearly temperature) must be identified, along with the external temperature.

Then, a transient thermal analysis is performed since the reaction is thermodynamically activated, and the total temperature is hence part of the constitutive model. Heat transfer by conduction and convection are accounted for, radiation is not (though it could be factored in. The selected incremental time was two weeks, and the initial reference temperature set to zero. Given the external air temperature, the pool elevation, and the water temperature boundary conditions were set to this initial boundary value problem. Analysis is performed with Merlin, and temperature fields examined. It was determined that after four years the temperature field is harmonic with a one year frequency. At that point, the analysis is interrupted and $T_{thermal}(x, y, t)$ saved.

Following the thermal analysis, $T_{thermal}(x, y, t)$ must be transferred to $T_{stress} x, y, t$ as in general we do not have the same finite element mesh (foundations, joints and cracks are typically not modeled in the thermal analysis). Following this, a comprehensive input data file must be prepared for the stress analysis. It includes:

MERLIN AAR Problems

1. Gravity load (first increment only).

2. $\Delta \dot{T}(x, y, t) = \dot{T}_{stress}(x, y, t) - T_{ref}$ in an incremental format. This is a delicate step which can not be overlooked. In particular the stress analysis is based on the difference between actual and stress free temperature. In addition an incremental analysis, requires this set of data to be given in an incremental form.

3. Stress free referenced temperature which will be added to the temperature data to determine the total absolute temperature needed for AAR.

4. Cantilever and dam/foundation joint characteristics. The first must be accounted for in an arch dam, as the expansion may lead to upstream joint opening. The second must be accounted for as the AAR induced swelling may result in separation of the dam from the foundation in the central portion of the foundation.

5. Uplift load characteristics (typically in accordance with the upstream hydrostatic load).

6. AAR data as described above.

Finally, the assembled set of data must be looped over at least fifty years to provide a complete and correct set of natural and essential boundary conditions. For a 2D problem, this will result in files approximately 45 MB.

MERLIN AAR Problems

Part II

RILEM Benchmark Problems

Chapter 2

P1: Constitutive Model

2.1   Problem Description

As previously mentioned, Merlin's constitutive model is completely disassociated from AAR's, and is first tested in this section. Hence, P1 seeks to capture the nonlinear response of concrete when subjected to a load history covering both tension and compression. Simulation is conducted for a 16×32 cm cylinder shown in Figure 2.1 (same mesh will be used for all test problems).

(a) Mesh of concrete cylinder

(b) Mesh of concrete cylinder and steel jacket
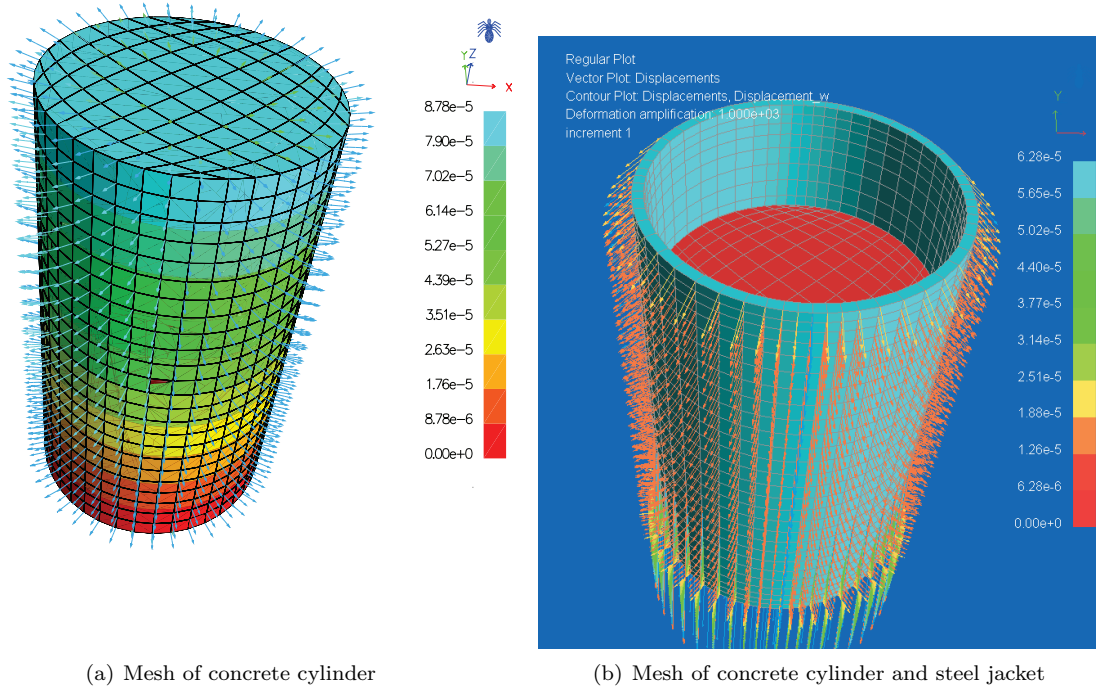
Figure 2.1: Finite element model for concrete cylinders

2.2   Simulations

Two simulations are conducted, the first without AAR, and for a strain history given by

$$0 => 1.5\frac{f'_t}{E} => 0 => 3\frac{f'_t}{E} => 1.5\epsilon_c => 0 => 1.5\epsilon_c \tag{2.1}$$

and the second for an identical strain history which is however preceded by a AAR expansion. For both cases, properties are given in Table 2.1.

Material parameters	Symbol	Unit	Value
Young's Modulus (Static)	E_s	MPa	37300.
Poisson's Ratio (Static)	ν_s	-	0.2
Tensile Strength	f_t	MPa	3.5
Fracture Energy	Γ_f	MN/m	$1.00\ 10^{-4}$
Compressive Strength	f_c	MPa	-38.4
Compressive Critical Displacement	w_d	m	-0.5
Return Direction Factor	β	-	0.
Failure Surface Roundness Factor	e	-	0.52
Onset of Compression Nonlinearity	f_{c0}	MPa	-13.3
Plastic Strain at f_c	ϵ_c	-	$-2.0\ 10^{-3}$
AAR parameters	Symbol	Unit	Value
Maximum Volumetric AAR Strain	ϵ^∞	-	50×10^{-4}
Characteristic Time	τ_{car}	ATU	3.34
Latency Time	τ_{lat}	ATU	8.29
Activation Energy for Characteristic Time	U_C	K	5400.
Activation Energy for Latency Time	U_L	K	9400.
Reference Temperature of Test	T_0	^oC	38.
Tensile Strength	f_t	MPa	3.5
Compressive Strength	f_c	MPa	-38.4
Residual Reduction Factor in Tension	Γ_r	-	0.1
Fraction of Tension pre-AAR Compressive Reduction	γ_t	-	0.23
Upper Compressive Stress Limit	σ_u	MPa	-10.
Shape Factor for Γ_c	β	-	-2.
Reduction Factor for Young's Modulus	β_E	-	0.35
Reduction Factor for Tensile Strength	β_f	-	0.4

Table 2.1: Constitutive Model and AAR Properties

Figure 2.2 plots the load-displacement curve at the top of the cylinder. In both cases, the curve load-displacement at the top of the cylinder surface is plotted. The AAR expansion vs time is also plotted.

First, we observe the model nonlinear response with a peak compressive strength of about -38 Mpa, and an onset of nonlinearity of about -13. MPa. The tensile strength of 3.5 MPa is also reduced by the specified $\beta_t = 0.4$ to about 1.4 MPa, and finally the elastic modulus degradation of β_E is also clearly captured.

MERLIN AAR Problems

(a) Compression

(b) Tension

(c) AAR Swelling
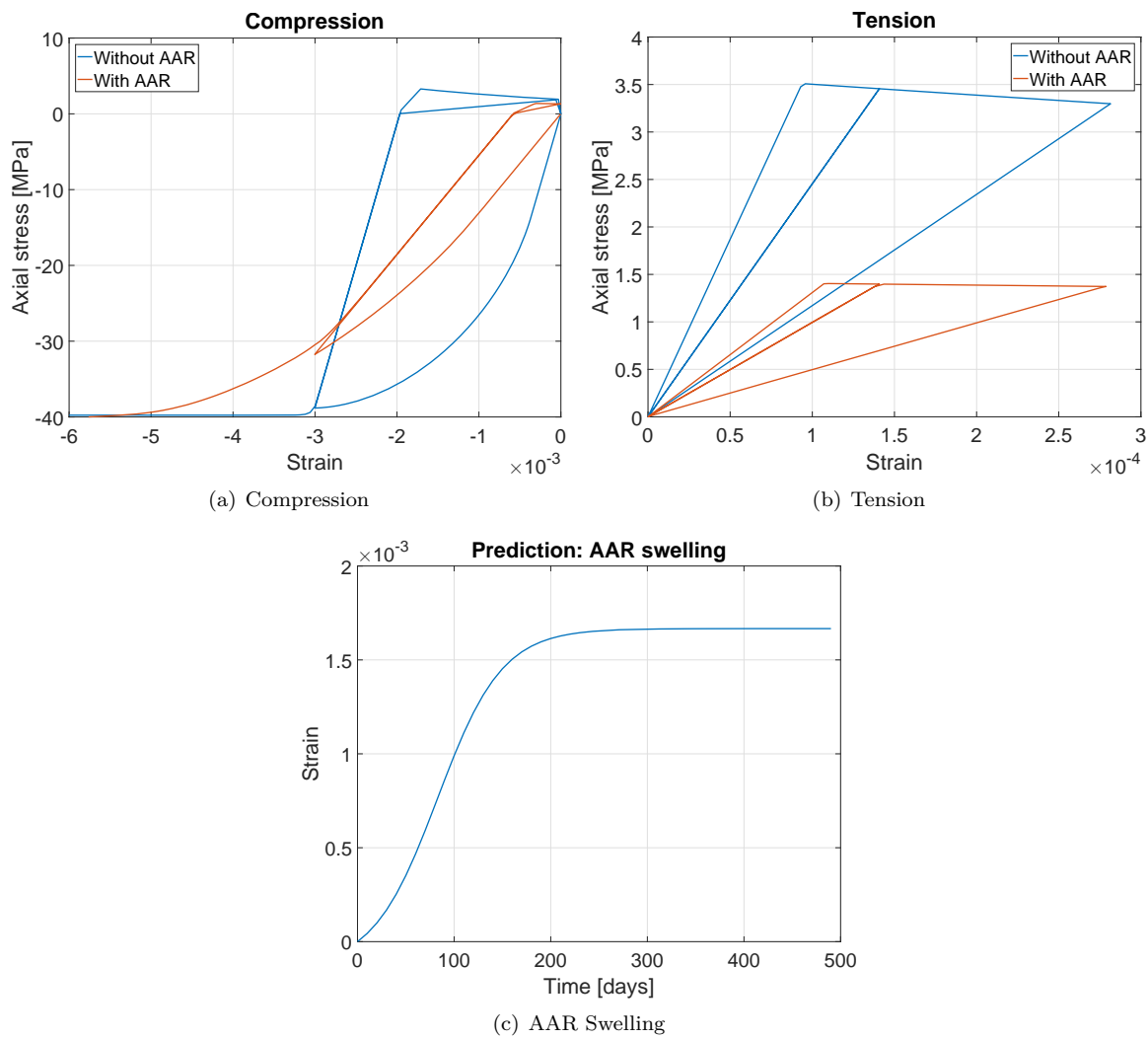
Figure 2.2: Results of Constitutive Model

MERLIN AAR Problems

Chapter 3

P2: Drying and Shrinkage

3.1 Introduction

This problem was not addressed for two reasons. First the importance of drying and shrinkage is really minimal for dams (except for an insignificant layer of concrete) and thus, the overall impact of such a simulation is almost nil. Furthermore, the effect of shrinkage is mitigated by the difference in time scales for shrinkage and AAR. However, this is only true for massive hydrostatic structures and not for reinforced concrete structures exposed to air under varying humidity conditions (though an accurate structural analysis to assess the effect of AAR for those structures is seldom, if ever, warranted). Secondly, Merlin is currently unable to handle shrinkage.

Chapter 4

P3: Creep

4.1 Introduction

It is well established that creep plays a dominant role in the long term response of massive concrete structures subjected to even moderate compression. Indeed, in some cases AAR's strain may be offset by the creep induced contraction.

A simple way to account for creep is to determine the time varying creep coefficient $(\Phi(t))$ as follows:

$$\sigma(t) = \frac{E_0}{1 + \phi} \varepsilon(t) \Rightarrow \phi(t) = \frac{E_0 \epsilon(t)}{\sigma(t)} - 1 \tag{4.1}$$

Since creep can not be explicitly modeled in Merlin, at each time step the young modulus is modified according to

$$E(t) = \frac{E_0}{1 + \phi(t)} \tag{4.2}$$

Figure 4.1(a) shows the experimentally determined vertical strain *vs.* time (for non reactive concrete) as reported by Multon (2004), and the correspondingly computed $\phi(t)$ in Figure 4.1(b).

(a) Experimental data from (Multon, 2004)

(b) Experimental vertical strain for non-reactive concrete
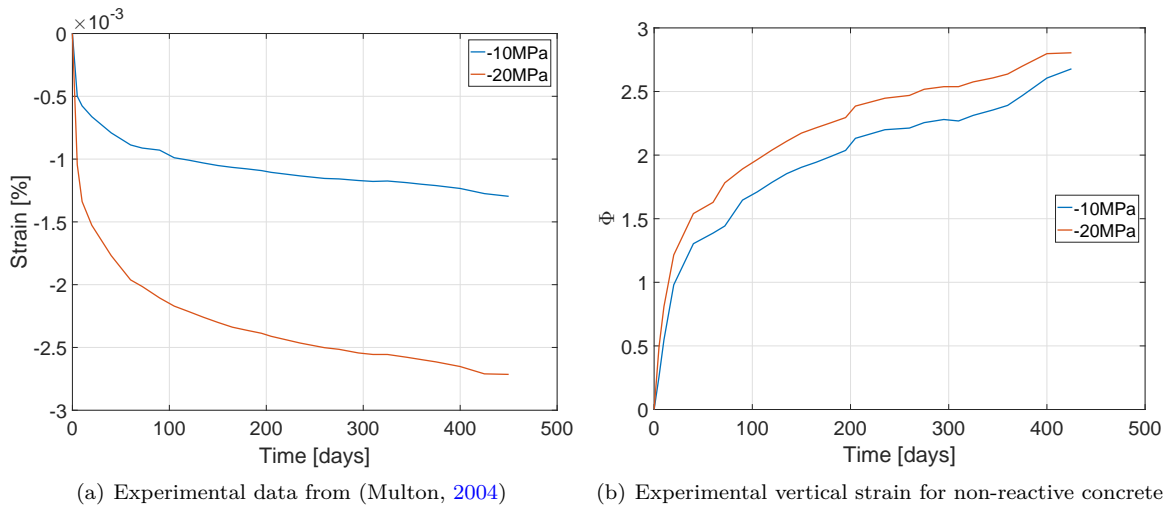
Figure 4.1: Determination of creep coefficient Φ from non reactive concrete

4.2 Simulations

A linear (visco-) elastic constitutive model, and the AAR's parameters shown in Table 4.1 are used for a 13×24 cm cylinder concrete cylinder.

Material parameters	Symbol	Unit	Value
Young's Modulus	E_s	MPa	33600.
Poisson's Ratio	ν_s	-	0.2
Maximum Volumetric AAR Strain	ϵ^∞	-	50×10^{-4}
Characteristic Time	τ_{car}	ATU	3.34
Latency Time	τ_{lat}	ATU	8.29
Activation Energy for Characteristic Time	U_C	K	5400.
Activation Energy for Latency Time	U_L	K	9400.
Reference Temperature of Test	T_0	^oC	38.
Tensile Strength	f_t	MPa	10.
Compressive Strength	f_c	MPa	-30.
Residual Reduction Factor in Tension	Γ_r	-	0.1
Fraction of Tension pre-AAR Compressive Reduction	γ_t	-	0.23
Upper Compressive Stress Limit	σ_u	MPa	-10.
Shape Factor for Γ_c	β	-	-2.
Reduction Factor for Young's Modulus	β_E	-	1.
Reduction Factor for Tensile Strength	β_f	-	1.

Table 4.1: Effect of Creep - Material and AAR Properties

Nine numerical simulations of experimental tests are performed:

Validation AAR expansion at -2, -5, -10 and -20 MPa with (using the creep coefficients shown in Figure 4.1) and without creep.

Prediction Based on a time-varying compressive stress history.

where traction was applied on the frictionless top of the cylinder. Convergence criteria (Energy Error, Relative Residual Error, Absolute Residual Error and Displacement Error) were all set to 0.01.

In Figure 4.2(a) we examine numerical and experimental axial strain:

- In the absence of creep, the experimental (a) and numerical (b) results without creep are reasonably close and in the absence of an axial compressive stress they are highest.
- Amongst experimental results, largest swelling is (a) (no compressive stress), followed by (c) and (e) (with axial stresses of -10 and -20 MPa respectively).
- Amongst numerical predictions, in descending order of expansion: (b) with no axial stresses followed by (c), (d), and (f), where the corresponding axial stresses are 0, -10 and -20 MPa respectively.

In Figure 4.2(b) the -2 MPa stress is still too low to overcome the AAR expansion, and thus it is the only case where a positive strain takes place. For stresses higher than -10 MPa, the AAR is zero and the combined elastic and AAR strain are thus well into the negative range, while for -5 and -10 MP the net axial strain is almost nil.

In Figure 4.2(c) we examine the radial strain. In this axi-symmetric problem, we note that, with an imposed axial stress of -10 and -20 MPa, both experimental and numerical strains are about equal to 2.5^{-3} which is half ε^∞ thus reinforcing the notion that AAR's strain redistribution (or anisotropic expansion) observed by experimentalists and the author's model. Then the smaller the imposed axial stress, the smaller the final radial AAR's strain is, and it would be about equal to ε^∞ when there is no creep.

MERLIN AAR Problems

In Figure 4.2(d) we examine the radial strain in this axi-symmetric problem, we note that both experimentally and numerically they are about equal to 2.5×10^{-3} which is half ε^{∞}, thus reinforcing the notion of AAR's strain redistribution (or anisotropic expansion) observed by researchers and embedded in the author's model. It should be noted that the radial strain is also mildly affected by the Poisson's radial expansion.

(a) Influence of creep in AAR swelling, axial total strain

(b) Total axial strain (numerical)

(c) Total radial strain with creep (numerical)

(d) Influence of creep in AAR swelling, radial total strain
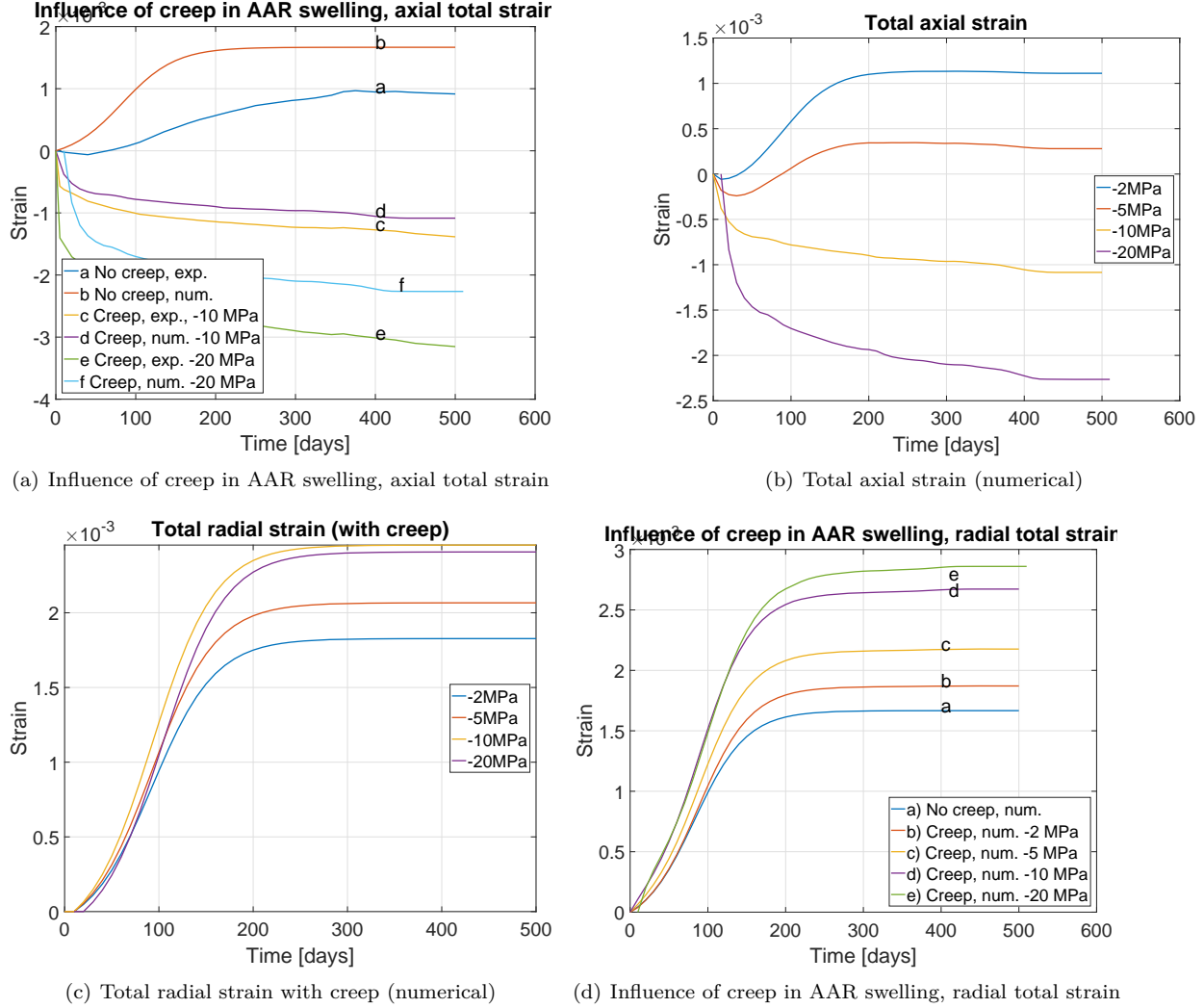
Figure 4.2: Numerical results of calibration for Creep; Part 1

We then examine each stress value separately. In Figure 4.3(a), -2 MPa shows that the effect of creep is almost nil. The largest expansion is radially (between third and half of ε^{∞} and the lowest is also radially (less than third of ε^{∞}). Creep has no influence on the axial strain which is still positive (that is the expansion is larger than the elastic/creep contraction), nor on the radial strain, which is still positive too (that is the expansion is larger than the Poisson's effect due to the elastic/creep contraction).

Figure 4.3(b) the stress is now -5 MPa, and observations are the same as for the preceding case of -2 MPa; however, the larger imposed stress accentuate them.

Figures 4.3(c) and 4.3(d) corresponds to the axial strain under -10 MPa, (c) with axial strains and (d) with radial strains. Curves (a) and (b) in Figure 4.3(c) shows that the creep doesn't have any impact on the vertical strain, which is correct: there is not supposed to be any AAR's expansion in the direction if

MERLIN AAR Problems

(a) Case -2MPa

(b) Case -5MPa

(c) Case -10MPa (axial strain)

(d) Case -10MPa (radial strain)

(e) Case -20MPa (axial strain

(f) Case -20MPa (radial strain)
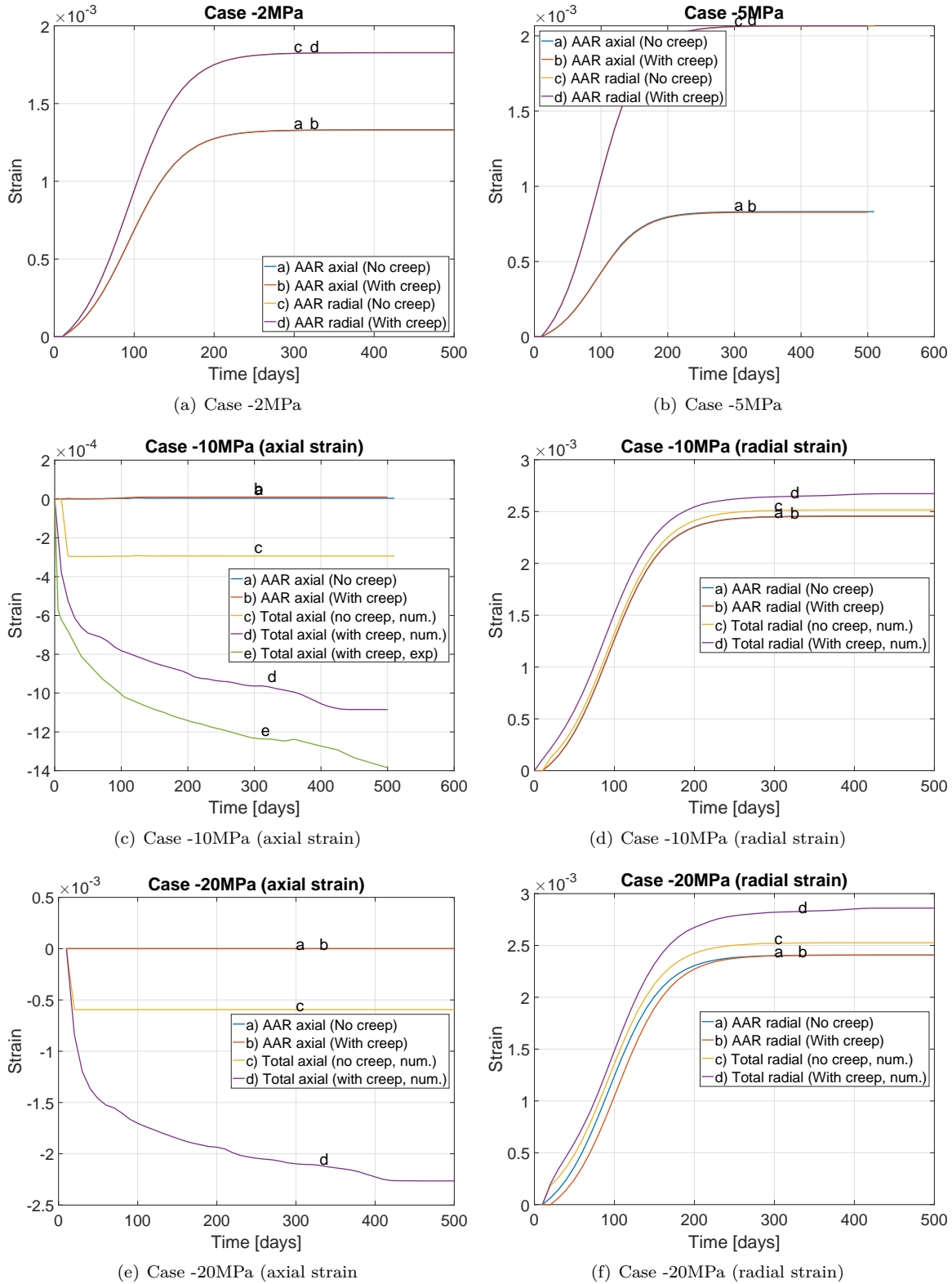
Figure 4.3: Numerical results of calibration for Creep, part 2

MERLIN AAR Problems

the stress exceeds -10 MPa. Curve (c) gives the total strain without creep, so this is the elastic strain (once again, there is no AAR's strain here). Finally, curves (d) and (e) show numerical and experimental strain in axial direction, they are reasonably close.

For Figure 4.3(d), we note that creep doesn't have any impact, except through Poisson's effect. Note that we reach half of ε^∞ i.e. 2.5×10^{-5}.

Figures 4.3(e) and 4.3(f) correspond to the axial strain under -20 MPa, (e) with axial strains and (f) with radial strains. Same conclusions can be made as with -10 MPa: creep doesn't have any impact on AAR strains, except through Poisson's effect.

Finally, a prediction for the response of a cylinder subjected to an time varying axial stress shown in Figure 4.4(a) is performed. Using an average of the two $\phi(t)$ (corresponding to -10 and -20 MPa), response is shown in Figure 4.4.

(a) Imposed Stress

(b) Axial and radial strains
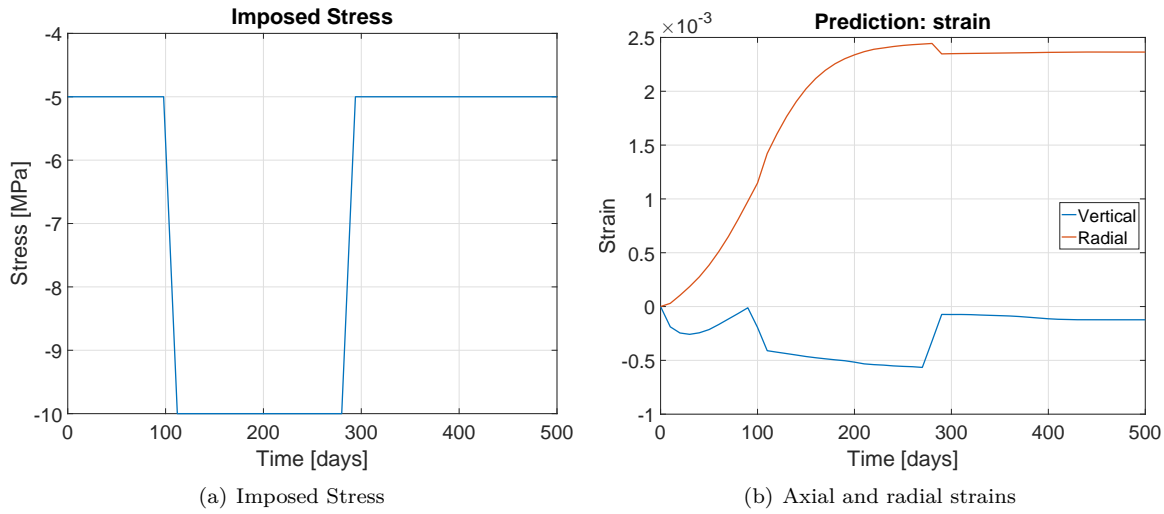
Figure 4.4: Numerical results of prediction

First, the vertical elastic strain, compounded by creep decreases down to a minimum of about -2.5×10^{-4} at about 20 days. At that point, AAR's expansion rate is almost nil, smaller than the contraction due to creep, and thus the strain decreases. Then the AAR's expansion starts, and the strain is increasing again, AAR's expansion is starting to overcome the elastic strain.

Then the axial stress is increased from -5 to -10 MPa, and the elastic strain compounded with creep causes a further contraction. At -10 MPa, the AAR axial expansion is completely inhibited (and redirected in the radial direction), and all strain increase is solely due to creep. When the stress is again dropped from -10 to -5 MPa there is a rebound, and from that point onward both creep contraction and (reduced) AAR's expansion are at work. However, at that point, the propensity for AAR has been exhausted, and mst of it occurred along the radial direction (which is close to 2.5^{-3} at the end), so it cannot compensate for the elastic strain. In the radial direction, we observe an opposite behavior. First, due to the basic AAR's expansion in this direction, plus the redirected AAR's expansion between 100 and 300 day, and finally because of Poisson's effect.

MERLIN AAR Problems

Chapter 5

P4: AAR Expansion; Temperature Effect

5.1 Introduction

All chemical reactions are thermodynamically driven. Reactive concrete expansions varies widely with temperature ranges usually encountered in the field of laboratories. Hence, it is of paramount importance that the kinetics of the reaction captures this dependency.

Hence, a simulation of Larive's tests (Larive, 1998) on a 13×24 cm concrete cylinder is performed using the corresponding properties given in Table 5.1.

5.2 Simulations

Three simulations are performed:

Validation : By simulating the free expansion at 23^oC and 38^oC for which Figure 5.1(a) shows the experimental data (the large variability should be noticed).

Prediction for a harmonic temperature variation given by

$$T(days) = \frac{T_{max} - T_{min}}{2} \sin(2\pi \frac{t/7 - 16}{52}) + \frac{T_{max} + T_{min}}{2} \tag{5.1}$$

Where T_{max} and T_{min} are 25^0C and 0^oC respectively, Figure 5.1(b).

Again analysis are performed on a cylinder and all the convergence criteria (Energy Error, Relative Residual Error, Absolute Residual Error and Displacement Error) are set to to 0.01.

Figure 5.2(a) shows the predicted expansion versus time for the two temperature. As anticipated, expansion is much faster at the higher temperature. Furthermore, the numerically predicted AAR strain are close to the experimentally obtained one from which critical data was calibrated (ε^∞, τ_{lat} and $\tau char$), Figure 5.1(a).

Results for the prediction are shown in Figure 5.2(b). The harmonic thermal strain ($\epsilon_{th} = \alpha.\Delta T$) is first given, and the one caused by AAR is simply given by $\epsilon_{AAR} = \epsilon_{total} - \epsilon_{th}$.

We note that the AAR strain is flat for low temperature (and thus the plateau), and the total strain increases with time due to the combined effects of AAR expansion and temperature. The decreases are

Material parameters	Symbol	Unit	Value
Thickness	h	m	1.
Mass Density	ρ	Gg/m^3	2.4 10^{-3}
Coefficient of Thermal Expansion	α	$/^oC$	1.0 10^{-5}
Young's Modulus	E_s	MPa	33600.
Poisson's Ratio (Static)	ν_s	-	0.2
Tensile Strength	f_t	MPa	10.
Compressive Strength	f_c	MPa	-30.
AAR parameters	Symbol	Unit	Value
Maximum Volumetric AAR Strain*	ϵ^∞	-	65.4×10^{-4}
Characteristic Time*	τ_{car}	ATU	3.34
Latency Time*	τ_{lat}	ATU	8.29
Activation Energy for Characteristic Time*	U_C	K	5400.
Activation Energy for Latency Time*	U_L	K	9400.
Reference Temperature of Test	T_0	^oC	38.
Tensile Strength	f_t	MPa	10.
Compressive Strength	f_c	MPa	-30.
Residual Reduction Factor in Tension	Γ_r	-	0.1
Fraction of Tension pre-AAR Compressive Reduction	γ_t	-	0.23
Upper Compressive Stress Limit	σ_u	MPa	-10.
Shape Factor for Γ_c	β	-	-2.
Reduction Factor for Young's Modulus	β_E	-	1.
Reduction Factor for Tensile Strength	β_f	-	1.

* Data extracted from Larive's tests.

Table 5.1: Effect of Temperature - Material and AAR Properties
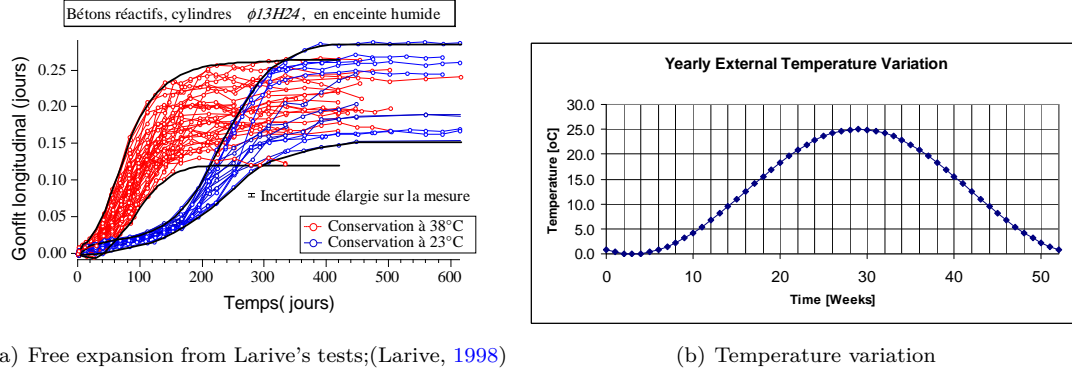
(a) Free expansion from Larive's tests;(Larive, 1998) (b) Temperature variation

Figure 5.1: Data for Calibration and prediction

driven by the decrease in the temperature.

(a) Vertical strains at 23°C and 38°C

(b) Predicted response to an harmonic temperature variation
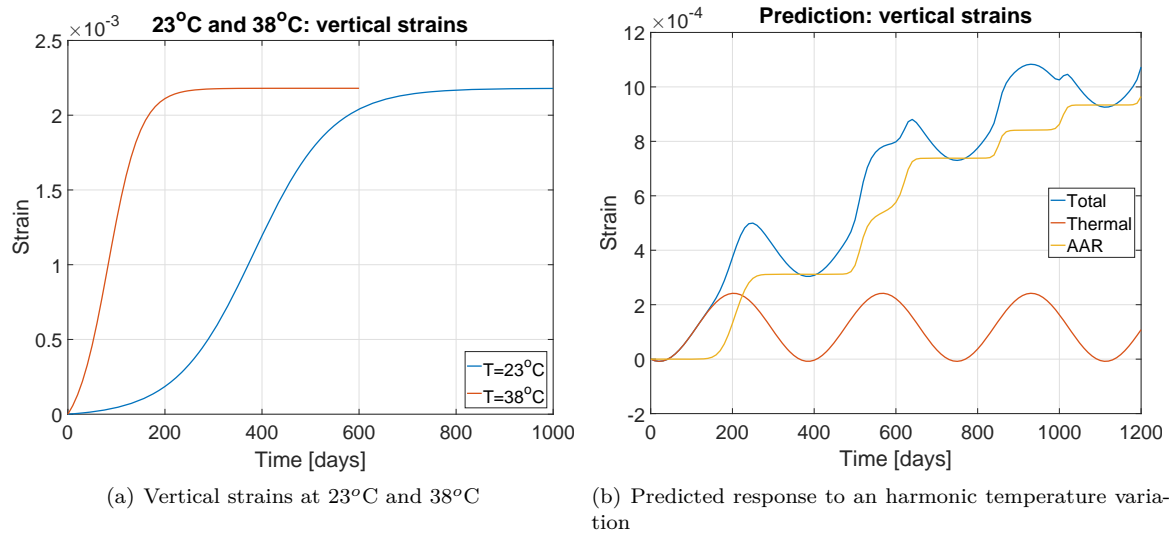
Figure 5.2: Numerical results for calibration and prediction for the effects of temperature

Chapter 6

P5: Free AAR Expansion; Effect of RH

6.1 Introduction

Relative humidity (RH) plays a critical role in the expansion of AAR-affected concrete. It is now well established (Poole, 1992) that AAR will start to expand at an RH equal to at least 80% and, afterwards, will continue to increase with RH. Capra and Bournazel (1998) suggested the following simple equation:

$$\varepsilon^{RH} = RH^m \varepsilon^{100\%} \tag{6.1}$$

where m is determined to equal 8 through a regression analysis of experimental data.

6.2 Simulations

Again, three simulations have been performed:

Calibration Two analyses with an external relative humidity of 100 and 30 percent using the experimental dataset of Multon (2004), as shown in Figures 6.1(a) and 6.1(b), respectively.
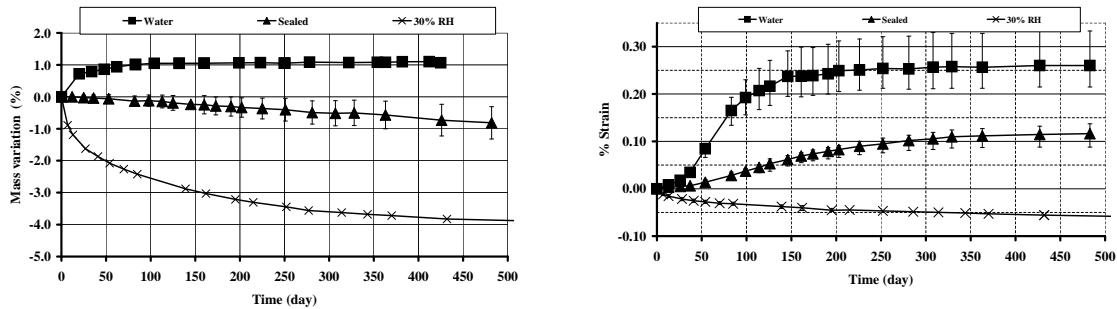
(a) Mass variation for reactive concrete under various RH conditions (b) Strain variation for reactive concrete under various RH conditions

Figure 6.1: Mass and strain variations under various RH conditions;Multon, 2004

Prediction of the expansion for a cylinder subjected to the RH histogram shown in Figure 6.2.
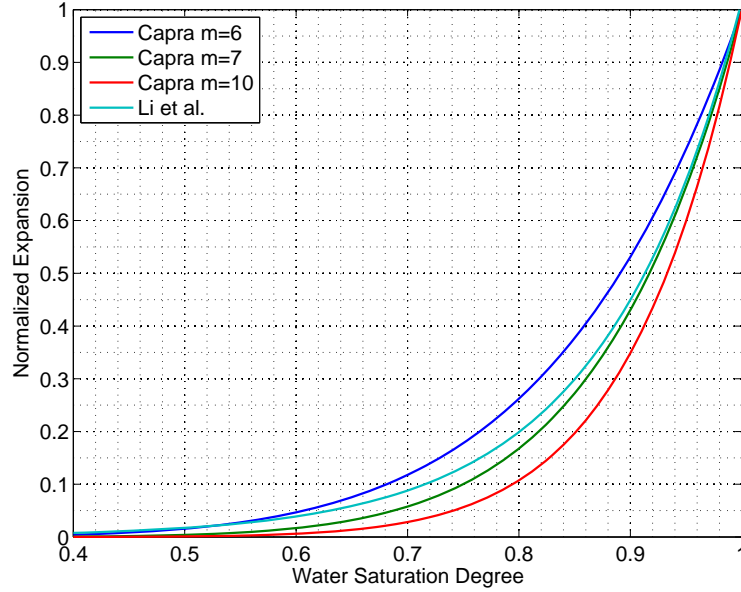
Figure 6.2: Cyclic variation of relative humidity used to simulate the prediction

The impact of RH on AAR swelling has been modeled as a modification of the final volumetric AAR strain according to the equation: $\epsilon^{AAR}(t) = \epsilon^{AAR}_\infty.RH^8(t)$. A constant relative humidity of 80% will thus lead to multiplying the final volumetric AAR strain by 0.17.

The factor 8 however, has not yet been well established, which led to simulating the Prediction case using three different values of this factor: 7, 8, and 9. All convergence criteria (Energy Error, Relative Residual Error, Absolute Residual Error and Displacement Error) have been set equal to 0.01.

(a) Expansion in terms of RH

(b) Effect of the variation in m
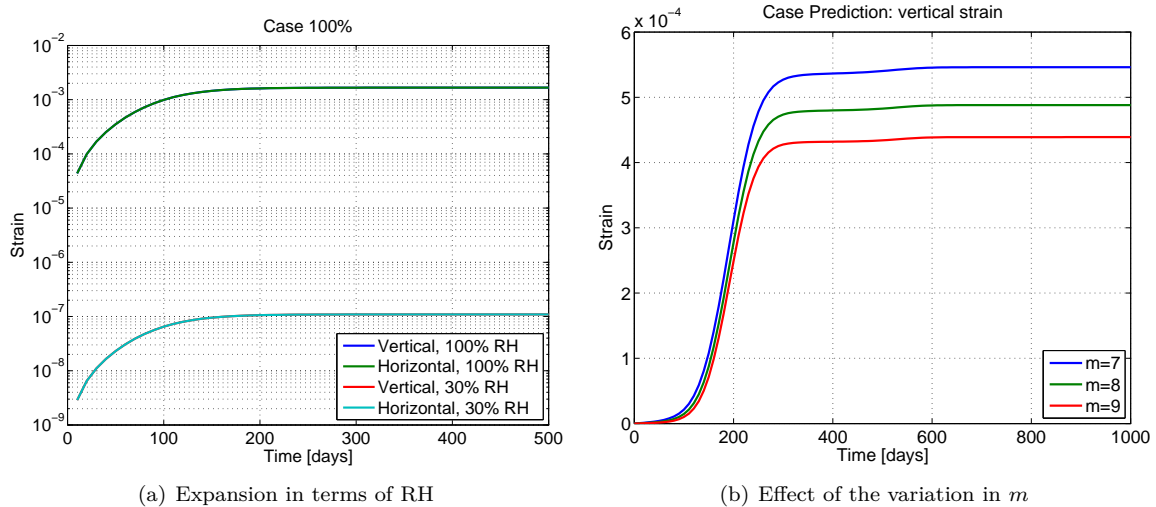
Figure 6.3: Calibration: Effect of Relative Humidity

The results of the first simulation are shown in Figure 6.3(a) for expansion in terms of RH; as expected at 30% RH, expansion is practically nil. Figure 6.3(b) shows the effect of factor m on this expansion: the

MERLIN AAR Problems

higher the exponent value, the lower the level of expansion. Let's point out that in this case, no attempt was made to calibrate input data with experimental results, and the final AAR-induced strain was set to 0.5% just like in most of the previous simulations.

A simulation with a cyclic variation of relative humidity, see Figure 6.2, will be performed next; these results indicate a sensitivity to m (Figure 6.4). As mentioned above, the higher m value leads to reduced expansion.
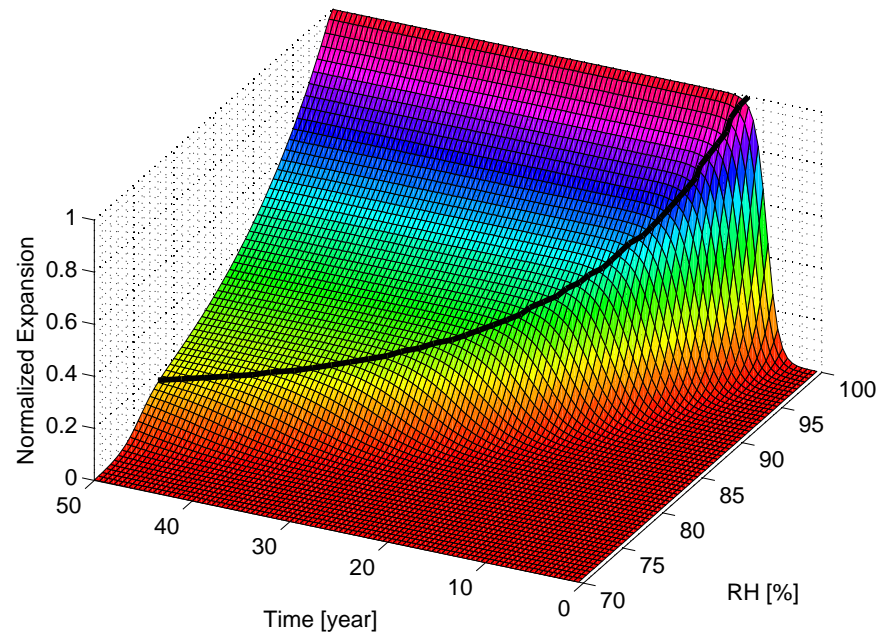
Figure 6.4: Prediction in terms of m

Chapter 7

P6: AAR Expansion; Effect of Confinement

7.1 Introduction

It has long been recognized that confinement inhibits reactive concrete expansion, (Charlwood et al., 1992), (Léger, Côte, and Tinawi, 1996) and most recently Multon and Toutlemonde (2006). This test series seeks to ensure that this is properly captured by the numerical model.

7.2 Simulations

Five simulations are performed:

Calibration Based on Multon's thesis in which four cases are considered:

- a) Free expansion, no confinement.
- b) -10 MPa vertical stress, no confinement.
- c) Free expansion, confinement.
- d) -10 MPa vertical stress, confinement

Prediction for the variable stress history with confinement.

Confinement is provided by a 5mm steel cylindrical jacket inside which the concrete is cast. Concrete, steel and AAR parameters are shown in Tables 7.1.

Numerically, concrete and steel are separated by an interface element which allows for axial deformation, and which allows for the steel to act as a confinement.

Concrete axial and radial strains are shown in Figure 7.1(a), whereas the steel strains are shown in Figure 7.2. Examining the concrete strains, and in descending strain order, we observe that:

1. (b) Radial, -10 MPa, no confinement. Since AAR is inhibited in the axial direction by the -10 MPa axial stress, it is entirely redirected in the radial direction. The AAR's strain is about 15×10^{-4} corresponding to a total volumetric AAR strain of 30×10^{-4} which is approximately equal to the specified $\varepsilon^\infty = 28.8 \times 10^{-4}$.

2. (c) Axial, free with confinement. In this case it is the radial expansion which is inhibiting the expansion, and hence it is redirected in the free axial one. As expected the magnitude is about twice.

3. (a) Axial and radial, free no confinement; they are both equal to approximately 9×10^{-4} at 350

Concrete	Symbol	Unit	Value
Mass Density	ρ	Gg/m^3	$2.4\ 10^{-3}$
Coefficient of Thermal Expansion	α	$/^oC$	$1.0\ 10^{-5}$
Young's Modulus	E_s	MPa	37200.
Poisson's Ratio (Static)	ν_s	-	0.2
Tensile Strength	f_t	MPa	10.
Compressive Strength	f_c	MPa	-36.5
Steel	Symbol	Unit	Value
Mass Density	ρ	Gg/m^3	0.
Coefficient of Thermal Expansion	α	$/^oC$	0.
Young's Modulus (Static)	E_s	MPa	193000.
Poisson's Ratio (Static)	ν_s	-	0.3
Tensile Strength	f_t	MPa	500.
Compressive Strength	f_c	MPa	-500.
AAR parameters	Symbol	Unit	Value
Maximum Volumetric AAR Strain	ϵ^∞	-	28.79×10^{-4}
Characteristic Time	τ_{car}	ATU	3.34
Latency Time	τ_{lat}	ATU	8.29
Activation Energy for Characteristic Time	U_C	K	5400.
Activation Energy for Latency Time	U_L	K	9400.
Reference Temperature of Test	T_0	^oC	38.
Tensile Strength	f_t	MPa	10.
Compressive Strength	f_c	MPa	-36.5
Residual Reduction Factor in Tension	Γ_r	-	0.1
Fraction of Tension pre-AAR Compressive Reduction	γ_t	-	0.2
Upper Compressive Stress Limit	σ_u	MPa	-10.
Shape Factor for Γ_c	β	-	1.8
Reduction Factor for Young's Modulus	β_E	-	1.
Reduction Factor for Tensile Strength	β_f	-	1.

Table 7.1: Effect of Confinement; Material and AAR Properties

days. This is indeed one third of the specified $\varepsilon^\infty = 0.288\%$ since we have an unconstrained isotropic expansion.

4. (d) -10 MPa confinement radial; Following an initial increase due to Poisson effect, some swelling occurs but is partially inhibited.

5. (c) Radial free confinement; unlike previous case, there is no initial strain, and a gradual increase in swelling. Swelling is reduced as most of it occurs in the axial direction.

6. (d) -10 MPa axial confinement the initial compressive strain corresponds approximately to the elastic one (σ/E or 2.7×10^{-4}, then as a result of AAR swelling it rebounds (specially that due to confinement, it can only expand axially).

7. (b)-10 MPa axial no confinement; -10 axial confinement the initial compressive strain corresponds approximately to the elastic one (σ/E or 2.7×10^{-4} however since there is no confinement all the AAR expansion is redistributed in the radial direction (contrarily to the preceding case).

As to the steel radial strains they reflect the gradual AAR's induced (swelling) radial strains in the confining jacket.

As to the prediction, Figure 7.2(a) shows the applied stress history, and Figure 7.2(b) the corresponding strains. Concrete undergoes an initial elastic axial deformation due to the -5 MPa traction, then it expands due to the AAR. When the -10 MPa traction is applied, there is an elastic strain, and at that point the AAR

MERLIN AAR Problems

(a) Calibration, concrete axial and radial strains

(b) Calibration, steel radial strains
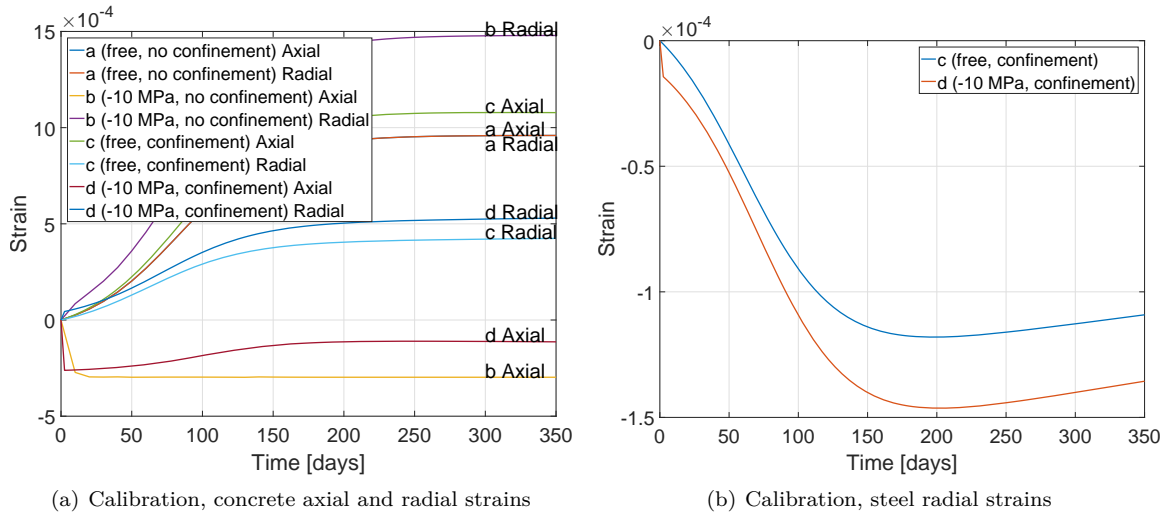
Figure 7.1: Calibration; Effect of confinement

is practically nil as the concrete is axially subjected to a stress equal to the threshold limiting value. When the -10 MPa is dropped to -5 MPa, there is again an elastic "rebounding" and the AAR is nil as it has been exhausted by that time.

(a) Imposed Stress

(b) Axial and radial strains
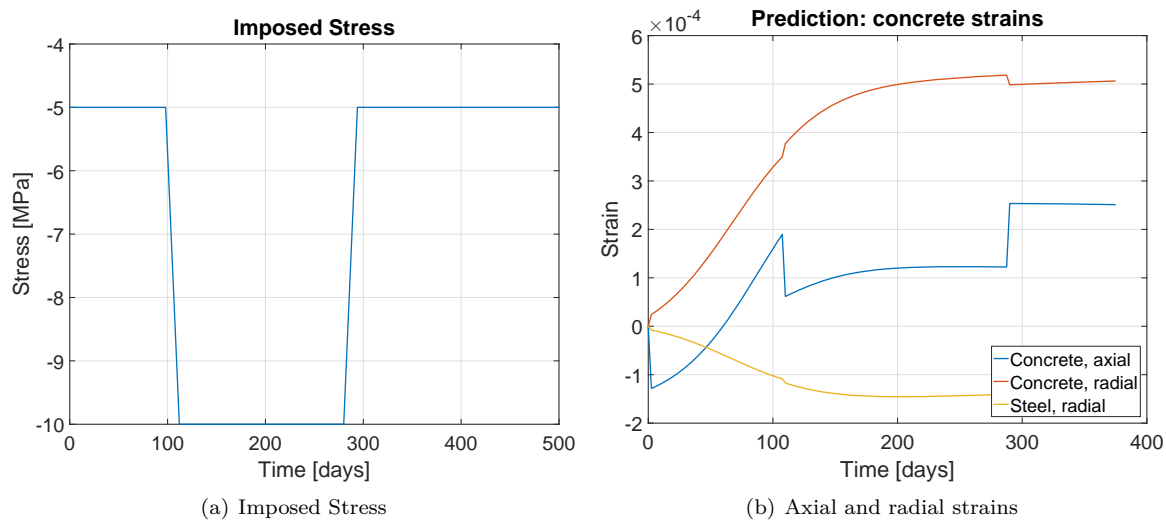
Figure 7.2: Prediction; Effect of confinement

The concrete radial strain is primarily driven by AAR (Poisson effect is shown but almost negligible),. Though partially constrained by the steel jacket, expansion is mostly in the radial direction in this case since axially expansion is constrained. Finally, the steel radial strain reflects the concrete time dependent expansion.

MERLIN AAR Problems

Chapter 8

P7: Effect of Internal Reinforcement

8.1 Introduction

Internal reinforcement inhibits expansion and AAR induced cracks would then align themselves with the direction of reinforcement as opposed to the traditional "map cracking", (Mohammed, Hamada, and Yamaji, 2003). This test problem seeks to determine how the numerical model account for a restrained (by a reinforcing bar) free expansion, and how does internal cracking affect the results. There is no experimental data with which results can be compared. The diameter of the internal steel rebar is 12 mm.

Concrete is modeled by the nonlinear constitutive model, and a linear elasto-plastic model is used for the steel, Table 8.1.

Figure 8.1 provides some snapshots of the mesh, and note that at about 5 mm away of the rebar, its effect on the AAR is almost nil. The steel axial stress is quite small, $\simeq 0.063$ MPa.

(a) Axial strain

(b) Axial stress
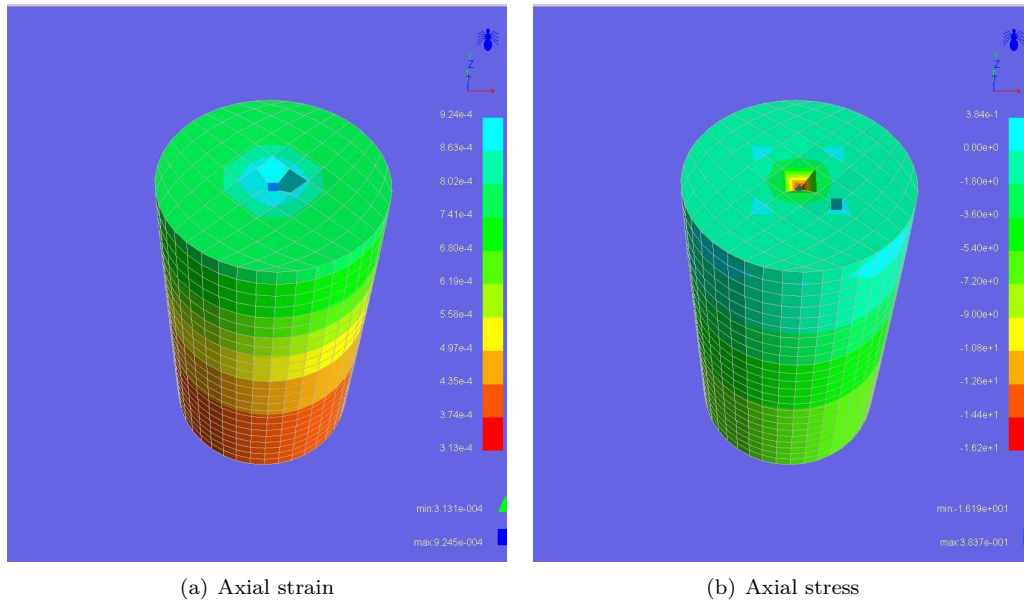
Figure 8.1: Effects of reinforcement on AAR

Concrete strains, Figure 8.1 are indeed restrained in the axial direction, and most of the expansion is in

Material parameters	Symbol	Unit	Concrete value	Steel value
Young's Modulus (Static)	E_s	MPa	37300.	200 000.
Poisson's Ratio (Static)	ν_s	-	0.2	0.3
Tensile Strength	f_t	MPa	3.5	500.
Fracture Energy	Γ_f	MN/m	$1.00\ 10^{-4}$	-
Compressive Strength	f_c	MPa	-38.4	-500.
Compressive Critical Displacement	w_d	m	-0.5	-
Return Direction Factor	β	-	0.	-
Failure Surface Roundness Factor	e	-	0.52	-
Onset of Compression Nonlinearity	f_{c0}	MPa	-13.3	-
Plastic Strain at f_c	ϵ_c	-	$-2.0\ 10^{-3}$	-
AAR parameters	Symbol	Unit	Value	
Maximum Volumetric AAR Strain	ϵ^∞	-	21.9×10^{-4}	
Characteristic Time	τ_{car}	ATU	3.34	
Latency Time	τ_{lat}	ATU	8.29	
Activation Energy for Characteristic Time	U_C	K	5400.	
Activation Energy for Latency Time	U_L	K	9400.	
Reference Temperature of Test	T_0	^oC	38.	
Tensile Strength	f_t	MPa	10.	
Compressive Strength	f_c	MPa	-30.	
Residual Reduction Factor in Tension	Γ_r	-	0.1	
Fraction of Tension pre-AAR Compressive Reduction	γ_t	-	0.2	
Upper Compressive Stress Limit	σ_u	MPa	-10.	
Shape Factor for Γ_c	β	-	-2.	
Reduction Factor for Young's Modulus	β_E	-	1.	
Reduction Factor for Tensile Strength	β_f	-	1.	

Table 8.1: Effect of Internal Reinforcement; Material and AAR Properties

the radial. $\varepsilon_{axial} + 2\varepsilon_{radial} = (0.35 + 2(0.85)) \times 10^{-3} = 20.5 \times 10^{-4}$ which is approximately equal to the specified ε^∞.

(a) Concrete

(b) Steel
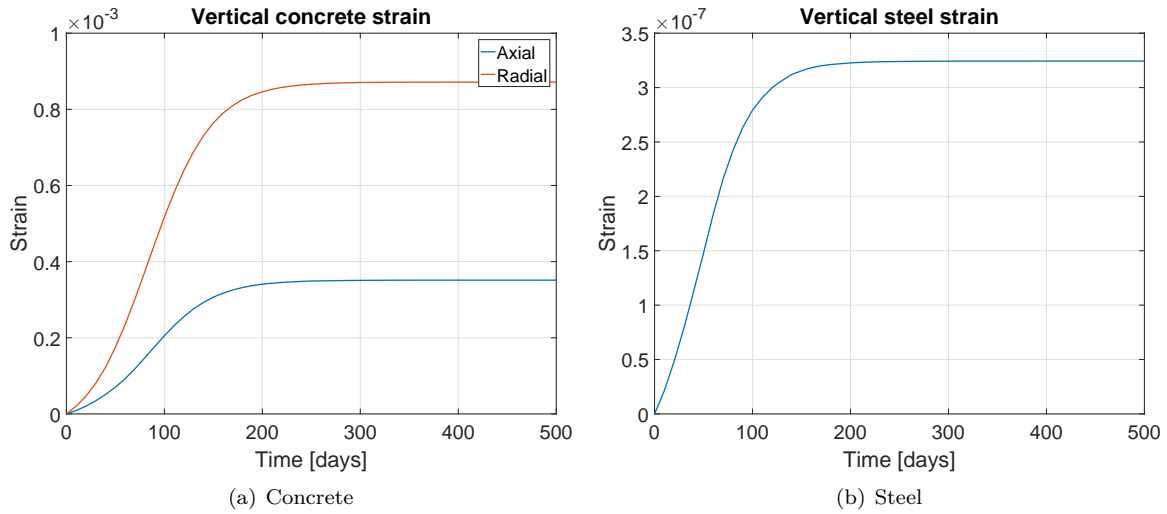
Figure 8.2: Effect of Internal Reinforcement

MERLIN AAR Problems

Chapter 9

P8: Reinforced Concrete Beam

To be completed later

Chapter 10

P9: AAR Expansion; Idealized Dam

10.1 Introduction

So far, focus has been on how individual effects affect material response. In this last case study, we consider an idealized dam with a slot. The dam will be subjected to a series of stressors (hydrostatic, creep, temperature, etc.).

A common remedy for AAR induced damage in dams is to cut a slot in the structure as in Mactaquac, (Gilks and Curtis, 2003). This will relieve the state of stress, and allow the concrete to expand freely. However, at some point concrete swelling will result in a contact between the two sides of the slot. Hence, this problem will test the model ability to capture the slot closure and ensuing stress buildup.

10.2 Problem Definition

The dam is shown in Figure 10.1 with the following conditions: a) lateral and bottom faces are all fully restrained; b)front back and top faces are free; c) slot cut at time zero, total thickness 10 cm; d) concrete on the right is reactive, and concrete block on the left is not reactive; e) hydrostatic pressure is applied only on the right block.

Using the fitting data of P6, and an friction angle of 50° for concrete against concrete, and zero cohesion, we consider two cases:

Homogeneous field of internal temperature (20^oC), relative humidity (100%), and an empty reservoir.

Transient field of external temperature (Figure 5.1(b)), relative external humidity (Figure 10.3), and pool elevation variation ((Figure 10.2) given by

$$EL(\text{week}) = \frac{EL_{\max} - EL_{\min}}{2} \sin \left(2\pi \frac{t}{52} \right) + \frac{EL_{\max} - EL_{\min}}{2} \tag{10.1}$$

where $EL_{\max}$ and $EL_{\min}$ are equal to 95 and 60 respectively.

For both analysis, the specified temperature and relative humidity is the one of the concrete surface. Zero flux condition between dam and foundation. Reference base temperature of the dam is 20^oC.

1. x, y, z displacements of point A.
2. F_x, F_y and F_z resultant forces on the fixed lateral face versus time (25 years). Assume the typical yearly variations of external air temperature and pool elevation shown in Figures 5.1(b) and 10.2,
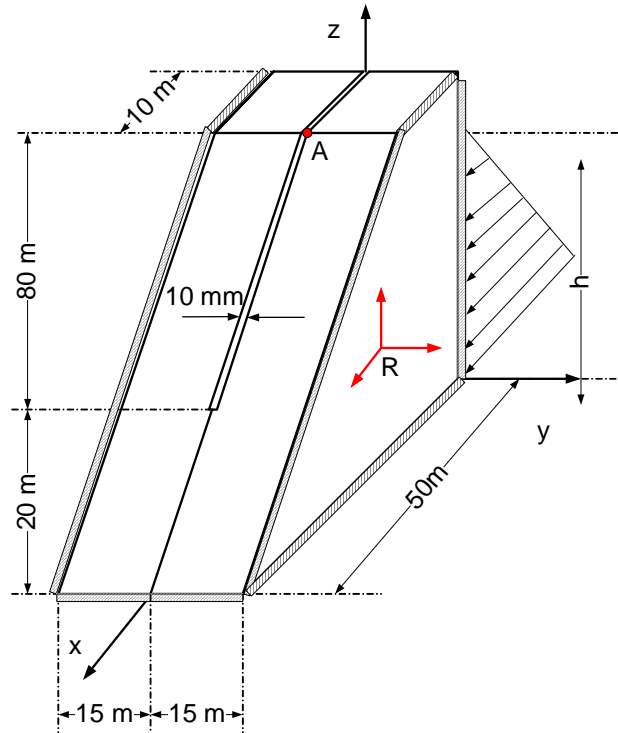
Figure 10.1: Idealized dam
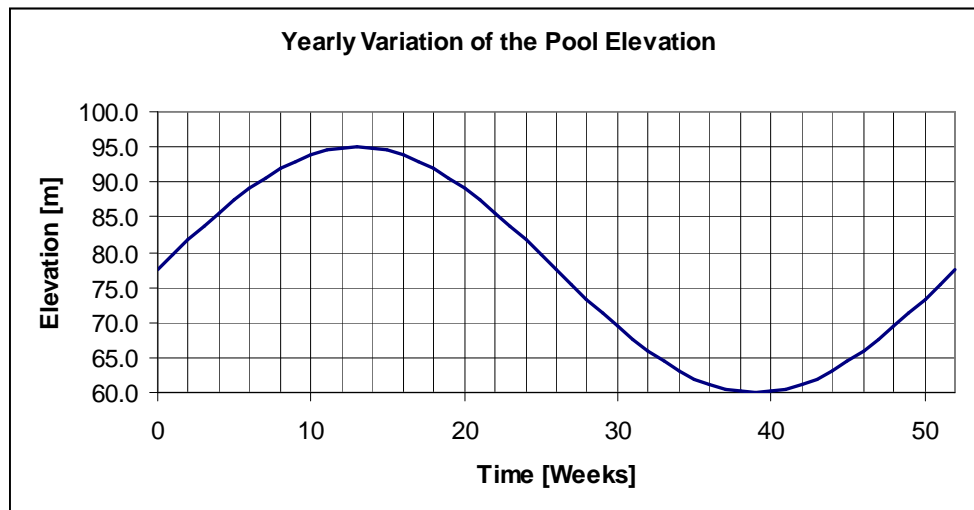
Figure 10.2: Yearly variation of pool elevation

respectively.

This model seeks to capture: a) general finite element program capabilities in modeling the joint response; b) ease (or difficulty in preparing the input data file for a realistic problem; and c) coupling of the various parameters.

MERLIN AAR Problems
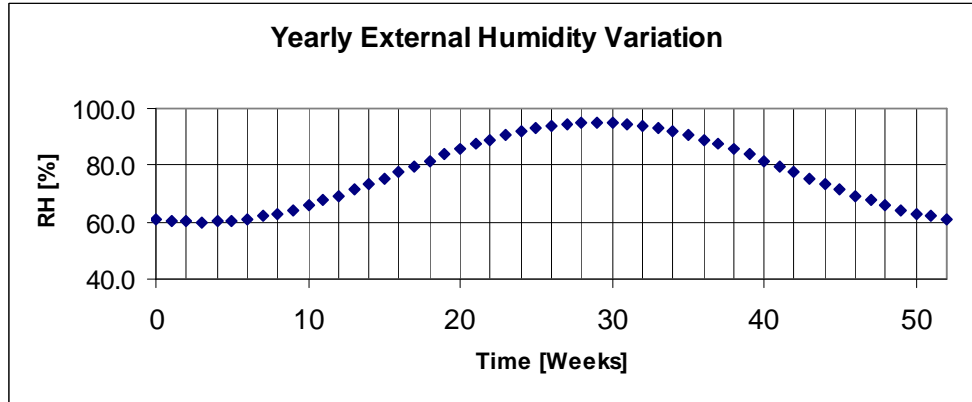
Figure 10.3: Humidity variation

10.3   Two-dimensional (2D)

First a 2D mesh is prepared to highlight the code ability to capture slot closure as a result of AAR, Figure 10.4. To capture this effect an interface element is inserted along the slot. However, contrarily to common implementations of this element, it does not have a zero thickness but a finite one (1 cm in the present case). Hence, the formulation of this element was slightly modified to consider the zero stress state te one corresponding to this non-finite initial COD.

(a) 2D finite element mesh outline

(b) 2D finite element mesh
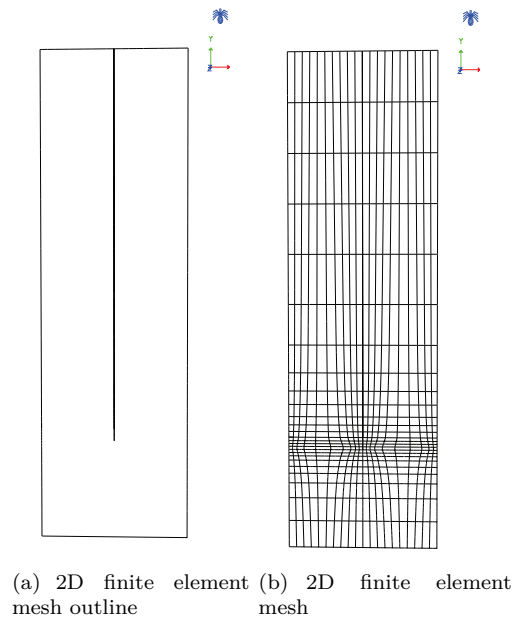
Figure 10.4: 2D Finite element mesh

We have a 5 cm slot, and apply an artificially increasing temperature. Each line corresponds to a point along the interface. Contact is first reached at the top first, but the bottom. Figure 10.5 shows the variation of the displacement versus the increment.

MERLIN AAR Problems
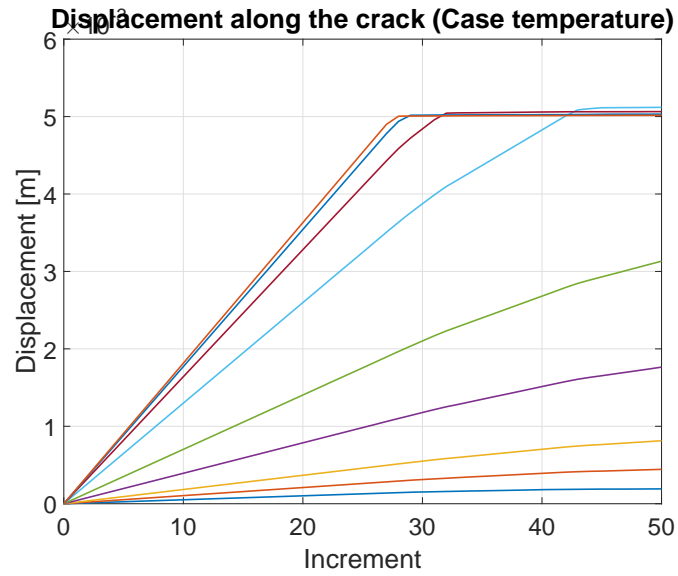
Figure 10.5: 2D analysis showing slot closure

Figures 10.6(a) and 10.6(b) show the initial mesh with the 10 cm slot and the final after AAR, highlighting crack closure.

(a) 2D mesh initial   (b) 2D mesh final)
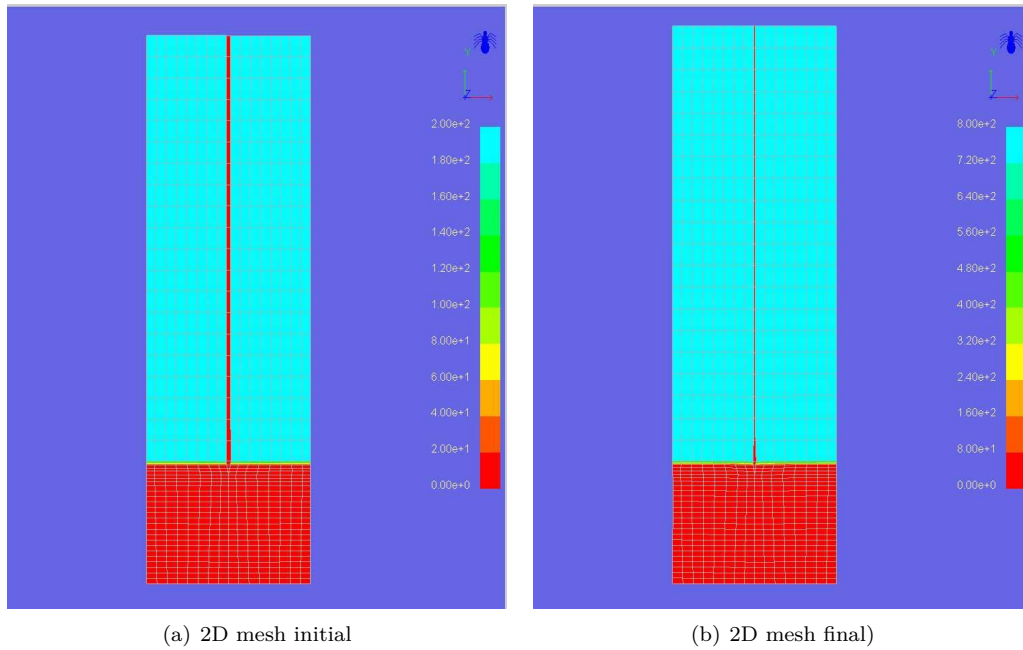
Figure 10.6: 2D slot closure

The ability of the code to capture slot closure as a result of AAR is shown in Figure 10.7(a). We note that already within increment 9 the slot has entirely closed (and the corresponding crack opening displacement is indeed 1 cm), and that there is a corresponding stress buildup. Focusing on the couple of first increments, Figure 10.7(b) we observe the gradual slot closure and corresponding stress increase.

In Figure 10.8(a), AAR (normal evolution) we observe the evolution of slot opening with time for different

MERLIN AAR Problems
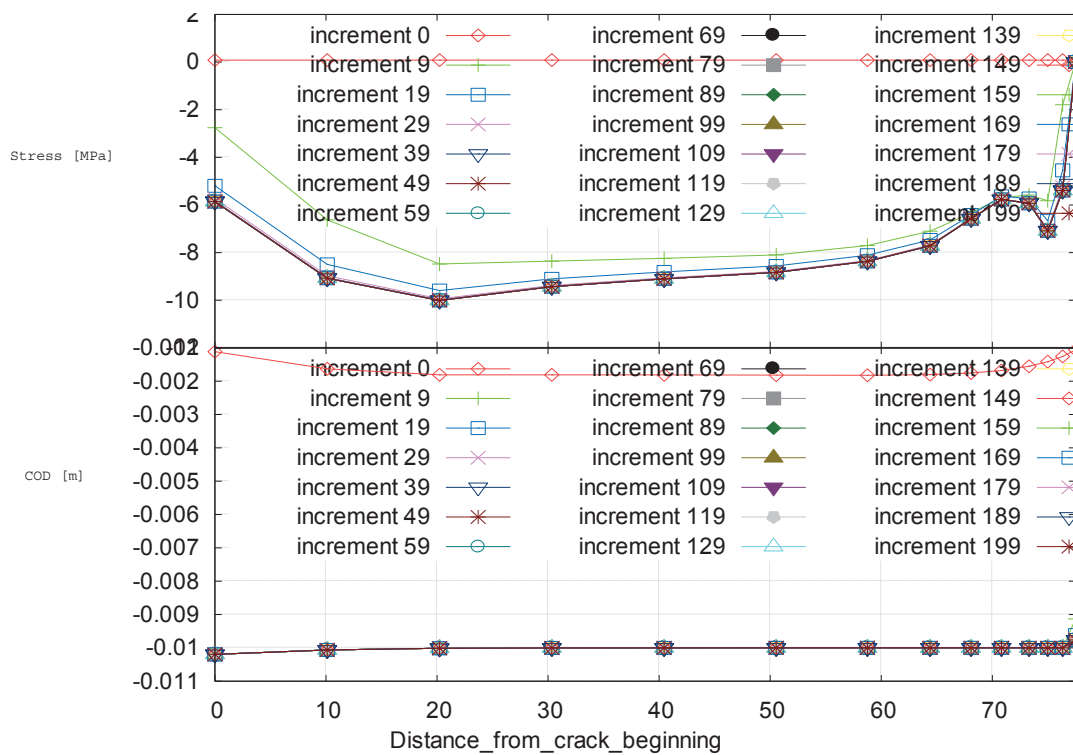
(a) 2D analysis (accelerated AAR)
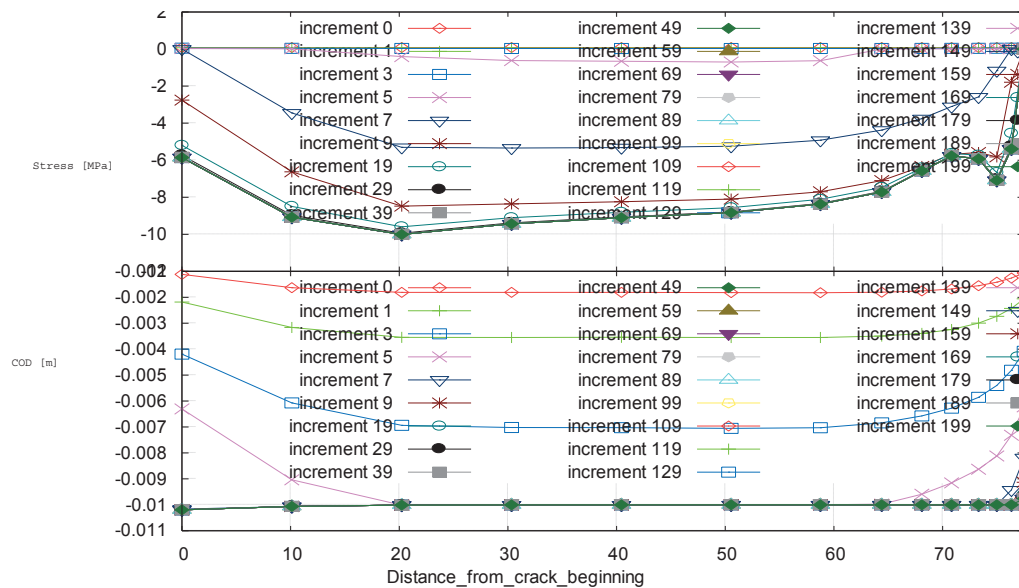
(b) 2D analysis (accelerated AAR)

Figure 10.7: 2D analysis; Crack closure

elevations. In this case after 12 years, the slot has entirely closed. The slot displacement is indeed 1 cm because AAR is applied only on one side of the dam. Figure 10.8(b) shows the corresponding stresses.

MERLIN AAR Problems

(a) Slot Opening
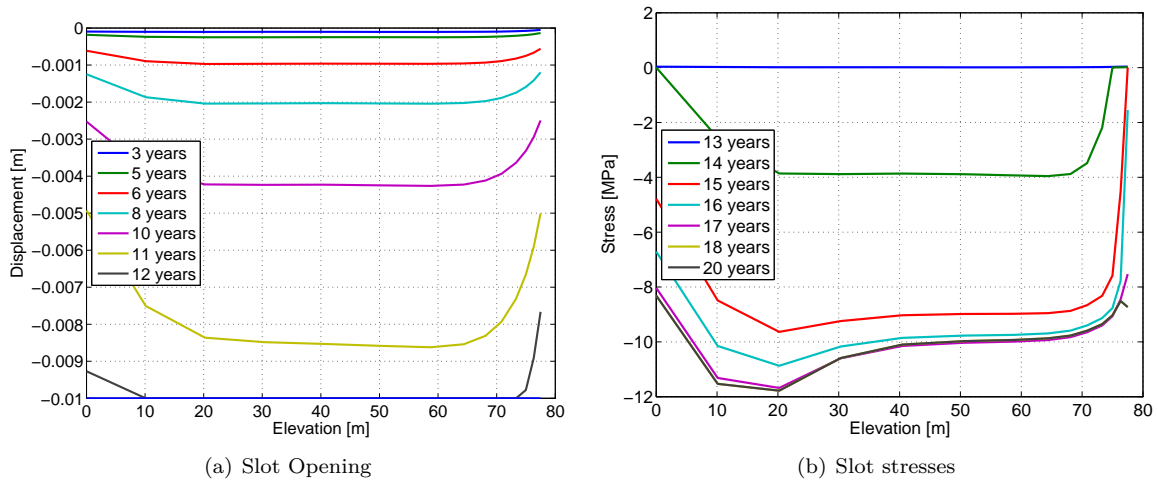
(b) Slot stresses

Figure 10.8: Slot Opening and Stresses

10.4 Three-dimensional (3D); AAR Only

Having been able to capture crack closure in 2D, the question is can it be done again in 3D? and if so, are there any idosyncracies about a three-dimensional simulation which can not be captured by a mere two dimensional one. The 3D mesh of the model of Figure 10.1 is shown in Figure 10.9.

(a) 3D finite element mesh outline (exagerated slot width)

(b) 3D finite element mesh
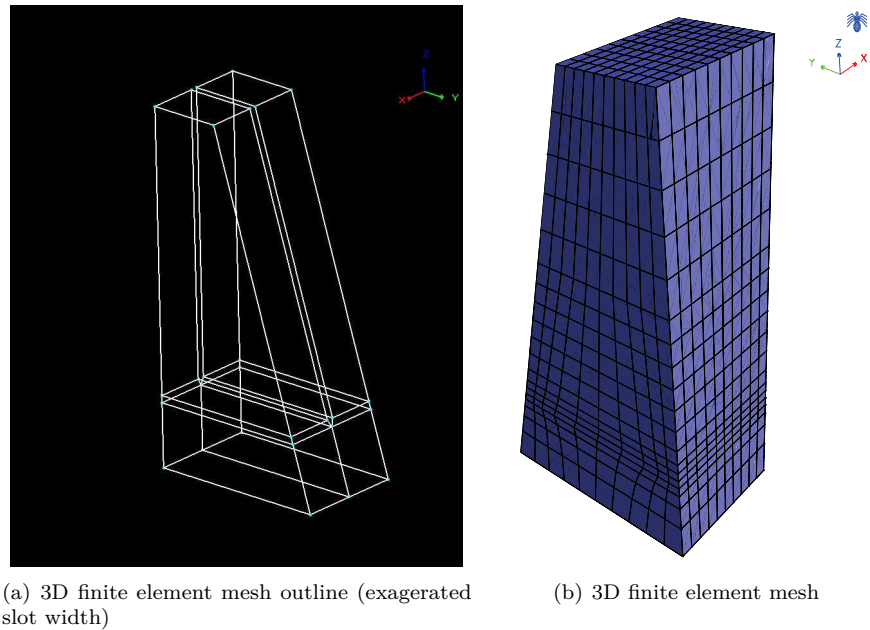
Figure 10.9: 3D Finite element mesh

In this first analysis, the dam is subjected only to AAR as shown in Table 10.1, and for the 10 mm slot, with AAR, we seek to determine the slot thickness in terms of time (as it is reduced by AAR), Figure 10.10(a) and the corresponding contact stresses, Figure 10.10(b).

From these plots, we conclude that

MERLIN AAR Problems
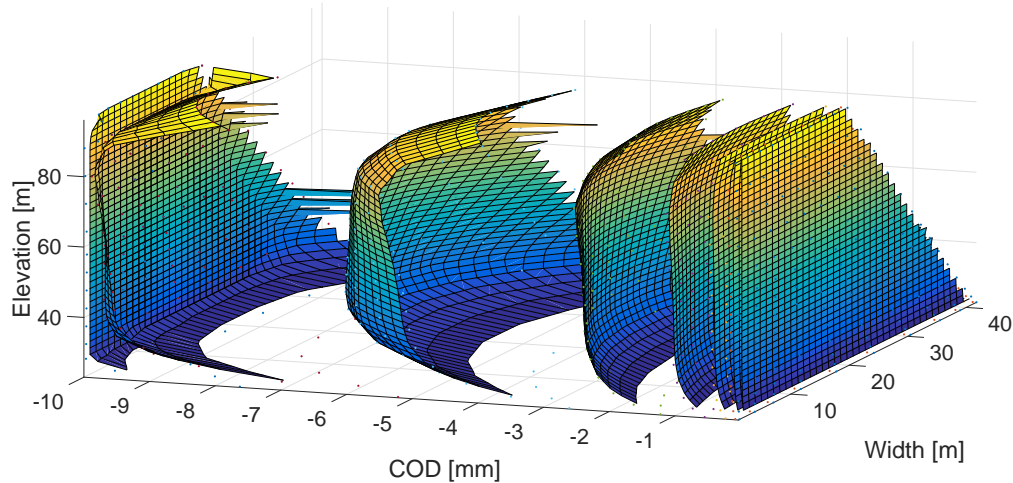
(a) Slot thickness for time: 0.167, 1.67, 3.33, 5, 6.67, 8.33, 10 and 11.67 years
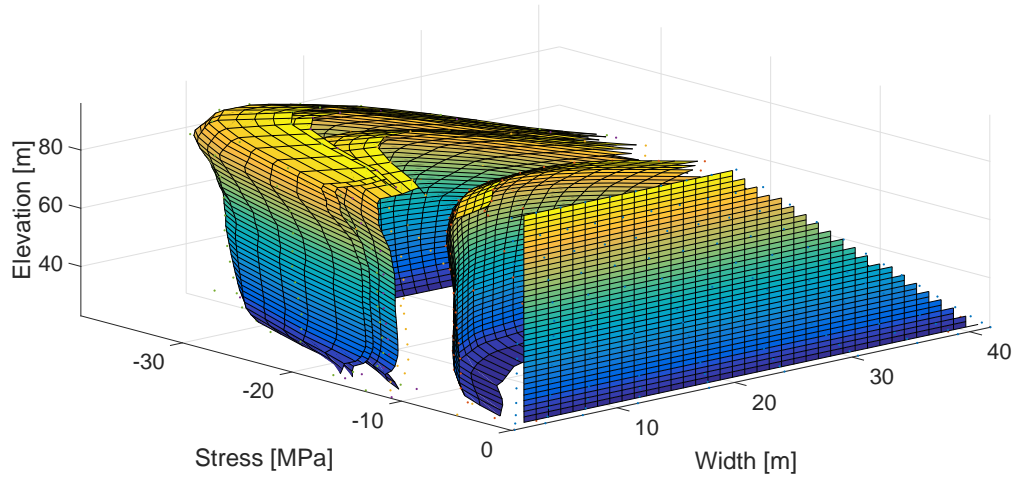
(b) Slot normal stresses for time: 8.33, 11.67, 15, 18.33 and 121.67 years

Figure 10.10: 3D response of a dam subjected to AAR

1. The slot is initially completely open (COD=0), and gradually the COD reaches -10 mm which is precisely the thickness of the slot. At that point, the interface element is activated, and there can be no more expansion.
2. The concavity of the surfaces is to be noted. There is more expansion in the center than on the edges. Eventually the expansion is entirely uniform and we have a nearly full contact at -10 mm.
3. Similarly, there is less expansion on the top than in the bottom.
4. The bottom has also reduced expansion due to the problem formulation as it is constrained to the bottom concrete.
5. Similarly, the stresses are zero in the beginning as there is no contact.
6. Gradually the stress increase, and we observe the same concavity as the one noted for the COD. In other words, stresses are much higher in the center than on the edges.
7. The concavity remains present even after many years, stresses will be higher in the central part than on the edges.

From these observations, we conclude that we were we able to capture the "true" response of the slot,

MERLIN AAR Problems

to anticipate the time of closure and to map the corresponding stresses. A salient observation is that the COD/stress state can be quite complex, and thus great care should be exercised in planning for and after slot cutting.

Material parameters	Symbol	Unit	Value
Thickness	h	m	1.
Mass Density	ρ	Gg/m^3	2.410^{-3}
Coefficient of Thermal Expansion	α	$/^oC$	1.010^{-5}
Young's Modulus (Static)	E_s	MPa	33600.
Poisson's Ratio (Static)	ν_s	-	0.2
Tensile Strength	f_t	MPa	10.
Fracture Energy	Γ_f	MN/m	$1.0\ 10^{-4}$
Compressive Strength	f_c	MPa	-30.
Compressive Critical Displacement	w_d	m	-0.5
Return Direction Factor	β	-	0.
Failure Surface Roundness Factor	e	-	0.52
Onset of Compression Nonlinearity	f_{c0}	MPa	-13.3
Plastic Strain at f_c	ϵ_c	-	$-2.0\ 10^{-3}$
Interface parameters	Symbol	Unit	Value
Thickness	h	m	1.
Mass Density	ρ	Gg/m^3	0.
Coefficient of Thermal Expansion	α	$/^oC$	0.
Tangential stiffness	K_t	MPa	1.
Normal stiffness	K_n	MPa	1.10^8
Uniaxial tensile Strength	σ_t	MPa	0.1
Cohesion	c	-	0.1
Angle of friction	ϕ_f	^{o}	10.
Dilatancy angle	ϕ_D	^{o}	0.
Specific mode I fracture energy	G_F^I	MJ	5.10^{-03}
Specific mode II fracture energy	G_F^{IIa}	MJ	5.10^{-03}
Ratio of irreversible deformation	γ	MPa	0.
Maximal displacement for dilatancy	u_{Dmax}	MPa	0.
Tensile stress at break-point for the bilinear law	σ_1	MPa	0.05
COD at break-point for the bilinear law	sw_1	m	0.025
Cohesion at break-point for the bilinear law	c_1	-	0.05
CSD at break-point for the bilinear law	cw_1	m	0.025

Table 10.1: Dam - Material and Interface Properties

10.5   Three-dimensional (3D); Prediction

`Analysis completed, currently data mining!`

10.6   Conclusions

Through a series of numerical simulations, of increasingly complexity, a better understanding of the structural implications of a AAR was achieved.

First simple simulations of a cylinder were performed in which one phenomenon at a time is considered. Then an idealized dam is modeled.

MERLIN AAR Problems

From these preliminary studies, it can be concluded that with exception to the variability of the relative humidity (of secondary importance for dams) all major AAR stressors were properly modeled, and most importantly the model was able to predict and capture slot closure was shown in both 2D and 3D. To the best of the authors knowledge, such an exhaustive study has not yet been reported in the open literature, and conclusions can be far reaching for the simulation of structures subjected to AAR.

MERLIN AAR Problems

Acknowledgements

MERLIN AAR Problems

Chapter 11

P10: Reinforced Concrete Panel

Extracted from *Akali-Silica Reaction in Nuclear Power Plants* Report Submitted by Saouma, Hariri-Ardebili and LePape to the Oak Ridge national laboratory.

11.1 Material Properties

This section explains the material properties which are used in the current research for assessment of RC panel. In general, material properties and modeling characteristics can be divided into the following major groups:

- Concrete panel properties
- Cushion ring properties
- Steel rebar properties
- ASR model properties

11.1.1 Concrete panel properties

General characteristics of the concrete used for the panel are summarized in Table 11.1. Mass density of the concrete is obtained from some of the all materials that are used in formation of the concrete. These materials are listed in Table 11.2. The coefficient of thermal expansion represents the volume change of a material due to temperature changes and is expressed as a change in length per degree of temperature change. Thermal expansion of concrete is complicated because there is interaction between the cement paste and aggregate. Because the aggregate generally constitutes a major proportion of the mix, it primarily influences the resultant coefficient of thermal expansion.

Table 11.1: General characteristics of concrete panel

Characteristics	Symbol	Unit	Mean	[STD]	[min]	[max]
Mass density	ρ	kg/m^3	2,250	[225]	[1,800]	[2,700]
Compressive strength	f'_c	MPa	-31	[3.1]	[24.82]	[37.24]
Tensile strength	f'_t	MPa	3.2	[0.32]	[2.56]	[3.84]
Elastic modulus	E	MPa	26,000	[2,600]	[20,800]	[31,200]
Poisson's ratio	ν	-	0.2	[0.02]	[0.16]	[0.24]

It is noteworthy that due to uncertainty in the material properties an appropriate range is considered for

them. It is assumed that the material properties follows the normal distribution. Thus, the properties are expressed using a mean and associated standard deviation. Also, an upper and lower bounds are limited the considered distributions. Obviously, sensitivity analysis is required to cover the relative importance of the parameters and also their property range.

Table 11.2: Concrete mixture in the case study RC panel

Component	Quantity
Coarse aggregate (SSD)	917kg/m^3
Fine aggregate (SSD)	674kg/m^3
Cement (Type III)	420kg/m^3
Water	231kg/m^3
W/C ratio	0.55
$NaOH$ added	2.43kg/m^3
Total Na_2O_e	5.25kg/m^3

The value of the concrete compressive strength is provided as 4500 psi or 31.03 MPa. Using this value, the elastic modulus of the concrete can be estimated using the approximate formulas proposed by ACI Building Code 318-83 as follows:

$$E_c = 4.7 f'^{0.5}_c \Rightarrow \text{Normal weight concrete} \tag{11.1}$$

$$E_c = 43\rho^{1.5} f'^{0.5}_c \times 10^{-6} \Rightarrow 1500\text{kg/m}^3 < \rho < 2500\text{kg/m}^3 \tag{11.2}$$

Using the above formulations, modulus elasticity of concrete is computed as 25564 MPa based on ACI method (ACI Building Code 318-83); however it will be considered as 26000 MPa in the analyses.

There are lots of relationships which connect the concrete compressive and tensile strength; however, in the present study the relations proposed by Raphael for static and dynamic loading conditions are used. These relations can be summarized as follows (also shown graphically in Figure 11.1):

$$(f'_t)_{st} = 1.7(f'_c)^{2/3} \tag{11.3}$$

$$(f'_t)^{app}_{st} = 2.3(f'_c)^{2/3} \tag{11.4}$$

$$(f'_t)_{dyn} = 2.6(f'_c)^{2/3} \tag{11.5}$$

$$(f'_t)^{app}_{dyn} = 3.4(f'_c)^{2/3} \tag{11.6}$$

where both the f'_t and f'_c are represented in psi. We recall that 1 MPa = 145.04 psi. In the present study the model based on the static relation is used.

11.1.2   Cushion ring properties

As mentioned before, the cushion ring is used only as a boundary condition for the main RC panel. The compressive strength of the concrete is f'_c= 68.948 MPa.

MERLIN AAR Problems
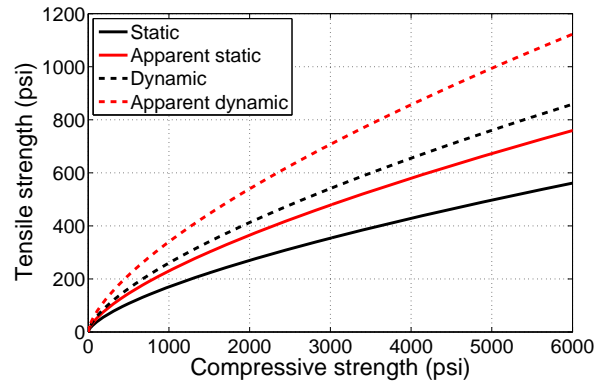
Figure 11.1: Design chart for tensile strength adopted from Raphael (1984)

11.1.3 Steel rebar properties

In the United States, rebar is graded according to its physical characteristics. The higher the grade, the wider and heavier the rebar is. #11 rebar is among the widest and heaviest of the available standard grades, and is thus well-suited for use in heavy-duty and demanding construction projects. General characteristics of #11 rebar are summarized in Table 12.3.

Table 11.3: General characteristics of rebar #11

Characteristics	Symbol	Unit	Quantity
Nominal diameter	d_N	mm	35.81
Nominal cross-sectional area	A_N	mm^2	1006
Mass per unit length	ρ_l	kg/m	7.924
Elastic modulus	E	MPa	207000
Poisson's ratio	ν	-	0.25
Yield stress	σ_Y	MPa	275

11.2 AAR Assessment of RC Panel

In this section the RC Panel is analyzed. No expansion is allowed in direction perpendicular to the side walls; however it is possible to panel to expand in vertical direction. Table 11.4 describes all the models and their characteristics. The finite element model consists of totally N=1001 node and E=720 quadrilateral elements as shown in Figure 11.2. Two sets of reinforcements are modeled at the top and the bottom of the specimen. In the Merlin finite element software, the rebars can be modeled easily by defining the the start and end nodes. Then, Merlin automatically applies the mesh on the rebars. The finite element mesh of the rebars for the panel is shown in Figure 11.3.

In all models, the panel is experienced only the ASR expansion and no external load (directly or indirectly) is applied to the panel. The models are expected to expand only in z direction. Figure 11.4 compares the un-deformed and deformed shape of the panel under two boundary conditions explained in Table 11.4. Based on Figure 11.4, restricting the side-walls in all three directions leads to expansion of the panel z direction. In this condition, the maximum deformation belongs to the middle point in the upper and lower faces. On the other hand, this figure shows the condition in which the side-walls are only restricted in x and y directions

Table 11.4: Different types of the models for the panel

ID	Reinf.	Loading	BC on xz plane	BC on yz plane	Material model
P1	No	ASR	x=y=z=0	x=y=z=0	Linear Elastic
P2	No	ASR	x=y=0	x=y=0	Linear Elastic
P3	Yes	ASR	x=y=z=0	x=y=z=0	Linear Elastic
P4	Yes	ASR	x=y=0	x=y=0	Linear Elastic
P5	Yes	ASR	x=y=z=0	x=y=z=0	Non-Linear
P6	Yes	ASR	x=y=0	x=y=0	Non-Linear
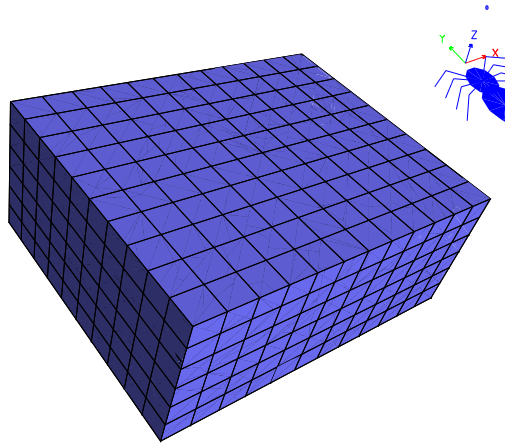
Figure 11.2: 3D finite element model of the RC panel
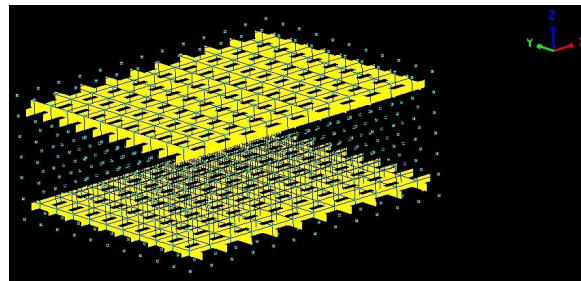
Figure 11.3: 3D finite element model of the reinforcement for panel

(not z). In this condition the model has a uniform expansion in both +z and -z direction. Considering the symmetry of the panel, in both boundary models the panel shows the same responses along the positive and negative z axis.

In order to investigate the structural responses of the panel, two index points are taken into account. These two point are selected in a way to reflect the general behavior of the panel. Figure 11.5 shows the spatial location of the index points and also different layers of the panel model. Index-1 is located on middle of the top layer and the Index-2 is located on the middle of the middle layer. These two point are selected as index points because the relative response of them may be useful. Index-1 is the point highly affected by ASR expansion.

MERLIN AAR Problems
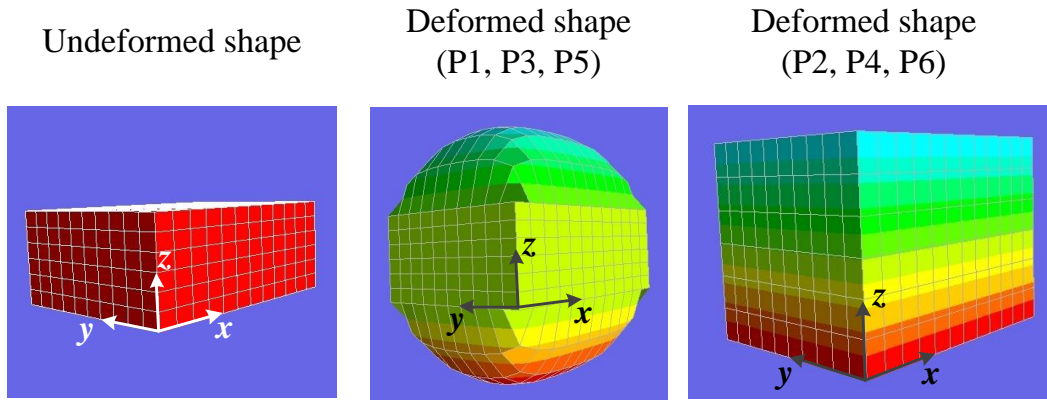
Figure 11.4: Comparison of the deformed and un-deformed shapes of the panel
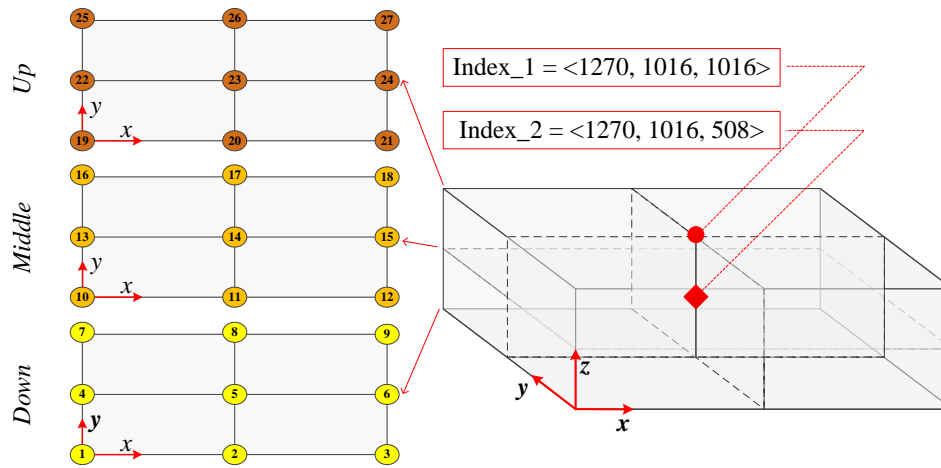
Figure 11.5: Spatial location of index points and layers of the panel

11.2.1 Model Pre-P2-P5

In this model, the side-walls are restricted in all three directions and thus there will be no expansion in the side-walls. The panel is modeled considering the reinforcements as shown in Figure 11.3. The concrete is modeled with smeared crack approach (with the ability of concrete cracking).

Figure 11.6 shows the response of the considered specimen for the two index points showed in Figure 11.5. The responses are only shown in vertical direction (z-direction). Based on this figure, the maximum vertical displacement of the Index-1 is about 2.90 mm, while Index-2 has very negligible displacement (1.7e-4 mm). Compared to P3 (the same model with linear material), P5 has larger vertical displacement about 11% at the Index-1. In addition, the value of the u_z at Index-2 was "absolute zero" for P3 (mainly due to symmetry of the model), while it has a small value for P5 (mainly due to cracking and un-symmetric condition).

Both the index points show vertical strain (ϵ_{zz}); however, the maximum vertical strain of the Index-1 is about 5 times of the Index-2. Also, it seems that the curve associated with Index-2 reaches earlier to the flat position than to the Index-1. Compared to P3, there is no significant differences.

MERLIN AAR Problems

The vertical stress (σ_{zz}) plots for both the index points do not follow the conventional sigmoid-like curves (in spite of the displacement and strain curves). The general trend of the vertical stress are different from the other cases (P1 and P3). In this model, P5, the Index-2 has higher stresses than the Index-1. The maximum vertical stress values reach to 0.64 MPa and 2.03 MPa for Index-1 and Index-2, respectively. It is noteworthy that in all previous cases (all linear elastic models), Index-1 had higher stress than Index-2. The initial stresses (at inc = 1) are the same as P3 which shows that both the P3 and P5 panels has initial elastic behavior. P5 shows some stress fluctuations at inc [100, 110] (which is close to the peak strain variation point) and mainly can be attributed to the cracking.

Finally, comparison of the volumetric AAR strain (ϵ_{AAR}^{vol}) reveals that none of the index points reach the maximum volumetric strain (ϵ_{AAR}^{∞}), 0.005, at the end of the analysis. The curves associated with Index-1 and Index-2 have almost the same trend up to Inc = 100; however, for higher increments the Index-1 shows the higher ϵ_{AAR}^{vol}. Compared to model P3, this model, P5, has a bit higher final strain value.
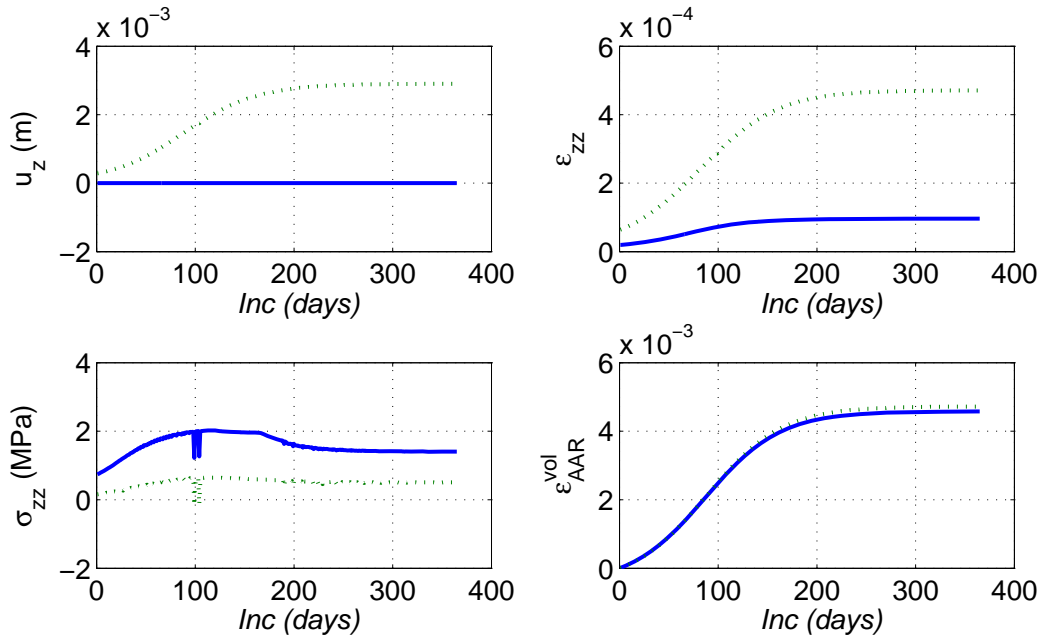
Figure 11.6: Response of model P5 ($x^- : (0,0,0); \ x^+ : (0,0,0); \ y^- : (0,0,0); \ y^+ : (0,0,0)$) at Index-1 (green dotted line) and Index-2 (solid blue line)

Figure 11.7 shows the non-concurrent maximum and minimum stresses experienced by rebars for all increments. As seen, at the first increment some of the rebars are under tension (mainly due to weight of concrete and steel) and some other are under compression. As seen, the maximum stress starts at about 7 MPa and increases to about 118 MPa. On the other hand, the minimum stress starts at about -9 MPa and increase up to -6 MPa, then decrease again to about -63 MPa at the end of analysis. It is noteworthy that based on Table 12.3 the yield stress at the rebars is 275 MPa. Thus the rebars are not failed in this case. Compared to P3, this model P5, experiences a bit smaller tensile stresses while considerable higher compressive stresses (about 35% higher). Also the curve associated with minimum stress in rebar is not uniform and there is a sharpness at the inc $\sim$ 110.

Figure 11.9 shows stresses in the two most critical rebars in x and y directions. Based on Figure 11.3 the longer rebar in x direction is divided into 12 segments (elements), while the shorter rebar in y direction is

MERLIN AAR Problems
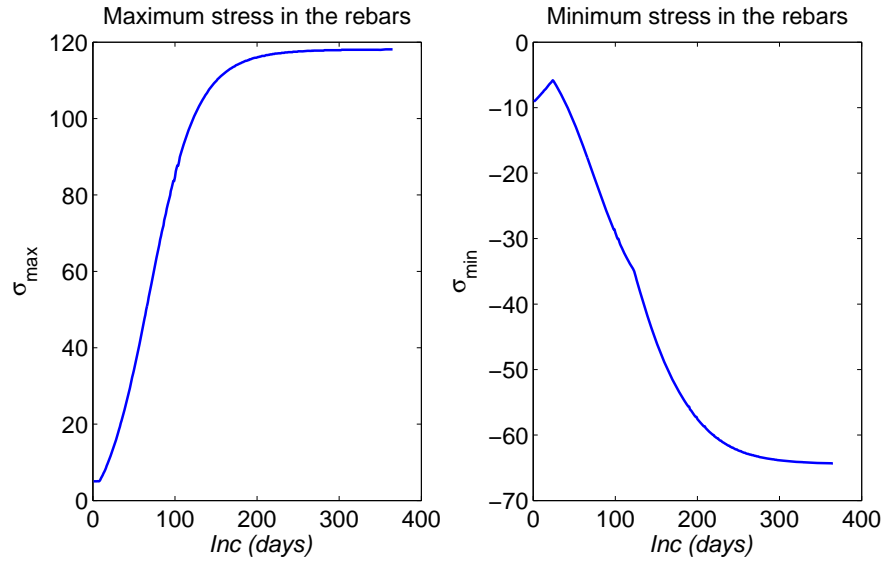
Figure 11.7: Non-concurrent maximum and minimum stresses in rebars for model P5 $\left(x^- : (0,0,0); \ x^+ : (0,0,0); \ y^- : (0,0,0); \ y^+ : (0,0,0) \right)$

divided into 10 segments.

Based on Figure 11.9, the most critical rebar belongs to the x direction (because it is longer). The maximum and minimum stresses in this case are in agreement with those already obtained in Figure 11.8 for whole the panel.
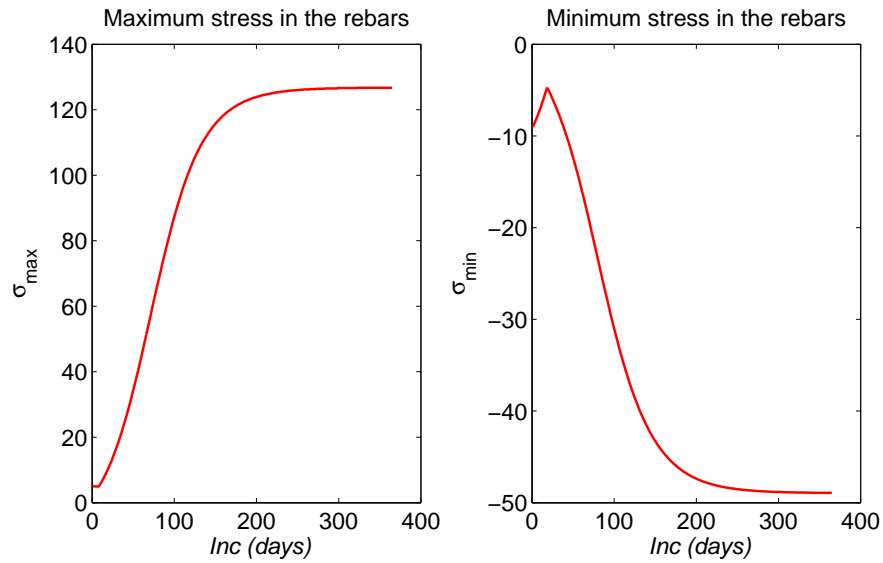
Figure 11.8: Non-concurrent maximum and minimum stresses in rebars for model P3 $\left(x^- : (0,0,0); \ x^+ : (0,0,0); \ y^- : (0,0,0); \ y^+ : (0,0,0) \right)$

According to Figure 11.9, the maximum stresses (in the form of tensile stress) are occurred near the two ends of the rebar. Also, the minimum stresses (in the form of compressive stress) are occurred in middle of the rebar. Based on this figure increasing the number of increments (expansion of the panel), leads to

MERLIN AAR Problems

increasing the stresses in vicinity of the ends; however, it has almost negligible effect in middle of the rebar. Compared to P3, the value of the tensile stresses is reduced in model P5 in both rebars (x and y directions). In addition, the stress distribution in shorter rebar (y direction) has partially non-uniform pattern.
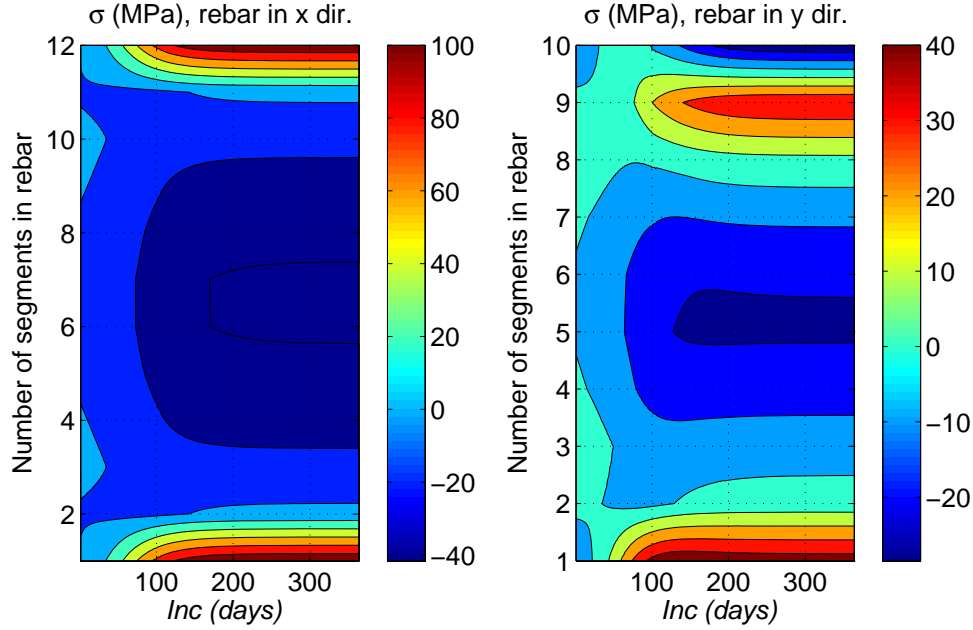
Figure 11.9: Stress at the most critical rebars in x and y directions for model P5 $\left(x^- : (0,0,0);\ x^+ : (0,0,0);\ y^- : (0,0,0);\ y^+ : (0,0,0)\right)$

Figure 11.10 shows the progressive failure of the panel model P5 under ASR expansion. As seen, the cracking first starts at the Inc = 109 at the corners of the panel (where is higher stresses is expected). Also, the starting increment (109) corresponds to the previously discontinuity in the stress time histories of the concrete (Figure 11.6) and reinforcement (Figure 11.7). The cracking is first propagate along the two opposite corner of the panel (it is symmetry). Another set of cracks appear in the center of the panel (around the Index-2) at Inc = 184. This is corresponds to the stress reduction in Index-2 (Figure 11.6) at the almost same increment.

11.2.2   Model Pre-P3-P6

In this model, the side-walls are restricted only in two directions x=y=0 and the model is permitted to expand freely in z direction. The panel is modeled considering the reinforcements as shown in Figure 11.3. The concrete is modeled by smeared crack approach.

Figure 11.11 shows the response of the considered specimen for the two index points showed in Figure 11.5. Based on this figure, the vertical displacement of the Index-1 and Index-2 is rapidly increased up to about 5 mm (Index-1 is exactly = 5.19 mm and Index-2 is 4.89 mm) in the first 10 increments. Then, the displacement is reduced up to Inc = 38 and take a stable flat form up to the end of the analysis. This increment corresponds to the beginning of the cracking in the panel. Compared to model P5, the present one ,P6, experiences a very large vertical displacement at the initial increments.

In this model, both the index points have more or less the same vertical strain (ϵ_{zz}). The general trend of the ϵ_{zz} is similar to that reported for model P5; however, there is a sudden jump at the Inc = 38 due

MERLIN AAR Problems
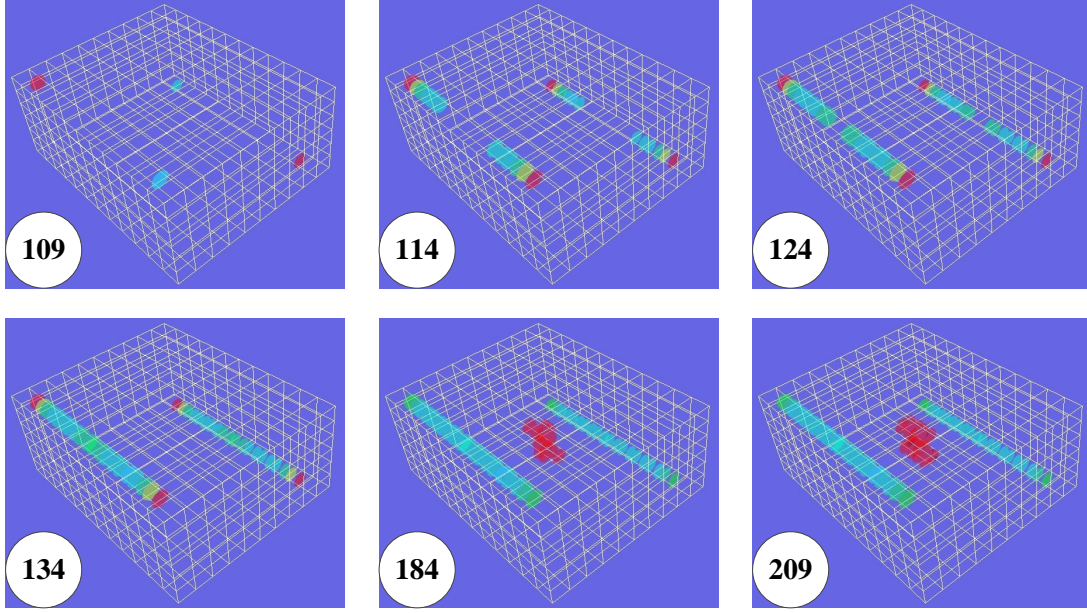
Figure 11.10: Progressive failure in panel Model P5 $\left(x^- : (0,0,0);\ x^+ : (0,0,0);\ y^- : (0,0,0);\ y^+ : (0,0,0) \right)$ under ASR expansion

to start of cracking. Also the curves are not completely smooth in this model. Compared to model P5, the present one, P6, has higher vertical strain in both index points.

The vertical stress (σ_{zz}) plots for both the index points have a similar trend. The value of the σ_{zz} is about -0.03 MPa up to Inc = 28, where there is a sudden jump in the stress time history about 0.5 MPa. Then, for the rest of the analysis the value of the stress is zero in both the index points. Therefore, it is possible to assume that the panel is stress-free in vertical direction.

Finally, comparison of the volumetric AAR strain (ϵ^{vol}_{AAR}) reveals that none of the index points reach the maximum volumetric strain (ϵ^{∞}_{AAR}), 0.005, at the end of the analysis. In spite of the previous models (specially, P4 and P5), the two index points do not have the same expansion. The Index-1 leads to higher expansion than to Index-2. The maximum ϵ^{vol}_{AAR} is about 3.9 mm and 2.6 mm for Index-1 and Index-2, respectively. It means that the panel does not have a uniform volumetric AAR strain along its thickness (in spite of its linear model, P4).

Figure 11.12 shows the non-concurrent maximum and minimum stresses experienced by rebars for all increments of model P6. Although there is fluctuation in stress response of the rebars, all the values vary between [0, 1.0] MPa. This model shows that the rebars have no effect when the panel is modeled based on free boundary condition in vertical (z) direction.

11.3 Shear Assessment of ASR-affected RC Panel

11.3.1 Models Post-P1-P2-P3

These three models are similar to those studied as P10, P11 and P12, except that the material nonlinearity in term of concrete cracking (smeared crack model) is taken into account. P13 is, in fact, the reference model
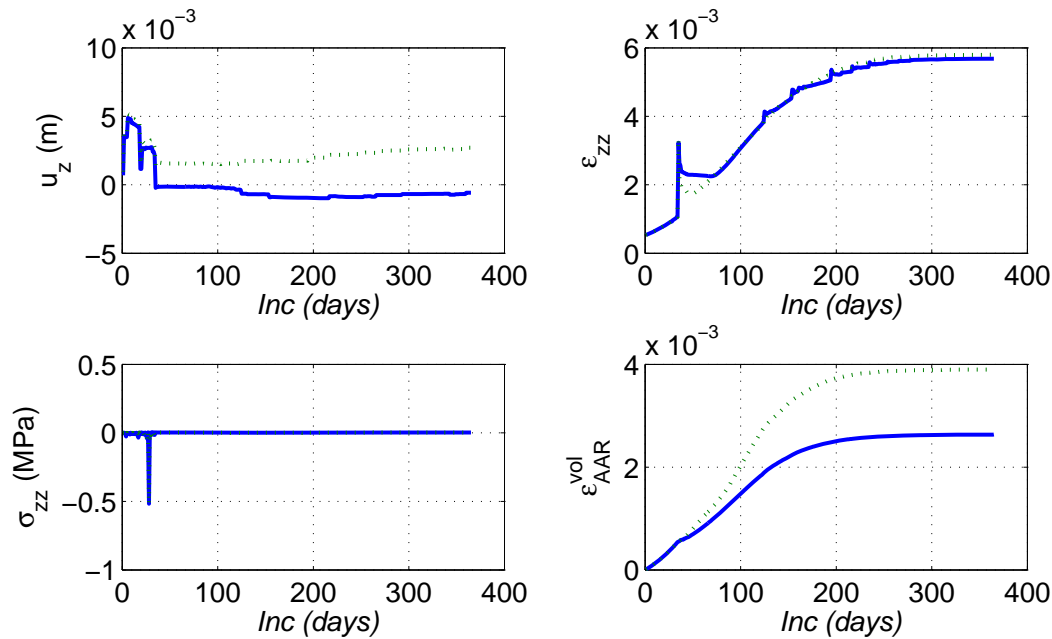
Figure 11.11: Response of model P6 $\left(x^{-} : (0,0,1);\ x^{+} : (0,0,1);\ y^{-} : (0,0,1);\ y^{+} : (0,0,1) \right)$ at Index-1 (green dotted line) and Index-2 (solid blue line)
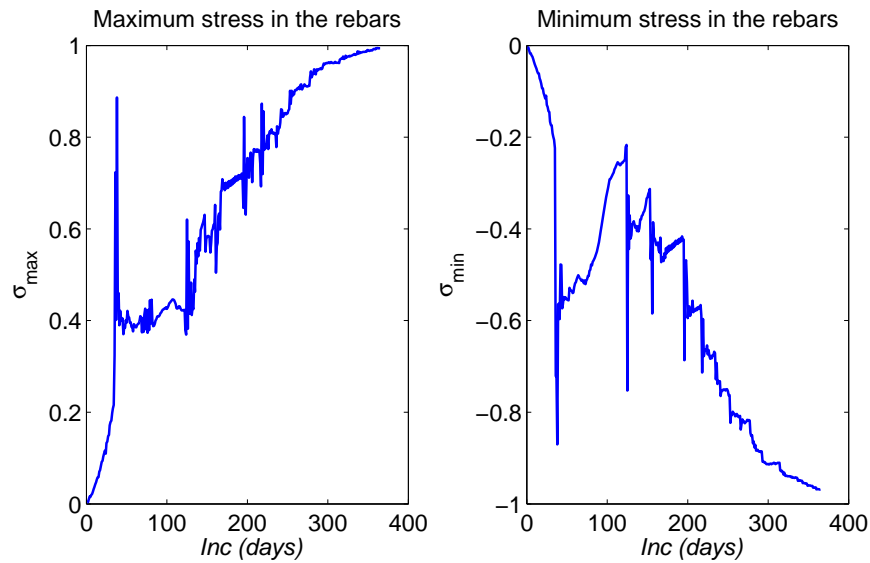
Figure 11.12: Non-concurrent maximum and minimum stresses in rebars for model P6 $\left(x^{-} : (0,0,1);\ x^{+} : (0,0,1);\ y^{-} : (0,0,1);\ y^{+} : (0,0,1) \right)$

for this group (no ASR expansion is applied). P14 and P15 are different in the boundary conditions applied under the ASR expansion.

Figure 11.14 shows the load-displacement curve of three cases. As seen, the load-displacement curve is nonlinear in all cases (nonlinear material assumption). Based on this figure, the initial slope of the P13 is more than P14 and P15, showing that the initial ASR expansion leads to softening of the panel (due to
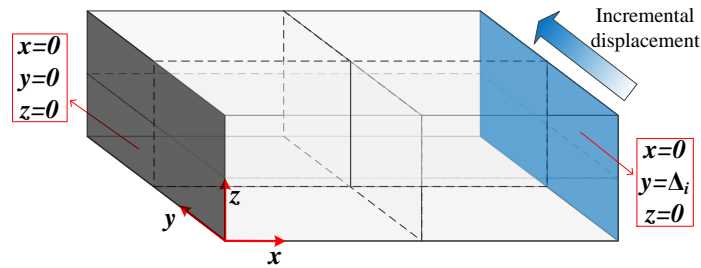
Figure 11.13: Boundary conditions for the shear analysis of the RC panel

cracking). There is a discontinuity in the capacity curve of the panel P13 at $\Delta = 2.14$ mm. This point corresponds to the initiation of the first set of the cracks in the diagonal form. There is not such a sudden jump or reduction in two other curves (P14 and P15) because they already experienced some cracking before applying the incremental displacement.

The capacity curve of the panel P14 is more than the P13, while the capacity curve of the P15 is less than P13. Both the P14 and P15 experience ASR expansion and some cracking before applying the incremental displacement. The differences of the capacity curves can be attributed to the boundary conditions applied in the ASR part. In the panel P14, full confinement of the model under ASR expansion make the panel strength. Based on Figure 11.10, the panel does not have critical cracking under ASR expansion. Also, most of the cracking is concentrated at the center which experience lower tensile stresses under incremental divorcement. On the other hand, panel P15 was free to expand along its thickness and thus had more cracked elements initially (before applying the incremental displacement). Therefore, this model has a lowest capacity curve among the three cases.
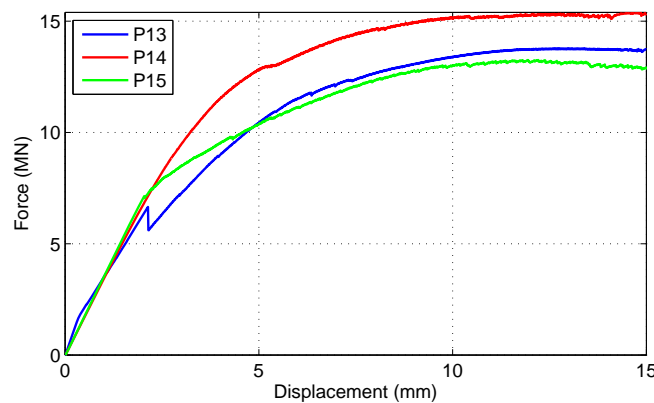
Figure 11.14: Load-displacement curve for the Panel P13, P14 and P15

Figure 11.16 shows the progressive failure mode of the panel model P13 under incremental displacement. As seen, the cracking starts at the upper right corner of the panel and then lower left corner. These two points correspond to the high tension area as shown in Figure 11.15.

The cracking proceeds in vertical direction along the walls. Then, a sudden diagonal cracked area appears in the panel which is believed to be the main failure mode. At this time, the crack pattern looks like "N" letter. Further cracking develops around this main path.

MERLIN AAR Problems
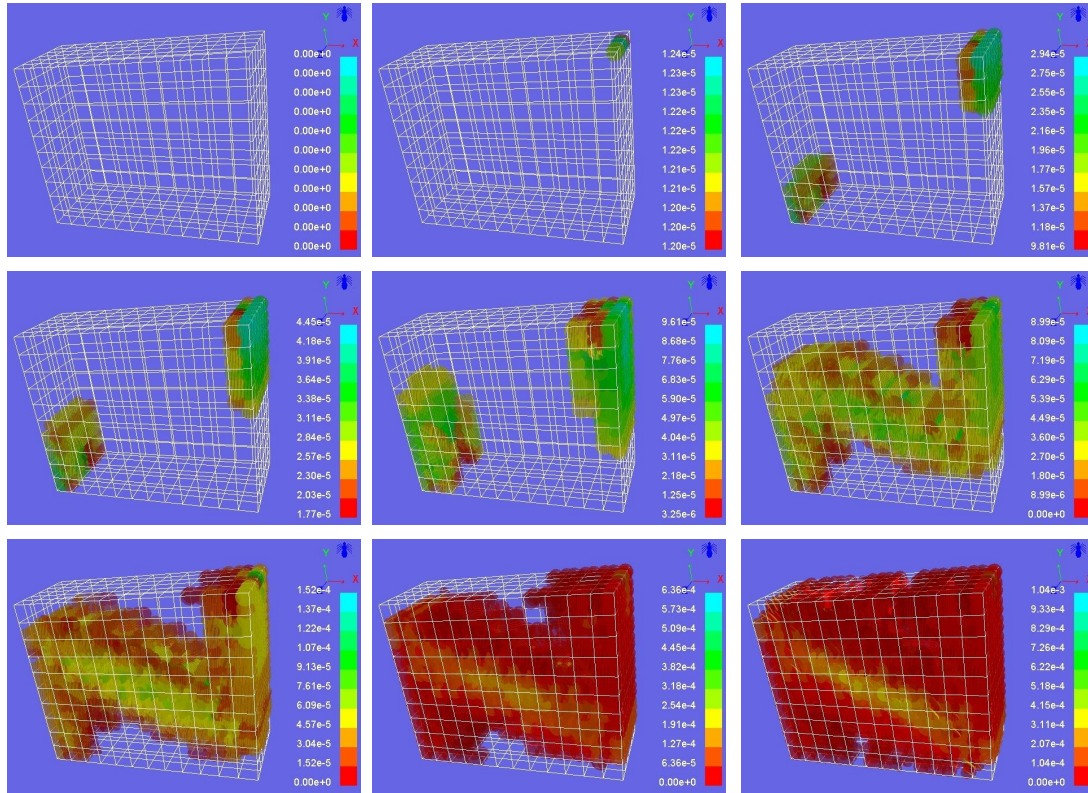
Figure 11.15: First principal stress distribution at the Inc = 1 on the panel model P7

Figure 11.17 shows the progressive failure mode of the panel model P14 under incremental displacement. The cracking of the panel at the last increment of the ASR expansion is taken as an initial condition for the incremental displacement. As seen, the failure mode in this model is completely different from P13 (the reference model). Considering initial cracking at the center of panel, the rest of the cracks propagate in the diagonal form in both directions. It makes the crack pattern looks like "X" letter. Further cracking develops around this main path.

Figure 11.18 shows the progressive failure mode of the panel model P15 under incremental displacement. The cracking of the panel at the last increment of the ASR expansion is taken as an initial condition for the incremental displacement. Based on this figure (and having in mind the boundary conditions of the P15 under ASR expansion), it can be seen that the panel experience almost a uniform cracking along its thickness under ASR expansion. This failure mode is completely different from P13 (the reference model) and P14 (the other ASR-affected model). It is not possible to define a specific failure mode in this model, because even under the incremental displacement the model has more or less uniform cracking (or opening of already cracked elements).

11.4 Out Of Plane Shear

These specific problems of the RILEM Benchmark have not been explicitly investigated.

MERLIN AAR Problems
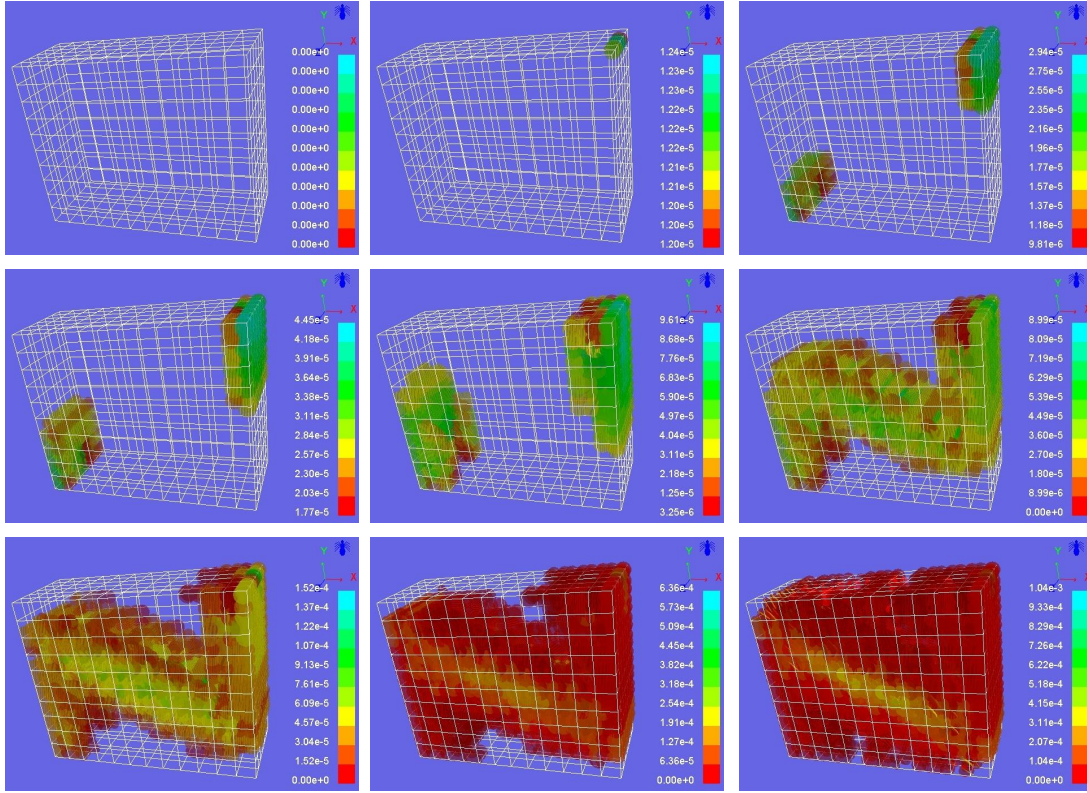
Figure 11.16: Progressive failure of the panel P13 under incremental displacement
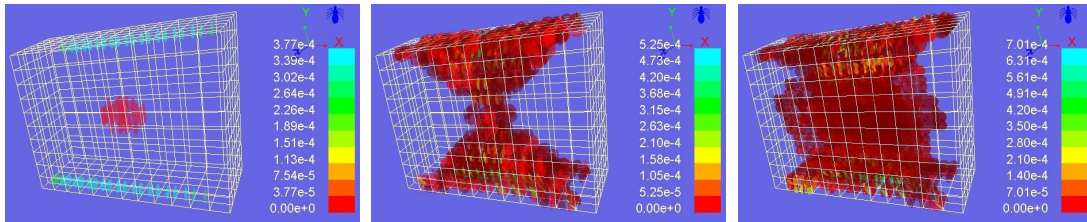
Figure 11.17: Progressive failure of the panel P14 $\left(x^- : (0,0,0); \; x^+ : (0,0,0); \; y^- : (0,0,0); \; y^+ : (0,0,0) \right)$ under incremental displacement
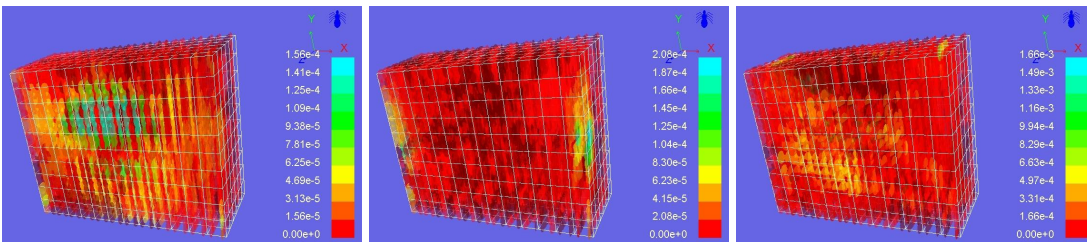
Figure 11.18: Progressive failure of the panel P15 $\left(x^- : (0,0,1); \; x^+ : (0,0,1); \; y^- : (0,0,1); \; y^+ : (0,0,1) \right)$ under incremental displacement

MERLIN AAR Problems

Part III

Other Analyses

Chapter 12

P-11: Nuclear Containment Structure

12.1   Case Study Description

In light of recent evidence that ASR can reduce the shear strength by up to 20% (Saouma, 2017), the impact of such a loss on the structural capacity of a NCVS excited by earthquakes is next ascertained through a state of the art driven analysis of a generic NCVS with dimensions inspired from NUREG/CR-6706 (2001). The structure will be first subjected to 40 years of ASR expansion followed by multiple seismic excitations (with or without ASR induced damage), and results will be compared with the response of the NCVS subjected to the same seismic excitations but without prior ASR expansion (Figure 12.1 B, C, and A respectively).
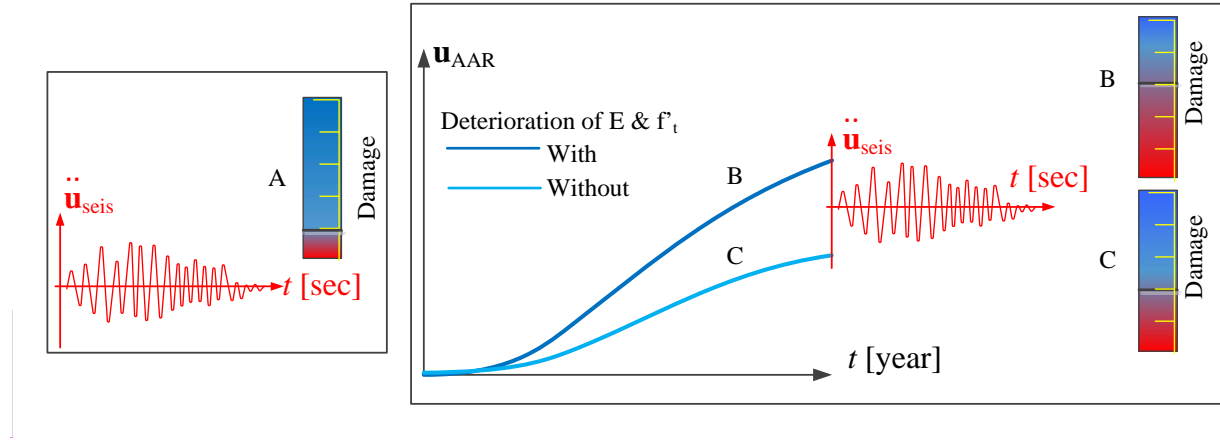
Figure 12.1: Three scenarios of investigation: A: No ASR; B: ASR with 40% damage; and C: ASR without Damage.

Outline of the analysis procedure is partially shown in Figure **??** where after identification of the physical model site characteristics, probabilistic seismic hazard analysis and seismic hazard de-aggregation are performed. Then, ASR properties are identified, and dynamic excitations are generated through: a) ETAF, and b) scenario-based stochastic ground motions. Then, the FE analysis is performed in the cloud (i.e. using multiple CPU's) and finally capacity and fragility curves are derived for ETA and stochastic models, respectively. In each case, three analyses were performed, Figure 12.1.

The selected and partially buried NCVS is schematically shown in Figure 12.2(a). Note that only the

concrete underneath the soil level will be subjected to ASR (as a result of the high relative humidity likely to be present in the surrounding foundation). Material properties are separately shown in **??**

(a) Geometry and dimensions

(b) Potential uplift modeled by joint elements

(c) Half 3D model with lateral viscous dampers and container mesh (with ASR expansion)
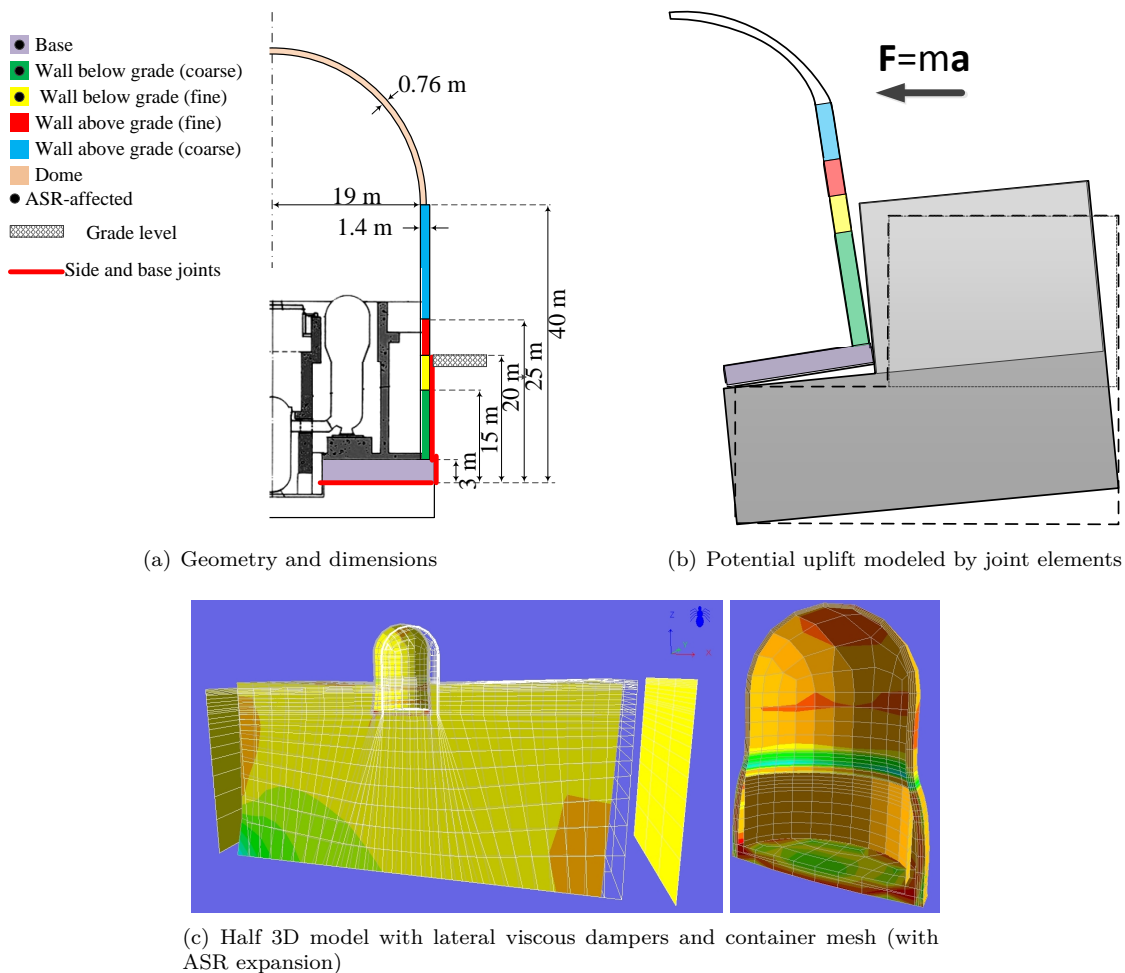
Figure 12.2: Geometry, material groups, role of joint elements, and finite element mesh

The potential secondary stresses induced by the uplift forces (caused by the eccentricity of the resulting inertial force), Figure 12.2(b), will be mitigated by the insertion of cohesive based joint elements (Cervenka, Chandra, and Saouma, 1998) where necessary. A 3D continuum model, Figure 12.2(c) is prepared. Reinforcement is modeled as "smeared" by altering the stiffness matrices of those continuum elements they cross. A 0.5% reinforcement was assumed in both directions, resulting in the reinforcement shown in Figure 12.3(b).

Different material groups are defined in the FE model. Concrete was modeled by four distinct groups according to location, mesh densities, and whether it is reactive, Figure 12.2(a). The dome is assumed to be linear elastic, whereas the wall and the base are modeled as nonlinear using the well-tested smeared crack model (Cervenka and Papanikolaou, 2008) of the FE code ATENA (Červenka and Jendele, 2016).

ASR is captured by the constitutive model described above, (Saouma and Perotti, 2006). It is assumed that the NCVS operates for 40 years during which it undergoes a relatively mild total expansion of 0.3% uniformly distributed over the "contaminated" zone as an additional internal strain. In actuality, ASR is not
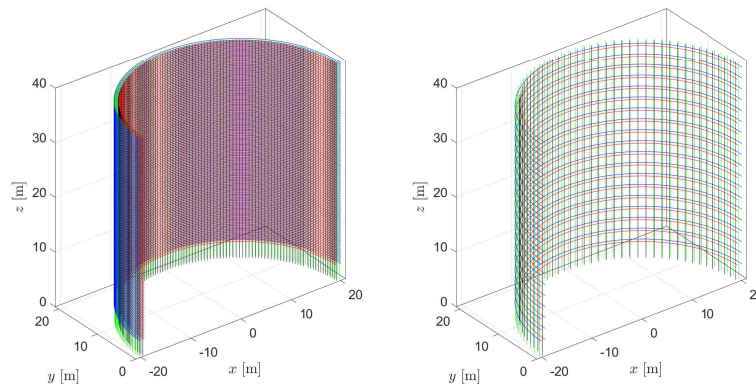
(a) Actual reinforcement in the NCVS (b) Adopted reinforcement in the model

Figure 12.3: Reinforcement details

so uniform and is more likely to be "spotty" to reflect the usage of reactive aggregates in some, but not all the pours. This stochastic process is not accounted for in this study, however a separate study indicates that a sparsely distributed ASR expansion may be more detrimental than a uniformly distributed one (due to the induced strain discontinuities) (Hariri-Ardebili, Saouma, and Merz, 2018). Accompanying this expansion are two levels of concrete degradation zero and 30% reduction of E and f'_t after 40 years. The 40 years expansion is simulated in two weeks increments assuming a constant temperature and RH. The external average temperature at the site is estimated to be 11^oC (external face of NCVS), the internal temperature is in turn estimated to be 25^oC. Hence, an average mean yearly temperature of $(25+11)/2 = 18 \ ^oC$ is assumed. Note that in a more refined analysis, the temperature distribution across the wall should be considered, and monthly average temperatures should also be refined.

Rock (both the foundation and lateral) is assumed to be linear elastic. Interface joints are placed around and below the NCVS to capture potential uplift of lateral separation of the container from the adjacent rock.

Table 12.1: Concrete mechanical properties

Characteristics	Symbol	Unit	Base	Wall below	Wall above	Dome
Mass density	ρ	Gg/m^3	0.002250	0.002250	0.002250	0.002250
Modulus of elasticity	E	MPa	39,000	39,000	39,000	39,000
Poisson's ratio	ν	-	0.2	0.2	0.2	0.2
Tensile strength	f_t	MPa	3.1	3.1	3.1	3.1
Fracture energy (Exponential softening)	G_F	MN/m	1.2e-4	1.2e-4	1.2e-4	1.2e-4
Compressive strength	f_c	MPa	-31.0	-31.0	-31.0	-31.0
Critical displacement in compression	w_d	m	-0.0005	-0.0005	-0.0005	-0.0005
Factor beta for return direction	β	-	0.0	0.0	0.0	0.0
Factor e for roundness of failure surface	e	-	0.55	0.55	0.55	0.55
Onset of nonlinearity in compression	f_{c0}	MPa	-20.0	-20.0	-20.0	-20.0
Plastic strain at compressive strength	ϵ_{cp}	-	-1e-3	-1e-3	-1e-3	-1e-3

MERLIN AAR Problems

Table 12.2: Characteristics of the ASR model

Characteristics	Symbol	Unit	Base	Wall
Reference temperature	T_0	-	18	18
Maximum volumetric expansion at T_0^{test}	$\varepsilon_{ASR}^{\infty}$	-	0.3%	0.3%
Characteristic time at T_0^{test}	τ_C	ATU	64	64
Latency time at T_0^{test}	τ_L	ATU	160	160
Activation energy for τ_C	U_C	-	5,400	5,400
Activation energy for τ_L	U_L	-	9,400	9,400
Residual reduction factor	Γ_r	-	0.5	0.5
Fraction of ε_t prior to reduction of ASR expansion due to macro cracking	γ_t	-	0.5	0.5
ASR expansion annealing stress	σ_U	MPa	-8	-8
Post-ASR residual relative Young modulus	β_E	-	70%	70%
Post-ASR residual tensile strength	β_{f_t}	-	70%	70%

Table 12.3: Rebar mechanical properties

Characteristics	Symbol	Unit	Vertical	Horizontal
reinforcement ratio	ρ	-	0.01	0.005
Modulus of elasticity	E	MPa	200,000	200,000
Poisson's ratio	ν	-	0.3	0.3
Yield stress	σ_Y	MPa	248	248

12.2   Intensifying Acceleration Functions

Six different randomly generated ETAFs, with main characteristics previously explained were used. Schematically, all the ETAFs are analogous Figure **??** as the base of all of them is a random white noise.
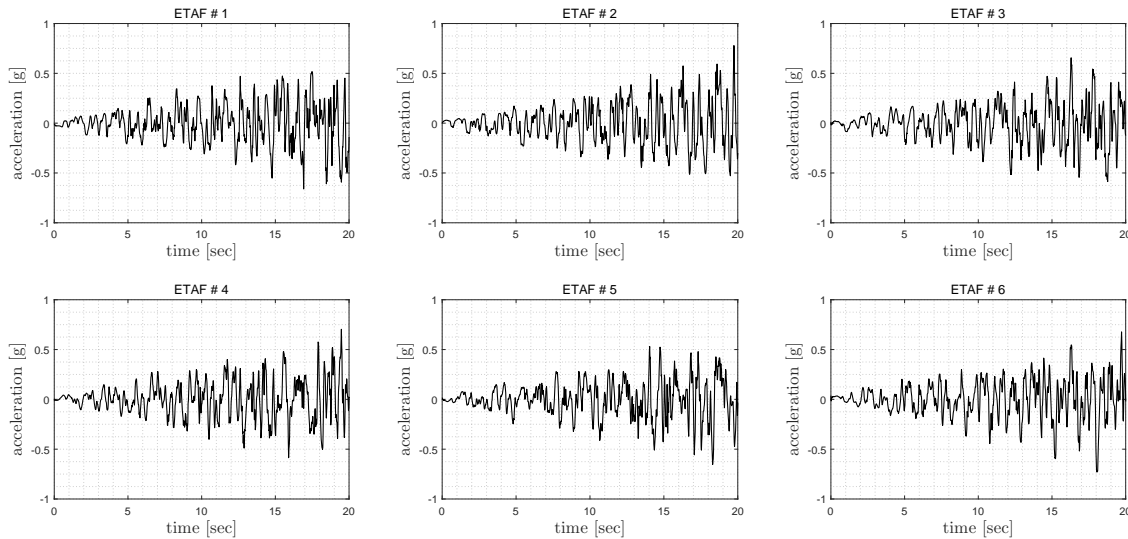
Figure 12.4: Six adopted ETF

Analysis was performed by the code Merlin (**merlin**) which to the best of the authors knowledge is the only code that has been "validated" by performing nearly all the analyses proposed by the RILEM (Saouma et al., 2017). Three sets of analyses were performed: 1) Static + ASR, 2) Static + Dynamic, and 3) Static + ASR + Dynamic (100 for the stochastic ground motions, and three for each of the six ETA).

MERLIN AAR Problems

12.2.1   Static + ASR Analyses

In this first analysis, 40 years of ASR in the NCVS is simulated. Figure 12.5(a) shows swelling of the container along with a closeup on the concrete-rock separation. Clearly ASR expansion interacts with the structure in what may be *a priori* counter-intuitive: a) the mat expands in a concave shape due to the structural constraints of the cylindrical vessel, Figure 12.5(b)-1; b) the wall pushes against the adjacent rock, but is constrained by both the base mat and the upper portion of the enclosure not subjected to expansion, Figure 12.5(b)-2, causing strong curvature, joint opening, and ensuing stress discontinuities; and c) sliding of the NCVS itself, Figure 12.5(b)-3. Furthermore, the evolution of concrete cracks is shown in Figure 12.5(c). It should be noted that cracking starts at the central region of the mat base and along a ring on the wall next to soil level.

(a) Swelling of contaminated zone

(b) Evolution of joint opening/sliding due to ASR

(c) Internal crack propagation (left to right)
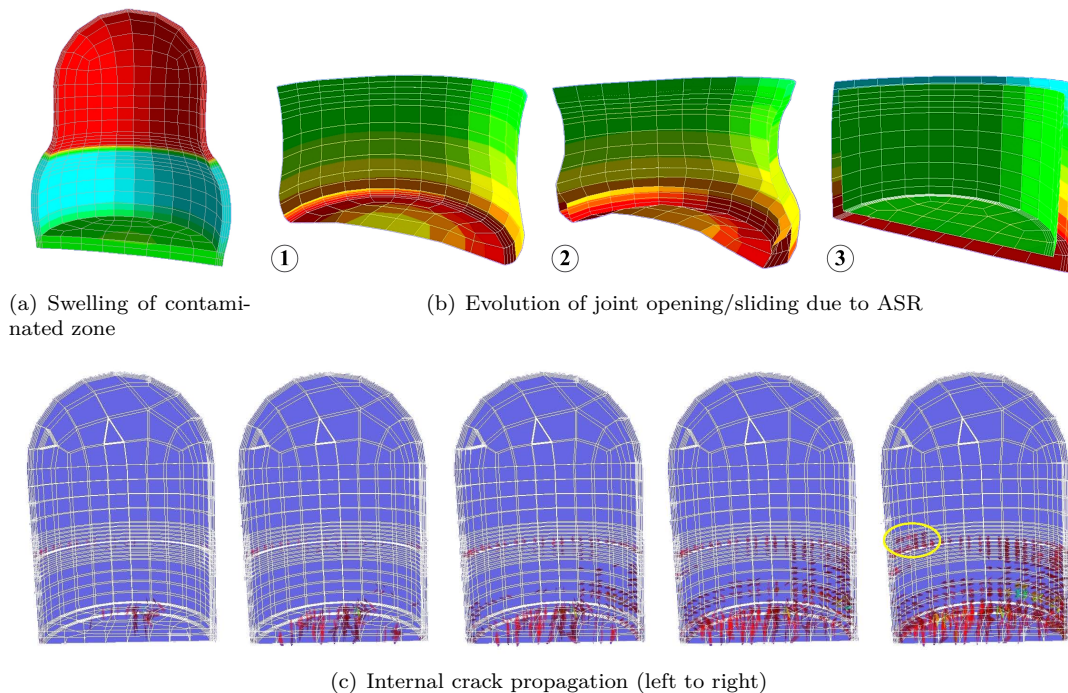
Figure 12.5: Response of NCVS under static + ASR analysis after 40 years

12.2.2   Impact of ASR on Capacity Curves

Impact of ASR on the structural response of the NCVS can now be ascertained by comparing "Static + Seismic" with "Static + ASR + Seismic" for displacement and stresses for six different ETA functions. Three sets of simulations are compared: a) Static + dynamic analysis (Referred to Dyn. in the plots); b) Static + ASR with degradation of f'_t and E over time + dynamic analysis; and c) Static + ASR (without material degradation) + dynamic analysis.

Displacements: The absolute value of the (horizontal) displacements corresponding to peaks in (the six) ETAFs is first extracted. Equation **??** is used to determine the maximum QoI (i.e. displacement). The mean of those six ETAFs for each of three assumptions are computed, Figure 12.6(a). These are ramping curves as the dynamic acceleration is indeed defined as a linearly increasing one (Figure **??**). To better grasp the impact of ASR, results are normalized with respect to the one without ASR

MERLIN AAR Problems

(dynamic only), Figure 12.6(b). The deviations are time-dependent and, as expected, model with ASR degradation is much more impacted than the one without. On average, and for this case study, ASR with degradation results in ∼20% change, whereas the one without has ∼8% variation with respect to the "Dyn. only" model. If material degradation is ignored (which is an erroneous abstraction) displacements are still lower than those cases without ASR, but greater than ASR with degradation. Note that discrepancy with respect to the case without ASR starts at around 9 s (i.e., until this point the ASR had little impact on deformation). The impact of ASR (with and without degradation) is time-dependent due to the complexities of the internal stress states induced by it or resulting from the seismic excitation, Figure 12.6(b).

(a) Displacement profile at the top   (b) Displacements normalized and mean differences
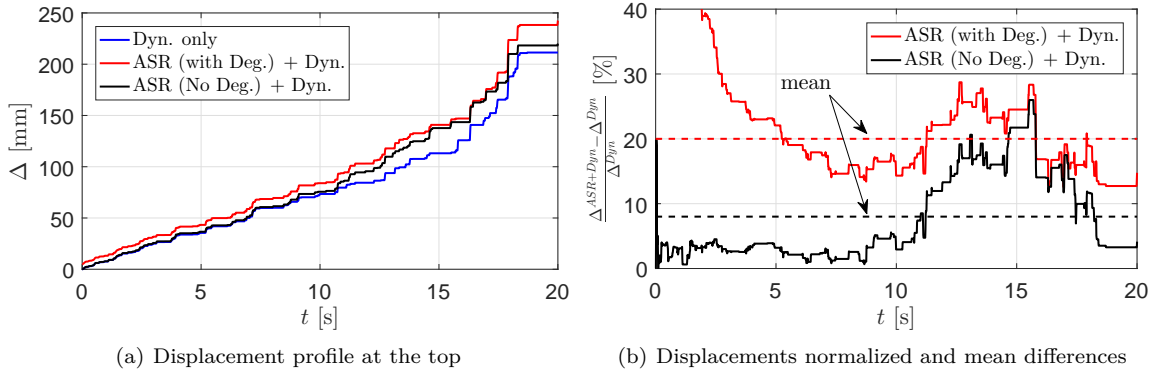
Figure 12.6: ETA-based displacements and the mean differences

Stresses: Time history of maximum principal stresses are recorded. The ASR affected responses result in higher stresses than those without degradation, and additional substantial damages will be induced by the ASR (with internal damage accounted for). At the base, Figure 12.7(a), maximum principal stresses are positive (cracking) and attenuate with time. Stresses are at first low when ASR dominates, but then suddenly increase with a localized damage at time $\simeq 17$ sec. At the grade elevation, Figure 12.7(b), stresses are much higher without ASR, and then gradually decrease with no indication of failure. Note that the tensile strength is 3.1 MPa. On the other hand, in the presence of prior ASR expansion, the stresses are negative, and a sudden localized failure appears at $t=14$ sec. For a point above grade, Figure 12.7(c), stresses are higher in the absence of ASR and there is indication of a localized failure at $t = 15$ s. In the presence of ASR, the failure is delayed to about 17 sec. Finally, at the base of the dome, Figure 12.7(d), the ASR stresses are substantially higher than without and localized failure occurs around 17 s. For this case, ASR has reduced the stresses at the base, but substantially increased them at the base of the dome. Indeed, stress attenuation with time is the direct result of a nonlinear analysis where upon cracking there is a substantial stress redistribution resulting in localized stress reduction.

Cracking: of the structure is shown Figure 12.8 at different times. In general, the crack pattern of ASR affected models are different and the previous observations are qualitatively confirmed by the crack profiles. Indeed, the damage index (DI), ratio of the cracked sections to the total area, is highest when ASR (with damage) preceded the seismic excitation. The ASR has a much higher impact of that portion of the NCVS below grade than above (where no ASR is modeled).

The sound NCVS experiences the major cracks at the soil level at about 12.8 s, while at the corresponding time the ASR-affect NCVS had already some major cracks though all the top-wall. Results

MERLIN AAR Problems

(a) Base

(b) Grade

(c) Above grade

(d) Base of dome
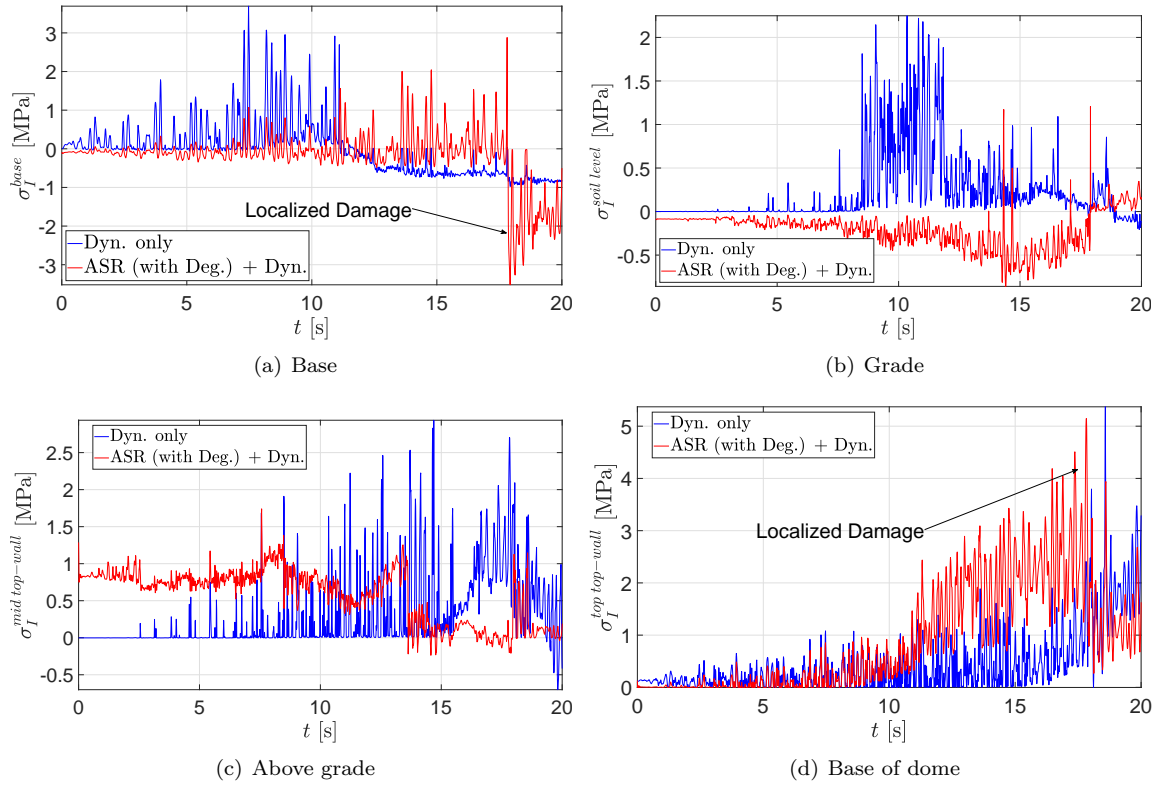
Figure 12.7: Principal stresses capacity curves

of ETA analysis prove that "endurance" of the NCVS is reduced when it is subjected to initial ASR.

MERLIN AAR Problems
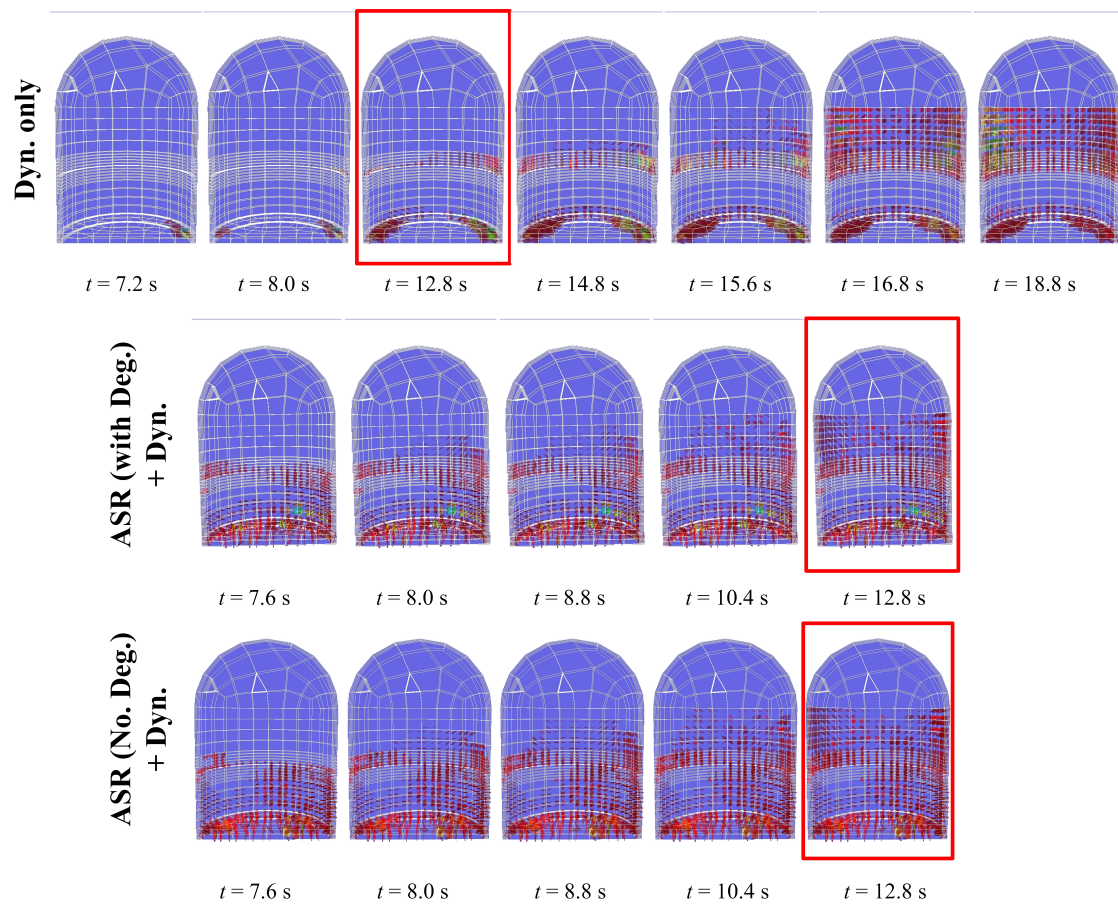
Figure 12.8: Crack profile from a sample ETA simulation at identical time steps

Chapter 13

P-12 Out of Plane Shear

Adapted from *Effect of Alkali-Silica Reaction on the Shear Strength of Reinforced Concrete Structural Members. A Numerical and Statistical Study* by Saouma, Hariri-Ardebili, Le Pape, and Balaji. Published in *Nuclear Engineering and Design*, 2016.

13.1   Introduction

Whereas ASR has been reported in numerous hydro-electric dams, only recently has there been evidence of such occurrences in NPP: In Japan, Ikata No.1, Shikoku Electric Power (Takatura et al., 2005) (Shimizu et al., 2005), in Canada, Gentilly 2 (Tcherner and Aziz, 2009) (Chiaramida, 2013), and in the US, Seabrook (NextEra-ML121160422, 2012) (Haberman, 2013) – The U.S.NRC issued Information Notice (IN) 2011-20, *Concrete Degradation by Alkali Silica Reaction*, on November 18, 2011, related to the ASR identified at Seabrook. Considering that US commercial reactors in operation have reached the age when ASR degradation could be visually detected and that numerous non nuclear infrastructures (transportation, energy production) have already experienced ASR in a large majority of the States (e.g., a U.S. DOT survey reported by Touma (2000)), the susceptibility and significance of ASR for nuclear concrete structures must be addressed in the perspective of license renewal and long-term operation beyond 60 years. Yet, ASR has seldom, if ever, been reported in the open literature in connection with its significance for Class I-safety nuclear concrete structural components, e.g., the concrete biological shield, the concrete containment building (CBB) and the fuel handling building. The evaluation of the structural significance of ASR-affected concrete structures in NPP presents some specificities in terms of design and exposure conditions, that limits a direct interpretation based on the analysis of transportation infrastructures or concrete dams, though the methodological pathways could be similar to a large extent.

The effects of ASR on structural members resistance are apparently contradictory. When shear reinforcement is present, the expansion confinement results in a prestressing of concrete that contributes to an increasing shear capacity, e.g., (Giannini et al., 2013), or an absence of significant change (Fan and Hanson, 1998). However, it was observed that shear failure may shift from a truss mechanism to a arch mechanism (Wang and Morikawa, 2012). Also, excessive ASR-induced self-prestressing may cause reinforcement yielding and failure (Miyagawa, 2013; Nakamura, Watanabe, and Koga, 2008). Of particular concern is the case of beams, or slabs, in absence of shear reinforcement (Bach, Thorsen, and Nielsen, 1993; Schmidt et al., 2014b; Uijl and Kaptijn, 2003). Uijl and Kaptijn (2003) and Uijl and Kaptijn (2002) tested the shear capacity of

6 beams sawn from two flat-slab bridges suffering from ASR in the Netherlands. The failure mode was of shear-tension type, whereas flexural-shear failure would have been expected if no ASR was present. The shear failure capacity was 25% lower than the expected theoretical resisting capacity in absence of ASR. In-situ shear tests on cantilever bridge deck conducted by Schmidt et al. (2014b) in Denmark showed a important loss bearing capacity in the zone severely affected by ASR.

The absence of shear reinforcement (i.e., in the thickness) permitted by ACI 318 (Building Code Requirements for Structural Concrete) is common in nuclear concrete structures resulting in a lack of confinement that imposes primarily the out-of-plane ASR expansion. Hence, the residual, i.e., post-ASR, shear bearing capacity relies, for a large part, on the concrete bulk shear resistance. The residual shear capacity, resulting from an accidental design scenario, such as a seismic excitation, of ASR-affected class I-safety structural components is expected to depend on two competitive mechanisms:

1. The extent of material damage, i.e., micro-cracking, facilitating the propagation of a shear fracture and,
2. The relative in-plane compressive prestressing induced by some level of structural confinement and the orientations of the reinforcement, potentially increasing the shear capacity.

This question remaining unresolved, further investigation is needed to determine the potential impact of ASR on the structural resistance of nuclear structures. This article presents an extensive parametric numerical study providing a novel insight of the effect of ASR on the shear capacity of RC members without shear reinforcement.

13.2 Model and methodology

13.2.1 Model Selection

The representativity of the analyzed structural components in regard to an actual CBB geometry is illustrated in Fig. 13.1(a). On the left side, are sketched the beam, truncated beam and the panel under investigation. Correspondingly, the right side shows the concrete model which will be separately tested by the first author within the framework of an NRC grant. Figure 13.1(b) presents in greater details the load support as well as the reinforcement of the container. To facilitate the visualization, the vertical reinforcement will be shown in blue and hoop reinforcement in red, Fig. 13.1(c) and 13.1(d). Because of the large curvature radius of the CBB, reinforcement are considered straight for the sake of simplicity.

13.2.2 Boundary Conditions

As stated earlier, two sets of boundary conditions are considered:

1. Those applicable during ASR expansion (simulation increments: 1-73), and,
2. those applicable during the external shear force application (simulation increments: 74-174).

The former is to capture potential ASR strain realignments caused by external constraints (Multon, 2004) as implemented in the author's model (Saouma and Perotti, 2006).

The choice of the varied geometries (beam, truncated beam and panel) and boundary conditions (unrestrained, restrained and fully restrained) reflects an attempt to model gradually increasing structural restraints, as existing in actual Class I-safety concrete structure due to the presence of adjacent or internal structures, as well as, other connecting structural members (basemat, floors, walls). Note that Class-I safety structures are not limited to the containment buildings: the International Agency for Atomic Energy
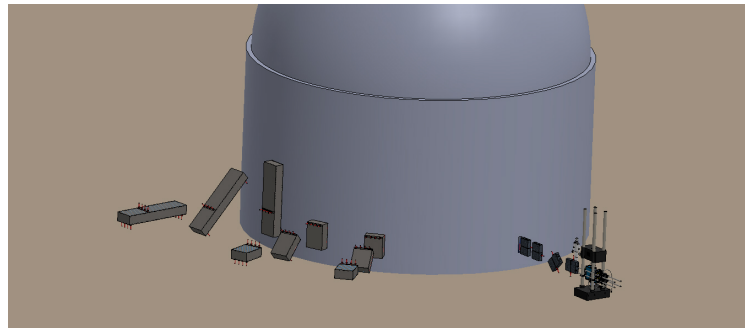
(a) Computational and Laboratory Models
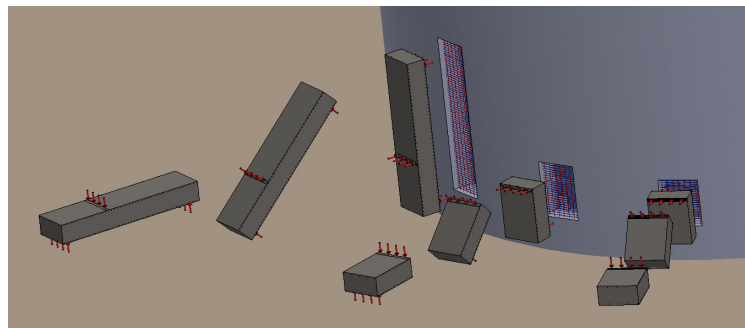
(b) Computational Models;
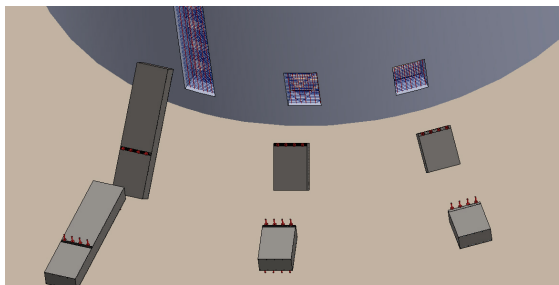
(c) Longitudinal and Circular Reinforcement; Structural Analysis;
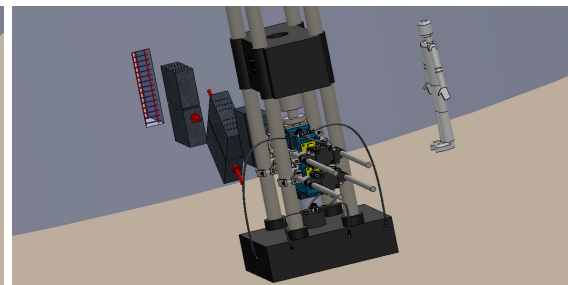
(d) Longitudinal and Circular Reinforcement; Structural Analysis;

Figure 13.1: From Containment Shell to Concrete Model; Beam, Truncated Beam and Panel (from left to Right)

(IAEA Specific Safety Guide No. SSG-30) labels Class-I safety "any structures, systems and components whose failure would lead to consequences of 'high' severity", e.g., primary containment, basemat, internal structures, auxiliary building, diesel generator building, part of the turbine building...

The boundary conditions are presented schematically in 13.5. Details are also provided in 13.1.

Finally, given the importance of the BCs, those are better visualized in Fig. 13.6, 13.7 and 13.8, for the beam, the truncated beam and the panel respectively. It should be noted that in all cases components are drawn to scale.

MERLIN AAR Problems
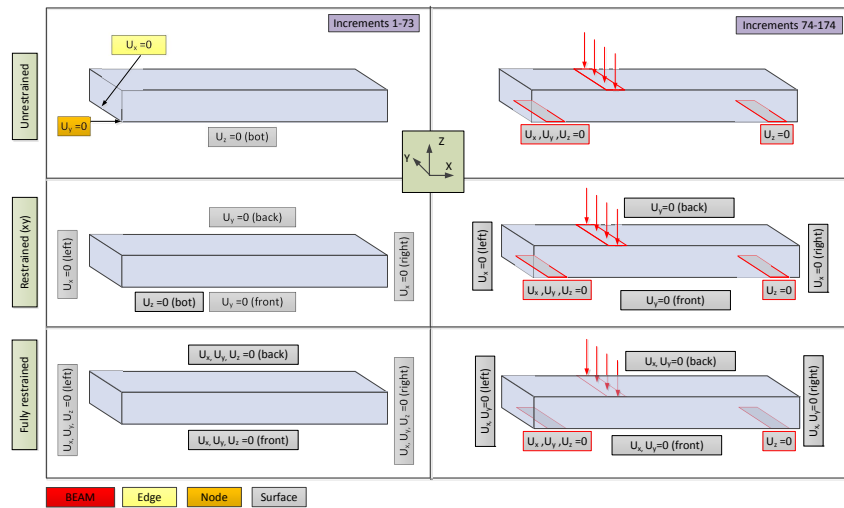
Figure 13.2: Beam Boundary Conditions
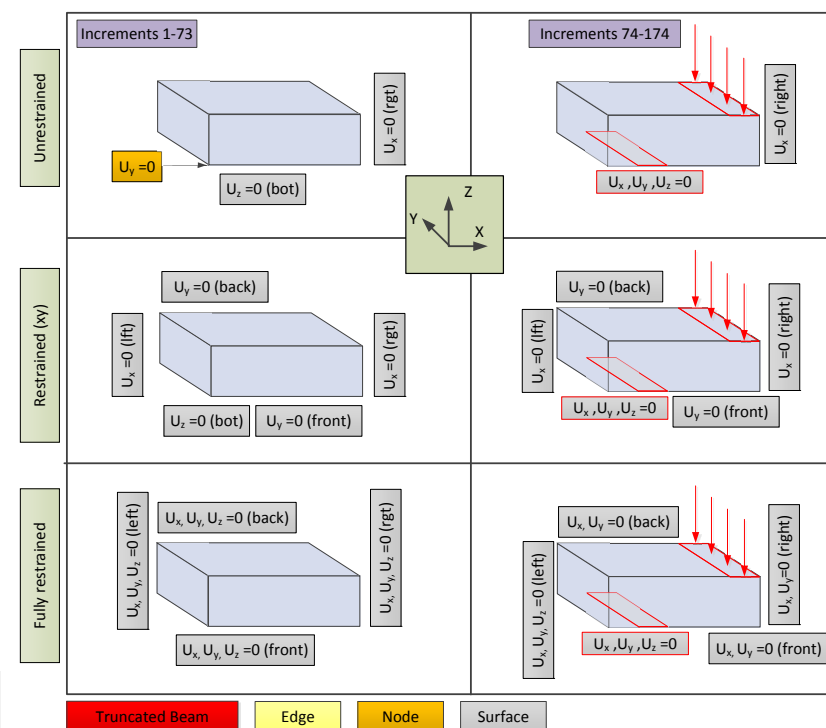
Figure 13.3: Truncated Beam Boundary Conditions

13.2.3 Dimensions

Two different depths are considered: 24 and 48 inches, (0.61 m and 1.22 m, respectively) in a attempt to cover the range of Class I-safety reinforced concrete walls in NPPs. In particular, the thickness of the CCB is typically greater than 3 feet (0.91 m). Actual dimensions of the three structural members under

MERLIN AAR Problems
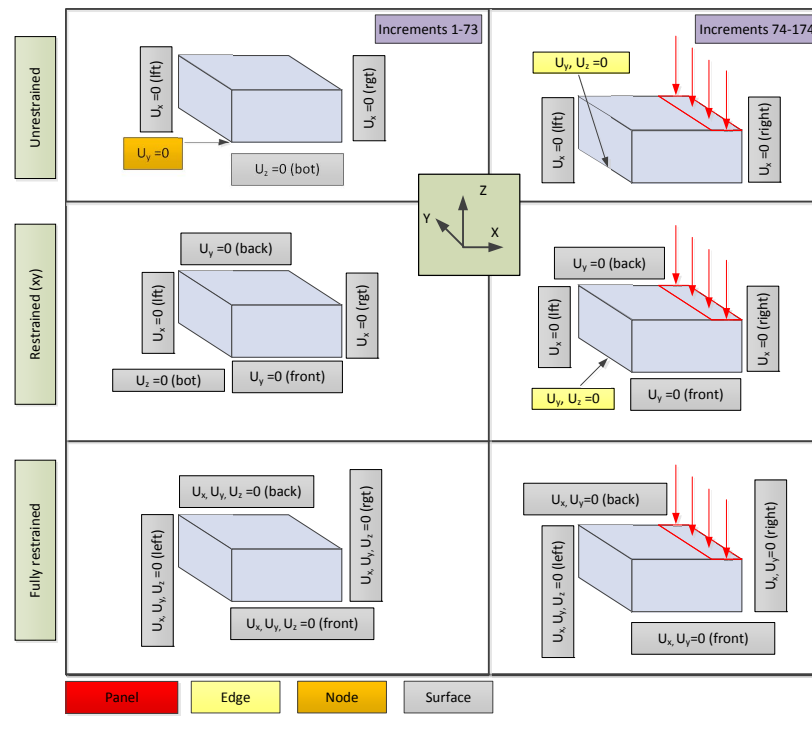
Figure 13.4: Panel Boundary Conditions

consideration in this study are shown in 13.9 with reference to 13.2.

13.2.4   Finite Element Meshes and Analyses

The finite element meshes were generated using Kumo (Saouma, 2009). The prepared 6 meshes are shown in 13.10 with the indication of the number of nodes and elements shown (same numbers for 24" and 48") in 13.3. 3D eight-node linear continuum elements are used in all cases. Meshes were "optimized" so as to guaranty sufficient refinement, yet to be computationally "affordable". This was achieved by testing various meshes, convergence criteria and comparing displacements. The mesh is refined at the location of applied load and also support (for the beam and truncated beam models) to capture properly the load transfer mechanism and also possible cracking at these locations.

All analyses were performed with the Merlin finite element code (**merlin**) using the Secant Newton algorithm and setting the maximum number of iterations to 300. Convergence criterion for both energy (ratio of the absolute values of the external work done by the applied incremental loads and the residual loads for the current increment) and displacements (ratio of the Euclidean norms of the iterative displacement correction and incremental displacement vectors) was set to 0.01. Though far from ideal, these analyses were compared with others having a tighter convergence criteria and though oscillatory behaviors in the post-shear failure, i.e., post-peak, were observed, they were kept in the interest of computability. A rotating crack model was used.

Four workstations are used to perform the analyses (Intel(R) Xenon(R) 3.6 GHz, RAM 8.00 GB). Each simulation lead a computational cost between 6 and 60 hours. Higher computational time is a results of unfavorable combinations of the random variables.

MERLIN AAR Problems
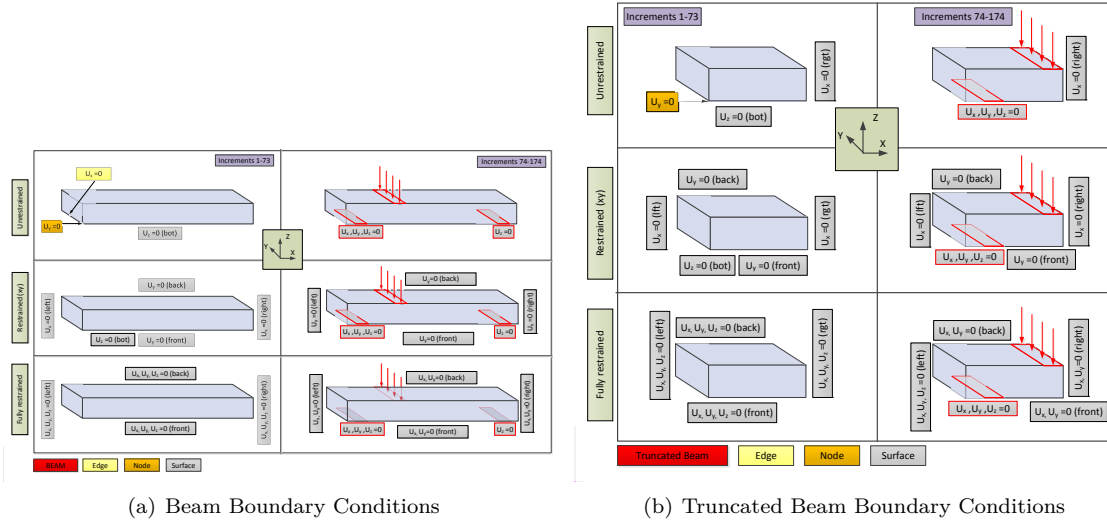
(a) Beam Boundary Conditions

(b) Truncated Beam Boundary Conditions
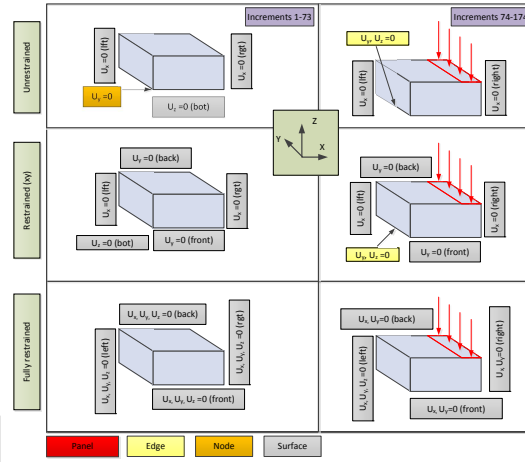
(c) Panel Boundary Conditions

Figure 13.5: Boundary Conditions

In all ASR simulation followed by a shear test (ASR+Shear), ASR was applied through the first 73 increments), while the incremental shear was applied starting from increment 74 through 174. At the end of the ASR expansion, visualization of results was made to assess that full expansion was reached.

Finally, it should be noted that a good indicator for discarding diverging results is the out-of-plane displacements. It was arbitrarily assumed that out-of-plane displacement exceeding 5 mm implied automatic discard of the corresponding simulation.

13.2.5   Variables

Two set of meshes are generated:

ASR + Shear cases for which seven variables were included in the study, See 13.4. Thus, for each of the three geometries a total of $(3 \times 2 \times 3 \times 3 \times 2 \times 2)$ 216 meshes were generated, i.e., 648 total.

Reference cases with no ASR modeling. For each of the three geometries a total of $(3 \times 3 \times 2 \times 3)$ 54

MERLIN AAR Problems

Spec.	BC	Bottom			Front			Back			left			Right		
		x	y	z	x	y	z	x	y	z	x	y	z	x	y	z
AAR Expansion (incr. 1-73)																
B	U	-	-	•	-	-	-	-	-	-	-	1	-	-	-	-
	R	-	-	•	-	•	-	-	•	-	•	-	-	•	-	-
	FR	-	-	-	•	•	•	•	•	•	•	•	•	•	•	•
TB	U	-	-	•	-	-	-	-	-	-	-	2	-	•	-	-
	R	-	-	•	-	•	-	-	•	-	•	-	-	•	-	-
	FR	-	-	-	•	•	•	•	•	•	•	•	•	•	•	•
P	U	-	-	•	-	-	-	-	-	-	•	3	-	•	-	-
	R	-	-	•	-	•	-	-	•	-	•	-	-	•	-	-
	FR	-	-	-	•	•	•	•	•	•	•	•	•	•	•	•
Shear Load (incr. 74-174)																
B	U		4		-	-	-	-	-	-	-	-	-	-	-	-
	R		4		-	•	-	-	•	•	-	-	•	-	-	-
	FR		4		•	•	-	•	•	-	•	•	-	•	•	-
TB	U		5		-	-	-	-	-	-	-	-	-	•	-	-
	R		5		-	•	-	-	•	-	•	-	-	•	-	-
	FR		5		•	•	-	•	•	-	•	•	•	•	•	-
P	U	-	-	-	-	-	-	-	-	-	•	6	•	-	-	-
	R	-	-	-	-	•	-	-	•	-	•	6	-	•	-	-
	FR	-	-	-	•	•	-	•	•	-	•	•	•	•	•	-

1:xxx;2:xxx; 3:xx;

4:xxx 5:xxx; 6:xx

Table 13.1: Boundary Conditions for AAR Expansion

Table 13.2: Models dimensions (in)

Model	Sub-model	a_1	a_2	a_3	a_4	a_5	d	L_{tot}	w	t
B	B2	8	4	51.5	4	111	23	190.5	48	24
	B4	8	4	111.5	4	231	47	370.5	96	48
TB	TB2	8	4	51.5	4	-	23	67.5	48	24
	TB4	8	4	111.5	4	-	47	127.5	96	48
P	P2	-	-	-	4	-	23	57.5	48	24
	P4	-	-	-	4	-	47	117.5	96	48

meshes were generated (or 162 total).

13.3 Material Properties

The constant material properties for the concrete nonlinear model described previously in (Saouma and Perotti, 2006), are given in Table 11.1. These values were adopted as representative of an ordinary structural concrete with a compressive strength of 4,500 psi (31 MPa). This value corresponds to a standard design requirement for structural concrete in NPP in the 70s and 80s, although higher values could have been obtained in practice (Granger, 1995). 12.2 provides the characteristics of the ASR model. The maximum ASR-expansion, in unrestrained conditions, is taken equal to 0.1%, 0.2% and 0.3% to increase the severity of the induced damage before applying the shear loading. The residual elastic modulus and tensile strength resulting form ASR degradation are assumed to be either 70% or 90%. The mechanical constitutive model for the reinforcing steel bars is assumed elasto-plastic. The corresponding properties are given in 12.3. Three

MERLIN AAR Problems

(a) 24" deep

(b) 48" deep

(c) Unrestrained AAR

(d) Unrestrained Shear

(e) Restrained AAR

(f) Restrained Shear

(g) Fully Restrained AAR

(h) Fully Restrained Shear
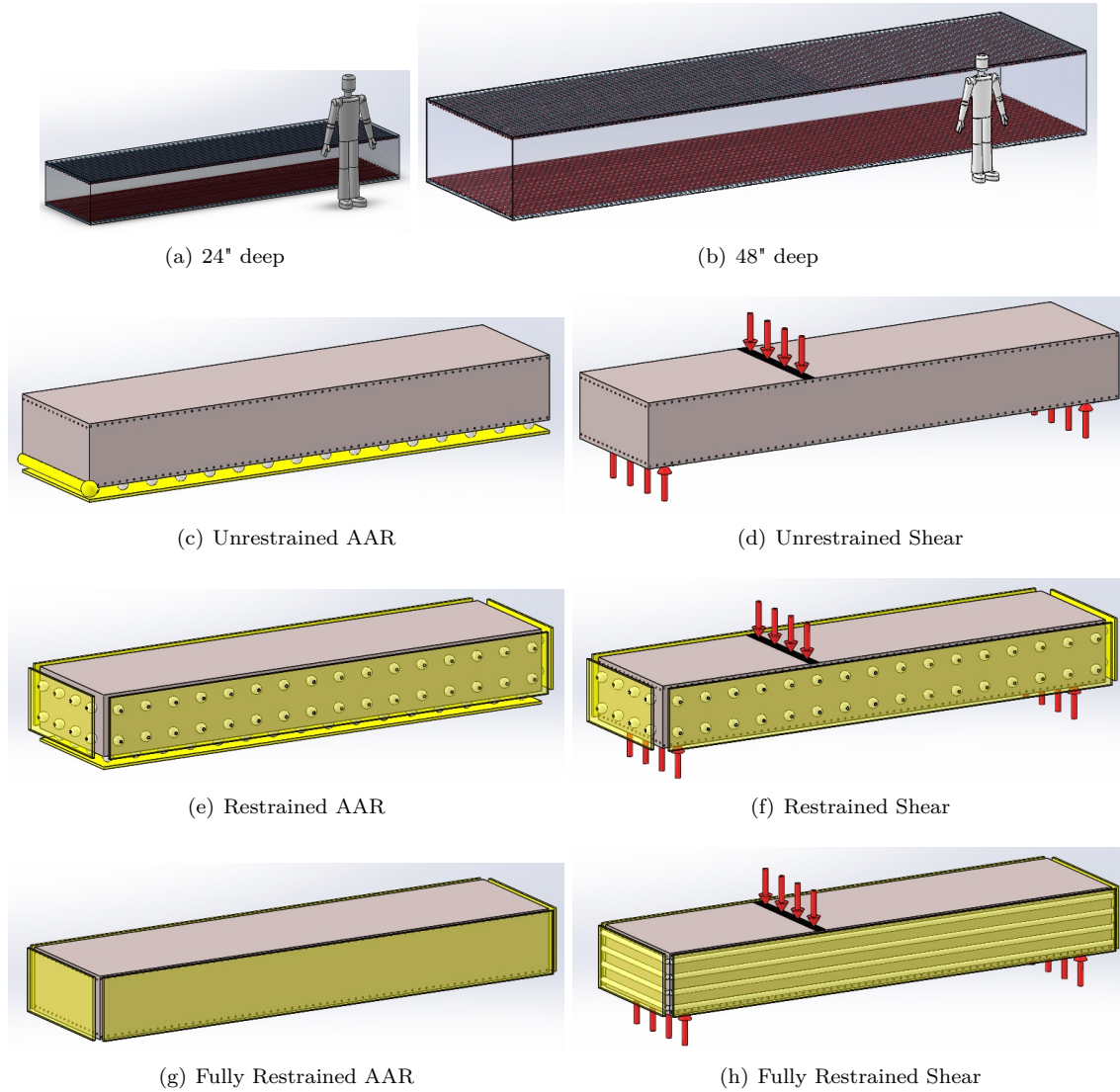
Figure 13.6: Boundary Conditions for the Beam

reinforcement ratios are considered: 0.2% 0.5% and 1%.

13.4   Deterministic simulation

A set of 648 cases were simulated corresponding to different geometries, condition or material properties:

   A Geometry (B|TB|P): for beam, truncated beam or panel;
   B Depth (2|4): for 24" (61 cm) and 48" (1.22 m);
   C Boundary Conditions (U|R|FR): for unrestrained, restrained, and fully restrained;
   D Final ASR expansion, ε^∞, (1|2|3): for 0.1%, 0.2% 0.3%;
   E Reinforcement ratio, ρ, (2|5|10): for 0.2% 0.5% and 1%;
   F Residual Young modulus relative coefficient, β_E, (7|9): for 70% and 90%;
   G Residual tensile strength relative coefficient, β_{ft}, (7|9): for 70% and 90%.

MERLIN AAR Problems

(a) 24" deep

(b) 48" deep

(c) Unrestrained AAR

(d) Unrestrained Shear

(e) Restrained AAR

(f) Restrained Shear

(g) Fully Restrained AAR

(h) Fully Restrained Shear
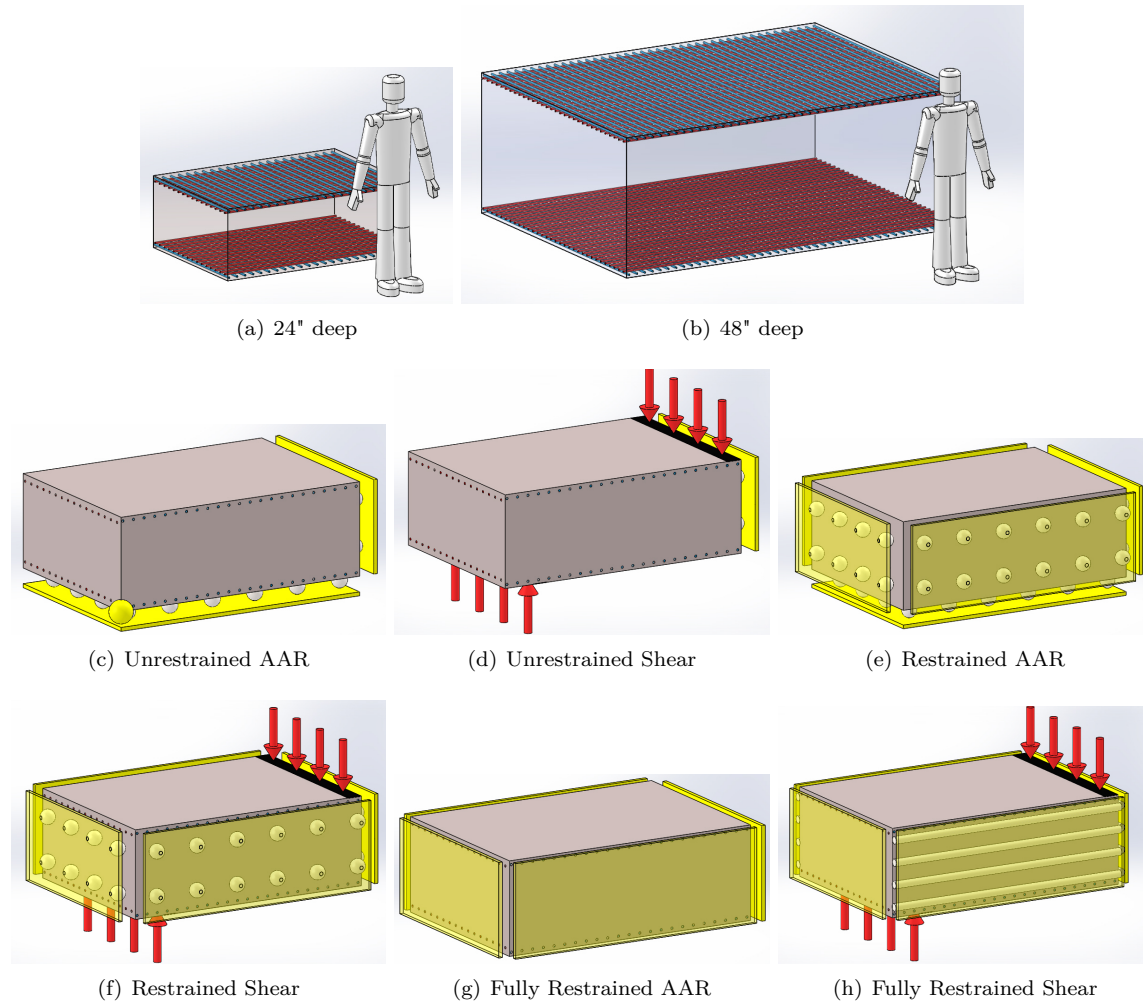
Figure 13.7: Boundary Conditions for the Truncated Beam

Each simulation corresponds to the successive modeling of:

1. the ASR development and induced damage (pre-shear-testing), and,

2. the residual shear test.

The results of the residual shear test are compared with the reference shear test obtained on the corresponding pristine structural element. For each simulation, a set of scalar outputs are calculated: variation of the shear capacity, variation of stiffness, ASR dimensional change in the unreinforced direction of the structural element, and, median and maximum stresses in the reinforcement bars in both directions. To rare exceptions, the general shear force-displacement curve exhibits a shear capacity peak followed by a sudden drop. Increasing post-peak displacements lead to varied behaviors including hardening or softening.

Note that the ultimate shear capacity is the absolute peak of the curve, whereas the yield value is defined as the shear deviating by 15% from the elastic stiffness Fig. 13.11). Whereas this definition of the yield shear may appear to be arbitrary, it was the most adequate convention for processing automatically the hundreds of simulation results.

648 2D-plots, similar to those presented in 13.12, are generated for each individual analysis. In the 2D-plots, the top-left portion shows the shear behavior in term of shear force vs. the shear displacement

MERLIN AAR Problems

(a) 24" deep   (b) 48" deep

(c) Unrestrained AAR   (d) Unrestrained Shear   (e) Restrained AAR

(f) Restrained Shear   (g) Fully Restrained AAR   (h) Fully Restrained Shear
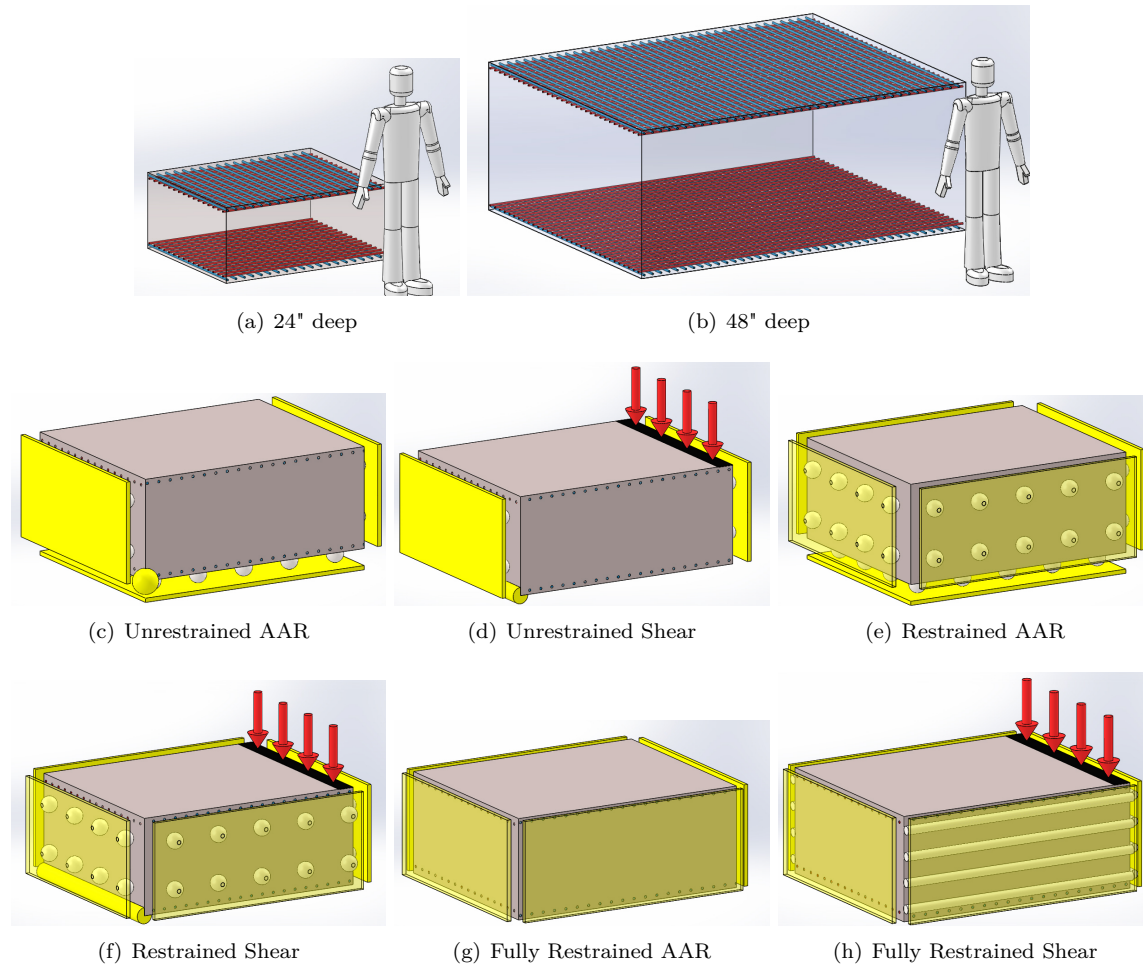
Figure 13.8: Boundary Conditions for the Panel

before ("only shear", solid red line) and after ASR ("ASR+shear". solid blue line). The variation of shear strength and stiffness are also provided in legend. The top-right portion shows the progression of the ASR out-of-plane expansion as a function of the computation increments.

Full expansion at the end of the 73rd is expected. The lower plots correspond to the representation of the stress distribution in the longitudinal and transverse reinforcing bar using *box-and-whisker* diagrams, also known as *boxplots*: the median value is represented by the red line; the 50% confidence interval by the solid blue box; The upper adjacent value (right bar) is the value of the largest stress that is less than or equal to the upper quartile plus 1.5 the length of the interquartile range. Analogously the lower adjacent value (left mark) is the value of the smallest observation that is greater than or equal to the lower quartile less 1.5 times the length of interquartile range. Outliers (red crosses) are stresses outside lower-upper mark range.

13.5   Probabilistic analysis

Though we started by looking at individual results, it quickly became clear that such an effort was not only monumental but could easily lead to erroneous interpretation.

As such, it was rapidly concluded that a thorough statistical analysis of results was the only practical

MERLIN AAR Problems

(a) Truncated Beam

(b) Panel

(c) Beam

(d) Physical Dimensions (inches)
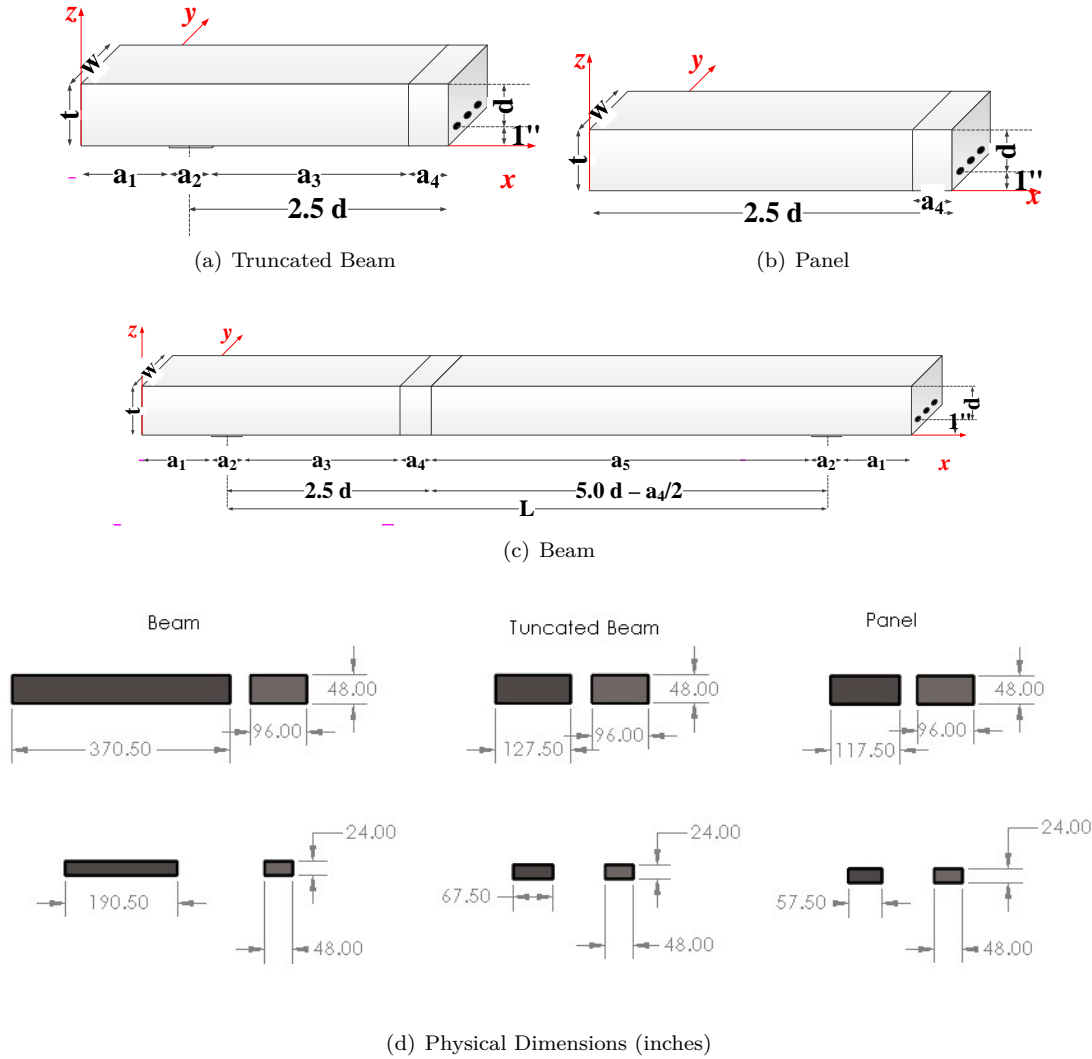
Figure 13.9: Dimensions

approach. A statistical analysis was performed using the R package (**R**). The results of the analysis is reported in the next sections.

13.5.1 ASR Effects on Material and Structures

The interaction of ASR with concrete shear strength is of primary interest. At the material level, the concrete degrades and undoubtedly its shear resistance decreased. On the other hand, at the structural level, ASR induces additional compressive stresses, similar to a prestressing effect, which increase the shear resistance of the structural component. An illustration of this effect is given by the analysis of the simple Mohr-Coulomb equation: $\tau = c + \sigma \tan \phi$. For a cohesion of $c = 3$ MPa and an internal friction angle of $\phi = 40^o$, then for a compressive stress σ of 0, 3 and 5 MPa, the resulting shear strength would be 3.0, 5.5 and 7.2 MPa respectively. Furthermore, the ASR expansion is likely to reduce the crack opening due to shear, hence additional aggregate interlock is present, (Blight and Alexander, 2008).

The nonlinear numerical model used in Merlin is a fracture-plastic based on the work (and implemented)

MERLIN AAR Problems

(a) Beam 24"   (b) Beam 48"

(c) Truncated Beam 24"   (d) Truncated Beam 48"

(e) Panel 24"   (f) Panel 48"
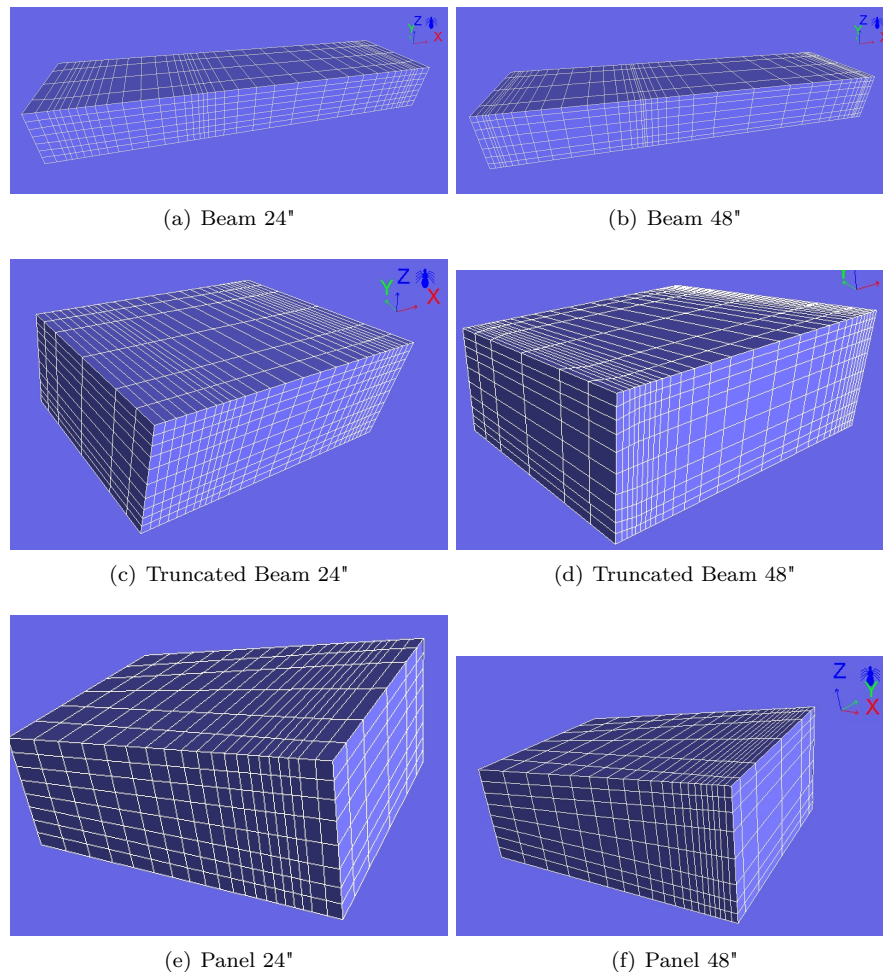
Figure 13.10: Finite Element Meshes

by Cervenka and Papanikolaou (2008). It combines constitutive models for tensile (fracturing) and compressive (plastic) behavior. The fracture model is based on the classical orthotropic smeared crack formulation and crack band model. It employs Rankine failure criterion, exponential (or user defined) softening, and it can be used as rotating or fixed-crack model. The hardening/softening plasticity model is based on Menétrey and Willam (1995) failure surface. Both models use return mapping algorithm for the integration of constitutive equations. The model can be used to simulate concrete cracking, crushing under high confinement, and crack closure due to crushing in other material directions. Dowel effects are not modeled, while interlocking effects are implicitly accounted for. Hence, the model does take into account the confining effect and will result in higher shear strength.

As such, differentiation will be made between results showing positive or negative shear strength changes. This task is simply achieved by properly filtering the R dataset in terms of the shear strength change. Amongst the full set of 648 analyses, 53% resulted in overall shear strength decrease, and 47% in increase.

MERLIN AAR Problems

Geometry	# of Nodes	# of Elements
Beam	1,520	1.036
Truncated Beam	1,323	960
Panel	2,233	1,680

Table 13.3: Finite Element Mesh Characteristics

Table 13.4: Varying Parameters

Variable	Values
Geometry	Beam (B), Truncated Beam (TB), Panel (P)
Boundary Conditions	Unrestrained, Restrained, Partially Restrained
AAR+Shear	
Thickness	2 ft, 4 ft
AAR Expansion	0.1%, 0.2%, 0.3%
Reinforcement Ratio	0.2%, 0.5%, 1%
Residual Elastic Modulus	0.7, 0.9
Residual Tensile Strength	0.7, 0.9
AAR	
Geometry	Beam (B), Truncated Beam (TB), Panel (P)
Boundary Conditions	Unrestrained, Restrained, Partially Restrained
Thickness	2 ft, 4 ft
Reinforcement Ratio	0.2%, 0.5%, 1%
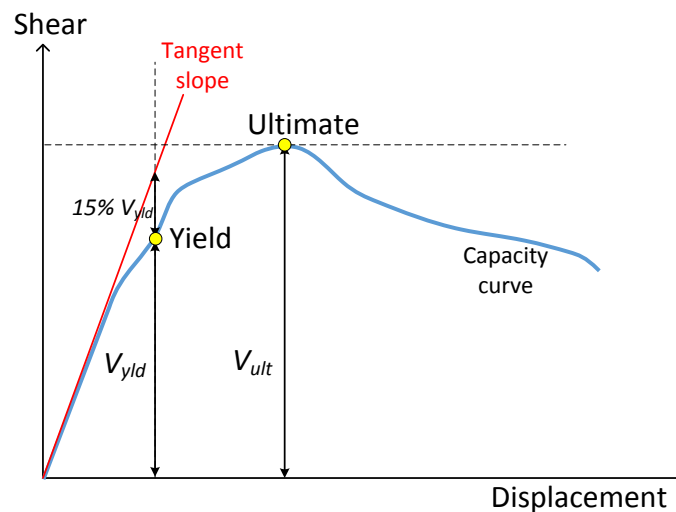
Figure 13.11: Definition of yield and ultimate points on the capacity curve

13.5.2   Statistical Analysis

In this second part of statistical based data interpretation, we seek to develop a model for the shear strength change not to gain a mathematical model, *per se*, that could be plotted (use of unordered categorical variables), but rather to identify the most relevant parameters amongst those used. In this exercise, each of the 18 sub-variables in Table 13.5 will be separately considered. The employed Multiple Linear Regression analysis is described in some details in A.1.

MERLIN AAR Problems
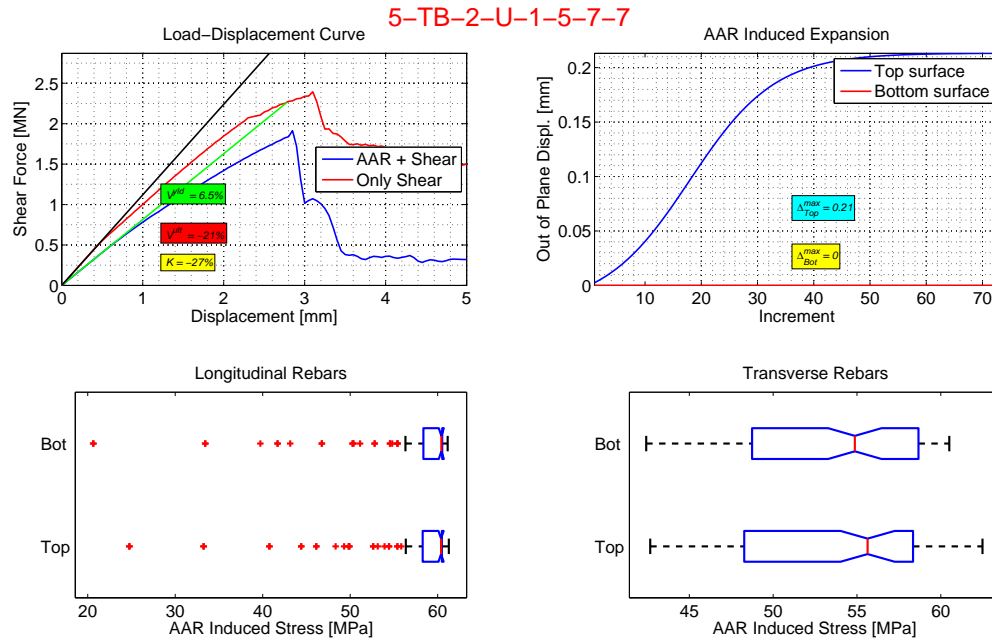
(a) Sample of shear strength reduction
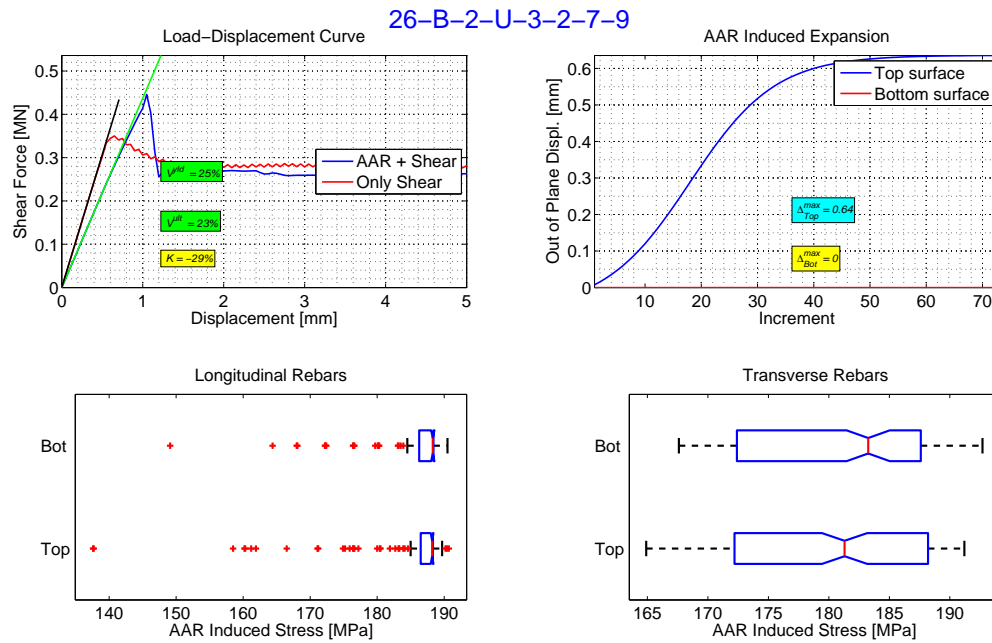
(b) Sample of shear strength gain

Figure 13.12: Examples of all individual 2D plots

Three fitting models are considered:

1. Full data set:
   - General model: considering all variables;
   - Best model based on Akaike Information Criterion (AIC): Filters the final sub-variables based on AIC;

MERLIN AAR Problems

Table 13.5: Main classes of variables and R Sub-variables

	Main Variables	Analyses	Normalized R	R Sub-variables
		B	1	1
1	Type	TB	2	2
		P	3	3
2	Depth	24"	2	4
		48"	4	5
		U	1	6
3	B.C.	R	2	7
		FR	3	8
		0.001	1	9
4	ε	0.002	2	10
		0.003	3	11
		0.002	1	12
5	ρ	0.005	2	13
		0.01	3	14
6	β_E	0.7	1	15
		0.9	2	16
7	β_{ft}	0.7	1	17
		0.9	2	18

- Best model based on Bayesian Information Criterion (BIC): Filters the final sub-variables based on BIC.

2. Increased Shear Strength Change Data Set:
   - General model;
   - Best model based on AIC;
   - Best model based on BIC.

3. Decreased Shear Strength Change Data Set:
   - General model;
   - Best model based on AIC;
   - Best model based on BIC.

13.6   Joint Statistical Analysis of The Full Dataset

13.6.1   Boxplots and Histograms

Before any statistical model is developed aiming at assessing the influence of the studied parameters, all results are presented as boxplots and histograms. However, rather than dealing with the 7 classes of main variables, it was deemed necessary to express the model in terms of each one of their possible values, see Table 13.5. It should be noted that the R code internally uses normalized/integer values for each of the 18 subvariables. Boxplots for each of the 18 sub-variables will be presented in the next section. For each specific case, it will be assumed to be a function of that specific sub-variable and the coupled effect of all 17 others.

The analysis separates the simulations for which the shear strength increases from those showing a decrease of the shear strength.

MERLIN AAR Problems

13.6.1.1   Shear Strength Increase

Fig. 13.13 presents the boxplots relative to increasing shear strength. The following observations can be made (trends corresponding to average values primarily):

(a) Type: B, TB, P   (b) Depth: 24", 48"   (c) BC: U, R, FR   (d) ε^{ASR}

(e) ρ (f) β_E (g) β_{ft}
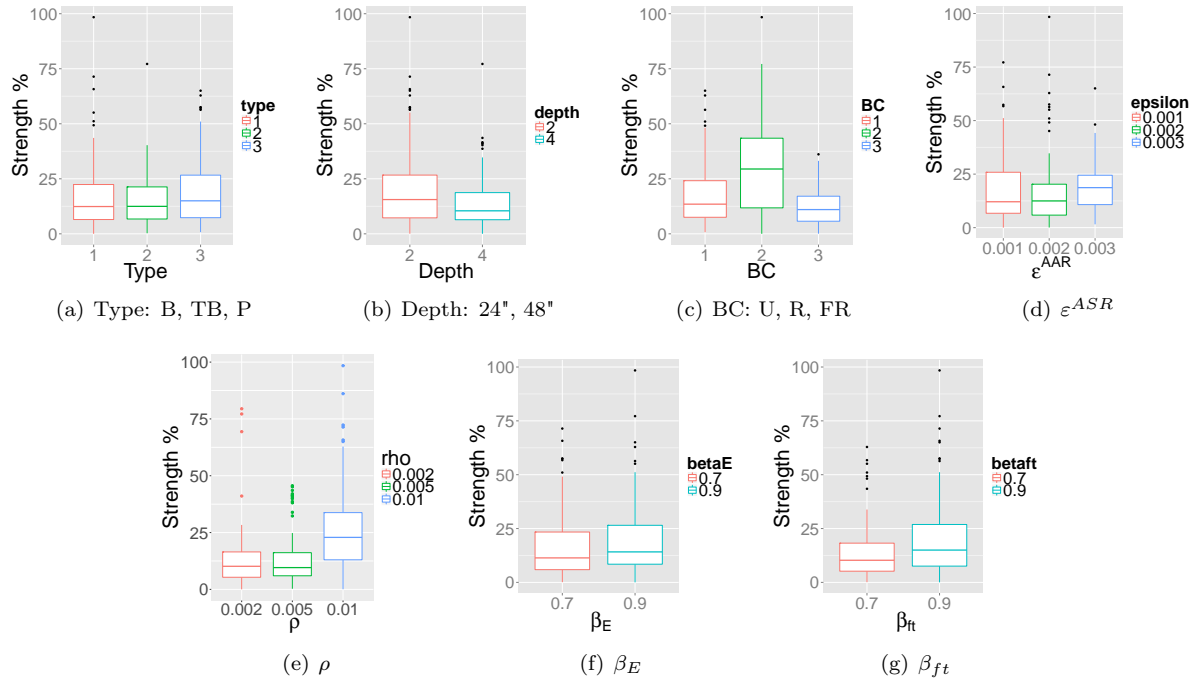
Figure 13.13: Boxplots for Shear Strength Increase in terms of each of the seven variables

- The impact of nature of the structural elements, (B) and (TB) geometries, on the shear strength increase is nearly identical; however, P geometry leads to increased variability, Fig. 13.13(a).
- 24"-thick specimens (smaller dimensions) have a slightly larger shear strength increase, possibly attributed to a size effect, than the larger specimens, Fig. 13.13(b).
- Restrained boundary conditions (R) appear to significantly increase the shear strength although important scatter is found, Fig. 13.13(c).
- Larger reinforcement (higher ρ) leads to larger shear strength increase, Fig. 13.13(e).
- Higher reduction in β_E results in higher reduction in stiffness, Fig. 13.13(f).
- Similarly, a larger decrease in β_{ft} results in smaller increase in strength, Fig. 13.13(g).

It should be noted that in all the above, factors of influence are what one may anticipate, although their quantitative impact may be judged quite limited.

13.6.1.2   Shear Strength Decrease (Negative Set)

Following a similar approach, this subsection seeks to understand the underlying reasons for shear strength decrease at the structural level due to each of the 18 sub-variables. Again, each boxplot is an indicator of the impact of a given subvariable in terms of all 17 others and its impact on shear strength decrease.

Fig. 13.14 shows the boxplots for the shear strength decrease and the following observations can be made:

- (P) geometry results in higher decreases than (B) or (TB) geometries Fig. 13.14(a).
- Greater depth (48") results in higher shear strength reduction than 24" components, Fig. Fig. 13.14(b).

MERLIN AAR Problems

(a) Type: B, TB, P   (b) Depth: 24", 48"   (c) BC: U, R, FR   (d) ε^{ASR}

(e) ρ (f) β_E (g) β_{ft}
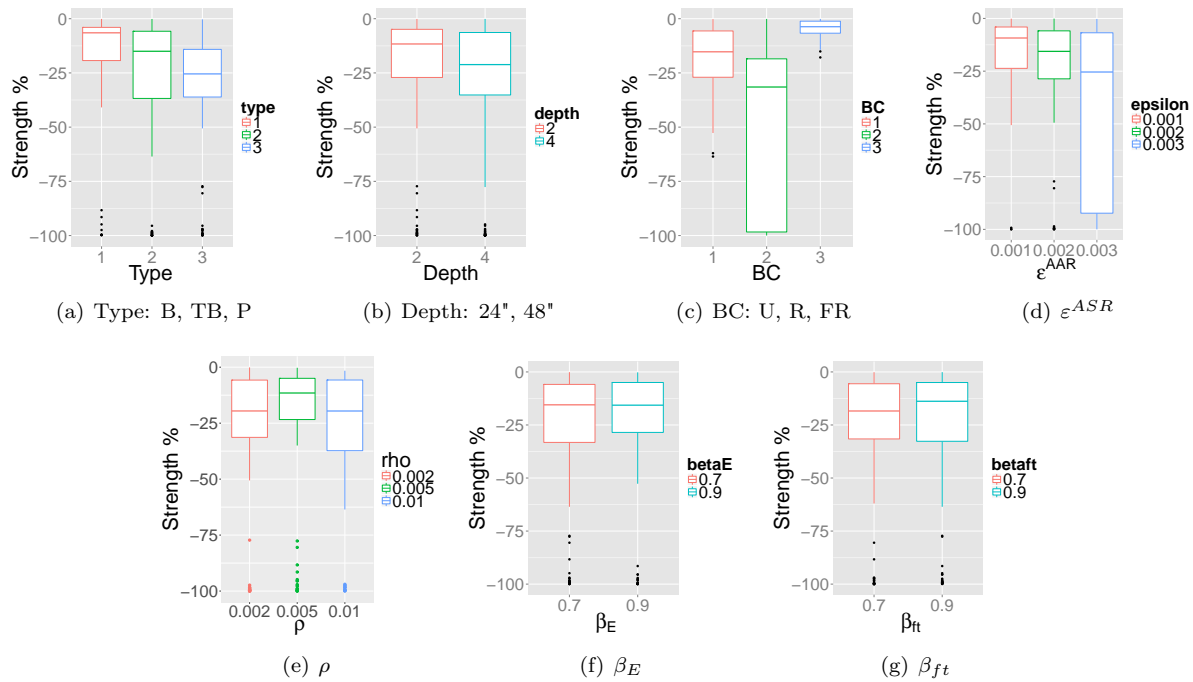
Figure 13.14: Boxplots for Shear Strength Decrease in terms of each of the seven variables

Also, the variation of the response for the larger structural members is smaller.

- The largest shear strength decrease occurs for the restrained (R) situation for which the out-of-plane expansion is uniform in the vertical direction and constrained in the lateral hoop direction only. It is noteworthy that this configuration is quite representative of large structural walls, Fig. 13.14(c). Furthermore, the variations corresponding to the (R) boundary conditions are much higher than when associated with the (U) and (FR) BCs. 50% of the strength reduction cases associated with the (R) BCs fall in the range of [20%; 95%] (higher reduction). Corresponding ranges for (U) and (FR) BCs are [7%; 27%] and [2%; 7%], respectively.

- Increasing ASR expansion, ϵ^{ASR}, increases the mean value of the strength reduction in the models. This is consistent with what the intuition would expect, Fig. 13.14(d). In addition, for the case with $\epsilon^{ASR} = 0.3\%$ (the largest expansion considered in this study) the structural responses are much scattered than for lower expansions. In particular, the number of cases with strength reduction of nearly 100% is significantly higher.

- The effect of reinforcement ratio is rather puzzling: strength reductions are close independently of the value of the reinforcement ratio, i.e., ρ may not have a determining effect in these analyses since steel may not have yielded, Fig. 13.14(e).

- β_E and β_{ft} do not seem to have important impact on the results. This is understandable as the zone in shear is largely dominated by compression. Their impact would be greater in assessing the out-of-plane displacements, Fig. 13.14(f) and Fig. 13.14(g).

13.6.1.3 Model Fitting and Preliminary Conclusions

As earlier mentioned, the effect of ASR on the shear strength of concrete structural components is a complex interplay between two effects:

MERLIN AAR Problems

Material degradation, where undoubtedly ASR reduces the tensile strength of the concrete and is very likely to affect the shear strength of concrete.

(2) Structural effect, where steel constrains the concrete expansion, thus putting the later in compression which will, *de facto*, increase its shear resistance.

Those effects coalesce in the 648 analyses performed, and which interpretation was provided through the statistical approach previously presented. 13.6 summarizes the three sets of results in terms of relevance of the 18 studied sub-variables. For each dataset and statistical method, the top 7 most relevant sub-variables are ranked (1 being the most prominent variable). The most important preliminary conclusions are:

1. The boundary conditions (R), i.e., "restrained", are the primary cause of shear strength increase or decrease. Note that this effect is masked when the whole results dataset is considered, i.e., when increasing and decreasing shear strengths are combined in the analysis.

2. For shear strength increase the second most important parameter is $\rho = 1\%$, i.e., the highest reinforcement ratio considered.

3. For shear strength decrease, the second most important parameter is the maximum ASR expansion $\varepsilon = 0.3\%$.

Table 13.6: Summary of linear model fitting

		Full Set			Positive Set			Negative Set		
		General	AIC	BIC	General	AIC	BIC	General	AIC	BIC
1	Type B									
2	Type TB	4	4					5	5	5
3	Type P	6	6					4	4	3
4	Depth 2									
5	Depth 4				6	7	7			
6	B.C. U									
7	B.C. R	7	7	5	1	1	1	1	1	1
8	B.C. FR	2	2	2	4	4	4	6	6	6
9	ϵ 0.001									
10	ϵ 0.002			7	7	6	6			7
11	ϵ 0.003	3	3	3	5	5	5	2	2	2
12	ρ 0.002									
13	ρ 0.005			6						
14	ρ 0.010	1	1	1	2	2	2	3	3	4
15	β_E 0.7									
16	β_E 0.9							7	7	
17	β_{ft} 0.7									
18	β_{ft} 0.9	5	5	4	3	3	3			

13.7 Statistical Analysis of Restrained Boundary (R) Conditions Scenario

The preponderant role played by the (R) boundary condition was just demonstrated. To better focus on that scenario, a more refined investigation of this specific case, and its 216 analyses is performed by filtering out the (FR) and (U) BCs cases.

MERLIN AAR Problems

13.7.1 BoxPlots

13.7.1.1 Shear Strength Increase (Positive Set)

Fig. 13.15 shows the boxplots for the shear strength increase only for the restrained BCs (R) models. It can
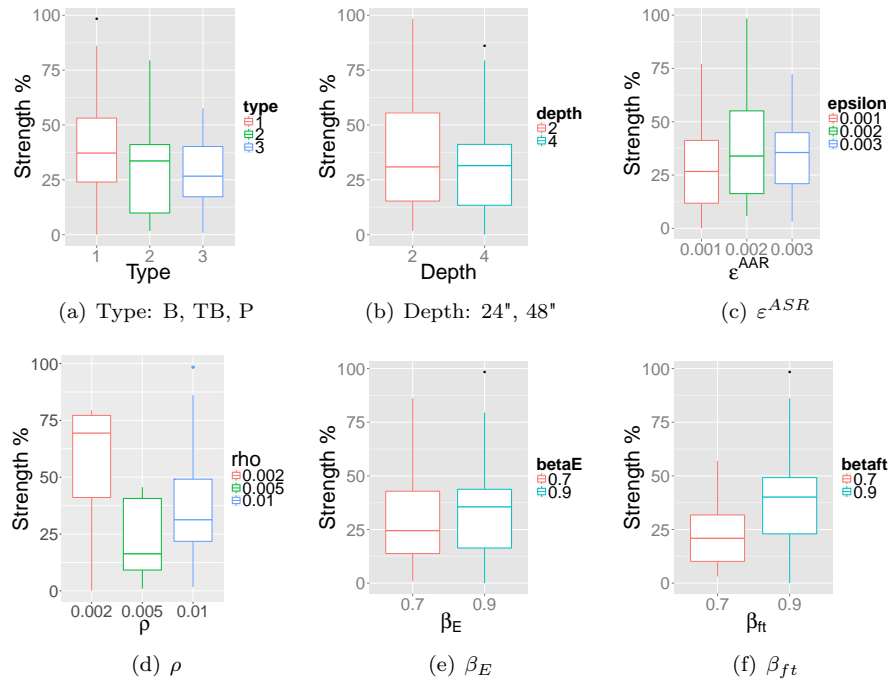
Figure 13.15: Boxplots for Shear Strength Increase in terms of each of the six variables; only restrained model

be noted that:

- The impact of (B) geometry on shear strength increase is more important than for (TB) and (P) geometries. Variability associated with the (TB) geometry is higher than for other geometries, Fig. 13.15(a).
- 24" specimens (smaller dimensions) have a slightly larger variability in shear strength increase (size effect?) than the larger specimens, Fig. 13.15(b).
- Higher reinforcement ratio leads to larger shear strength increase, Fig. 13.15(d).
- Higher ASR-induced reduction of the Young modulus (β_E) results in smaller shear strength increase, Fig. 13.15(e).
- Similarly, a larger decrease in of the ASR-induced loss of strength (β_{ft}) results in smaller increase in shear strength, Fig. 13.15(f).

Fig. 13.16(a) shows the histogram of the reduced dataset relative to shear strength increase (due to ASR). Fig. 13.16(b) shows the probability distribution function (PDF) of this data set. The dataset does not appear to follow a specific standard distribution. About 80% of the data falls in the range [0; 50%] of loss of strength.

MERLIN AAR Problems

(a) Histogram   (b) Probability Distribution Function
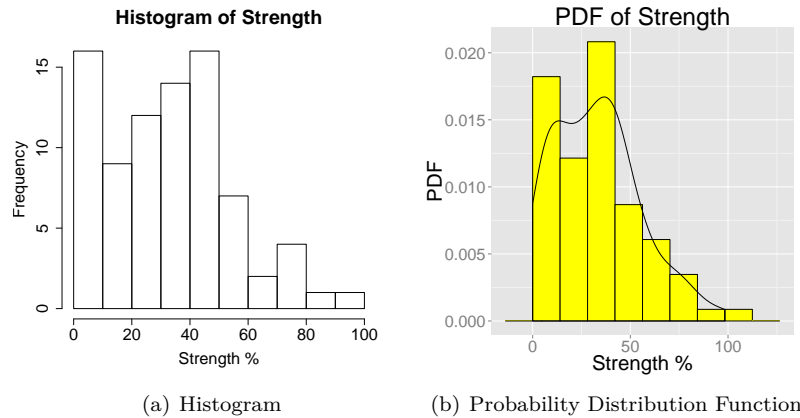
Figure 13.16: Histograms for Shear Strength Increase; only restrained model

13.7.1.2 Shear Strength Decrease (Negative Set)

As previously, this subsection seeks to understand the underlying reasons for shear strength decrease at the structural level due to each of the 15 sub-variables. Again, each boxplot is an indicator of the impact of a given sub-variable in terms of all 14 others and its impact on shear strength decrease.

Fig. 13.17 shows the boxplots for the shear strength decrease and only the restrained model. The

(a) Type: B, TB, P   (b) Depth: 24", 48"   (c) ε^{ASR}

(d) ρ (e) β_E (f) β_{ft}
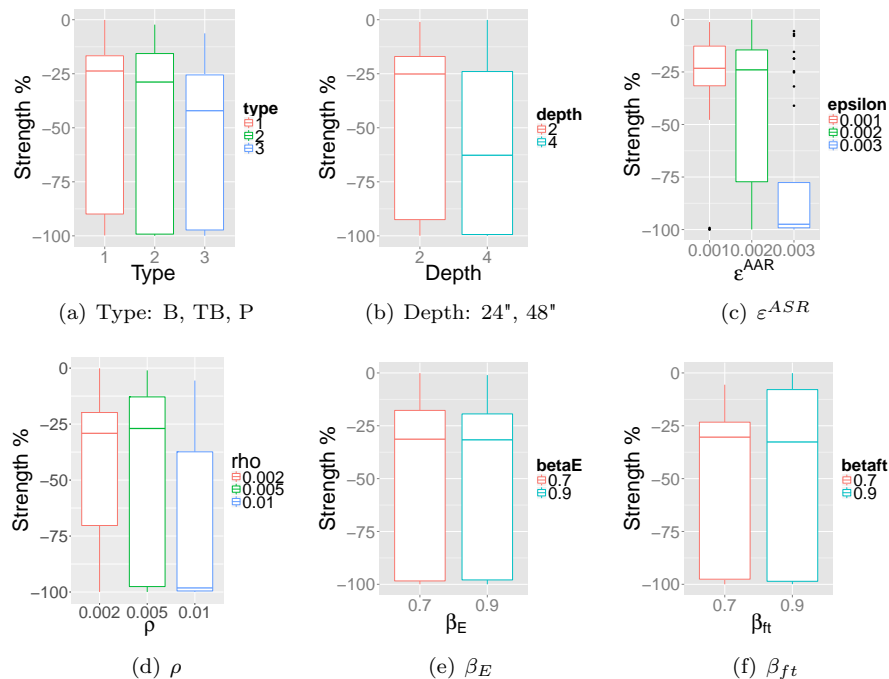
Figure 13.17: Boxplots for Shear Strength Decrease in terms of each of the six variables; only restrained model

following observations can be made:

- (P) geometry results in higher decreases than (B) and (TB) geometries, Fig. 13.17(a). However, the variability of the data are nearly identical.

MERLIN AAR Problems

- Greater depth (48") result in higher shear strength reduction than 24" members, Fig. 13.17(b). The variation of the output strength is nearly identical in both cases.
- Increasing the ASR expansion, ϵ^{ASR}, increases the mean value of the strength reduction in the models, as the intuition would suggests, Fig. 13.17(c). Considerable higher variation is observed for the 0.2% expansion-case.
- The values of β_E and β_{ft} do not seem to have a significant impact on the loss-of-strength distribution. Their impact would be greater while assessing the out-of-plane displacements, Fig. 13.17(e) and Fig. 13.17(f).

Fig. 13.18(a) shows the histogram of the data set for shear strength decrease. Fig. 13.18(b) displays the probability distribution function (PDF) of this data set. About 20% of the data falls in the range of [-100%; -90%], i.e., corresponding to very limited, if any, residual shear capacity.

(a) Histogram

(b) Probability Distribution Function
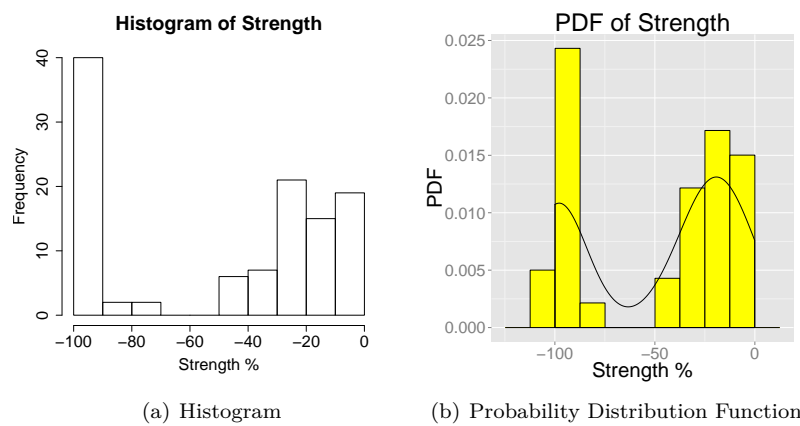
Figure 13.18: Histograms for Shear Strength Decrease; only restrained model

13.7.2 Model Fitting: Increased Shear Strength

This sub-subsection, repeats the statistical analysis previously presented, but is limited to positive shear strength change data points (i.e. strength increase) and is limited to the restrained model. First the general model is fitted, followed by the AIC and BIC best-fit models.

13.7.2.1 General Model for Increased Shear Strength Data Set

Table 13.7 shows the results of linear model fitting based on positive shear strength change data points.

Three different techniques are used for fitting the data points, general model, AIC, and BIC. These three approaches provide nearly identical results.

The main factors influencing the gain of shear strength for a structural member exhibiting only out-of-plane expansion, labeled in this study by type-(R) boundary conditions are:

1. higher reinforcement ratios of 0.5% and 1%;
2. an ASR-induced residual the tensile strength at 90% of its initial value;
3. ASR-expansion of 0.2%; and to a lesser extent,
4. the nature of the structural member, as (P)-member appears also as a factor of importance.

The role of ASR expansion on the shear strength increase appears non monotonic: while the 0.2%-value

MERLIN AAR Problems

Table 13.7: Three Fitting Models for Positive Shear Strength Data Set; (restrained model only)

	Coefficients:	Estimate	Std. error	t value	$Pr(> |t|)$	
General	(Intercept)	48.887	11.795	4.145	9.16E-05	***
	TB	-9.443	5.384	-1.754	0.083711	
	P	-12.887	5.196	-2.48	0.01546	*
	48"	-6.444	4.804	-1.341	0.183982	
	$\varepsilon^\infty = 0.002$	7.699	4.728	1.628	0.107809	
	$\varepsilon^\infty = 0.003$	4.478	5.645	0.793	0.430251	
	$\rho = 0.005$	-28.164	9.588	-2.937	0.004442	**
	$\rho = 0.01$	-16.081	9.585	-1.678	0.097734	
	$\beta_E = 0.9$	2.996	4.287	0.699	0.486908	
	$\beta_{ft} = 0.9$	15.207	4.277	3.556	0.000671	***
AIC	(Intercept)	56.016	10.688	5.241	1.42E-06	***
	TB	-9.993	5.342	-1.871	0.065292	
	P	-13.615	5.162	-2.638	0.01014	*
	48"	-7.074	4.782	-1.479	0.143296	
	$\rho = 0.005$	-29.831	9.413	-3.169	0.002215	**
	$\rho = 0.01$	-17.79	9.376	-1.897	0.061634	
	$\beta_{ft} = 0.9$	15.598	4.267	3.655	0.000474	***
BIC	(Intercept)	41.581	9.414	4.417	3.19E-05	***
	$\rho = 0.005$	-27.611	9.53	-2.897	0.00488	**
	$\rho = 0.01$	-13.706	9.224	-1.486	0.14133	
	$\beta_{ft} = 0.9$	14.806	4.417	3.352	0.00124	**

is a significant factor of influence, lower expansion value (0.1%) does not contribute notably, and higher expansion value (0.3%) contribute more moderately. This tends to support the hypothesis of a potential ambivalent role of ASR on the structural capacity of members without shear reinforcement: ASR in-plane-restrained expansion results in a prestressing effect that enhances the shear resistance of the member, but loss of materials properties affects the shear resistance, i.e., fracture propagation, in the bulk og the structural member. Limited loss of concrete tensile strength (10%) impacts the structural shear capacity as it helps the transfer of shear force in the bulk of the member. Higher loss (30%) of the concrete tensile strength does not play a role in potential increase of the structural shear capacity, suggesting that a significant portion of the shear capacity is related to shear stress in concrete that could rapidly vanish with even limited material strength loss. That the (P) geometry appear a factor, albeit low, of influence could be related to the failure mechanism for this specific geometry and loading conditions: while the (B) beam and (TC) truncated beam develop flexural behavior accompanying shear, the (P) condition develop primarily shear failure mode.

13.7.3 Model Fitting: Negative Shear Strength Change Data Set

The analysis presented here is limited to the simulation outputs exhibiting decreased shear strengths. Table 13.8 shows the results of linear model fitting. First, the general model is fitted, followed by the AIC and BIC best-fit models. The important parameters are:

- General model: $\epsilon^{ASR} = 0.3\%$, $\rho = 1\%$, and member height, 48" are the most significant sub-variables.
- AIC: The number of contributing sub-variables reduces to 5 (compared to the original 9 sub-variables). Still $\epsilon^{ASR} = 0.3\%$, $\rho = 1\%$, and the member height of, 48" are the most significant sub-variables.
- BIC: The number of contributing sub-variables reduces to 2. $\epsilon^{ASR} = 0.3\%$, and $\epsilon^{ASR} = 0.2\%$ are the most significant sub-variables.

MERLIN AAR Problems

Table 13.8: Three Fitting Models for Negative Shear Strength Data Set; (restrained model only)

	Coefficients:	Estimate	Std. error	t value	$\Pr(> |t|)$	
General	(Intercept)	-15.6835	8.7845	-1.785	0.0772	
	TB	-12.1158	8.0128	-1.512	0.1336	
	P	-10.0268	7.6347	-1.313	0.192	
	48"	-13.6526	6.4079	-2.131	0.0355	*
	$\varepsilon^\infty = 0.002$	-9.0327	7.612	-1.187	0.2381	
	$\varepsilon^\infty = 0.003$	-45.1145	7.5992	-5.937	4.04E-08	***
	$\rho = 0.005$	-4.61	6.6249	-0.696	0.4881	
	$\rho = 0.01$	-20.2409	10.1427	-1.996	0.0486	*
	$\beta_E = 0.9$	5.7823	6.0569	0.955	0.342	
	$\beta_{ft} = 0.9$	-0.3567	6.0729	-0.059	0.9533	
AIC	(Intercept)	-20.639	6.384	-3.233	0.00163	**
	48"	-13.423	6.139	-2.186	0.03098	*
	$\varepsilon^\infty = 0.002$	-9.436	7.569	-1.247	0.21527	
	$\varepsilon^\infty = 0.003$	-45.082	7.557	-5.965	3.27E-08	***
	$\rho = 0.005$	-4.462	6.586	-0.677	0.49956	
	$\rho = 0.01$	-22.453	9.607	-2.337	0.02131	*
BIC	(Intercept)	-28.141	5.588	-5.036	1.90E-06	***
	$\varepsilon^\infty = 0.002$	-11.857	7.741	-1.532	0.128	
	$\varepsilon^\infty = 0.003$	-50.139	7.558	-6.634	1.31E-09	***

That higher expansions lead to loss of shear strength is somewhat in agreement with the intuition, as more damage develop in the bulk of concrete. More surprising is the importance of the reinforcement ratio. Higher reinforcement ratio is susceptible to increase the ASR-induced prestressing of the structural member. Conversely, lower reinforcement ratios reduce the benefit of ASR-induced pre-stressing on the structural shear capacity. That the highest value of reinforcement ratio chosen for this particular study is identified by the general and the AIC model as high significance for the reduction of structural shear capacity, is an indication that other combined factors, such as the anisotropic expansion-induced damage, play a significant role regarding the susceptibility of deteriorating the members shear resistance.

13.7.4 Partial Conclusions on the Model Fitting (Level 2)

The model fitting analysis limited the structural members subjected to (R) restrained boundary condition provides indication that the impactful variables, i.e., ASR-induced expansion and loss of mechanical properties, reinforcement ratio, and structural member geometry, in terms of structural shear capacity reduction or gain, are not intuitive. The convergent results obtained by the general model, AIC and BIC analysis, suggest that "competitive" mechanisms drive the structural response against shear loading; ASR-induced prestressing against materials properties degradation, in particular.

13.8 Conclusion

A parametric numerical study of the residual structural shear capacity of structural members without shear reinforcement and subject to ASR was conducted using finite element analysis. Different sets of parameters were investigated: geometry of the structural members, boundary conditions, ASR-induced loss of materials properties, ASR expansion and reinforcement ratio. Amongst the full set of 648 analyses, 53% resulted in overall post-ASR shear strength decrease, and 47% in an increase. The range of variation in post-ASR shear

strength is particularly large.

Statistically speaking (mean and deviation), highest gains of structural shear strength are achieved for greater reinforcement ratio and restrained boundary conditions, while highest loss are observed for the same boundary conditions and higher ASR expansions.

Because the restrained boundary (R) configuration, i.e., causing out-of-plane expansion only, produces large variations of shear resistance and is representative of nuclear Class-I large 'wall', a subsequent analysis, focusing on that particular case, was performed.

In terms of variation (mean values), it was found that:

1. highest gains of shear resistance are obtained with the lowest reinforcement ratio;

2. multilinear regression and parameter selections analysis show that minimal loss of concrete tensile strength has a significant impact on potential gain in structural resistance;

3. the loss shear capacity amplitude is extremely scattered; and,

4. the greater losses appear to result from large ASR expansions and, unintuitively, high reinforcement ratios.

However, these general trends cannot be generalized to any specific set of configuration as complex interactions appear to occur. In particular, the role of the structural constraint during the development of ASR appears critical to the out-of plane shear resistance of the structures, which results from the competition between the ASR-induced prestressing of reinforced concrete and the degradation of the materials properties. These results indicate that each structural configuration needs to be studied specifically. This implies, in particular, that large-scale laboratory test results may not be directly applicable to other in-situ structural configuration. However, these tests provide valuable data for the validation of structural models that can be applied subsequently to analyze the resilience of Class I-safety nuclear concrete structures under accidental scenarios. It is recommended that a full three-dimensional analysis of such structures be undertaken to further confirm this finding.

MERLIN AAR Problems

Chapter 14

P13: Massive Reinforced Concrete Structure

Analysis performed by Y. Yagome, H. Noguchi (Tokyo Electric Power Company) with V. Saouma; reproduced here with permission

14.1 Description

AAR makes no distinction with respect to the type of structure it will affect; its effects however are most drastic in massive (in terms of volume) concrete structures that are regularly subject to monitoring, e.g. dams. Other unmonitored structures may also be adversely affected by AAR expansion, but only the most strategically important structures receive proper attention from their owners. Such is the case for the massive reinforced concrete support of a high-voltage transmission tower with 1.5 m by 1.5 m cross-girders (13.7 m span) and 2.0 m by 2.0 m columns. The girders are heavily reinforced both longitudinally (14 H 29 and 14 H 22) and vertically (H 16 spaced at 250 mm).

An unusual crack pattern, within a localized section, was observed with AAR expansion being suspected (Fig. 14.1). This pattern was later confirmed through laboratory tests.

Figures 14.2(a) and 14.2(b) show the geometry, loading and dimensions of this massive structure. The corner transmission tower exerts both tensile and compressive loads on its supports.

Of particular concern herein is girder CD, where AAR had been observed at one end. Figure 14.3(a) illustrates the field-recorded cracks on the four faces, while Figure fig:aar-TT-9 shows the AAR strain measurements recorded using a procedure described in Section **??** (crack index). This massive structure is also heavily reinforced (Fig. 14.4).

14.2 Model

Four finite element models have been considered:

(a) Location of the zone affected by AAR

(b) Close-up

(c) Structural cracks along with FE simulation results
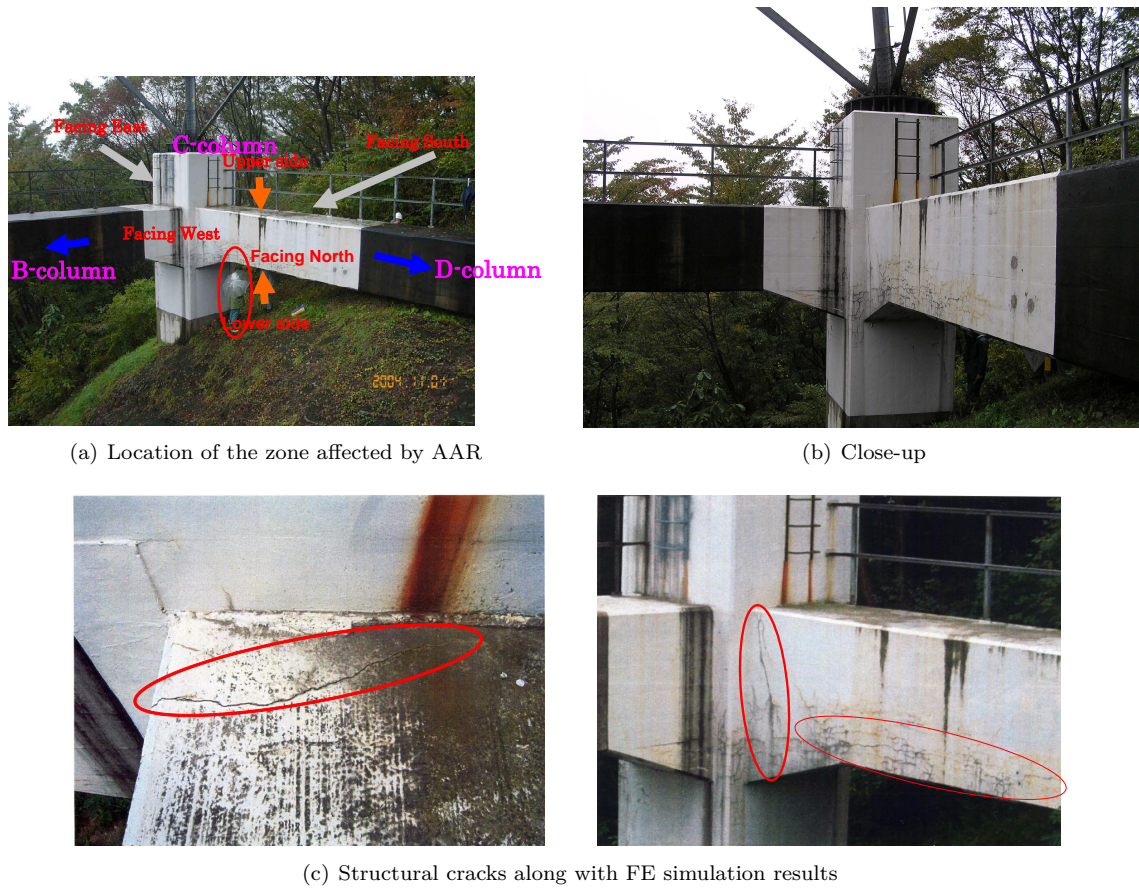
Figure 14.1: Heavily reinforced transmission tower foundation partially affected by AAR

Model	Model	Extent of Expansion
1	Frame C-D	Entire Girder C-D
2	Entire	Entire Girder C-D
3	Frame C-D	Localized in Girder C-D
4	Entire	Localized in Girder C-D

and the finite element mesh (6,271 elements and 3,176 nodes) associated with the 3D model is shown in Figure 14.5. Let's point out the heavy internal reinforcement that has been explicitly modeled along with the Winkler springs surrounding a portion of the columns buried below ground. This becomes an important consideration in the presence of a large lateral load.

14.3   Results

The results for each of the four analyses will be presented separately.

For case 1, Fig. 14.6(a): No cracks are observed in girder C-D or columns D. On the other hand, an unreasonably large crack is found in column D.

For case 2, Fig. 14.6(b): A few cracks are observed in C-D, no cracks in column D, and large cracking in column C.

MERLIN AAR Problems

Loading					
	a脚	b脚	c脚	d脚	Units
Load	155	165	125	130	T
	1.52E+06	1.62E+06	1.23E+06	1.27E+06	N
Area	4.0	4.0	4.0	4.0	m^2
Traction	3.798E+05	4.043E+05	3.063E+05	3.185E+05	Pa
	3.798E-01	4.043E-01	3.063E-01	3.185E-01	Mpa

(a) Geometry

(b) Dimensions
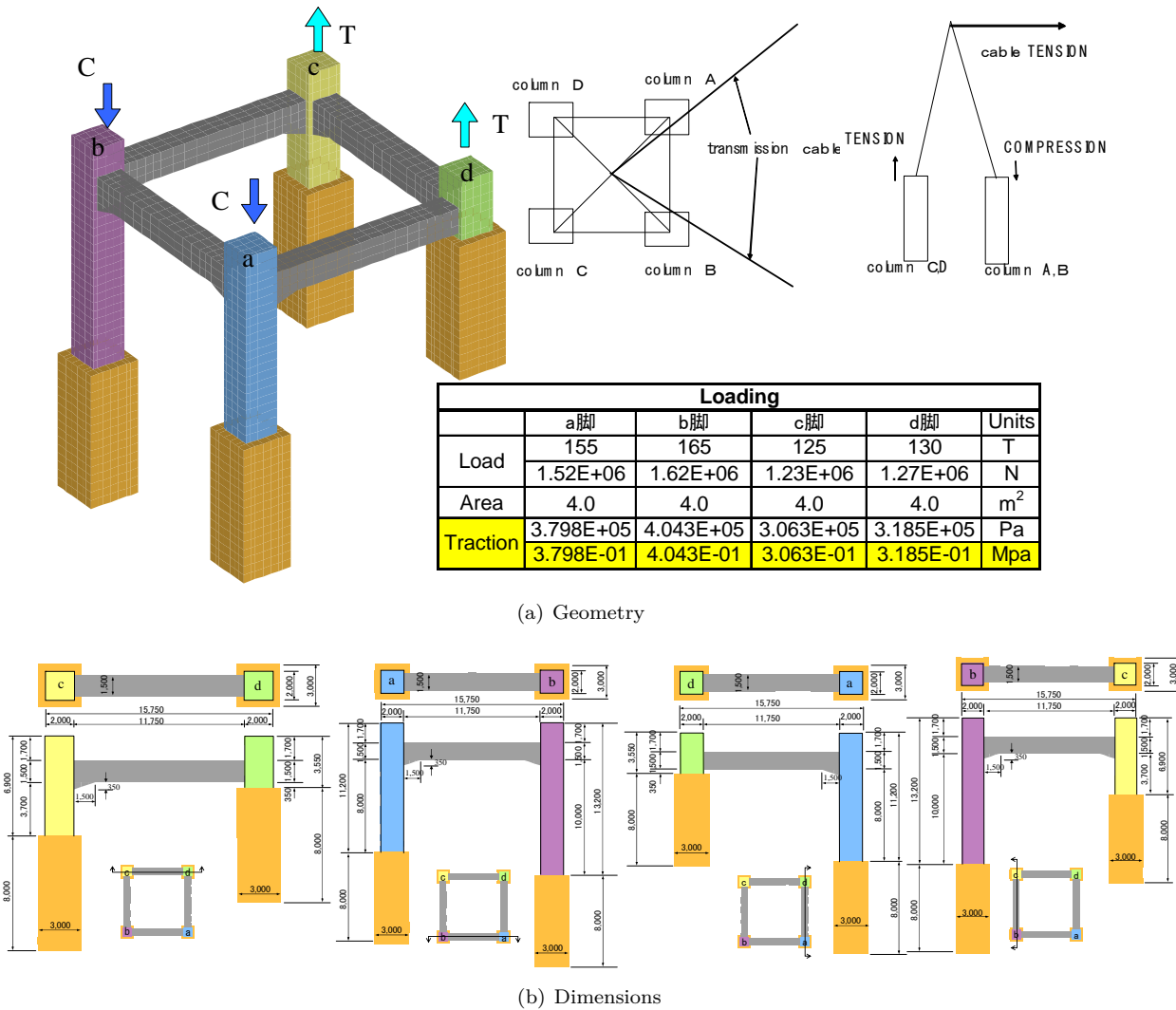
Figure 14.2: Geometry of the massive reinforced concrete structure

As for case 3, Fig. 14.6(c): Excessive cracking is noted in girder C-D and in column C.

Lastly, for case 4, Fig. 14.6(d): The cracking is finally close to the observed pattern, and only a few cracks are computed in column C.

The computed crack opening displacement can now be compared with the measured displacement (through the crack index) in Figure 14.7; this comparison confirms the earlier qualitative assessment that case 4 indeed yields the closest values.

This finding has further been confirmed by a closer examination of the damaged zone in analysis 4, Fig. 14.8, where the strains are in fact very close.

Moreover, the temporal evolution of strains is shown in Figure 14.9.

MERLIN AAR Problems
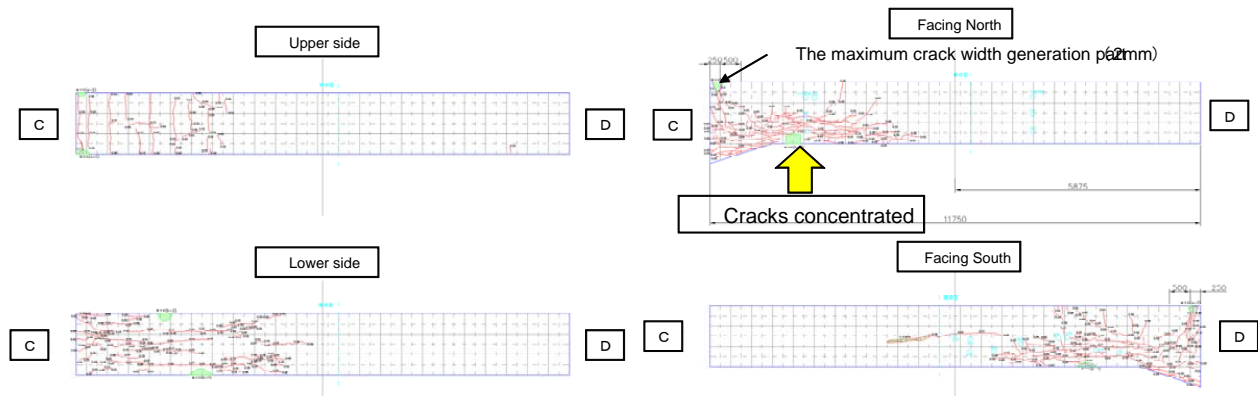
(a) Girder C-D
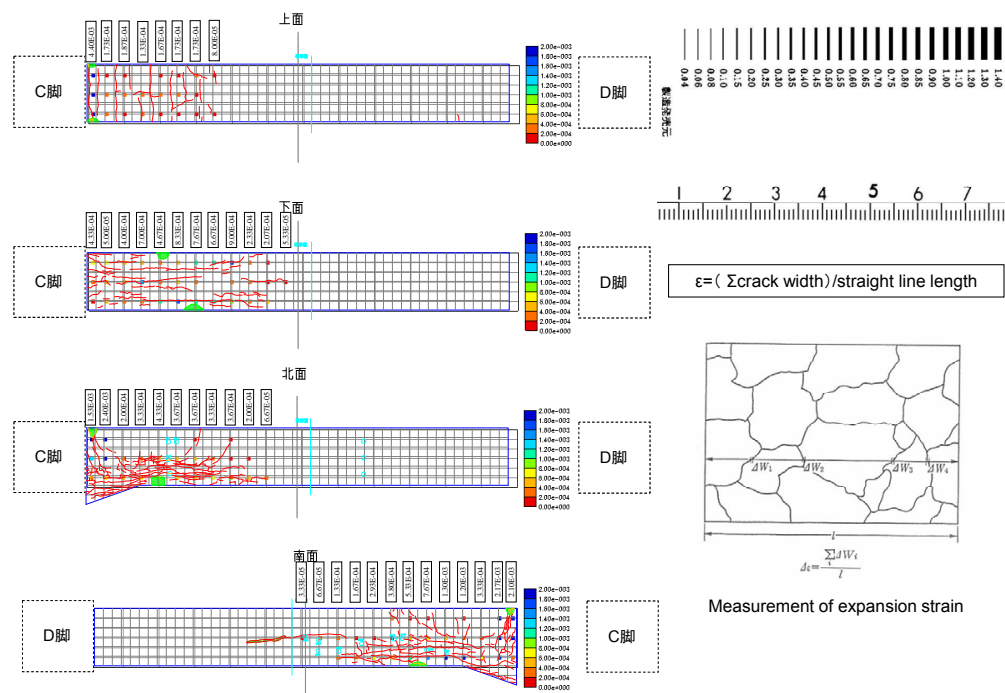
(b) Field strain in CD

Figure 14.3: Field strain measurements

14.4 Seismic Analysis Following AAR Expansion

Following a static analysis of the structure, which has more or less captured both the observed crack pattern and strain recordings in the field, a seismic analysis was performed.

It would be erroneous to undertake such an analysis simply with the degraded tensile strength and Young's modulus, since the "locked-in" stresses caused by AAR and existing cracking would not be taken into account. Instead, the analysis was performed via a "restart" feature in the Merlin finite element code. Per owner's request however, these results cannot be published.
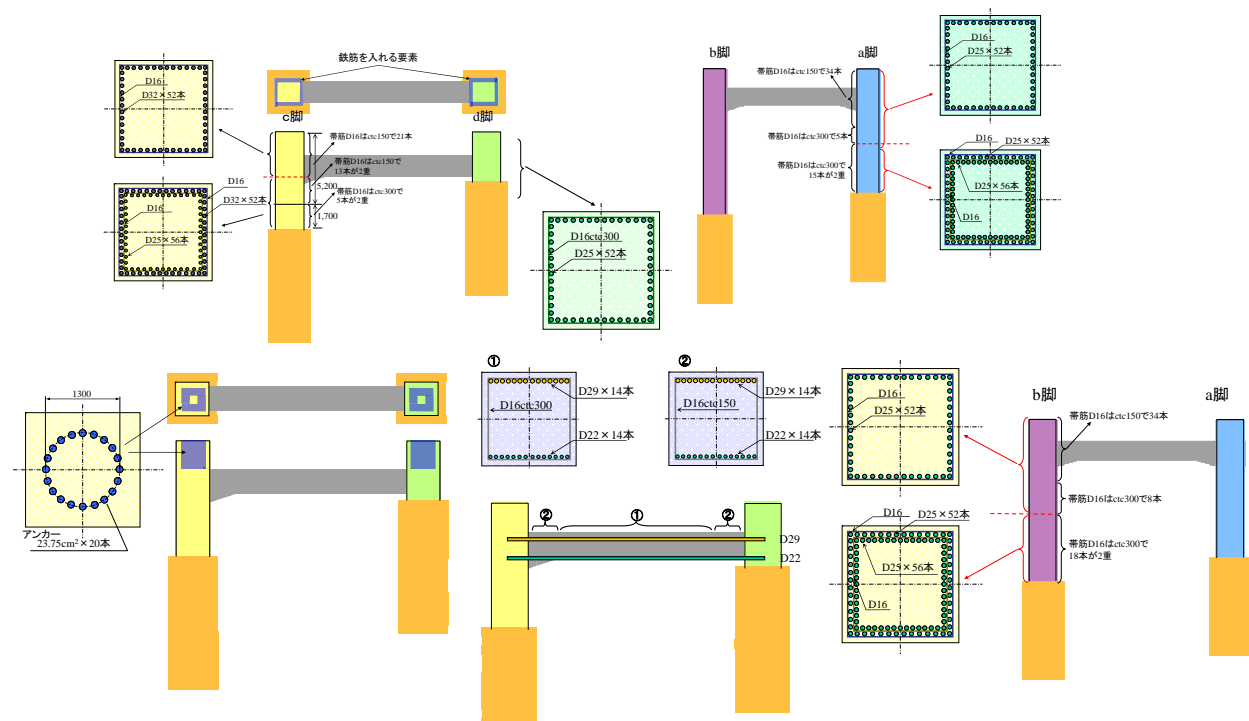
Figure 14.4: Reinforcement
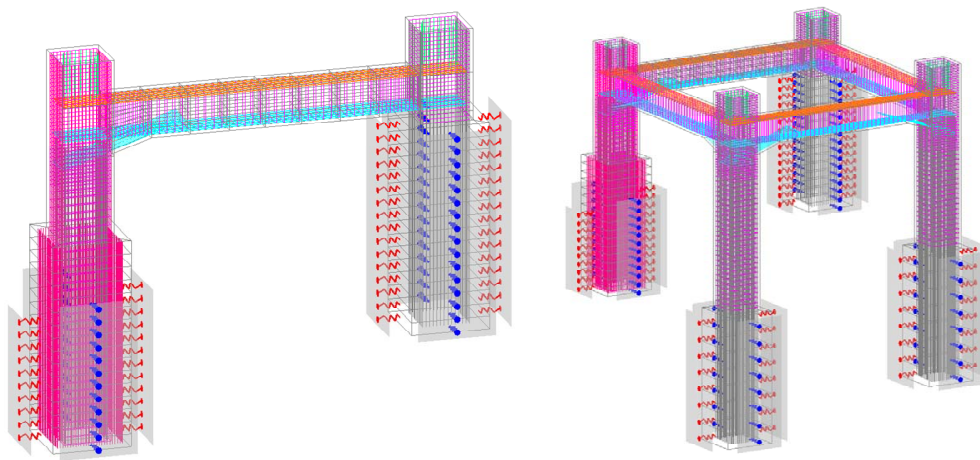
Figure 14.5: Finite element mesh

14.5   Summary

AAR engineering simulation is of paramount importance to engineers confronted with a degraded structure. The most important questions concern how long the structure will continue to expand (given constant exposure to the reactive alkali and aggregates), and what would be the accompanying structural response. This chapter has presented a rigorous procedure, based for the most part on our model, that accounts for both thermal and load time fluctuations. Its application typically entails a preliminary transient thermal analysis,

Maximum principal strain   Crack distribution

(a) 1. Frame C-D; AAR over the entire C-D

Maximum principal stress   Crack distribution

(b) 2. Entire Frame; AAR over the entire C-D

Maximum principal stress   Crack distribution

(c) 3. Frame C-D; AAR in the localized part of C-D

Maximum principal stress   Crack distribution

(d) 4. Entire Frame; AAR in the localized part of C-D
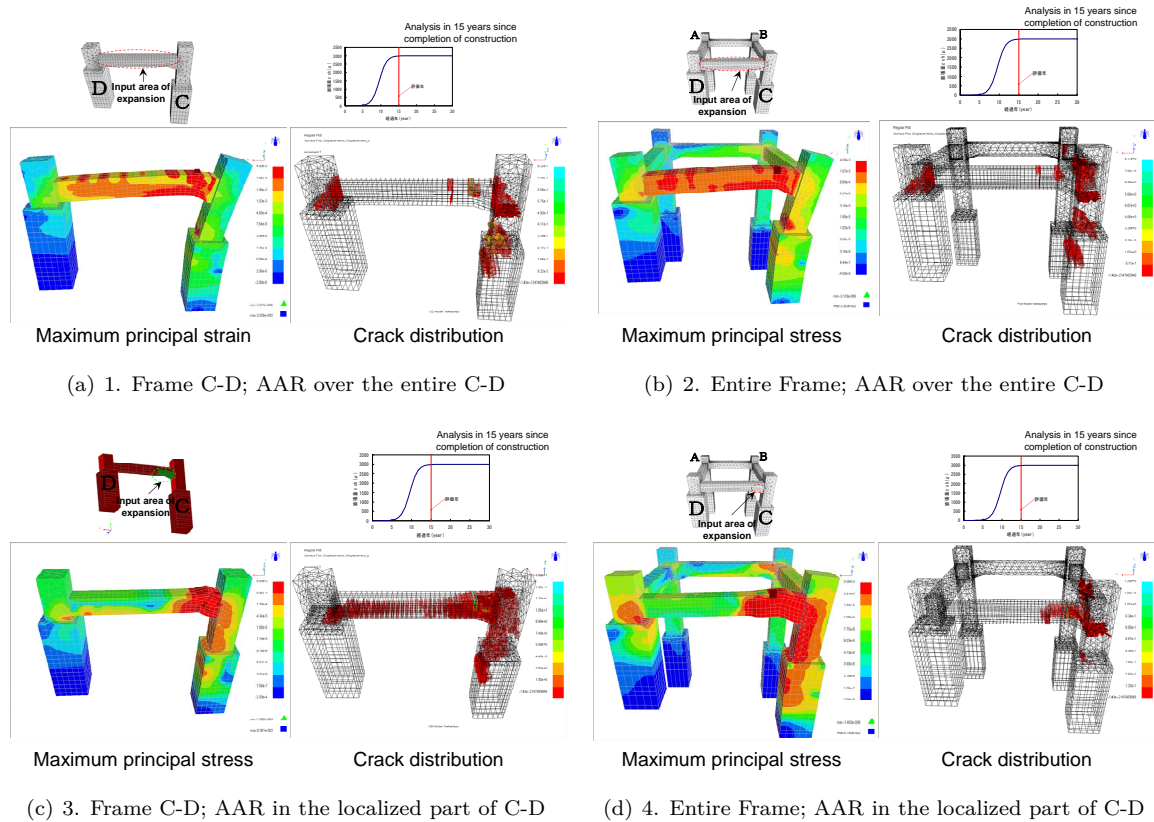
Figure 14.6: Finite element analysis of various cases
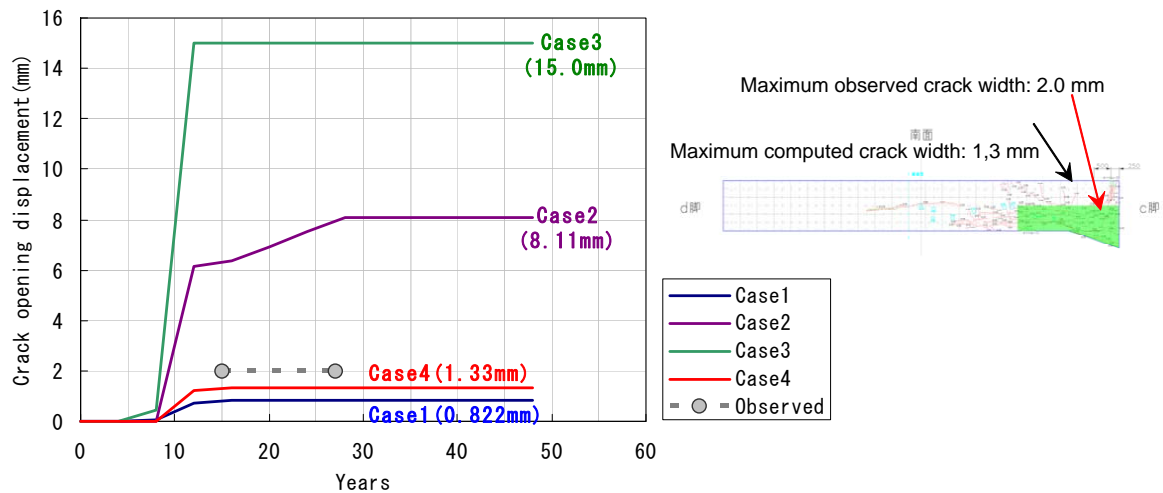
Figure 14.7: Finite Element Analysis summary; COD

to be followed by a system identification procedure provided the necessary field measurements are available. The feasibility of this methodology has been illustrated through an analysis of three different structures. To

MERLIN AAR Problems
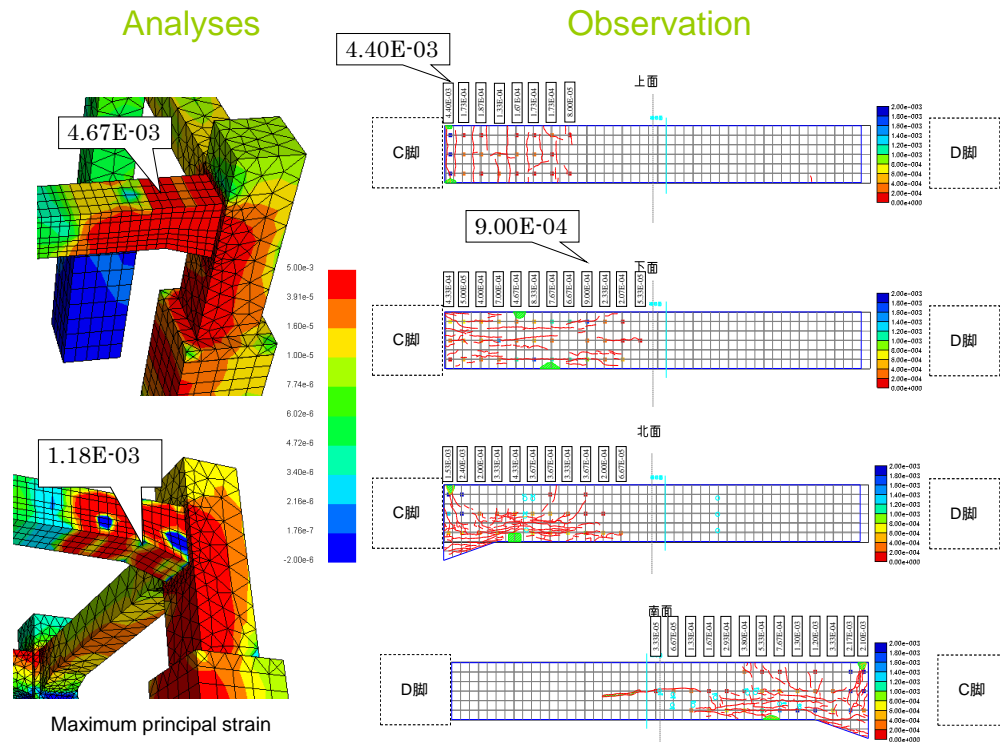
Figure 14.8: Close-up of analysis 4: Strains
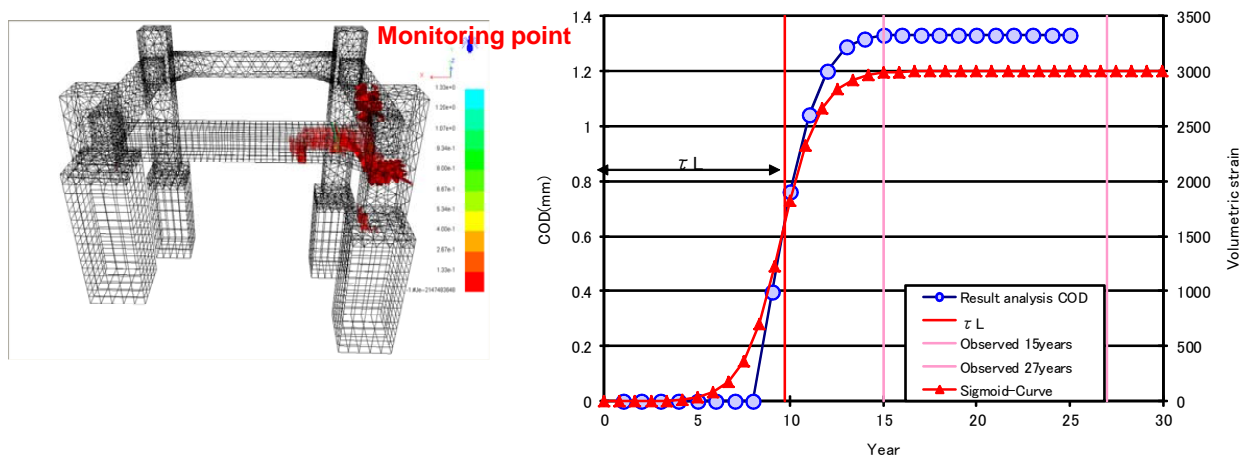
Figure 14.9: Kinetics of analysis 4

the best of the author's knowledge, this approach represents the most comprehensive analytical methodology for investigating AAR-affected structures to date (based upon a realistic assessment of the investigated structures) and will hopefully stimulate further research and applications along these lines.

MERLIN AAR Problems

Chapter 15

P14: Risk-Informed Conditional Assessment of a Bridge with Alkali Aggregate Reaction

15.1 Introduction

With the aging of infrastructure, Alkali Aggregate Reactions (AAR) are increasingly burgeoning as most of them were built at a time when the nature of the reaction was poorly understood, and standards for the detection of potential AAR in concrete mixes not well established. Whereas the problem has been traditionally associated with dams, it has also affected numerous bridges worldwide West, 1996. In an early study, Plum, 1961 it was reported that in *Denmark 600 bridges (roads and railways) and an unknown number of municipal ones are potentially AAR dangerous.*

In a widely reported case, AAR expansion has caused rupture of the reinforcement Miyagawa et al., 2006. The 6th street viaduct in Los Angeles was constructed in 1932 using what was then state-of-the-art concrete technology and the use of on-site batching plant. Yet, over the past 75 years, concrete elements have cracked and deteriorated due to AAR. As a result, the viaduct's concrete has lost significant strength, and the structure is subject to failure under predictable seismic loads Montez, C. and Stokes III, W.E., 2009. The bridge was recently dismantled and became yet another casualty of AAR.

Studies have mostly focused on field observations and assessments Barbosa et al., 2016 Schmidt et al., 2014a Shayan, Xu, et al., 2015 where not only are residual expansions performed, but increasingly petrographic analyses performed Rivard and Ballivy, 2000 Lukschová, Přikryl, and Pertold, 2009 Merz, 2013. It has not been unusual to tear down a structure on the sole basis of field/petrographic studies without an attempt to conceptualize findings into engineering parameters that can be used by structural engineers for a final structural integrity assessment.

Surprisingly, and to the best of the authors knowledge, there has been very few publications related to "science based" numerical prediction of the structural response of bridges affected by AAR. Indeed, the

FHWA report FHWA, 2010 does not even mention the term "finite element" once in its 154 pages.

Most recently, the deterministic finite element simulation of a viaduct Omikrine et al., 2016 undergoing a delayed ettringite formation (a swelling reaction so similar to AAR that quasi-identical swelling model are adopted) was reported. Regretfully, very little details (if any) are provided with regard to the numerical assumptions of the model, and how are they obtained. Huang et al., 2014 presented an interested probabilistic based investigation of the steel-concrete bond in AAR affected structures. The deterministic analysis of an entire bridge, albeit with a rather simplified model was reported in Wojslaw and Wisniewski, 2014. It did, once again, highlight potential deficiency in shear Saouma et al., 2016 where a set of parametric analyses on shear capacity of concrete beams and panels is followed by multi-linear regression model based on Akaike and Bayesian information criterion to quantify the most sensitive parameters.

The case study of this paper is a major precast segmental bridge in Switzerland (commonly referred as the *Viaduct de Chillon*) that was recently found to suffer from AAR (albeit at an early stage) and as a result underwent major rehabilitation Brühwiler et al., 2015. First, the currently known conditions, from field and laboratory (petrographic, mechanical and residual expansion tests) will be critically reviewed and findings reinterpreted in terms palpable for a finite element structural analysis (albeit with wide margins of uncertainties). Then, given those uncertainties, an innovative probabilistic based model, inspired by Latin Hypercube Sampling (LHS) is proposed. This model is then applied to run a large set of analyses. Finally, predictive results are presented, and proper conclusions drawn.

15.2   Description of the Viaduct

The *Viaduct de Chillon* is a precast post-tensioned bridge spanning between 92 m and 104 m over a total length of 2,120 m. The French double-cantilever construction system was used with precast voussoirs. It was opened to traffic in 1969 and is a well-known innovative and iconic structure widely recognized Piguet, 1971, Fig. 15.1.
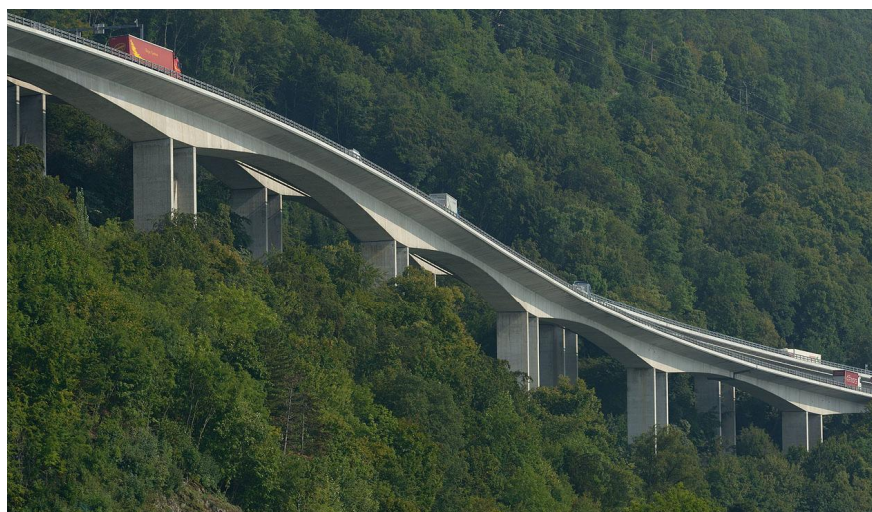
Figure 15.1: General view of the viaduct Kronenberg et al., 2013

15.3 Concrete Conditions

Scheduled inspections have revealed a significant increase in reinforcement corrosion due to chloride diffusion through cracks. Ensuing preliminary investigations of the deck (concrete compressive strength, mild and pre-stressing steel tensile strength) were performed and repairs conducted in 2012-2013. However, poor adhesion of the repair overlay mortar to the subjacent concrete was observed. Should the concrete have been sound, this should not have occurred, and as such AAR was strongly suspected. In 2012 many samples were extracted along the nearly 2 km in order to properly account for the inherent and inevitable variabilities encountered in such a structure. Cores were extracted from the slabs and webs and not from the inclined segments as their structural role was perceived as minimal. Tests included: Microscopic analysis (composition and micro-structure, state of degradation), residual expansion measurements, compressive strength of cores, direct tensile strength, tensile axial splitting, static elastic modulus in compression, and hardened concrete mass density. Findings Kronenberg et al., 2013 led to the following observations.

Topological Damage Distribution: The central zone of the deck exhibited most deterioration. This may be related to concrete casting, storage and curing conditions. Indeed, segregation and bleeding of the fresh concrete may have caused micro-structural weaknesses. Traffic, temperature changes and exposure to deicing salts also constituted aggravating factors.

Concrete Degradation: The aggregates used come from a mixture of silica and silicate metamorphic rocks of sedimentary and crystalline nature, with a slow/late reaction potential. The Portland cement content of the deck ranged from 350 to 400 kg/m^3 (350 kg/m^3 specified).

So far, concrete has undergone relatively small expansions as it has been in a relatively dry condition (there were no visible signs of micro cracks), and the potential for expansion is intact. It is estimated that present (45 years after construction) expansion is less that 0.1% and that future expansion (after an additional 45 years) should be between approximately 0.4 and 0.9%.

Expansion tests have not revealed a "plateau', this is often the case when aggregates do also contain alkali. It was estimated that the laboratory maximum rate of expansion is 0.7-0.8 mm/m/year. Based on Arrhenius law, it is estimated that at 11°C expansion is about 5 slower than at 38°C, yielding a guesstimate 0.1-0.2 mm/m/year in the worst case scenario. This in turn will result in 0.45-0.9% future expansion *in the most unfavorable conditions*, that is wet surfaces without protection. Indeed, this concrete was labeled as one of the most reactive concrete known in Switzerland.

Mechanical Properties were obtained from 100 mm diameter cores and maximum aggregate size of 32 mm. Values are shown in Table 15.1 and corresponding percentage losses (determined from concrete in unaffected zones) are also shown. The mechanical properties of the inclined members were not tested as they play a relatively minor structural role. Beside the concrete used in these components is likely to have been quite different than the one used in the main box girder. Finally, in anticipation of a possible strengthening, a crude estimate of the possible evolution of mechanical strength in the next 30 years has been attempted ibid., Table 15.1.

15.3.1 Remedial

The conclusions attributing the damage to AAR, it was decided to strengthen the slab by adding a layer of 40 mm of an ultra high performance fiber reinforced cement-based composite (UHPFRC) material, reinforced with steel rebars. Strain-hardening UHPFRC with its low permeability is an ideal sealant to reduce ingress of water and thus slow/stop AAR expansion Brühwiler et al., 2015.

MERLIN AAR Problems

Table 15.1: Mean and minimum values of concrete properties Kronenberg et al., 2013

Property	Current (year 2015, age 45 years)								
	Intact	Mean values degraded				Minimum values degraded			
	Bottom	Center Top	Loss %	Bottom Side	Loss %	Center Top	Loss %	Bottom Side	Loss %
f_c'[MPa]	90 ± 10	75 ± 10	5-20	90 ± 10	0	65	30	80	10
f_t' [MPa]	4.5 ± 0.5	2.5 ± 0.7	40-45	3.7 ± 0.7	15-20	1.8	60	3.0	30
E [GPa]	40 ± 4	32 ± 4	15-20	38 ± 4	0-5	28	30	30	15
	Projected (year 2045, age 75 years)								
f_c' [MPa]	90 ± 10	55 ± 10	35-40	70 ± 10	20-25	40	30	55	10
f_t' [MPa]	4.5 ± 0.5	2.0 ± 1.0	50-60	2.0 ± 1.0	30-35	1.0	60	2.0	30
E [GPa]	40 ± 4	25 ± 5	30-35	30 ± 5	20-25	21	30	25	15

15.4   Finite Element Model

Based on the engineering report Kronenberg et al., 2013 three zones were identified, Fig. 15.2. The top
deck layer (T) is the warmest and has the maximum exposure to water, and hence is assigned the largest
volumetric expansion $\varepsilon^i nfty$. The other two zones (C and B/S for center and bottom/side), are better
protected from both the water and the radiant heat, and are thus assigned 80% and 70% of the deck value.
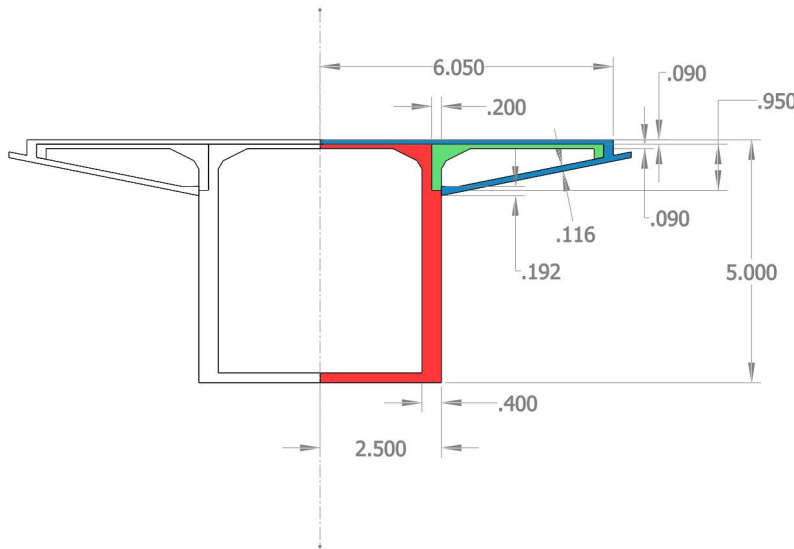
Figure 15.2: Modeled section identifying the T, C and B/S regions (blue, green and red)

13 reinforcement groups are identified, Fig. 15.3. 8 mm reinforcement for the lateral reinforcement
(x direction) spaced at @100 and at 125 mm from the external faces, and 7 mm @125 mm for the rest.
Also shown in the figure, are the "index" points for which the finite element analyses will be recording the
engineering demand parameters (EDP) such as deformations and displacements.

Since the computational cost load for a probabilistic based nonlinear finite element analysis of the viaduct
will be prohibitive, and as this is the first attempt to provide such a solution, only one (half, by virtue of
symmetry) segment is modeled, and it is assumed to be fully supported at the base, Fig. 15.4.

The model has 6,380 nodes and 4,820 eight-node brick elements. Longitudinal displacements are con-
strained on the front and rear faces (z axis), whereas free expansion is allowed along the lateral and vertical
directions (x and y axis) except along the plane of symmetry (constrained in the x direction) and along
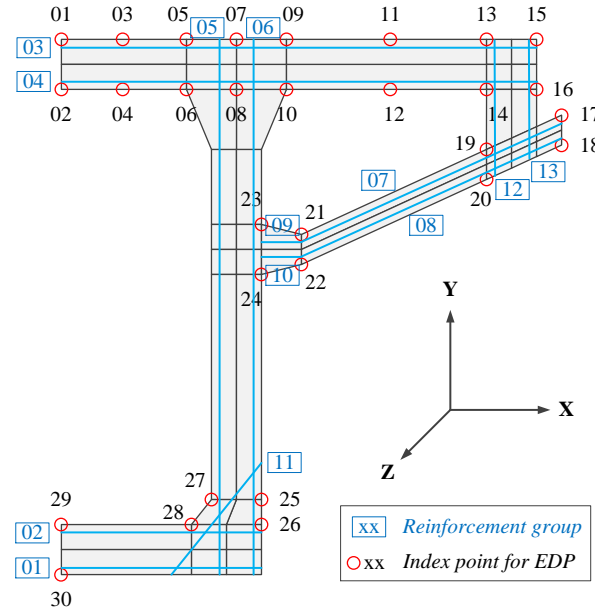
Figure 15.3: Location of index points and rebar groups
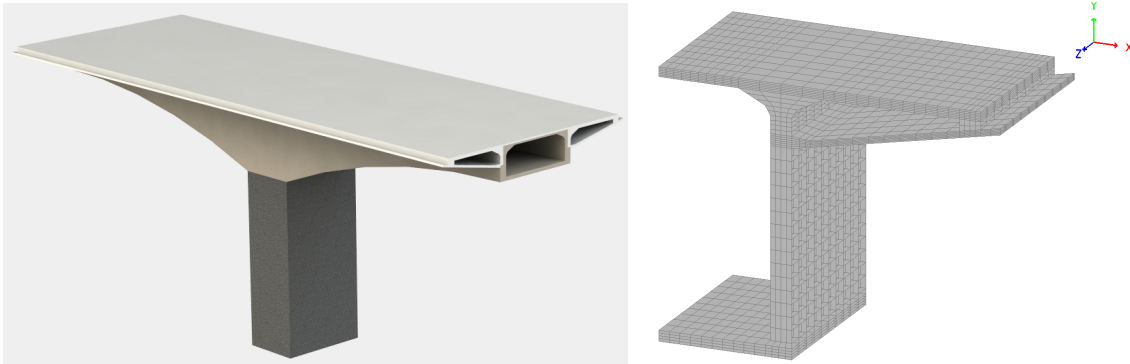
Figure 15.4: Finite element mesh

the base (in the y direction) as the model assumed to be supported vertically. There are 10 layers in the longitudinal direction, and the mesh is sufficiently by at least four layers of elements to properly capture flexure in all segments. The self weight is applied in the first increment, and it is rapidly overwhelmed by the response to concrete swelling due to the subsequent AAR increments.

Coupled with previously described AAR model is a nonlinear damage-fracture constitutive model for the concrete Cervenka and Papanikolaou, 2008 both implemented in the code Merlin **merlin**.

Given that the viaduct is 45 years old, the analyses seek to predict the incremental response over a total of 100 years. A time increment that is too short will be computationally prohibitive, too long of a one will result in gross imprecision. Hence, and following some parametric studies, a time increment (known as Analysis Time Unit - ATU - in the model) of 40.56 days was selected, and 900 increments will be needed for each of the (implicit) analyses.

Selection of concrete physical properties is critical for this epistemic study, they are tabulated in Table 16.1. The assignment of the AAR properties, Table 15.3 was more delicate and had to account for field

MERLIN AAR Problems

measurements (Table 15.1). Again different AAR volumetric expansions are assigned to the T, C, and B/S regions (Fig. 15.2). Selection of the controlling expansion (at the top) is discussed below. Likewise, different reduction (or degradation) factors are accordingly assigned based on findings summarized in Table 15.1.

Table 15.2: Nonlinear concrete model Cervenka and Papanikolaou, 2008 parameters

Characteristics	Symbol	Unit	Distributional model	Mean / COV	[min, max]
Mass density	ρ	Gg/m^3	Deterministic	0.0024	-
Thermal expansion coefficient	α	$1/^oC$	Deterministic	9.9e-6	-
Modulus of elasticity	E	MPa	Uniform Dist.	40,000	[36,000 44,000]
Poisson's ratio	ν	-	Deterministic	0.2	-
Tensile strength	f_t	MPa	Uniform Dist.	4.5	[4.0 5.0]
Exponential softening	G_F	MN/m	Normal Dist.	1.2e-4/0.2	[9.0e-5 1.5e-4]
Compressive strength (T and C)	f_c	MPa	Uniform Dist.	-67.0	[-77.0 -57.0]
Compressive strength (B/S)	f_c	MPa	Uniform Dist.	-78.0	[-88.0 -68.0]
Compressive critical displacement	w_d	m	Deterministic	-0.0005	-
Factor beta for return direction	β	-	Deterministic	0	-
Factor e for roundness of failure surface	e	-	Normal Dist.	0.60/0.15	[0.5 1.0]
Onset of nonlinearity in compression	f_{c0}	MPa	Normal Dist.	-20/0.1	[-24 -16]
Plastic strain at compressive strength	ϵ_{cp}	-	Deterministic	-0.001	-

Table 15.3: Characteristics of the AAR model

Characteristics	Symbol	Unit	Distributional model	Mean/COV	[min, max]
Maximum volumetric strain (T)	$\left(\varepsilon_{AAR}^\infty\right)_T$	-	Trapezoidal	-	[0.004 0.020]
Maximum volumetric strain (C)	$\left(\varepsilon_{AAR}^\infty\right)_C$	-	Deterministic	$80\% \times \left(\varepsilon_{AAR}^\infty\right)_T$	[0.0032 0.016]
Maximum volumetric strain (B/S)	$\left(\varepsilon_{AAR}^\infty\right)_{B/S}$	-	Deterministic	$70\% \times \left(\varepsilon_{AAR}^\infty\right)_T$	[0.0028 0.014]
Characteristic time	τ_c	ATU	Trapezoidal	-	[40 75]
Latency time	τ_l	ATU	Trapezoidal	-	[480 610]
Activation energy associated with τ_c	U_C	^oK	Uniform Dist.	5,400	[4,900 5,900]
Activation energy associated with τ_l	U_L	^oK	Uniform Dist.	9,400	[8,900 9,900]
Residual reduction factor	Γ_r	-	Normal Dist.	0.15/0.2	[0.1 0.2]
Fraction of ε_t prior to reduction of AAR expansion due to macro cracking	γ_t	-	Normal Dist.	0.5/0.2	[0.3 0.7]
Compressive strength (T/C)	f_c	MPa	Uniform Dist.	-67.0	[-77.0 -57.0]
Compressive strength (B/S)	f_c	MPa	Uniform Dist.	-78.0	[-88.0 -68.0]
Tensile strength	f_t	MPa	Uniform Dist.	4.5	[4.0 5.0]
Shape factor	a	-	Deterministic	-2	-
Reference temperature	T_0	^oC	-	10.1	-
Upper compressive stress beyond which there is no more AAR expansion	σ_U	MPa	Deterministic	-8.0	-
Reduction fraction for Young's modulus (T/C)	β_E	-	Uniform Dist.	-	[0.68 0.78]
Reduction fraction for Young's modulus (B/S)	β_E	-	Uniform Dist.	-	[0.45 0.60]
Reduction faction for tensile strength (T/C)	β_{f_t}	-	Uniform Dist.	-	[0.18 0.57]
Reduction faction for tensile strength (B/S)	β_{f_t}	-	Uniform Dist.	-	[0.10 0.41]

The average yearly temperature at the viaduct location is 11°C, and will be used. Hence laboratory values for τ_L and τ_C (measured at 38°C) are adjusted per Equation 1.2.

As to the reinforcement, only the yield stress (in an elastic-perflectly plastic model) is considered variable and is assigned a normal distribution function with a mean of 248 MPa and a range of [225250].

15.5   Preliminary Deterministic Analysis

A preliminary deterministic set of analyses were performed to assess the impact of the spatial distribution of the concrete properties and the corresponding computational time. As reported earlier, three distinct zones

MERLIN AAR Problems

of AAR exposure were identified, Fig. 15.2. Hence the same (arbitrarily selected) high ultimate volumetric
AAR strain of 1.0% was assigned to three analyses (identified as uniform, partial and full nonuniform). In
the first, identical properties were uniformly assigned to all regions. In the second and third, 1.0, 0.8 an 0.7
percent expansion were assigned to the three regions, however the latency and characteristic times were kept
constant in the second and varied in the last.

It was quickly noticed that the CPU time was commensurate with the model heterogeneity: 6.1, 7.7 and
19 hours respectively. Indeed, the first model with uniform property assignment gave no sign of cracking,
minor and extensive cracking were observed in the last two.

Deformed shape, crack pattern, horizontal and vertical displacements of three index points (1, 7 and 15
in figure 15.3) were scrutinized for all three analyses to better understand the impact of the non-uniform
assignment of AAR properties, Fig. 15.5.

As expected, the more heterogeneous are the concrete properties assigned, the more convoluted (and
un-predictive) is the deformed shape from which one can identify zones of tensile and compressive stresses
(Figs. 15.5(a), 15.5(b) 15.5(c) where the shaded surfaces correspond to the vertical displacement). In these
analyses, the web undergoes relatively small flexure, and the inclined deck support appears to play an
important role in the expansion. Induced (smeared) cracks at the end of the 900 increments (100 years, 0.1%
volumetric strain) are shown in Fig. 15.5(d), 15.5(e) and 15.5(f). Consistent with the previous figures, the
most realistic model (full non-uniformity) exhibits most cracks in the deck and the web-deck connection.

Figs. 15.5(g) and 15.5(h) show the stress distribution along the center lateral (groups #4 shown in Fig.
15.3) top reinforcement in terms of time (as measured from the centerline). As one would expect, the stress
increase with time until it reaches the rebar yield stress. Of concern, is that the yield stress is reached within
the 45 years (i.e. presently). This finding must be tempered by the high assumed final volumetric strain of
0.1%. The uniform case has only a small discontinuity, while the full nonuniform case exhibits strong stress
jumps at the deck intersection with the supporting components.

Finally, Fig. 15.5(i) and 15.5(j) show the lateral (x) and vertical (y) displacements of three index points,
i.e. Loc.01, Loc.07 and Loc.15 (Fig. 15.3). The displacement trend of the partial uniform case is very similar
to the uniform one (not shown) but with smaller values. On the other hand, the displacement curves for the
non-uniform case are slightly different. Whereas the lateral displacement follow the same smooth sigmoid
shape, the vertical displacements exhibit a peak, and then a "softening". *a priori* this could be attributed
to a phase shift caused by the differences in the characteristic and latency times.

15.6   Uncertainty Quantification Framework

To perform a deterministic analysis of this bridge would be too presumptuous as there are so many poorly
quantified variables. Those are either aleatory in nature such as random distribution of pockets of high
reactivity in the bridge, or they are epistemic since we do not fully know the concrete characteristic. In light
of the above, a probabilistic investigation is undertaken. For the finite element investigation to be properly
carried out, a mathematical representation of the kinetics should be given.

Consistent with the model presented earlier, the maximum volumetric strain ε^∞ (Eq. 1.1) and the
degradations of the elastic modulus and tensile strength β_E, and β_{ft} (Eq. **??**) must be determined in a
manner consistent with the findings of the laboratory observations (Table 15.1).

Starting with ε^∞, and as previously mentioned, the estimated present expansion is less than 0.1%, and
the future expansion at age 90 years is expected to be in the range of 0.45-0.9%. Hence, for the sake of

(a) Uniform; deformation

(b) Partial Non-uniform; deformation

(c) Full Non-uniform; deformation

(d) Uniform; damage

(e) Partial Non-uniform; damage

(f) Full Non-uniform; damage

(g) Uniform; Reinf # 4

(h) Full Non-uniform; Reinf # 4

(i) Partial Non-uniform; displacement

(j) Full Non-uniform; displacement
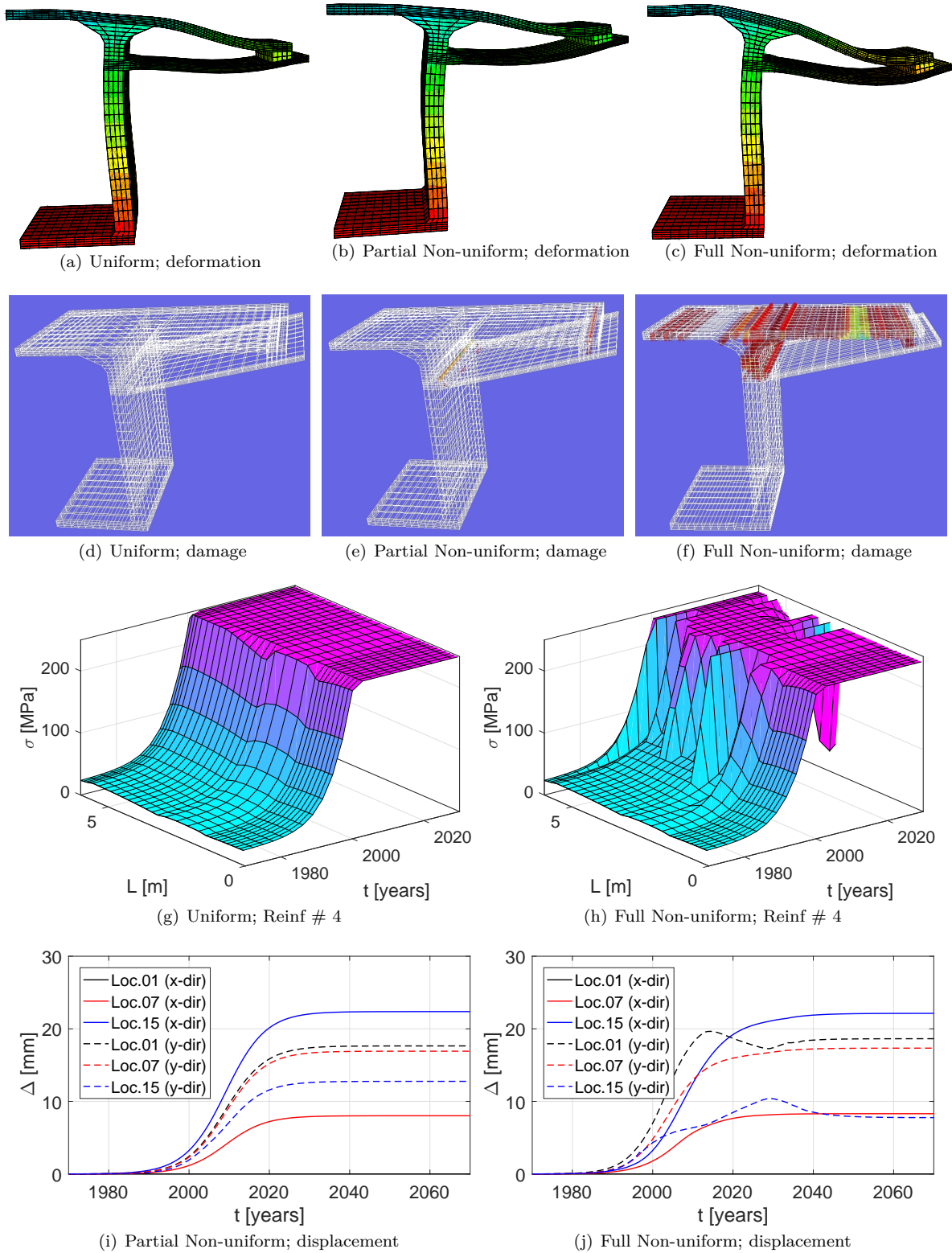
Figure 15.5: Comparison of the uniform, partial and fully non-uniform models

the analysis, it is assumed that the range of current expansion (after 45 years) is 10% of those values or
0.045-0.09%. As to the estimate of total expansion in the subsequent 35 (45+45-10) years (under most
unfavorable conditions) it will be 0.45-0.9%. Finally, guesstimating for a total of 100 (45+45+10) years, the
lower bond is maintained at 0.45% and the upper bond is 2.0% (again based on the reported 0.2 mm/m/year
estimated from laboratory tests). Hence, the domain of uncertainties is illustrated by Fig. 15.6 broken in
three zones: present, near and far future.

Finally, having two points from current uncertainty and four points from future one, eight potential
expansion curves (marked as corner curves) are fitted which is shown in Fig. 15.6.
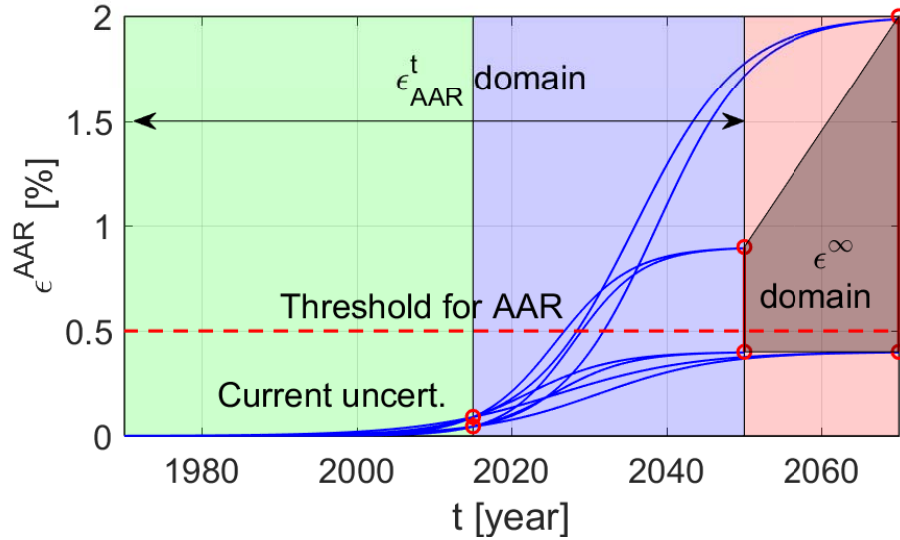
Figure 15.6: Domain of investigation for AAR expansion (1970-2015: dry and 2016-2070: wet condition)

At this point, a strategy must be devised on how to generate the random expansion curves for the Monte-
Carlo simulation (MCS). The curves, can be defined by three points: 1) the origin; 2) a random point at
the current time (2015) and 3) a random point bounded by the time interval of 2050-2070, and expansion
intervals of 0.45-0.9% and 0.45-2.0 %. The approach taken is heavily inspired by the LHS-wised technique
of MCS Iman and Conover, 1982.

First, n_{sim} points are orderly identified within the (trapezoidal) domain of future uncertainly and another
n_{sim} are randomly located within the axis of present uncertainty. Then, those points are randomly paired
together, and along with the origin provide a set of three points which could uniquely define the expansion
curve characterized by Eq. **??**. The end point providing the time of reaction saturation and the maximum
volumetric expansion ε^∞, a curve is then passed through those points (using a simple numerical algorithm)
and τ_l, τ_c are determined, Fig. 15.7(a).

Then, the corresponding distributions of the degradations must be defined as a set of random variables.
Starting with f_t and E, the degradation model is given by Eq. **??** and must be calibrated with estimated
material degradations shown in Table 15.1 defined as $M \pm m$. Hence, three sets of nonlinear least-squares
optimizations are run to obtain the β values. Results are shown in Fig. 15.8.

Finally, a simple approach was adopted for the degradation of the compressive strength f_c. As the
constitutive model does not currently account for its degradation. The average values of 67 and 78 MPa
(from Table 15.1, for top-center, and bottom/side respectively) is taken as a mean with a range of $\pm$ 10

MERLIN AAR Problems

(a) LHS-wised sampling approach

(b) Determined variable histograms
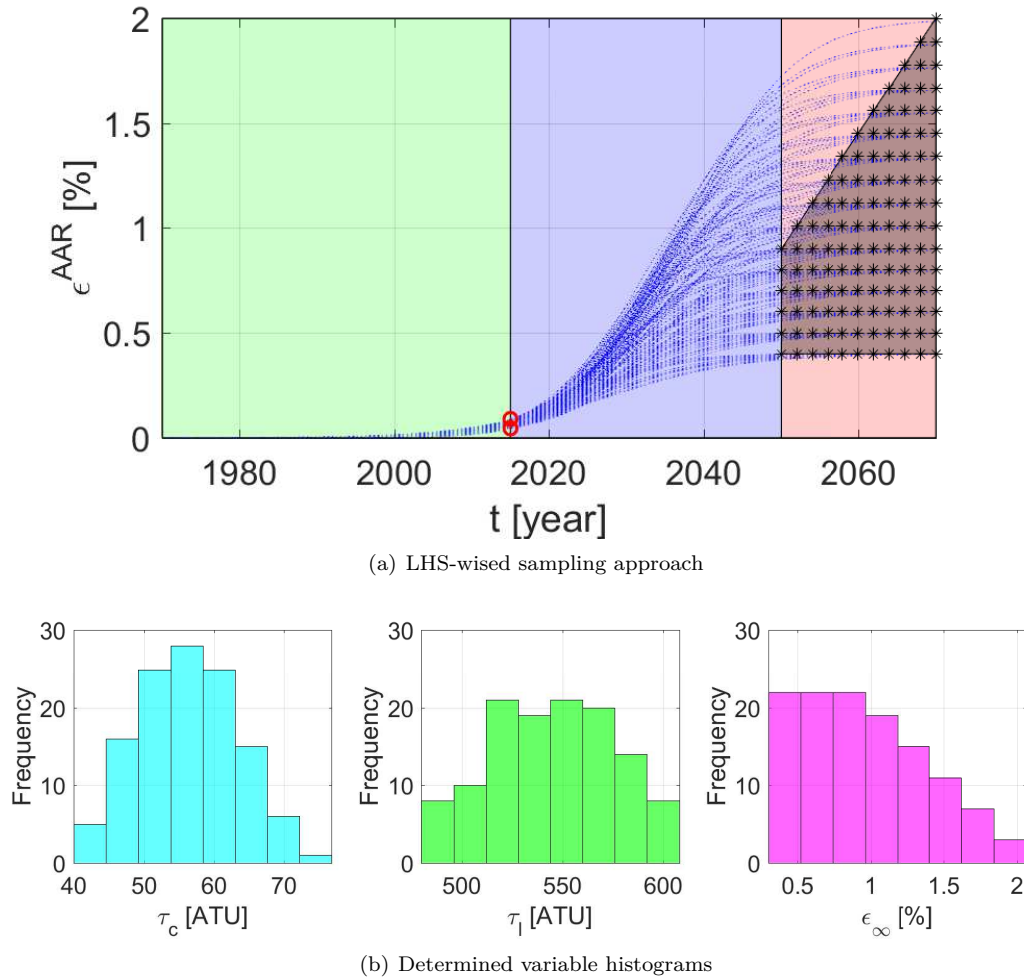
Figure 15.7: Latin Hypercube based sampling method

MPa.

So far variables have been independently defined, however there is a strong correlation amongst some of them. Unfortunately, there is no literature on what should be the correlation of key concrete parameters, hence "engineering judgment" was exercised in assigning those coefficients ρ: $\rho_{(G_F \leftrightarrow f_t)} = 0.5$, $\rho_{(G_F \leftrightarrow f_c)} = 0.6$, $\rho_{(f_c \leftrightarrow f_t)} = 0.6$, $\rho_{(E \leftrightarrow f_c)} = 0.6$, $\rho_{(U_l \leftrightarrow U_c)} = 0.6$, $\rho_{(\beta_E \leftrightarrow \beta_{f_t})} = 0.7$ and $\rho = 0.0$ for the rest.

In summary, this section has detailed how the material properties have been previously assigned in Tables 16.1 and 15.3.

15.7   Automation of Probabilistic Analysis

In the previous section, all variables were defined, then preparation of the input file had to be carefully planned. This task of data preparation, and subsequent data analysis and extraction was made possible through a series of Matlab codes `P1.m`, `P2.m`, `P3.m`, `P4.m` and `P5.m` whose inter-connectivity is illustrated in Fig. 16.11.

(a) β_E for bottom/side

(b) β_E for top/center

(c) β_{ft} for bottom/side

(d) β_{ft} for top/center
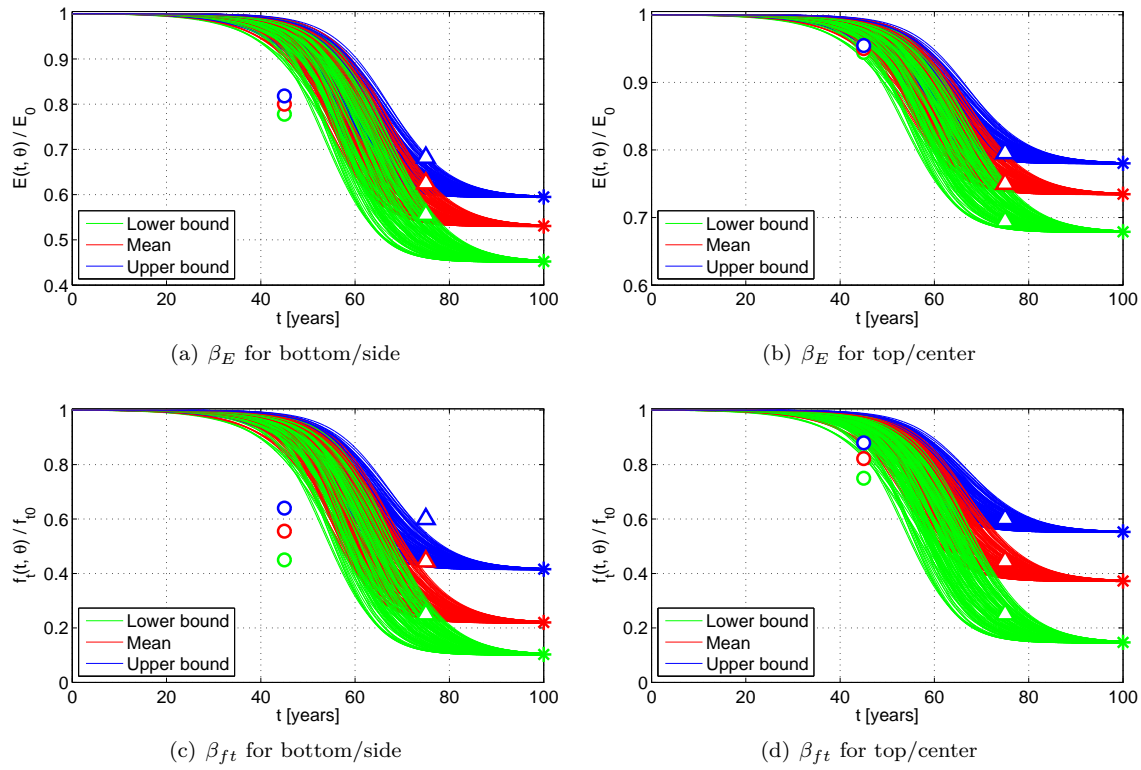
Figure 15.8: Predicting degradation of E and f_t based on optimization of experimental tests
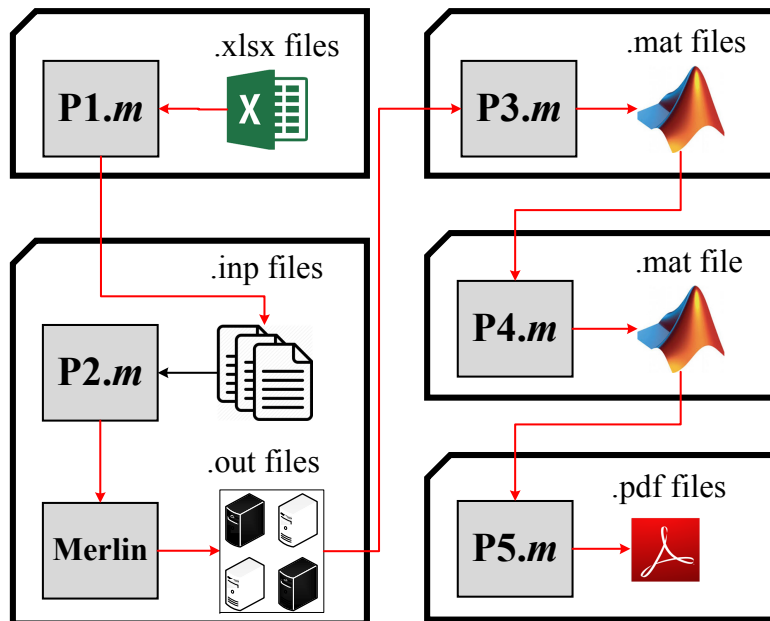
Figure 15.9: File generation and automation algorithm

MERLIN AAR Problems

p1.m reads the user specified variables, probability distribution models, ranges, and correlation coeffi-
cients, and then generates the 121 input files. Those in turn are executed through p2.m which calls the finite
element code Merlin. Results are then individually extracted from 121 output files and stored as binary files
(p3.m) and consolidated into a single data-base (p4.m). Finally, p5.m extract the results from the data base
and generates the desired results. For each output parameter, results are plotted along with their 16, 50
and 84 fractiles ranges, Fig. **??**. This figure will provide the engineer with a rational about the conditional
behavior of the viaduct. The individual time-dependent simulations are shown with light gray lines, while
the summarized curves are black. The vertical axis represents an engineering demand parameter (EDP)
(e.g., displacement, stress, etc.) and the horizontal axis is time (which is a metric for intensity).
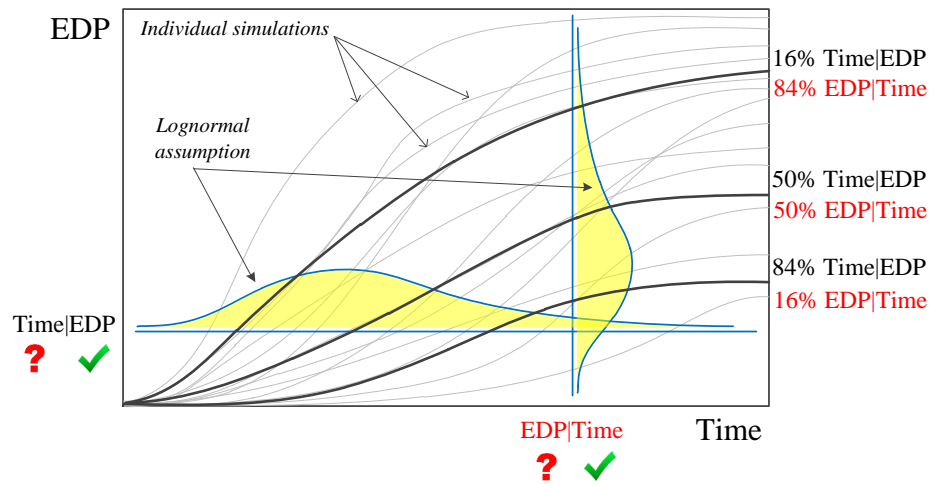
Figure 15.10: Interpretation of the results based on summarized curves

15.8   Analyses Results

An initial attempt to interpret results brought up an unanticipated set of two responses that resulted in two
drastically different deformation shapes of this complex structure. Hence, the next section will examine the
peculiar idiosyncracy of the problem, and results of the 121 analyses will be addressed next.

15.8.1   Effect of Kinetics (classification)

Scanning all 121 analyses results, two major deformation trends emerged, Figs. 15.11(a) and 15.11(b)
(with colored shaded contour corresponding to the volumetric AAR expansion), tagged as Class I and II
respectively. In the first one notes the great "distortion" of the section with much flexure in both the
flanges but also the web. In Class II, the vertical elongation of the web is clearly dominant, resulting in
smaller curvatures in the web. Examining the corresponding (randomly generated) input data for each class
of response, the cause was immediately attributed to the set of latency and characteristic times and the
corresponding activation energies rather than with the values of ε^∞ associated with different regions. From
this set of analyses, importance of differential kinetics properties (used in Eq. 1.2) was highlighted.

This cause was confirmed by Figs. 15.11(c) and 15.11(d) where the time lag in expansion amongst
components is much more accentuated in the second, hence prioritizing the vertical expansion of the web

MERLIN AAR Problems

(a) Class I; deformation

(b) Class II; deformation

(c) Class I; expansion

(d) Class II; expansion

(e) Horizontal and vertical displacements

(f) Stress σ_{xx}
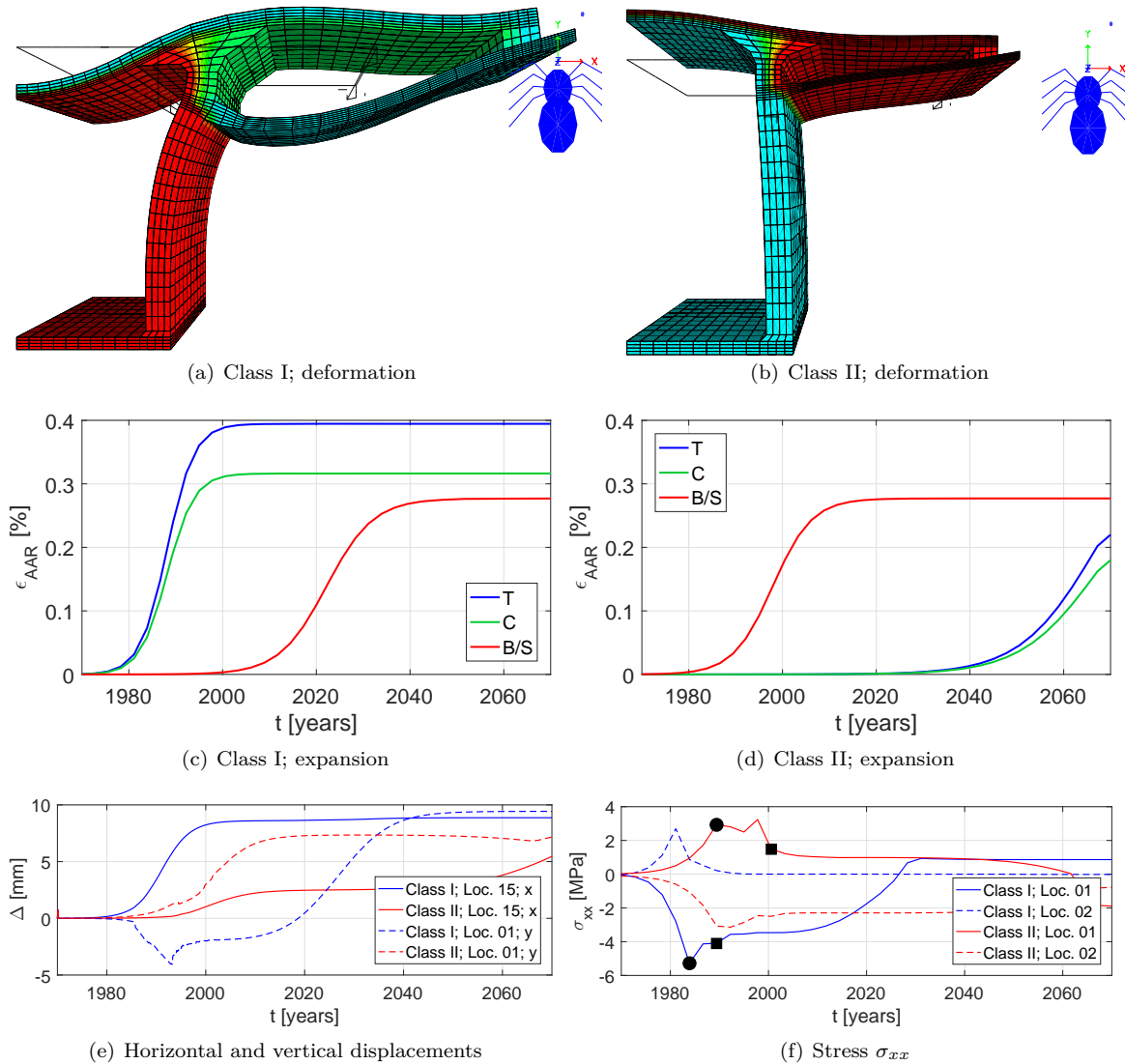
Figure 15.11: Identification of two distinct structural responses attributed to delayed AAR expansion

in Class II. The displacements of the deck center lice (Loc01) and edgs (Loc15) in the y and x directions
further illustrate this response, Fig. 15.11(e). Time-wise, the vertical displacement of the deck center line
in class I moves downward for the first 25 year, and then with the stress release caused by cracking (Fig.
15.12(c)) it reverses and displaces upward.

The rebars (located at the bottom and across the deck) stresses, in class I yield entirely after about 30
years, Fig. 15.12(a). Again, locations are from the deck centerline. However, in class II, reinforcement only
partially yield in vicinity of the center line. This is confirmed by the high curvature in the center part of
the deck in Fig. 15.11(b). On the other hand, throughout most of the life span of the structure, the bottom
reinforcement stress away from the centerline is very small for Class II, Fig. 15.12(b). This finding is further
supported by the absence of cracking in the corresponding part in Fig. 15.12(c), where in addition the crack
initiation corresponds to discontinuity in stress diagram. In this figure the crack initiation and propagation
correspond to the solid circle and square points shown in stress time history curve, Fig. 15.11(f).

(a) Class I; rebar #4

(b) Class II; rebar #4

(c) Crack profile
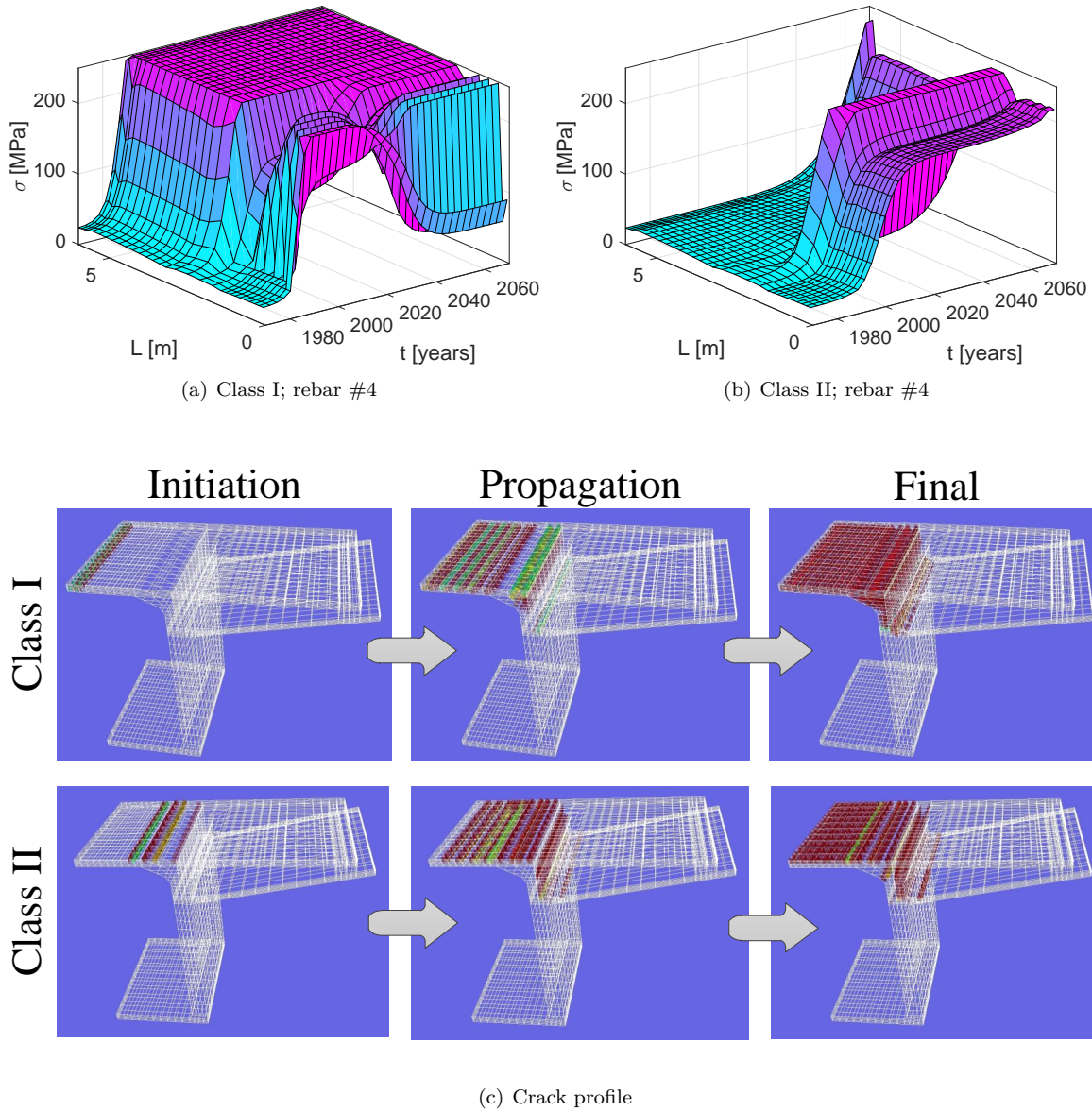
Figure 15.12: Rebar spatial and temporal stress distributions and cracking for two identified structural responses

15.8.2 Probabilistic Based Assessment

The initial batch of 121 simulations, yielded a set of 13 ($\sim$ 10%) nonlinear analyses which terminated prematurely due to lack of convergence. This was attributed a pathological combination of variables which stretched the capabilities of the models. Otherwise, CPU times ranged from 4 to 187 hours each, with a mean of 15.2 hours. Thus, the complete set of analyses required about 2 months computations on a Dell Precision Tower (dual Intel Xeon Processor E5-2687W, 3.5GHz Turbo, 32 GB RAM).

Following the earlier classification of analyses into two classes (I and II), 59 fell into the first and 49 into the second. Out of the 30 index points with identifiable results (Fig. 15.3), only three EDPs are reported (Fig. 15.13(a)): the lateral (x) displacement of the edge deck (Loc15), vertical displacement at the deck

(a) Horizontal displacement; Loc15

(b) Vertical displacement; Loc01

(c) σ_{xx} stresses; Loc01
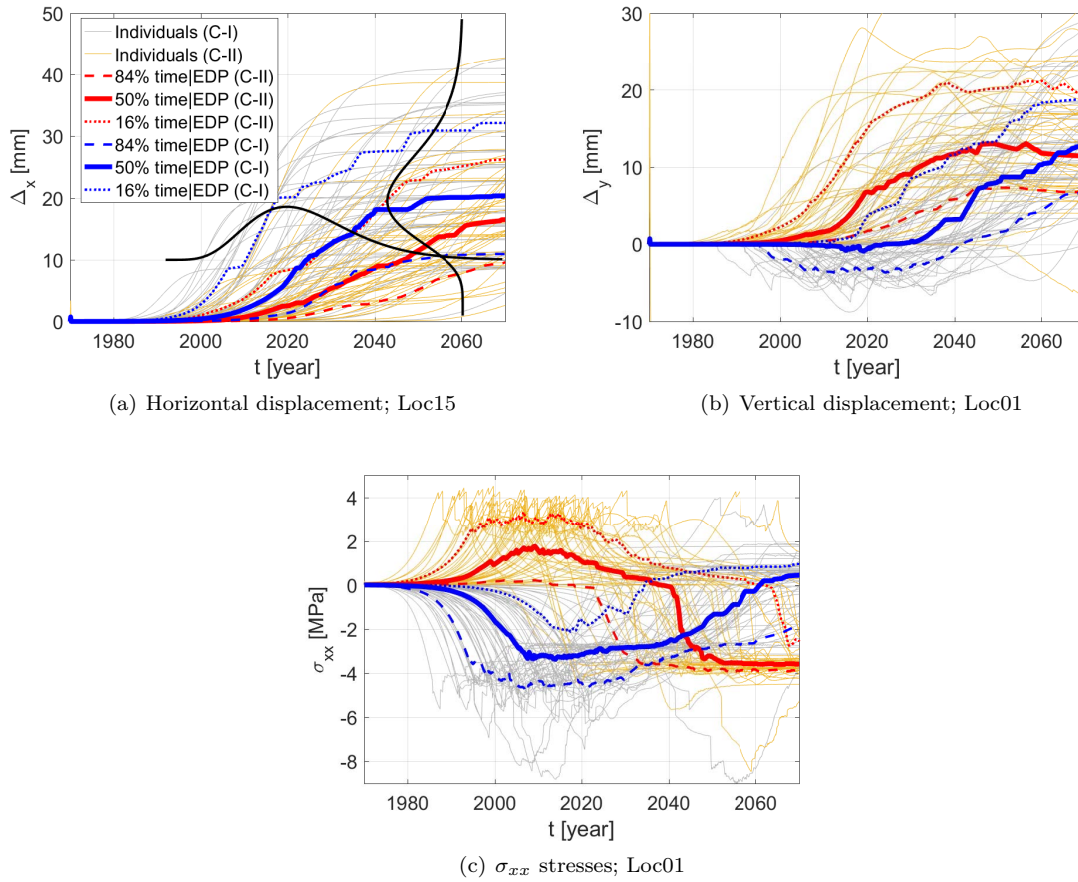
Figure 15.13: Individual probabilistic-based simulations and the 16, 50 and 84% fractiles

center line (Loc01), and the corresponding σ_{xx} stress. The maximum anticipated horizontal and vertical
displacements are 43 and 30 mm, and remain relatively small compared to the dimensions of the voussoir.
The corresponding median, 16th and 84th fractiles for each set of curves is shown as well. Again, consistent
with previous observations, the vertical displacements are higher for Class II, while they have lower lateral
displacements, and lower for the lateral one. Finally, the stress reversal for class II is worth noting. In all
cases, the maximum tensile stress is capped by the $\simeq$ 4 MPa tensile strength specified. On the hand, the
compressive stresses are nearly negligible compared with the compressive strength of 67 MPa.

15.9   Risk Informed Conditional Assessment

This probabilistic based analysis of a major infrastructure suffering from AAR can now serve as a vehicle to
finally define the risk informed conditional assessment (RICA) of similar structure. Though this paradigm
is not entirely new, Ellingwood, 2005 it has seldom been used in the context of evaluation of structures
suffering from AAR. First a few terms, commonly used in earthquake engineering will be introduced.

Stressor, S can be: 1) an incrementally-increasing, cyclic or time-dependent load (or displacement,
acceleration, pressure); 2) an incrementally-decreasing resistance parameter or degradation of strength prop-
erties. In earthquake engineering, S is typically called an IM parameter. In the present paper however,

S is time. It is the increase in time (in accordance with the second law of thermodynamic) that causes aging/deterioration of the concrete.

Response, R As the name implies is merely the response of a structure to a stressor S. R may be either scalar or vectorial (single or multiple) damage variable (DV), such as drift or displacement. A limit state (LS) may be assigned to a DV and thus define a damage index (DI); for example a stress (DV) should not exceed the strength (LS) according to a simple strength based DI. In earthquake engineering, R is often referred as an EDP.

Capacity Function is the relationship between S and R.

Fragility Function is a continuous function showing the probability of exceedance of a certain LS for specific level of IM. This important concept was first introduced by Kennedy et al. (1980) and is mathematically expressed as

$$\text{Fragility} = P\left[\text{LS}|\text{IM} = im\right] \tag{15.1}$$

where $P\left[A|B\right]$ is the conditional probability that A occurs given that B is equal to a particular im.

Fig. 15.14(a) illustrates this concept typically used in earthquake engineering: What is the probability of a LS exceeding a certain value in terms of the seismic excitation, and what would be the corresponding level of damages. Similarly, for structures affected by AAR, Fig. 15.14(b) would be a corollary that gives the probability of a volumetric expansion exceeding a value in terms of time.

(a) Earthquake   (b) AAR
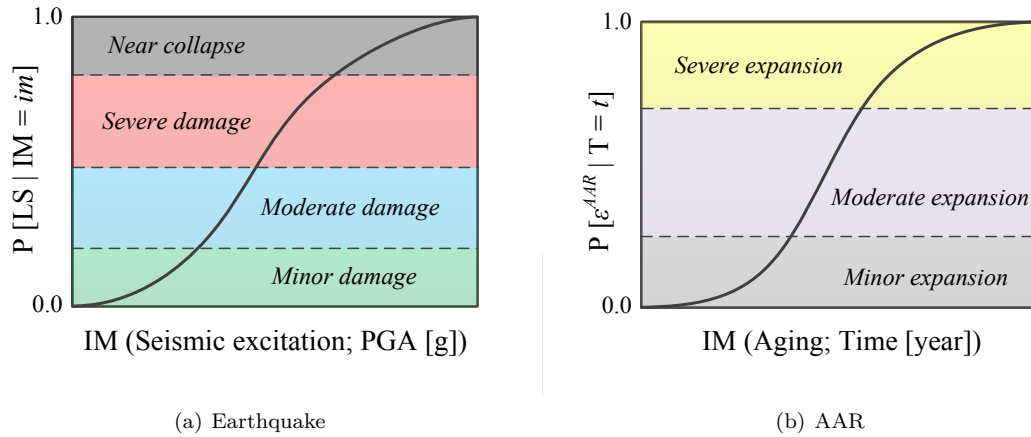
Figure 15.14: Fragility curves

Following this brief introductory remarks, attention is returned to the problem previously analyzed. The DV is considered to be the vertical displacement (Fig. 15.13(a)) and a LS of 50 mm is assumed based on ASCE? Ref. (that is should the vertical displacement exceed 50 mm, then the structure is considered to have locally failed). Then, per Fig. 15.10, the temporal distribution of the DI is shown in Fig. 15.15(a) where 6 points are identified: the intersection of the 16th, median, and 84th fractiles with: A) a vertical line corresponding to the year 2040 and, B) a horizontal one corresponding to a DI=0.2 (or displacement of 10 mm).

Two conditional assessments are then extracted: 1) time|DI and 2) DI|time. The former is associated with the time needed for a given DI to occur (horizontal line), and the second with the likely of a given DI occurrence at a given time (vertical line), Table 15.4.

MERLIN AAR Problems

(a) 16, 50 and 86th Percentile temporal evolution of the DI

(b) PDF and CDF for the DI
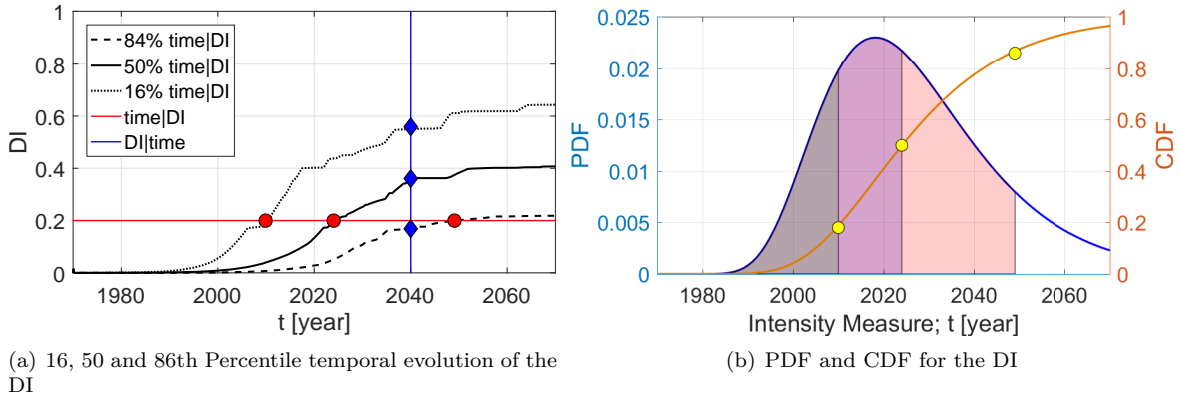
Figure 15.15: Engineering interpretation of results

Table 15.4: Central fractiles for the two conditional assessments of Class I case; number inside the paranthesis represents absolute date

Conditional Assessment	Central Fractiles		
	16th	50th	84th
time|DI [years]	40 (2010)	54 (2024)	79 (2049)
DI|time [-]	0.17	0.36	0.56

From three fractiles, one can estimate the mean μ and the log-normal standard deviation β, (Mood, Graybill, and Boes, 1974)

$$\mu_{\text{time}|DI} = \ln(\text{time}^{50\%}) \tag{15.2}$$

$$\beta_{\text{time}|DI} \approx \frac{1}{2}\left(\ln(\text{time}^{84\%}) - \ln(\text{time}^{16\%})\right) \tag{15.3}$$

which result in $\mu_{\text{time}|DI} = 3.99$ and $\beta_{\text{time}|DI} = 0.34$. From these values the lognormal probability density function (PDF) and corresponding cumulative distribution function (CDF) are determined, Fig. 15.15(b). This last curve, for all practical purposes is the fragility curve of the bridge assessed in terms of the DI of a potentially excessive displacement.

Similar curves could then be determined from other sets of quantities, and engineers could meaningfully and rationally answer such basic and important questions as: A) how long would it take for a certain degradation to occur? or B) what is the degradation likely to occur at a given time. This is the essence of RICA presented in this paper for AAR.

15.10   Conclusions

Borrowing from the earthquake engineering literature, this paper presented a new paradigm to scientifically assess the structural integrity of structures affected by AAR. It is clearly a more palpable approach to regulators than the deterministic ones that are too often reported, and is relatively simple to perform. Indeed, this was made possible by the increased computational power available, and our ability to perform meaningful Monte Carlo simulation with sufficient reliability.

Other results that emerged from this investigation is the importance of properly modeling the kinetics of the AAR in an incremental nonlinear analysis, and not limit oneself to simply applying the maximum

expansion. This analysis has highlighted the near impossibility to use intuition or "engineering judgment" to estimate the deformed shape (and thus location of stress concentration) given the idiosyncrasy of the complex model (nonuniform expansion, nonlinear time dependent analysis, complex geometry).

Chapter 16

P15: Sensitivity and Uncertainty Analysis of AAR Affected Shear Walls

16.1 Introduction

Increasingly engineers are confronted with the need to perform predictive structural assessment based on limited or incomplete data set. This may include damage up to failure assessment (in the context of so-called performance based engineering), or round robin benchmarks. As such deterministic analyses are of limited predictive values, and a stochastic analysis is warranted.

This paper focuses on the development of a methodology for such assessment, and is believed to be the first such contribution in the context of structural failure following alkali aggregate reaction (AAR) (or alkali silica reaction - ASR) induced expansion. As a vehicle for such an application, analysis of a previously tested concrete reinforced shear wall is performed.

In light of this potential problem which may affect numerous nuclear containment vessel structures (NCVS), various research projects were put in place. The Department of Energy (DOE) is sponsoring large scale mockup tests to assess the effect of confinement on AAR expansion (Le Pape, Y. and Ma, Z. and Cabage, J. and Lenarduzzi, R., 2014). The Nuclear Regulatory Commission (NRC) has entered into an inter-agency agreement with the National Institute of Science and Technology (NIST) to conduct a multi-million dollars research program on the structural performance of nuclear power plants (NPP) affected by AAR (NRC-NIST Project, 2014). NRC is also funding a grant and cooperative agreement with the University of Colorado to assess the effect of AAR on the shear strength deterioration, and for the integrity assessment of a NCVS suffering from AAR subjected to seismic loading (NRC-CU Grant, 2014). Furthermore, Nextera has funded a major research program at the University of Texas to assess the effect of AAR on the shear strength of concrete specimen (NextEra-ML121160422, 2012). Similar effort have been undertaken abroad. Most notably in Canada through funding from the Canadian Nuclear Safety Commission (CNSC) where shear wall affected by AAR have been tested (and whose analyses are reported below) (Orbovic et al., 2015). Finally, a major project on the same theme was recently initiated in France through support from the Institut de Radioprotection et de Sûreté Nucléaire (IRSN) (Marquié, 2016).

In terms of related numerical simulations, the authors have investigated the shear response of nuclear containment panels (Saouma et al., 2016), and thus this work constitutes a natural extension of past analyses combined with the separately developed methodology for probabilistic assessment (Hariri-Ardebili and

Saouma, 2016a,b).

Surprisingly, very few publications address the impact of AAR on the response of an engineering structure (i.e. not a laboratory specimen) through a finite element analysis. Most of the effort at the structural level seems to have been limited on the analyses of dams (**SaoumaPerottiShimpo2007**; **ComiFedelePerego2009**; Léger, Côte, and Tinawi, 1996; Pan et al., 2014; Sellier et al., 2009). Fewer publications address the impact of AAR on containment structures. Takatura et al. (2005) and Chénier et al. (2012) investigated containment structures affected by AAR in Japan and Canada respectively. Again there is a limited number of publications reporting the structural analysis of bridges (Hariri-Ardebili, 2018; Li and Coussy, 2002; Omikrine et al., 2016; Wojslaw and Wisniewski, 2014) or massive reinforced concrete structures (Saouma, V.E., 2014). However, many researchers have focused their attention to merely analyze laboratory tests such as (Multon, Seignol, and Toutlemonde, 2005). As to the nonlinear finite element analysis of reinforced concrete shear walls, there is a wide set of literature (**damoni2014numerical**; **massone2010strength**; **KoutromanosStavridisShingWillam2011**; **gattesco2015experimental**).

16.1.1   Objective

Through the auspices of the Organization for the Economic Cooperation and Development (OECD), a project for the Assessment of Structures subject to Concrete Pathologies (ASCET) was setup with one of its objectives being the organization of a blind simulation benchmark to predict the behavior of structural elements with AAR. The selected structure to be modeled was a reinforced concrete shear wall with AAR and subjected to reverse cyclic load. The wall had been tested at the University of Toronto (Habibi et al., 2015). Participants were given the opportunity to calibrate their models through the first phase (I) of the project where experimental data after eight months was made available, and asked to submit their numerical prediction for the wall responses (with and without AAR) after thirty months of swelling.

This paper will detail the advanced analysis performed, and focus will be placed on its main contribution: casting an AAR analysis (notoriously plagued by large uncertainties) within a probabilistic framework.

16.2   Test Description

The tested shear wall is shown in Figure 16.1, as well as the location of LVDTs (which measure the displacement between the bottom of the upper beam and the top of the lower beam). Detailed dimensions of the shear wall itself as well as two columns and two beams are illustrated in Figure 16.2. Reinforcement distribution is also shown in this figure. The 10M and 20M reinforcements have cross-sectional areas of 100 and 200 mm^2, yield stresses of 430 and 465 MPa, and elastic moduli of 182,000 and 190,000 MPa, respectively. In the experiment, a constant vertical force of 800 kN is applied through a 2″ thick steel plate, and the wall is subjected to a reverse cyclic pushover displacement (not to be confused with a seismic load). The bottom beam is anchored to the strong floor.

A total of three walls were cast, one without AAR (SW) and two others with AAR (SW-260 and SW-1000). The first two (one with and the other without AAR) were tested about 260 days (one of them was tested couple of days earlier) after casting, and the results made available for calibration. The third wall was tested about 1,000 days after casting and participants in the benchmark round robin were asked to make predictions. The reported mechanical properties for the concrete at 260 days are: 79.0/63.7 MPa for f'_c, 4.76/3.24 MPa for f'_t, 179.3/120.2 N/m for G_F, and 47,150/35,750 MPa for E.

Results of the tests are summarized in Figure 16.3. It should be noted that the peak loads with (SW-260)

(a) Full test set up
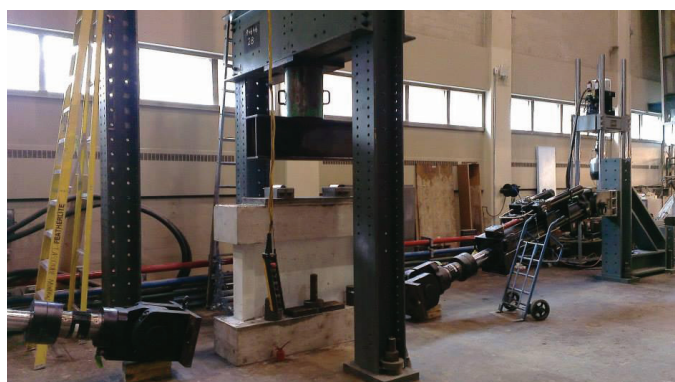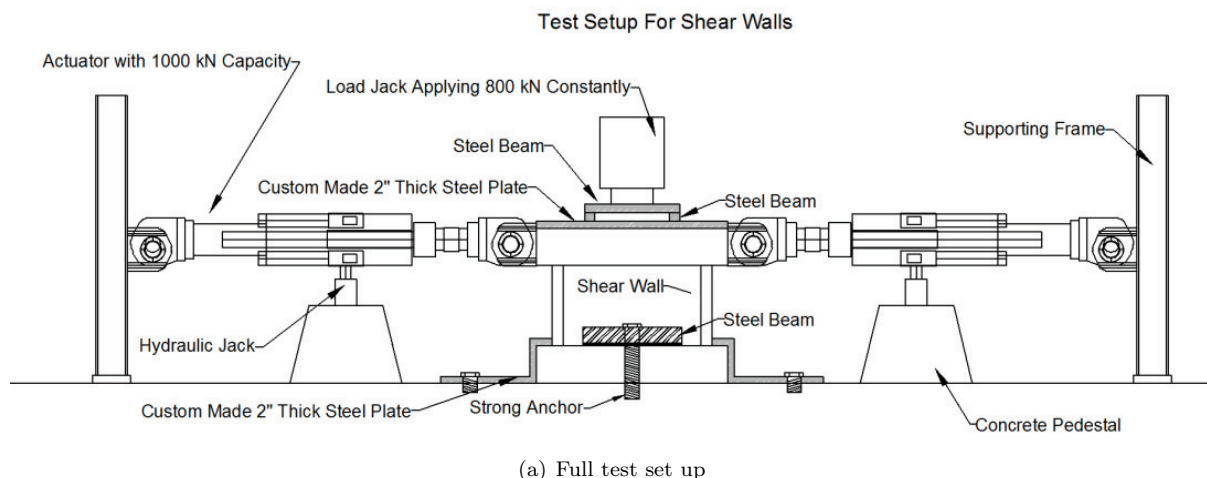
(b) Photo of shear wall inside the actuator
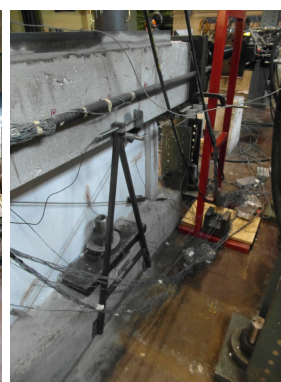
(c) Instrumentation; LVDT

Figure 16.1: Test setup for the shear wall (Habibi et al., 2015; Sheikh, 2017)

and without AAR (SW) expansion are 1,354 and 1,180, or 14% difference. This is a relatively small change, and given the uncertainties in measurement that difference may not be entirely attributed to the effect of expansion.

As no creep data was made available, and in light of the relative young age of the tested specimens, creep was ignored. On the other hand, based on simple "engineering judgment", it was apparent that potential bond loss at the juncture between column and base had to be addressed. This could be done by either wrapping joint elements (with hard to define characteristics) around the rebars at this location, or approximately by reducing the cross-sectional area of the steel at that location. This reduced cross-section will trigger large plastic deformation (akin of the ones induced by debonding) before the other segments yield.

16.3   Modeling Approach

In performing the numerical simulation of an experimental test, one must recognize that four possibilities are present:

1. An inconsequential analysis where results are simply to meet basic engineering common sense expectations.
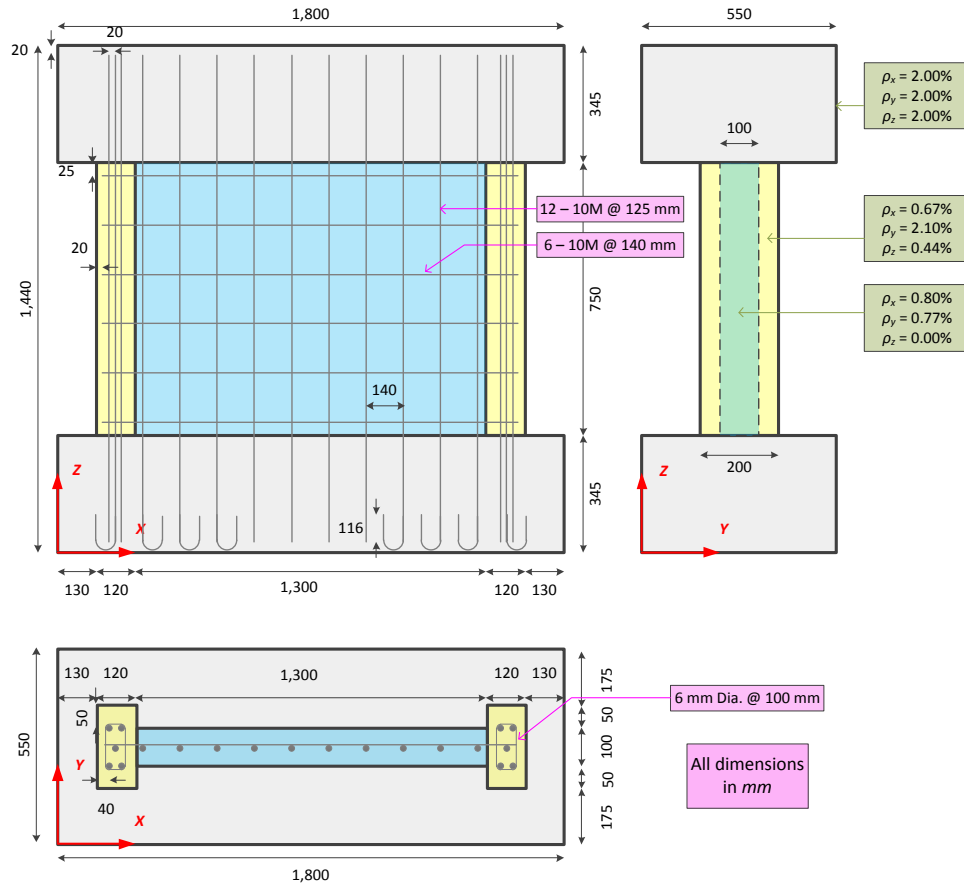
Figure 16.2: Dimensions of the shear wall, beams, columns and the reinforcement distribution
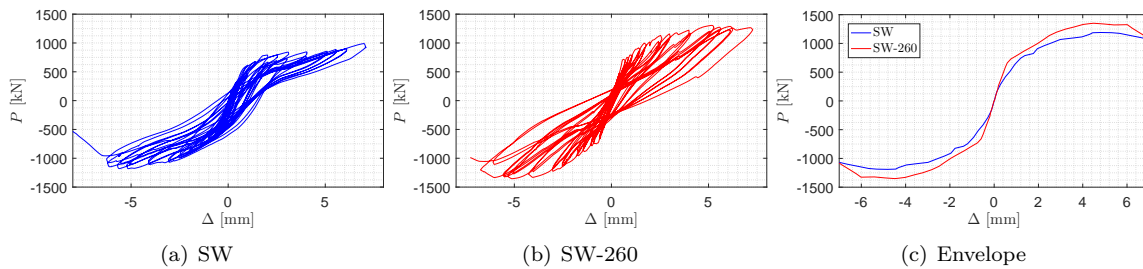
Figure 16.3: Force displacement results for the first set of walls after 8 months, adapted from (Habibi et al., 2015)

2. *Post-mortem* simulation where one has the luxury to fine-tune/calibrate a model until near exact results are obtained (which is nearly always possible, irrespective of the model accuracy).

3. Predictive analysis for the future response of a structure.

4. Blind simulation benchmark of an experimental test. However, it should be noted that there are two major sources of uncertainties:

   • Experimental: How accurately was the test performed?, how credible are the results?, are the reported results sufficiently clear and unambiguous?, and is it the model or the test that is being

checked?

- Numerical: Can one perform a single deterministic and predictive analysis, or wouldn't a probabilistic-based analysis be more appropriate given the epistemic nature of the uncertainties?

The current benchmark study does allow calibration (level 2 above) and requires prediction of known results (level 4). As to the two level of uncertainties (experimental and numerical), those are separately addressed below prior to the analyses results.

16.3.1 Uncertainties

Experimental: Though experimental uncertainties (accuracy and precision) are inherent in any test program, this benchmark exercise suffered from the additional pitfall of limited and incomplete data[1]. This made the exercise quite intractable problem, if it was to be handled in detail, and as a (partial) remedy a stochastic analysis is reported.

Epistemic: Simply put, epistemic uncertainties are those caused by an incomplete knowledge of the exact material properties (Der Kiureghian and Ditlevsen, 2009).

16.3.2 Study Objectives

Given that a nonlinear constitutive model for concrete contains numerous variables, most of which not provided or even measurable, a two prone approach should be followed:

Sensitivity Analysis: To determine which of the many random variables in the shear wall model are most sensitive.

Uncertainty Analysis: After selection of the most sensitive random variables, perform a Monte Carlo Simulation to provide a probabilistic estimate of the prediction.

This approach was recently followed by the authors for the analysis of a major bridge suffering from AAR (Hariri-Ardebili, 2018).

16.4 Data Preparation

The analysis hinges on two constitutive models: one for the concrete nonlinearity (a fracture-plasticity smeared crack model) (Cervenka and Papanikolaou, 2008), and the other for the AAR (Saouma, V.E., 2014). Both have been implemented in the authors finite element code Merlin (**merlin**), and most importantly validated in accordance with the RILEM TC 259 report (Saouma et al., 2017).

16.4.1 Concrete Smeared Crack Model

The concrete constitutive model was a fracture plasticity model (Cervenka and Papanikolaou, 2008) implemented as a so-called smeared crack model. As most constitutive models, this one has a number of parameters and not all can be directly measured experimentally. Hence, some are assigned values based on other calibrations or experience. This will invariably lead to uncertainties, and as such can be treated as random variables. Table 16.1 lists the 12 identified variables including: a) mean values, b) authors best estimates for the coefficients of variation, c) lower and upper bonds for uncertainty quantification, and d)

---

[1]During the ensuing meeting, it was evident that boundary conditions assigned lead to many differing assumptions, and only one set of load displacement was given to participants

minimum-maximum ones for the sensitivity analysis. The fourth and fifth columns show the activation or
deactivation of the variables in sensitivity and uncertainty analyses (1: active, 0: de-active).

Table 16.1: Material parameters used in numerical simulations

Characteristics	Symbol	Unit	SA	UQ	Mean	COV_{UQ}	$[LB, UB]_{UQ}$	$[min, max]_{SA}$
					Smeared crack model			
Mass density	ρ	Gg/m^3	0	0	0.00244	-	-	-
Thermal expansion coefficient	α	$1/{}^oC$	0	0	9.9e-6	-	-	-
Modulus of elasticity*	E	MPa	1	1	47,150	0.2	[28,290 66,010]	[23,575 70,725]
Poisson's ratio	ν	-	0	0	0.2	-	-	-
Tensile strength*	f_t	MPa	1	1	4.76	0.2	[2.86, 6.66]	[2.38, 7.14]
Exponential softening*	G_F	MN/m	1	1	1.79e-4	0.2	[1.08e-4, 2.51e-4]	[8.95e-5, 2.68e-4]
Compressive strength*	f_c	MPa	1	1	-79.0	0.2	[-110.6, -47.4]	[-118.5, -39.5]
Compressive critical displacement	w_d	m	1	0	-5e-4	-	-	[-7.5e-4, -2.5e-4]
Factor for return direction	β	-	1	0	0.50	-	-	[0.25, 1.0]
Factor for roundness of failure surface	e	-	1	0	0.55	-	-	[0.5, 1.0]
Onset of nonlinearity in compression	f_{c0}	MPa	1	0	-20	-	-	[-30, -10]
Plastic strain at compressive strength	ϵ_{cp}	-	1	0	-1e-3	-	-	[-2e-3, -5e-4]
					Reinforcement			
Yield stress of main rebar (vertical and horizontal)	f_y^R	MPa	1	0	430	-	-	[215, 645]
Yield stress of main stirrups	f_y^S	MPa	1	0	430	-	-	[215, 645]
Yield stress of crossing rebar	f_y^{R-Cr}	MPa	1	0	430	-	-	[215, 645]
Modulus of elasticity of crossing rebar	E^{R-Cr}	MPa	1	0	182,000	-	-	[91000, 273000]
Cross sectional area of crossing rebar	A_r^{R-Cr}	m^2	1	1	8e-5	0.2	[4.8e-5, 1e-4]	[6e-5, 1e-4]

* Reported values from experiments; SA: sensitivity analysis; UQ: uncertainty quantification; LB: lower bound; UB: upper
bound

In all analyses, random variables are assumed to have a normal distributional model (though a log-normal
may have been more suited for some variables) with mean and coefficients of variations (COV) shown in the
table. However, those values were subsequently adjusted since the distribution was truncated, Figure 16.4.
One should note that the normal distribution has maximum entropy over the real numbers with a specified
variance, i.e., a particular moment (Hariri-Ardebili and Pourkamali-Anaraki, 2018). It should be emphasized
that reported values are the authors best estimates in the context of this proposed analysis, and what some
may perceive as incorrect values should not detract attention from the objective of this study. Furthermore,
the range for the sensitivity analysis is different from the one for uncertainty quantification. In the former
it is set to 50% of the mean (unless it is constrained by the constitutive model), this choice is dictated by
a need to accentuate impact of RVs on the Tornado Diagram. In the second it is fixed to 20% of the mean
value in all random variables.

16.4.2   Reinforcement and Bond-Slip

The material properties for the reinforcement (either in web and columns or in the beams) were shown in
Section 16.2. Though reinforcement properties exhibit little if any epistemic uncertainty, the approach taken
was to reduce the area of the reinforcement crossing the beam-column (or beam-web) intersection to account
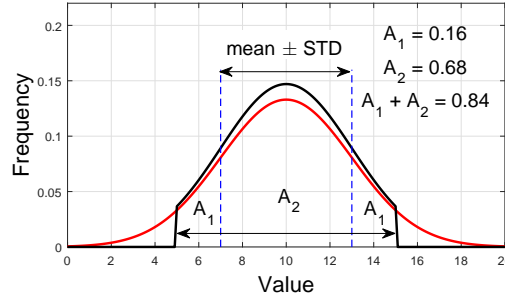
Figure 16.4: Truncation of normal distribution model and bounds

for possible bond-slip. As such, the cross-sectional area was arbitrarily reduced by 20% and treated as the only steel random variable in the uncertainty quantification.

16.4.3   AAR Expansion

16.4.3.1   Model

Proper modeling of the AAR expansion is of paramount importance to this study, and as such has received great scrutiny. The adopted AAR model is described in **??**, where the kinetics of the expansion is given by Eq. **??** and 1.2, while the degradation in Eq. **??**. Those two equations define what will be the variables associated withe the uncertainty quantification (they were not considered in the sensitivity analysis):

τ_L	Latency time, Eq. **??** and 1.2
τ_C	Characteristic time, Eq. **??** and 1.2
ε^∞	Maximum AAR expansion, Eq. **??**
U_L	Activation energy of the latency time, Eq. 1.2
U_C	Activation energy of the characteristic time, Eq. 1.2
β_E	Residual elastic modulus at the end of the reaction, Eq. **??**
β_{ft}	Residual tensile strength at the end of the reaction, Eq. **??**

Warning: It should be emphasized that whereas in this exercise the entire wall will be assigned the same expansion as the one observed from laboratory specimens, this is not exactly valid. There is ample evidence in the literature that actual structural expansions are (in most cases) much lower than those determined from laboratory prisms (due to different ambient conditions and ensuing leaching). This issue has been partially addressed by Fournier et al. (2009), Ideker et al. (2012), Leemann and Merz (2013), and Lindgård et al. (2010, 2012). Furthermore, and despite the (relatively) small size of the walls, material heterogeneity would imply that one can not *strictu sensus* apply the same AAR property throughout the wall without an attempt to use some homogenization techniques in the spirit of (Xu and Graham-Brady, 2005). Those two problems were not addressed in the reported analysis, as the added complication could have hampered the primary focus of this contribution: applicability of a stochastic approach for AAR modeling.

16.4.3.2   Parameter Identification

Data for expansion over the first 260 days was available (from experiment), as well as the corresponding degraded tensile strength and elastic modulus (See Section 16.2).

MERLIN AAR Problems

t = 260 days: In Figure 16.5, the reported expansions for SW and SW-260 (longitudinal and transverse) in Orbovic et al. (2015) are shown. The indicated points, while not exactly matching the ones reported by experiment; however, they are sufficiently close to be retained.
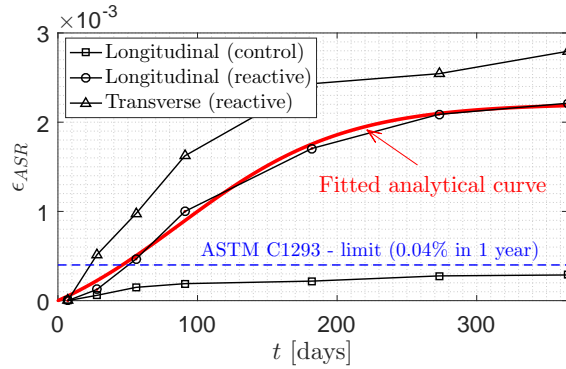
Figure 16.5: Reported expansion from (Orbovic et al., 2015) and corresponding fitted analytical curve

A simple Matlab code was developed to fit a curve (based on Eq. 1.1) to the reported experimental time-expansion values. As a result, the following parameters were obtained: $\tau_c = 81$ days, $\tau_l = 61$ days, and $\varepsilon^\infty = 0.00223$ (0.22%). It should be noted that the concrete expansion at 260 days is relatively small.

t = 1000 days: Determination of the AAR key parameters at 1,000 days is more problematic and values will be extrapolated from the current one with a margin of uncertainty. With reference to Figure 16.6(a), expansion up to ~ 250 days is known, and we need to guesstimate the one at time $t = 1,000$ days.

> **Kinetics:** It was assumed that the expansion at that time will obey a uniform distributional model ranging from a minimum 0.25% and a maximum of 0.45%. Then, using a Latin Hypercube sampling (LHS) technique, 100 curves are fitted between those points. The corresponding 100 values of τ_l and τ_c are shown in Figure 16.6(b) where the zero values of τ_l are associated with those expansion with a quasi-linear early expansion.

(a) Expansion curve

(b) Predicted τ values
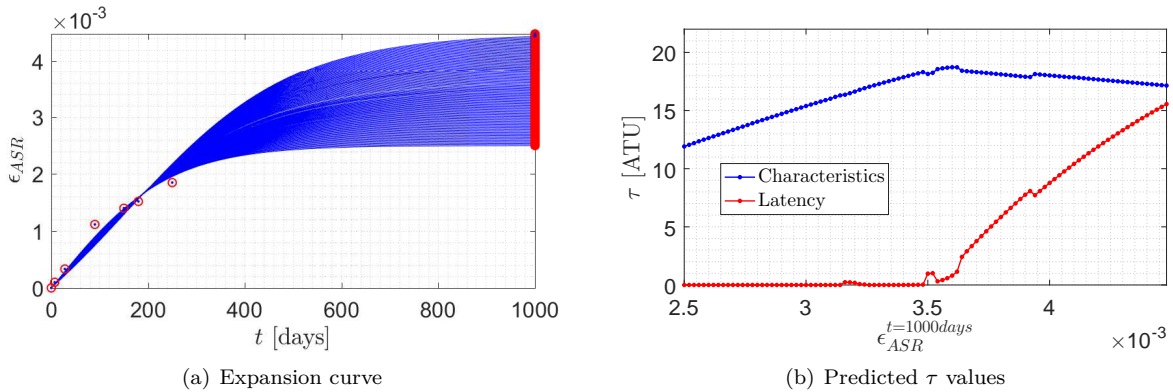
Figure 16.6: Optimization-based curve fitting to find the future expansion

> **Deterioration:** E and f'_t at time t_0 and t_{260} are given. Using these values a normal distribution model is assumed with the reported values as mean, and a COV reported in Table 16.1. Then,

MERLIN AAR Problems

based on Eq. **??** and the set of 100 values of τ_l and τ_c, degradation curves are obtained, Figure
16.7.

(a) f'_t (b) E
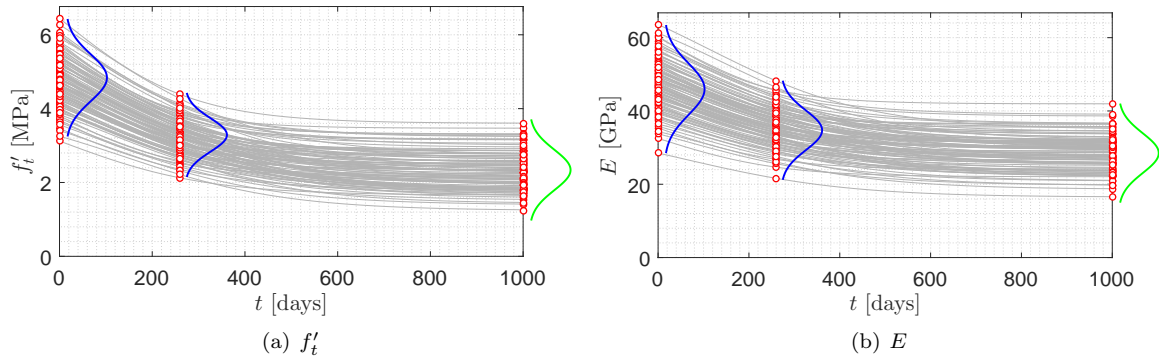
Figure 16.7: Estimation of residual coefficients

16.5   Finite Element Model

The prepared finite element mesh, shown in Figures 16.8(a) and 16.8(b), consists of quadrilateral elements.
There are three layers of elements in the web and five layers in the columns. Top and bottom beams are
assumed to be linear elastic while the columns and web have the smeared crack model parameters. Over all,
there are 1,240 solid elements in the model. All the elements in the web and the columns are cubic, while
those in the beams do not have a regular pattern. This is due selection of optimal mesh size in the beam
(larger elements than the web and column) and does not affect the results since the beam is linear elastic.

   The bottom beam is fixed at the base and the sides. The incremental displacement is applied on the left
side of the top beam. Moreover, there is a traction on the upper face of top beam, Figure 16.8(c). Note
that the applied boundary conditions are based on our understanding of the tests. As later found, the base
beam may allow the slippage with respect to the support (i.e. strong floor), and hence the adopted model for
numerical simulation is too rigid. The reported cyclic load is identical to the one shown in Figure 16.8(d).
Each load cyclic is applied though 10 increments.

16.6   Results

Results will be presented as follows:

1. Deterministic analysis of SW and SW-260, followed by calibration.
2. Sensitivity analysis of SW.
3. Uncertainty quantification of SW and SW-1000 along with probability of non-exceedance of a specific
   shear wall capacity.

16.6.1   Deterministic Analysis and Calibration

In this first set of analyses, the meshes shown in Figure 16.8 and mean values from Table 16.1 are used for
the SW and SW-260. The preliminary envelope for SW was obtained (not shown here) and it is evident
that the numerical response is too stiff, and an adjustment has to be made. In light of the experimental

(a) Finite element mesh   (b) Reinforcement   (c) Boundary conditions

(d) Reversed cyclic loading and increments
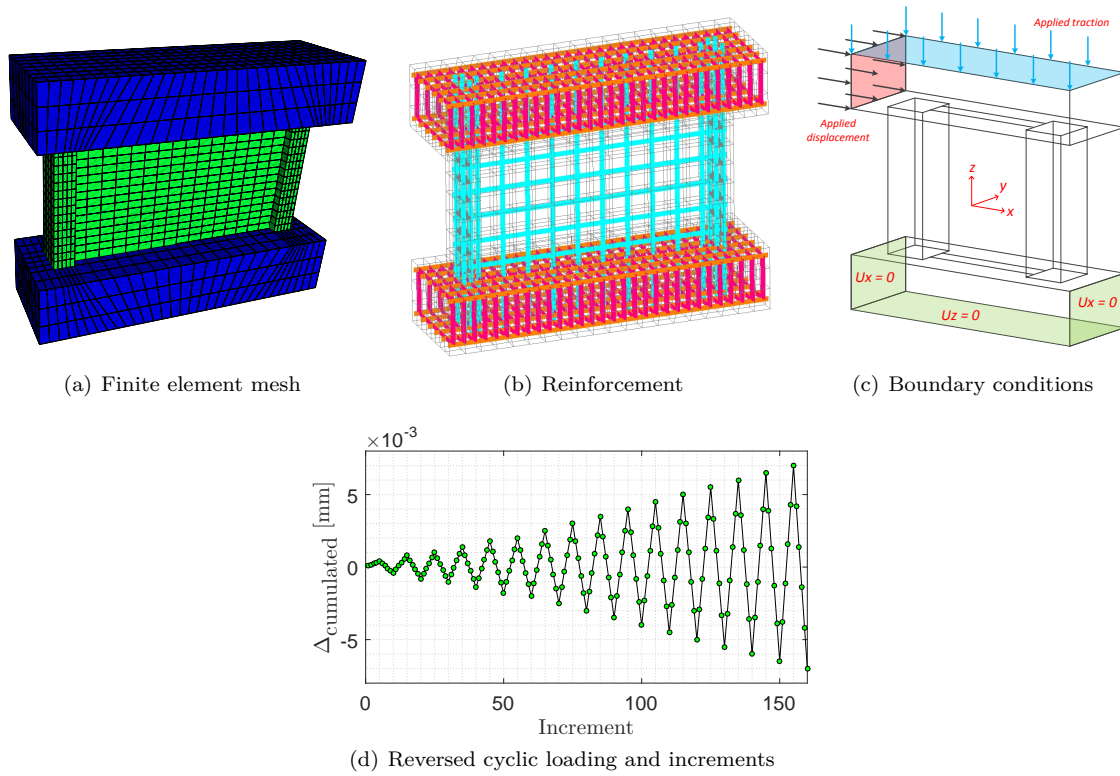
Figure 16.8: Finite element model, boundary condition and loading

uncertainties addressed in Section 16.3.1 and the assumed rigid supports, this discrepancy is attributed to
"slack" in the system and an adjustment is to be made. Thus, and in the spirit of this benchmark where
calibration is indeed expected first, the displacements were simply multiplied by 2.3 resulting in a shift of the
results which closely matched the experimental results. Indeed, the final report of the Benchmark workshop
concluded (among other things), (Nevander and Orbovic, 2017) that

> *The wall measurements were not sufficiently documented. A single measurement of the displace-*
> *ment of the upper beam is not enough to calibrate numerical models. Simulated displacements are*
> *lower than measured displacements in all simulations and based on numerical simulations, the*
> *wall boundary conditions have more important impact on wall displacements than the constitutive*
> *laws.*

Hence, from this point onward, all numerical results will be subjected to this calibration factor. Then,
the results of SW-260 were compared, Figure 16.12 and again, the two curves are nearly identical. For
illustrative purpose, the deformed shape with maximum principal stresses are shown in Figure 16.9(a), and
the evolution of the accompanying (smeared) cracks is finally shown in Figure 16.9(c). As seen, the regions
with high principal stresses correlate well with the computed failure path; both are in good agreement with
the observed failure mode from the test. Visual inspection of these plots provides a graphical confirmation
of the reliability of the analysis.

(a) Deformed shapes; Contour shows the maximum principal strains   (b)   Observed   failure
(**jurcut2015modelling**)

(c) Crack propagation under reverse loading (first rightward, then leftward)
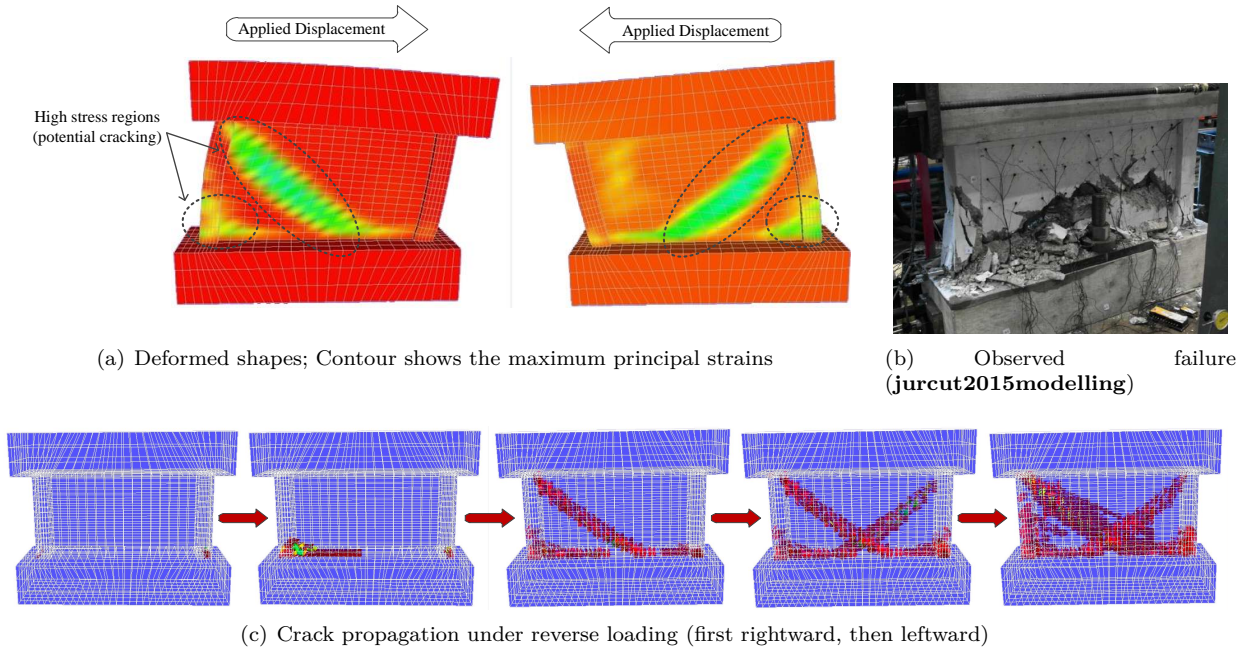
Figure 16.9: Structural response of shear wall under cyclic displacement (without ASR)

16.6.2   Sensitivity Analyses

The sensitivity analysis procedure is rooted in the Taylor's Series-Finite Difference Estimation described in
A.2. In the context of this analysis, $n = 15$ random variables identified in Table 16.1 are retained, thus a
total of $2n + 1 = 31$ analyses are performed. First the capacity curves (Hariri-Ardebili and Saouma, 2017)
of all the analyses are obtained, Figure 16.10(a). It is noted that the experimental curve does indeed fall
within the range of results, and that in some cases there is an early failure characterized by a sudden drop in
the post-peak load carrying curve (whereas some softening resulting from induced displacements would have
been expected). Then the sensitivities are sorted and results shown in the format of a so-called Tornado
diagram (Lee and Mosalam, 2006), Figure 16.10(b).

(a) Capacity curves   (b) Tornado diagram
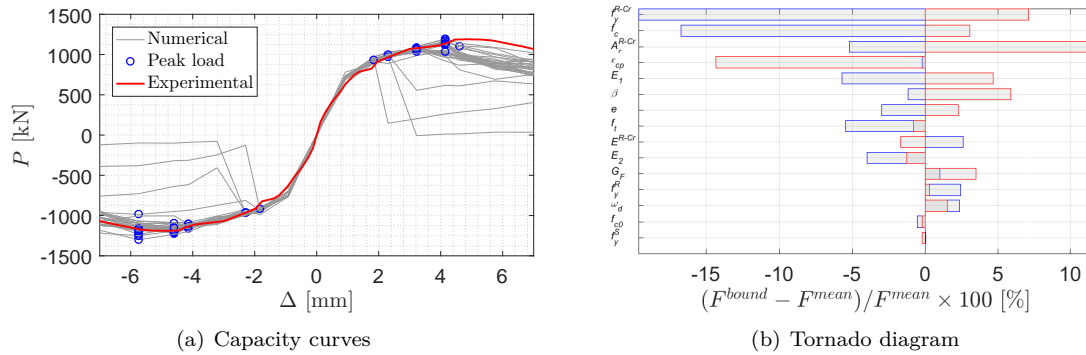
Figure 16.10: Results of sensitivity analysis on concrete constitutive model

From this figure, it was determined that the steel reinforcement whose crossing the beam-wall interface

plays a prominent role in the response through the yield stress and cross-sectional area. As to the concrete, the predominant variables affecting the shear wall carrying capacity are: the compressive strength, plastic strain at compressive failure, modulus of elasticity are amongst the major factors influencing the response. The least important variables are the yield stress of the stirrups and onset of concrete nonlinearity in compression, and concrete compressive critical displacement. Concrete tensile strength and fracture energy are among the intermediary sensitive variables.

It should be emphasized that though the Tornado diagram gives an indication of the response sensitivity to the variables, not all of them are actually random. For instance, the uncertainty in the steel material properties is smaller than that in concrete, and thus for simplicity and practical purposes, it is not treated as a random variable.

16.6.3   Uncertainty Quantification

Uncertainty quantification has retained the variables listed in Table 16.1 (column 5) as random with a normal distributional model. Selection of those are based on the Tornado diagram and engineering common sense. Since there is no solid information about the inter-correlation among the random variables, it is assumed that they are independent. This is one of the limitations of the study which may affect the dispersion of the results (Hariri-Ardebili and Saouma, 2016a).

16.6.3.1   Automation of Probabilistic Analysis

Given the complexity in data manipulation from input data definition, random variable selection, generation of finite element meshes, execution, data mining to extract results, and plotting key diagrams an automated procedure was set up. This was accomplished through a Matlab (**Matlab2016**) based set of sequential programs `P1.m`, `P2.m`, `P3.m`, `P4.m` and `P5.m` whose inter-connectivity is illustrated in Figure 16.11.
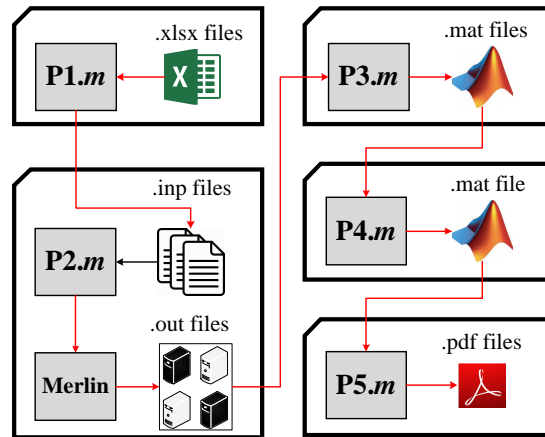
Figure 16.11: File generation and automation algorithm

`p1.m` reads the user specified variables, probability distribution models, ranges, and correlation coefficients, and then generates N_{sim} (in this study 100) input files. Those in turn are executed through `p2.m` which calls the finite element code Merlin. Next, the results are individually extracted from 100 output files and stored as binary files using `p3.m`. Results are further consolidated into a single data-base using `p4.m`. Finally, `p5.m` extracts the results from the database and generates the desired plots. For each output

parameter, results are plotted along with their mean, 16% and 84% fractiles ranges (which correspond to minus and plus one standard deviation in a log-normal distributional model).

16.6.3.2 Prediction

Following completion of the 100 analyses (it should be noted that five analyses did not converge most likely due to an unfavorable set of AAR material parameters), P5.m generated the capacity curves for SW. Then, the 16% and 84% fractile curves are sought. This is simply achieved by sweeping through the full range of displacements, and for each one identify the points below which 16% and 84% of the load fall. The capacity curves for SW, Figure 16.12, is in close agreement with the experimental data. However, contrarily to the first sensitivity analysis, the uncertainty one shows that the experimental tests fall within the 16% and 84% fractiles. Finally, we reach the objective of this study which is to provide a probabilistic-based assessment of the shear wall capacity when tested 1,000 days after casting. This will be shown later in Section 16.6.4.
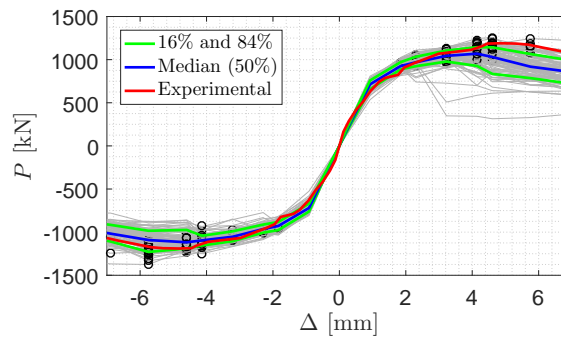
Figure 16.12: Results of uncertainty quantification on capacity curves in SW-260

Results warrant additional examination to fully grasp the structural responses. As such, Figure 16.13(a) plots the shear wall capacity for SW and SW-1000 along with the corresponding histograms and probability distribution function. Figure 16.13(b) shows the cumulative distribution functions (CDF) for empirical (dashed lines) and fitted (continuous lines based on log-normal assumption) for both SW and SW-1000. Mean and logarithmic standard deviation are 1.14 MN and 0.090 MN for SW, and 1.13 MN and 0.11 MN for SW-1000 respectively. It should be noted that there is higher standard deviation in SW-1000 as there are more RVs. Moreover, note that in ∼ 60% of the analyses, the shear capacity was reduced by the pre-existence of AAR, and in ∼ 40% it increased. Finally, the point in which the CDF rotates from SW to SW-1000 is located at probability of 0.65.

Last by not least, a similar scheme where AAR may increase or reduce the shear strength capacity was observed by the authors in a separate study (Saouma et al., 2016), shown in Figure 16.14. The monotonic shear strength of a panel was numerically determined with and without initial AAR expansion. In both cases, the initial stiffness was reduced by AAR.

Regretfully, it was not possible to clearly identify the set of parameters which cause an increase (or decrease) in shear strength capacity due to previous AAR. It is speculated that the increased in strength is associated with a particularly unfavorable combination of variables (not necessarily reflecting a likely physical scenario) randomly selected by the Latin Hypercube Simulation. However, this remains an open question of the utmost importance which requires further in depth study.

MERLIN AAR Problems

(a) Individual peak points and histograms   (b) Cummulative density function
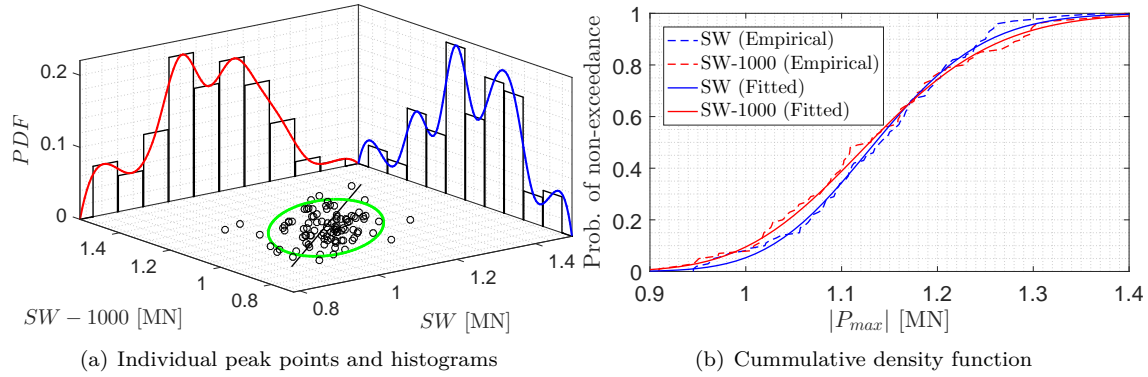
Figure 16.13: Comparison of SW and SW-1000 models

(a) Shear capacity reduction   (b) Shear capacity increase
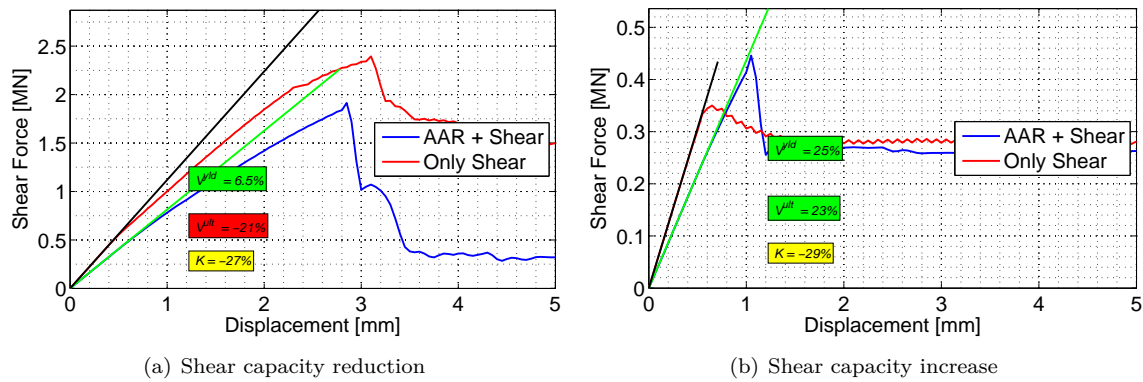
Figure 16.14: Impact of AAR on shear capacity of concrete panels from a NCVS (Saouma et al., 2016)

16.6.4   Comparison with Experimental Results

Following the submission of blind prediction, the organizers provided the results of the three tests (one at
260 days used for calibration by participants) and two others performed at 1,000 days (expansion to be
predicted). Whereas SW-260 includes all 15 cycles, SW-1000 does not report all of them. Hence, without
the benefit of all cycles, it is impossible to clearly and unequivocally compare force and displacement with
great accuracy. Finally, and most importantly the comparison between reported experimental results and
blind numerical prediction is plotted in Figure 16.15 which shows a good correlation between the prediction
and measurements. One of the experimental tests (B1) exhibits two sudden large cycles at the end which
can be associated with the global failure of the wall.

16.7   Conclusions

Originally motivated by a participation in a Round-Robin predictive study of the load carrying capacity
of a shear wall affected by AAR, the authors have broadened their analysis into a stochastic one. The
viability of a two pronged approach to the prediction of an AAR affected complex structure was proven.
The combination of a sensitivity analysis followed by uncertainty quantification, proved to be ideal tools for
a stochastic analysis of a structure.

   In the narrower context of the shear wall, facilitated by the nearly identical expansions at 260 and 1,000

MERLIN AAR Problems
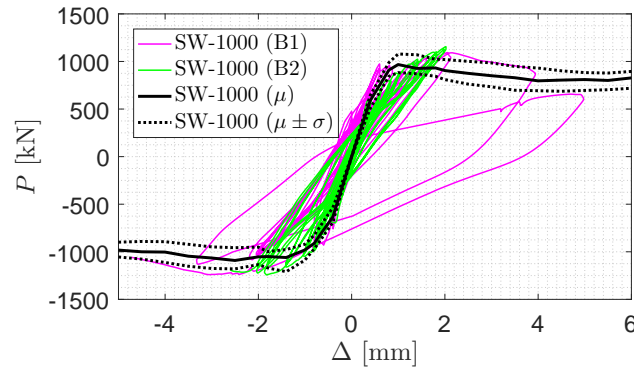
Figure 16.15: Comparison between blind numerical prediction (mean and $\pm$ standard deviation) and exper-
imental tests at 1,000 days (two tests) adapted from (Nevander and Orbovic, 2017)

days, good prediction was achieved. However, and this could only be highlighted from the multiple analyses
needed by the stochastic model, it was found that in some cases the AAR increased the shear resistance,
while in others it decreased it. Within the scope of this study, it was impossible to identify the combination
of variables leading to either one of the two cases.

Finally, though the shear wall analysis is only applicable to an internal structural element in a nuclear
power plant, conceptually it may elucidate better understanding of the response of the NCVS. As AAR
is unlikely to affect the structural integrity of the NCVS by itself, it is very likely to affect the shear
resistance under a seismic excitation. This interaction of AAR and seismic excitation, within the context of
a deterministic and stochastic analyses is the subject of development by the authors through a grant from
the NRC.

Chapter 17

P16: Dams

17.1 Arch Gravity Dam; Isola

This section reports on a highly detailed analysis of an arch gravity dam (see Figure 17.1) and is intended to serve as a reference for the steps required to perform a diagnosis of major infrastructure adversely affected by AAR. The data preparation for such an analysis may prove to be complex and will be reported first, followed by a discussion of results.

(a) Section   (b) Internal stresses
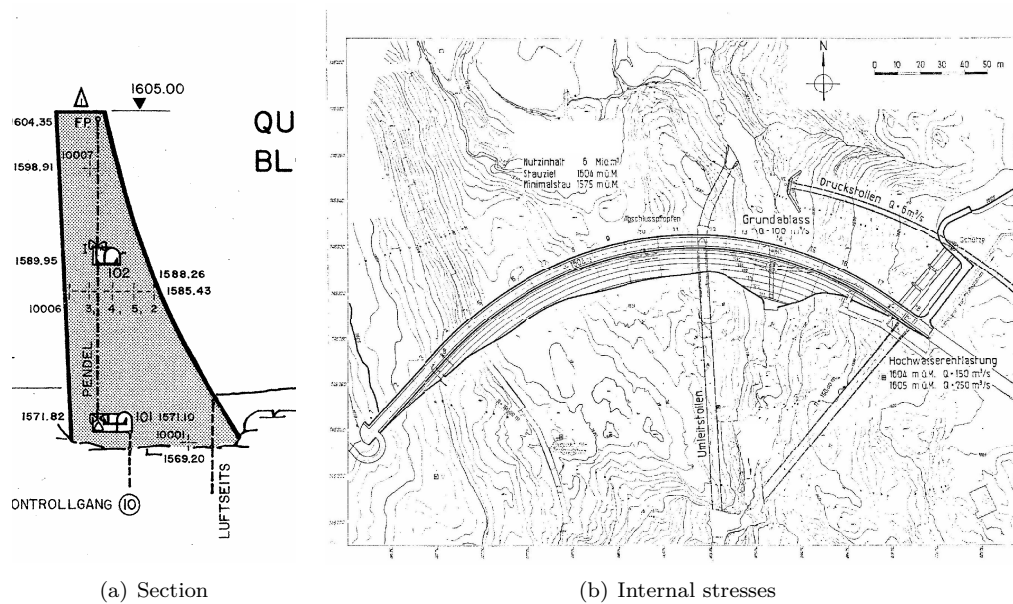
Figure 17.1: Arch gravity dam geometry

17.1.1 Data Preparation

The comprehensive incremental AAR analysis of a concrete dam is relatively complex, regardless of the selected AAR model, given that data preparation for the load can be as cumbersome as it is voluminous (see Figure 17.2(a)).

The seasonal pool elevation variation (for both the thermal and stress analyses) must first be identified (Figure 17.2(b)); moreover, the stress-free temperature, T_{ref} (typically either the grouting temperature or the average annual temperature) needs to be identified, along with the external temperature (Figure 17.2(d)). The pool elevation will affect the internal state of stress, which in turn will alter AAR expansion (through Eq. **??**, **??** and **??**). This situation is more relevant for high Alpine dams (where the annual pool variation is greater than for low-head, low-altitude dams). This variation will then be replicated over n years for the duration of the analysis (Figure 17.2(c)). External air and water temperatures will be considered next (Figure 17.2(d)). In the absence of precise field data, the air temperature may be obtained from NOAA (2013).

(a) Loads

(b) Pool elevation, 1 year

(c) Pool elevation, 30 years

(d) Water and air temperatures
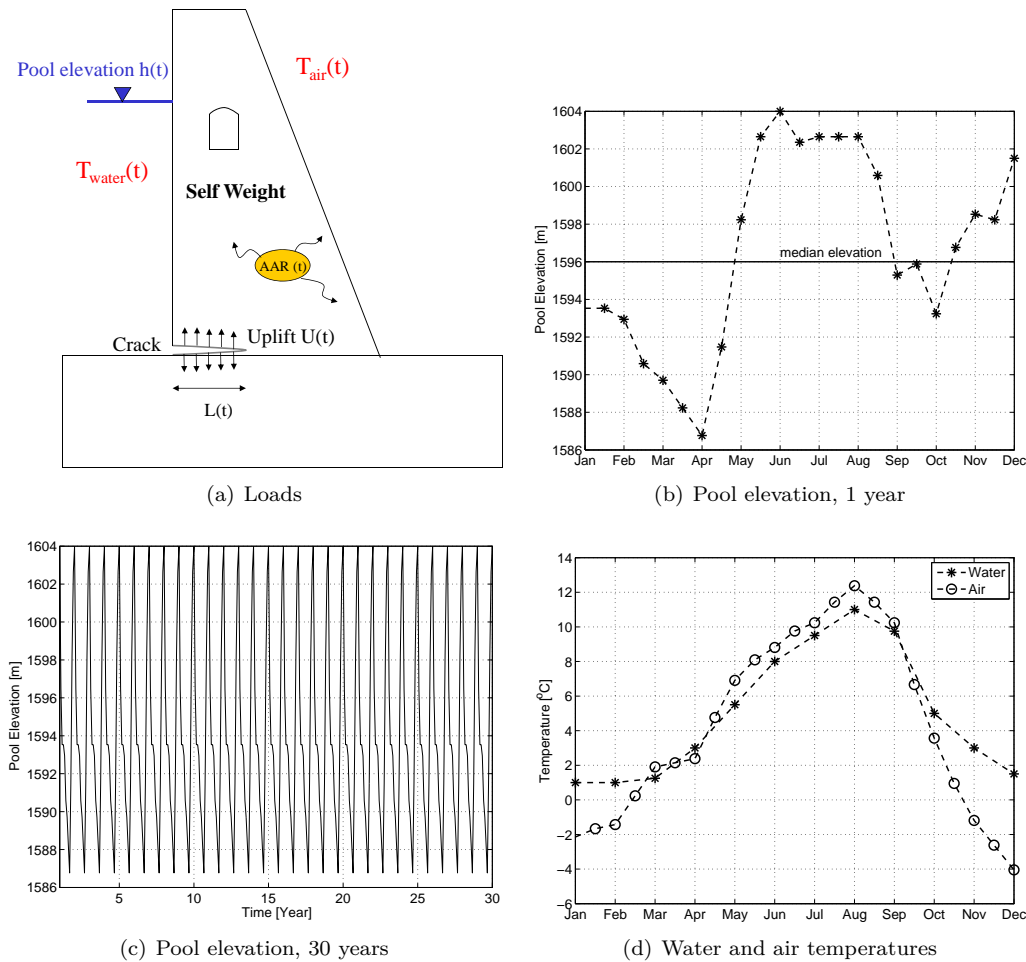
Figure 17.2: Preliminary load data to be collected for the AAR analysis of a dam

The units adopted are MN, Gg and ATU for F, M and T respectively. For time, the ATU (Analysis Time Unit) has been adopted, corresponding to 4.35 weeks or 30.42 days (i.e. 12 ATU span one year).

The next step calls for conducting a transient thermal analysis since the reaction is thermodynamically activated. Consequently, the total temperature is included as part of the constitutive model. Heat transfer by both conduction and convection are taken into account, whereas radiation is implicitly incorporated (Figure 17.3(a)).

The thermal analysis is conducted using the parameters listed in Table 17.1.

MERLIN AAR Problems

(a) Governing equations for the thermal analysis

(b) Thermal boundary conditions

(c) Upstream and downstream air temperatures with inclusion of radiation

(d) Preliminary transient analysis
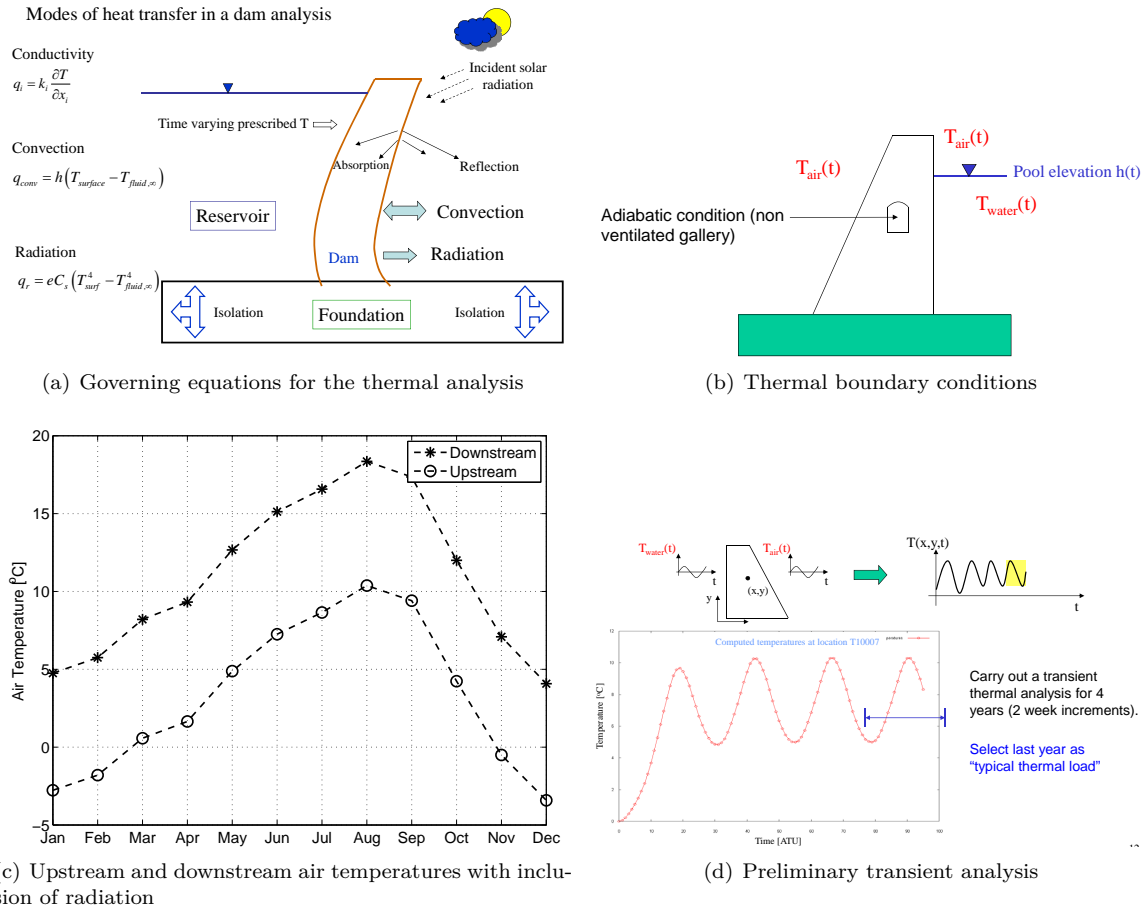
Figure 17.3: Data preparation for thermal analysis of a dam subjected to AAR

Reference temperature	T_{ref}	^{o}C	7.0
Conductivity	k	MN.m/(m.ATU.^{o}C)	7.738
Specific heat	c	MN.m/(Gg,^{o}C)	887
Density	r	Gg/m^3	2.510^{-3}

Table 17.1: Thermal properties found in an arch gravity dam

Radiation (Eq. **??**) is implicitly included by means of a simplified procedure, whereby ambient air temperature is modified (Malla and Wieland, 1999):

$$\begin{aligned} T_{us} &= 0.905 T_{air} - 0.4^o\text{C} \quad \text{Upstream} \\ T_{us} &= 0.937 T_{air} + 7.2^o\text{C} \quad \text{Downstream} \end{aligned} \tag{17.1}$$

resulting in the temperature distribution shown in Figure 17.3(c).

Even though the external boundary conditions can be readily determined, the condition associated with the gallery is of primary importance for potential internal cracking (Figure 17.3(b)). More specifically, it is important to know whether during construction the gallery is closed or open to the outside air. The precise thermal analysis should be performed in accordance with Figure 17.3(a).

Next, the transient thermal analysis is to be performed for at least 3-5 years, until the annual variation

MERLIN AAR Problems

appears to converge (Figure 17.3(d)). These analyses enable deriving, among other things, the spatial and temporal variations of temperature ($T(x, y, z, t)$).

The dam however must first be discretized. As is the case with most dams, a set of analytical parametric curves defining the arches (in general, circular segments in the US, while parabolic or elliptical segments elsewhere) is (typically) given. These curves are plotted in Figure 17.4(a).

(a) Mathematical model of the dam

(b) Dam and foundation outlines

(c) Full 3D mesh for initial load increments

(d) Simplified 3D mesh for AAR expansion
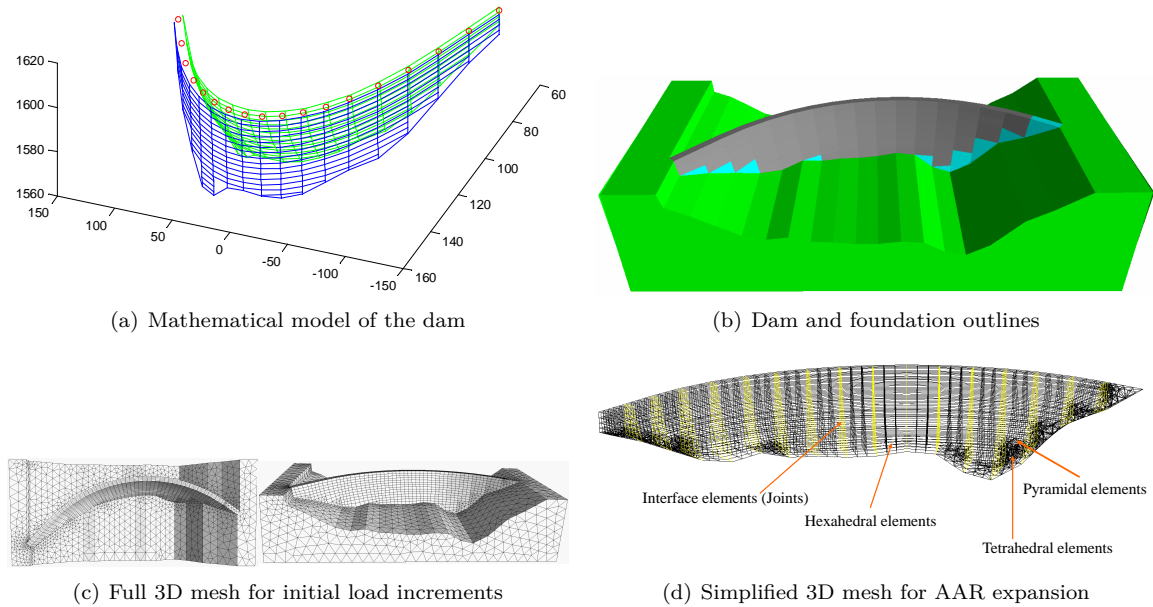
Figure 17.4: 3D Finite element mesh for the stress analysis

Using a special program (e.g. Beaver developed by the author), the surface can be discretized. The boundary representation of the dam is then entered into a preprocessor, such as Saouma (2009), in order to generate the finite element mesh. Figure 17.4(c) shows the resulting full 3D mesh used for the stress analysis. Joint elements are placed at both the joints and the rock-concrete interface (Figure 17.4(d)). Let's point out that a different mesh was required for the thermal analysis, since the interface elements needed to be removed.

As previously indicated, the time increment of one ATU corresponds to 4.35 weeks, and the initial reference temperature was set to zero. Given the external air temperature, both the pool elevation and water temperature boundary conditions were input into this initial boundary value problem. The analysis was performed using MERLIN (??), making it possible to examine the temperature fields. It was found that after four years, the temperature field was harmonic with a one-year frequency. At this point, the analysis was interrupted and $T_{thermal}(x, y, z, t)$ recorded. The computed temperature distribution is shown in Figure 17.5. Note that these temperatures are to be used to evaluate the thermal strains, given that for the AAR analysis the total (i.e. absolute) temperature is needed (as simply obtained by adding the reference temperature of 7^oC).

Subsequent to the thermal analysis, $T_{thermal}(x, y, t)$ must be transferred to $T_{stress}x, y, t$ since, in general, the same finite element mesh is not available (the foundations, joints and cracks are not typically modeled as part of the thermal analysis).

Lastly, a comprehensive input data file must be prepared for the stress analysis; this file includes:

1. Gravity load (first increment only).

MERLIN AAR Problems

(a) January-June

(b) July-December
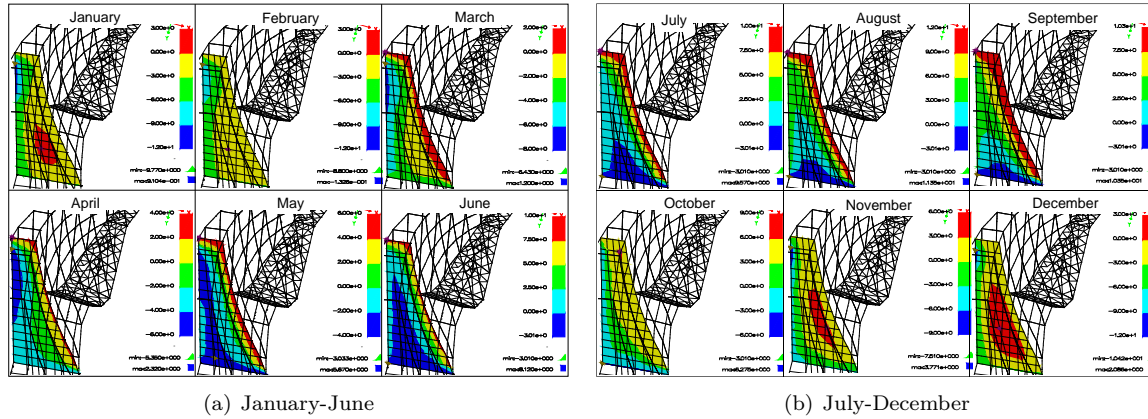
Figure 17.5: Computed internal temperature distribution variation

2. $\Delta\dot{T}(x,y,t) = \dot{T}_{stress}(x,y,t) - T_{ref}$ in an incremental format. This is a subtle step that must not be overlooked. The stress analysis is in fact based on the difference between the actual and stress-free temperatures. In addition, an incremental analysis requires this set of data to be provided in an incremental format.

3. Stress-free referenced temperature, which is to be added to the temperature data in order to determine the total absolute temperature needed for AAR.

4. Cantilever and dam/foundation joint characteristics. The former must be included in any arch dam, since expansion may lead to an upstream joint opening, while the latter must be taken into account given that AAR-induced swelling may result in a separation of the dam from the foundation in the central portion of the foundation.

5. Uplift load characteristics (typically matching the upstream hydrostatic load).

6. AAR data, which has been described above.

Moreover, the compiled set of data must be looped over at least 50 years in order to provide a complete and correct set of natural and essential boundary conditions (Figure 17.6).

		January		February		March		April		May		June	
Incr.		**6.00**	**7.00**	**7.00**	**8.00**	**9.00**	**10.00**	**11.00**	**12.00**	**13.00**	**14.00**	**15.00**	**16.00**
Body force		dam											
Hydrostatic	**Pool Elevation**	1596.47	1593.53	1593.53	1592.94	1590.59	1589.71	1588.24	1586.76	1591.47	1598.24	1602.65	1604.00
	Incremental Elevation	-5.03	-2.94	0.00	-0.59	-2.35	-0.88	-1.47	-1.47	4.71	6.76	4.41	1.35
Uplift	**Pool Elevation**	1596.47	1593.53	1593.53	1592.94	1590.59	1589.71	1588.24	1586.76	1591.47	1598.24	1602.65	1604.00
	Incremental Elevation	-5.03	-2.94	0.00	-0.59	-2.35	-0.88	-1.47	-1.47	4.71	6.76	4.41	1.35
Temperature [^{o}C]	**Air**	-3.10	-2.14	-1.67	-1.43	0.24	1.90	2.14	2.38	4.76	6.90	8.10	8.81
	Water	1.00	1.00	1.00	1.00	1.00	1.50	3.00	3.00	5.00	6.00	8.00	8.00

		July		August		September		October		November		December	
Incr.		**17.00**	**18.00**	**19.00**	**20.00**	**21.00**	**22.00**	**23.00**	**24.00**	**25.00**	**26.00**	**27.00**	**28.00**
Body force		dam											
Hydrostatic	**Pool Elevation**	1602.35	1602.65	1602.65	1602.65	1600.59	1595.29	1595.88	1593.24	1596.76	1598.53	1598.24	1601.50
	Incremental Elevation	-1.65	0.29	0.00	0.00	-2.06	-5.29	0.59	-2.65	3.53	1.76	-0.29	3.26
Uplift	**Pool Elevation**	1602.35	1602.65	1602.65	1602.65	1600.59	1595.29	1595.88	1593.24	1596.76	1598.53	1598.24	1601.50
	Incremental Elevation	-1.65	0.29	0.00	0.00	-2.06	-5.29	0.59	-2.65	3.53	1.76	-0.29	3.26
	Air	9.76	10.24	11.43	12.38	11.43	10.24	6.67	3.57	0.95	-1.19	-2.62	-4.05
Temperature [oC]	**Water**	9.00	10.00	11.00	11.00	11.00	8.50	6.00	4.00	3.00	3.00	2.00	1.00
AAR	**AAR**	Activated											

Figure 17.6: Data preparation, cyclic load

The dead load is applied during the first increment. Following this step, displacements are reset to zero,

MERLIN AAR Problems

while maintaining the internal strains/stresses. During increments two through five, the hydrostatic (and uplift) load is applied, and the AAR expansion only initiates at increment six.

17.1.2   Stress Analysis

Following completion of the transient thermal analysis, the stress analysis may be performed. It should be noted however that the finite element mesh for the stress analysis of a dam affected by AAR must differ from the mesh used for the thermal analysis and moreover includes joints, the interface between dam and rock foundation, and the rock foundation. These components are not required in the thermal analysis but are very important to capturing the real behavior of a dam affected by AAR (and thus capturing the real crest displacements on which parameter identification is based, as will be explained in the following section). AAR expansion can indeed result in: 1) opening of the downstream vertical joints and closure of the upstream vertical joints in an arch dam; 2) possible movement of the various buttresses on a gravity dam along the joints; and 3) sliding of the dam when subjected to a compressive state of stress on the foundation joint.

With regard to the temporal and spatial variations of temperature, it should be kept in mind that the stress analysis requires a temperature difference with respect to the stress-free temperature (namely the grouting temperature $T(x, y, z) - T_{grout}$), whereas AAR evolution depends on the total absolute temperature inside the dam $T(x, y, z)$.

17.1.3   Results

Since the "proper" AAR parameters were not known *a priori*, the system identification process described in Section **??** was adopted with the initial and final values shown in Table 17.2.

Parameter	Initial	Final	Unit
$\varepsilon^\infty \times 10^3$	3.8947	3.5500	-
τ_C	1.564	1.453	ATU
τ_L	3.279	4.072	ATU

Table 17.2: Initial and final parameter values in system identification study; Reference temperature 60^oC

Figure 17.7 illustrates the real-time graphical display of the evolution of the three key parameters as well as the comparison between computed and actual crest displacements. Each data point, constituting a full 30-year analysis (or about 360 increments), is thus a CPU-intensive operation (requiring a few days of CPU time).

The final results are shown in Figure 17.8(a), where the field measurement of crest displacements are plotted along with the first and last numerical simulations. These results are "sharper" upon examination of Figure 17.8(c). In either case, given the complexity of the simulation and the randomness of actual material properties (as "smoothed" through the system identification process), the results can be qualified as "good" and then used for prediction purposes.

The stress and strain comparisons are shown in Figure 17.9. A zone of high tensile stresses can be noted at the center of Block 10.

Of special interest herein are the stresses and displacements along the base, as indicated in Figure 17.10(a). Let's note the positive crack opening displacement of the joint, with confirmation provided by the deformed shape (Figure 17.10(b)).

MERLIN AAR Problems
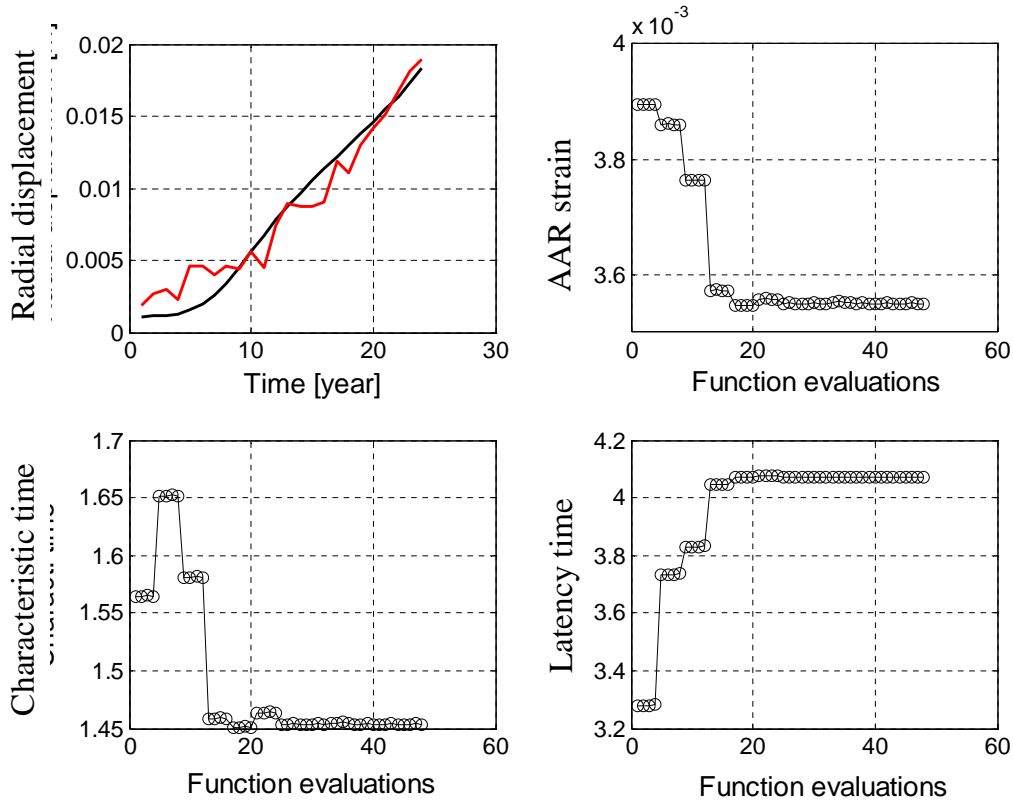
Figure 17.7: System identification process for the AAR analysis of an arch gravity dam

(a) System identification and results with seasonal variation

(b) Field-recorded crest displacements

(c) Final annual comparison
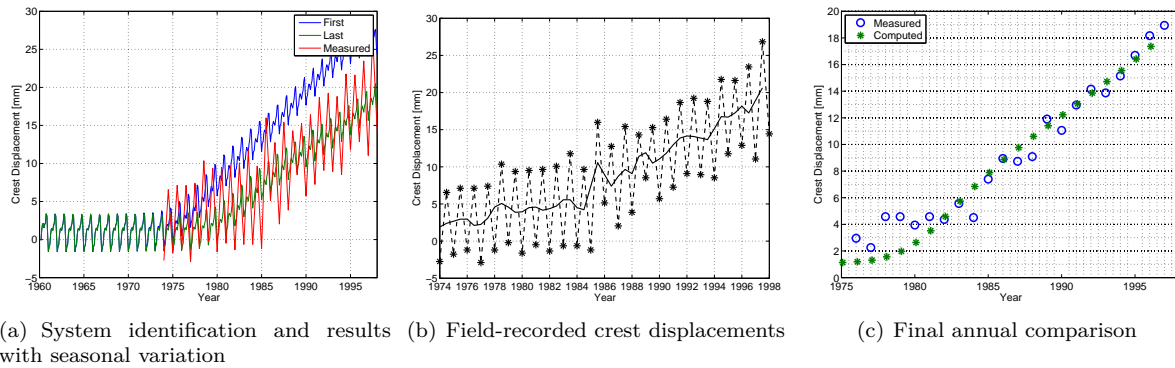
Figure 17.8: Crest displacement comparison

The zone of high tensile stresses at the center of Block 10 is indicative of a potential internal crack. Such a crack was actually observed in the gallery, though it appears to be confined (for now) inside the dam and has not yet "daylighted" on the downstream face (Figure 17.11).

MERLIN AAR Problems
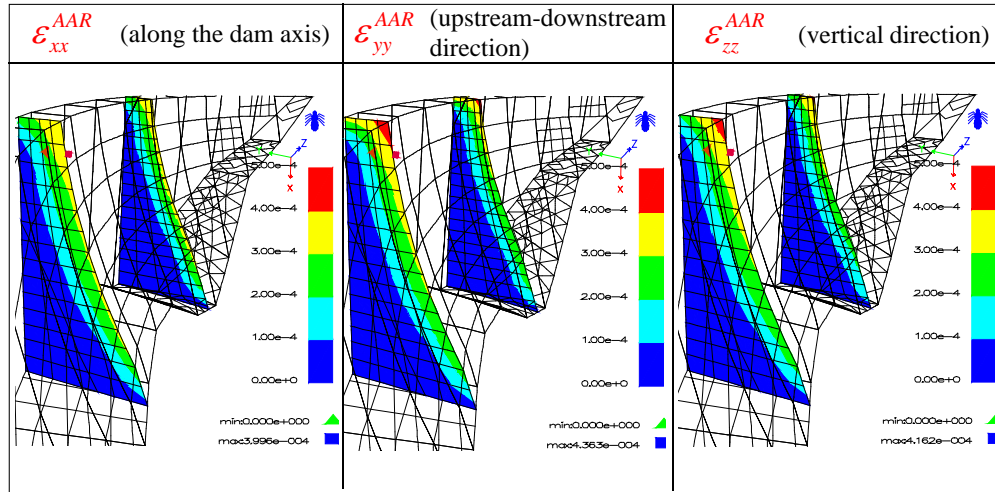
(a) Internal strains caused by AAR
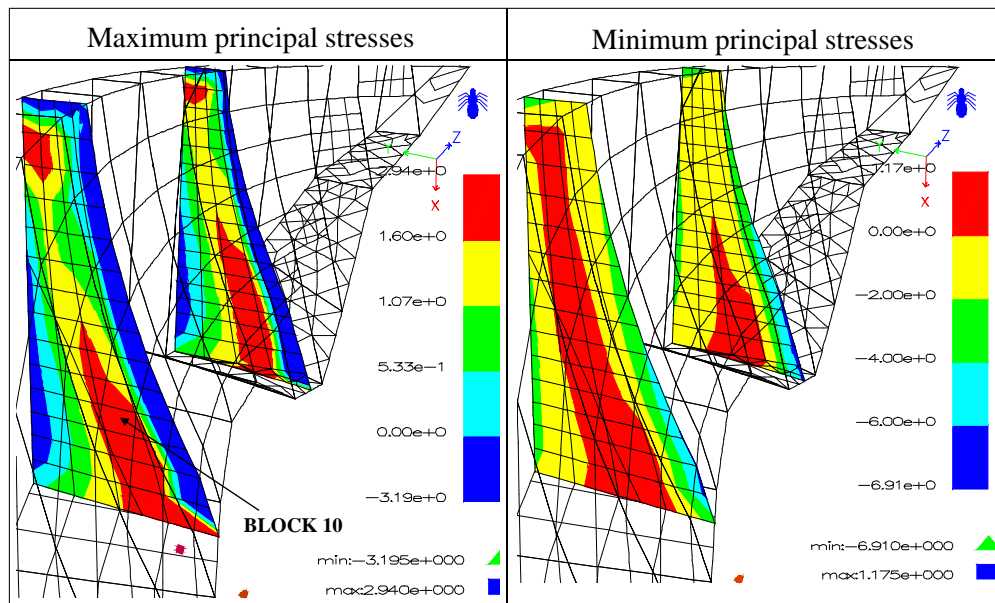
(b) Internal stresses

Figure 17.9: Internal AAR and stresses

17.2 Hollow Buttress Dam; Poglia

This example has been drawn from the contribution by the authors to the 8th ICOLD Benchmark Workshop on the Numerical Analysis of Dams (held in Wuhan, Hubei, China on Oct. 23-30, 2005), during which the contributors were asked to assess the safety of Poglia Dam, (Saouma, Perotti, and Uchita, 2005). The dam in Figure 17.12 is a hollow gravity dam composed of two lateral gravity dams and four hollow central diamond-head buttress elements.

This dam is characterized by a 137.1-m crest length, a 50-m height, two 14-m wide spillways and a 22-m joint spacing. The concrete volume equals 34,600 m^3, while the reservoir volume is 500,000 m^3. The base, maximum and operating pool elevations are 628.1, 632 and 625-628 m, respectively. The concrete features:

MERLIN AAR Problems

(a) Minimum/maximum stresses (MPa) and displacements (m) along the rigid rock/concrete interface; maximum principal stresses (MPa)

(b) Deformed shape of dam section
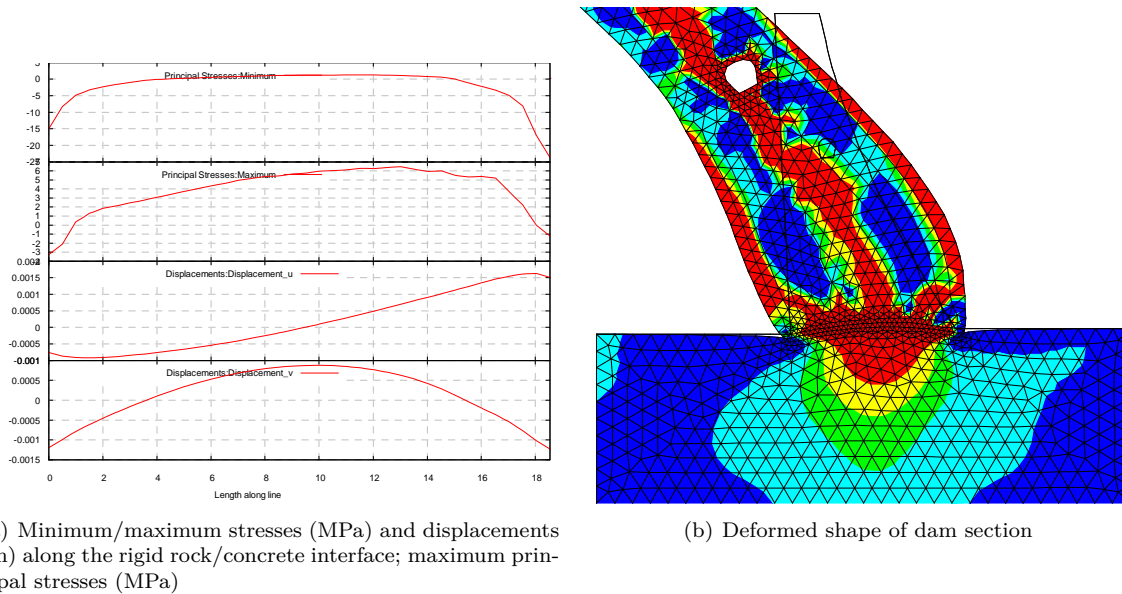
Figure 17.10: "Lift-off" of central portion of dam due to AAR

(a) Internal crack
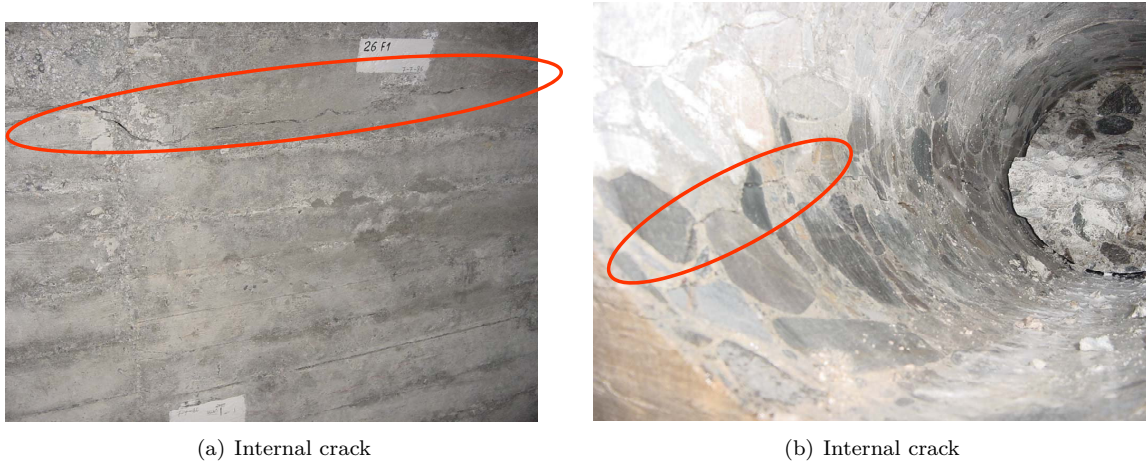
(b) Internal crack

Figure 17.11: Observed internal crack

a mass density of 2,400 kg/m^3, an elastic modulus of 18,000 MPa, a Poisson's ratio of 0.2, and compressive and tensile strengths of 32 and 1.5 MPa respectively. Accelerated expansion tests were conducted on cores extracted from Poglia Dam at both 38 and 80°C. From these tests, it was determined that the residual expansion equals approx. 0.095%. Rock has an elastic modulus of 10,000 MPa and a Poisson's ratio equal to 0.1. The compressive and tensile strengths amount to 32 and 0.15 MPa, respectively. Let's also closely observe the rock/concrete joint, with a friction angle of 37 degrees and a cohesion of 1.0 MPa.

The dam monitoring system is essentially based on: 1) 12 monitoring points along the dam for recording vertical displacements, 2) 6 targets for recording horizontal crest displacements in the stream direction, and 3) 2 pendulums for recording both longitudinal and lateral displacements. The targets have been placed on either side of the vertical joints. Additional instrumentation consists of extensometers and piezometers.

MERLIN AAR Problems

(a) Section   (b) Plan
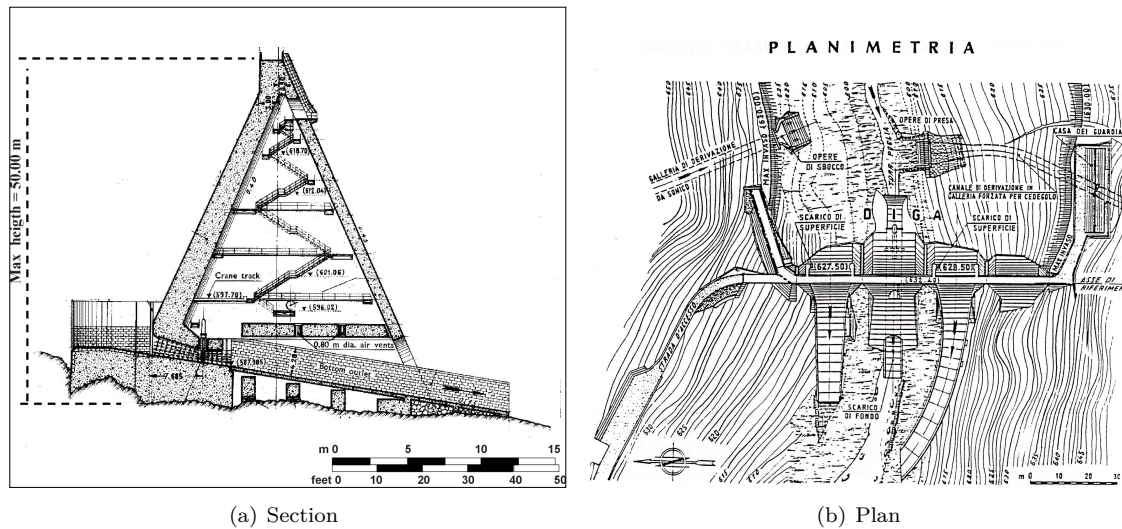
Figure 17.12: Section (central element) and layout of Poglia Dam

Though no chart exists to plot crest displacement vs. time, it is understood that the crest vertical drift (which started in 1970) reached 8 mm in 1982 and then a total value of 30 mm in 2000. This increase is quasi-linear with a slightly greater rate during the later years (Figure 17.13).
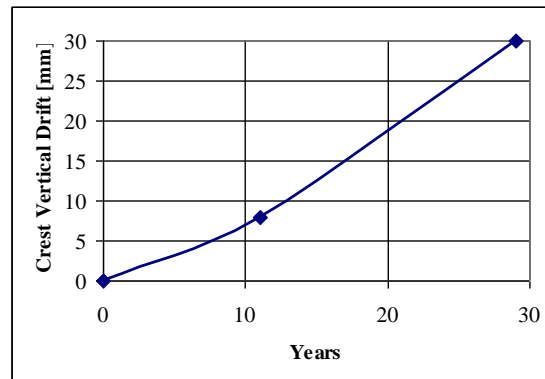
Figure 17.13: Measured crest vertical displacement

In addition, irreversible displacements of about 0.1 mm/year and 0.2 mm/year were recorded in the cross-valley direction (i.e. toward the right side) and along the stream direction, respectively. A downstream displacement recorded on the right-hand corner may prove to be the most worrisome finding (due to lateral expansion of the two adjacent blocks).

17.2.1   Transient Thermal Analysis

Since our AAR model is highly dependent on temperature, a preliminary transient thermal analysis needs to be performed. In this analysis, only the dam is considered. Half the central element was modeled, and due to symmetry, adiabatic boundary conditions could be applied on the plane of symmetry. Convection was neglected, and the recorded temperatures were assigned on the faces exposed to air (both outside and

inside) and to water (Figure 17.14).
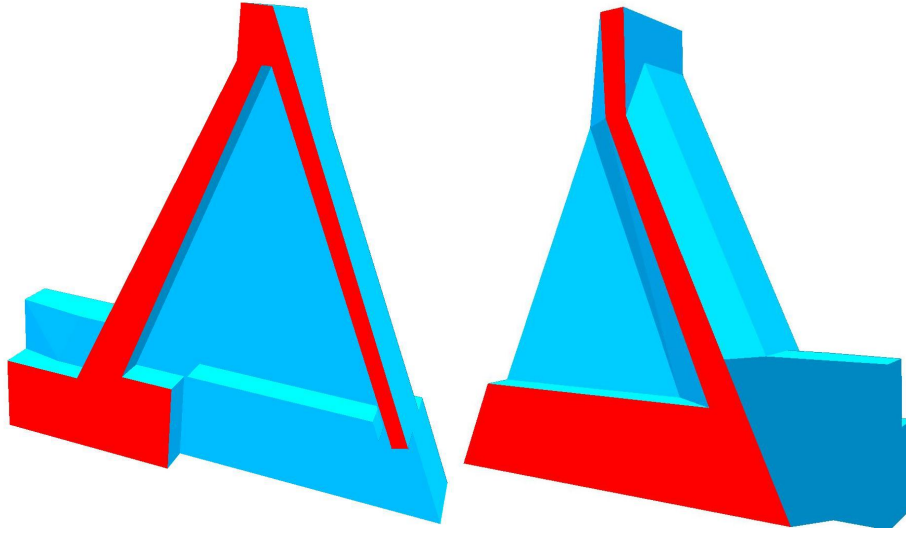
Figure 17.14: Adiabatic boundary conditions for the thermal analysis

Conductivity k was set to 44.67 MN.m/(mATU.^{o}C) and the mass density to 2.4310^{-3} Gg/m^3. In the context of our analysis, one ATU (Analysis Time Unit) corresponded to 6 months, hence 2 time increments per year were used. The temperatures are listed in Table 17.3.

Season	Inside	Outside	Water
Winter	4.4	0.1	2.9
Summer	19.2	29	12.6

Table 17.3: Temperatures used for the Poglia Dam analysis

It should be noted that the average (stress-free condition) temperature was subtracted from these values when conducting the thermal analysis. This average temperature was subsequently added to the nodal temperature for the AAR analysis (given that expansion depends on the total temperature and not on the temperature differential). The transient analysis was performed for five years; since results stabilized after four years, the Year 5 results were considered to be representative of the annual temperature variation. Figure 17.15 displays the internal dam temperature.

17.2.2 Stress Analysis

Following the thermal analysis, a stress analysis was conducted using a mesh that included the dam, its foundation and the rock/concrete interface joints.

The material properties adopted for the analysis are those specified by the Benchmark, with one notable exception. The tensile strength and cohesion of the dam/foundation interface were increased to 1.5 and 1.0 MPa (rather than the specified 0.15 and 0.10 MPa) because the preliminary analysis had indicated that these specified values were too small to resist the pool elevation. It should be noted that only initial guesses were introduced for the maximum volumetric strain latency and characteristic time, since these values were to be determined subsequently from an automated system identification procedure (see Section **??**). Following
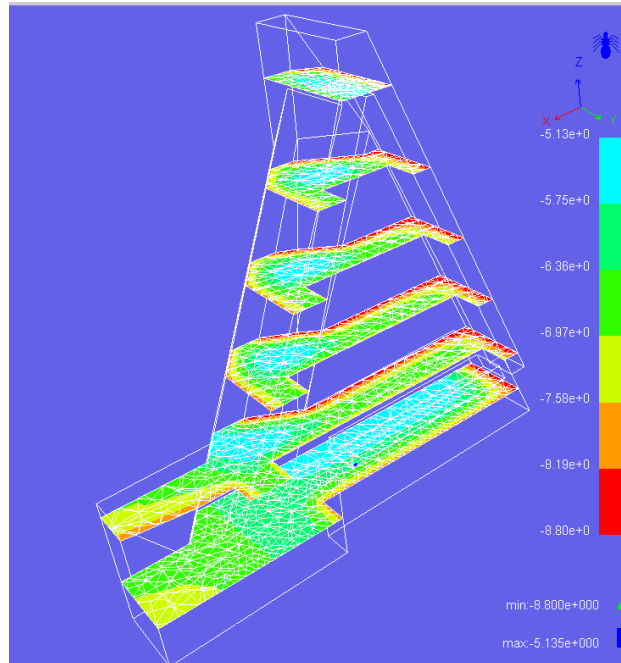
MERLIN AAR Problems

Figure 17.15: Internal temperature of Poglia Dam

convergence of this minimization (of the error between computed and measured crest displacements), "fine-tuning" was manually performed to further reduce this error. The final (numerically obtained) volumetric strain was 3.50×10^{-3}, whereas the experimentally obtained value (from laboratory tests) was 0.95×10^{-3}. Total dam expansion however could only be justifiably determined from the numerical calculation.

The gravity load (for the dam only) was applied in the first increment and the displacements (but not the stresses) were subsequently reset to zero (to remove self-weight displacements from the results). The pool elevation was then raised from base elevation 582.10 m to maximum elevation 628.09 m in four increments of 11.5 m. each. It should be noted that as the pool elevation was increased, not only did the hydrostatic pressure rise, but so did the uplift pressure distribution under the dam. This pressure distribution will be automatically adjusted from triangular to trapezoidal should the dam base crack. From the sixth increment forward, pool elevation was kept constant and the AAR was active (increments 6 and 7 correspond to winter and summer of the first year). An analysis corresponding to 55 years of dam operations was carried out and the resulting crest displacements were compared with measurements from the inverse analysis.

17.2.3 Analysis and Results

The 3D finite element mesh contained 6,145 nodes and 24,133 elements. The 3D nonlinear analysis employed the Tangent Stiffness method along with a Line Search and comprised 115 increments. The convergence criteria were set to 0.01, 0.02, 0.05 and 0.02 for the Energy, Relative Residual (ratio of the Euclidian norm of the current to the initial residual load vectors), Absolute Residual (ratio of the infinity norm of the current to the initial residual load vectors), and Displacement Error, respectively. A 50-iteration maximum was allowed. Each analysis lasted roughly 7 hours on a 3.00-GHz Xeon processor with 1.5 GB of RAM.

Figure 17.16(a) shows the crest displacements for the first seven increments, thus highlighting the crest displacement resulting from gravity and resetting the displacements to zero, followed by the four increments

MERLIN AAR Problems

associated with impounding. Crest displacements over the entire analysis are provided in Figure 17.16(b); let's note that while the measured crest displacement has not been captured, all later displacements have been (accounting for about 3 cm). This situation may be partially due to the scarcity of field observations (moreover, indication is lacking as to whether they were taken during the summer or winter) as well as to the fact that the lateral and significant dam displacement/sliding has been neglected.
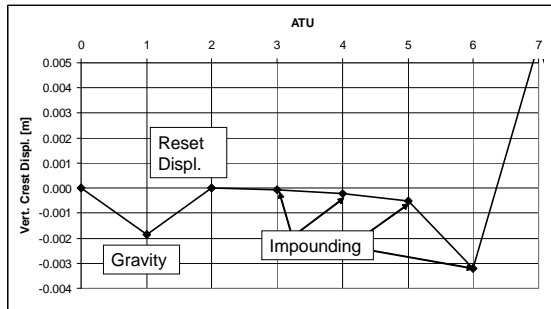
(a) Initial crest displacement during first seven increments
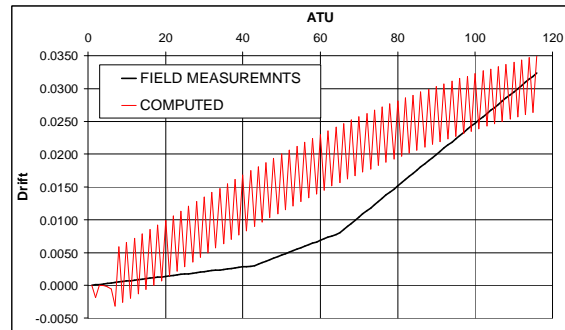
(b) Drift
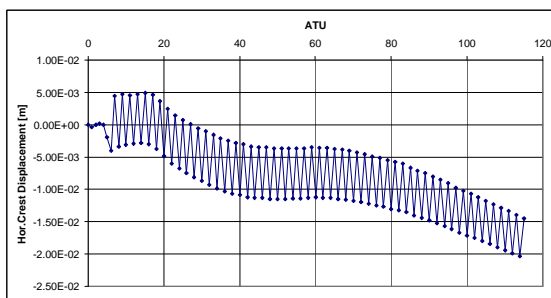
(c) Horizontal crest displacement
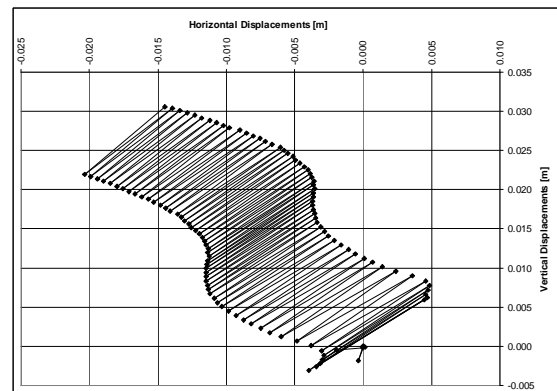
(d) Horizontal vs. vertical displacements

Figure 17.16: Analysis results for the Poglia Dam

shows both the vertical and horizontal crest displacements. Let's note that the seasonal variations are not negligible (possibly due to the thermal gradient between air trapped inside the dam and outside air), as compared to the total irreversible AAR variation. As expected (due to lateral stresses), the horizontal displacements are substantially smaller than vertical displacements.

The overall deformed shape however is somewhat puzzling (Figure 17.17).

It appears that for the given numerical assumptions, most of which have been stipulated by the Benchmark organizers, the dam is failing because of sliding. The sharp curvature of the top deformation corresponds to the pool elevation, which indeed lies 2 m below the crest.

Figure 17.18 illustrates various contour lines for the main rock/concrete joint. It is interesting to note that the crack opening displacements are maximum in the middle and then minimum on the upstream/downstream side. This finding had already been observed in the arch gravity dam analyzed previously. The normal stresses are mostly zero, and full uplift develops over most of the joint. The joint sliding displacement is linear and equal at most to 4.5 cm (note that adopting the Line Search method may

MERLIN AAR Problems

(a) Volumetric AAR strain

(b) Maximum principal stresses (MPA)
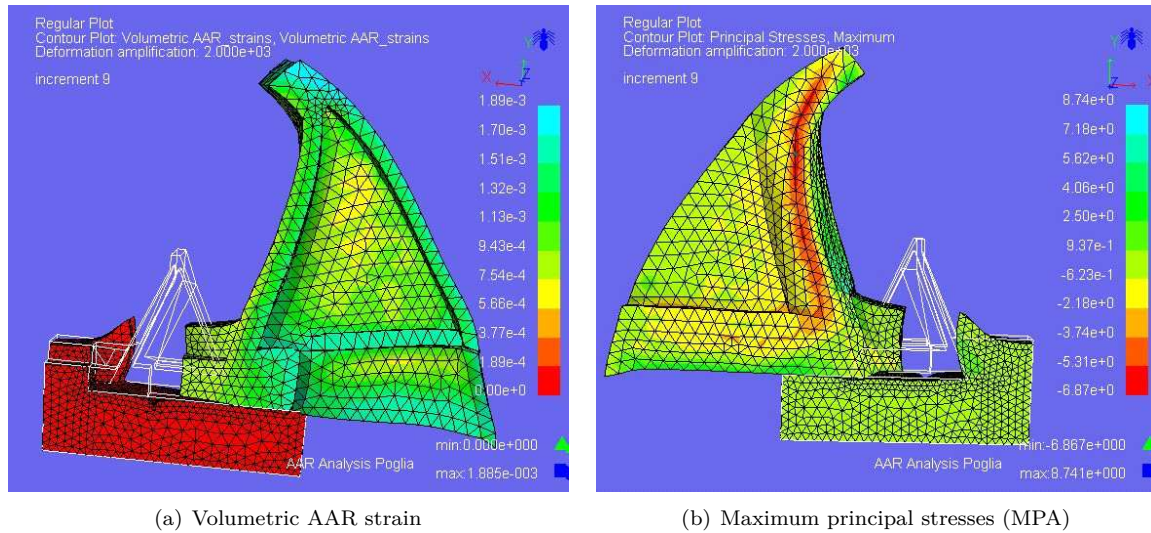
Figure 17.17: Deformed shape of the Poglia Dam
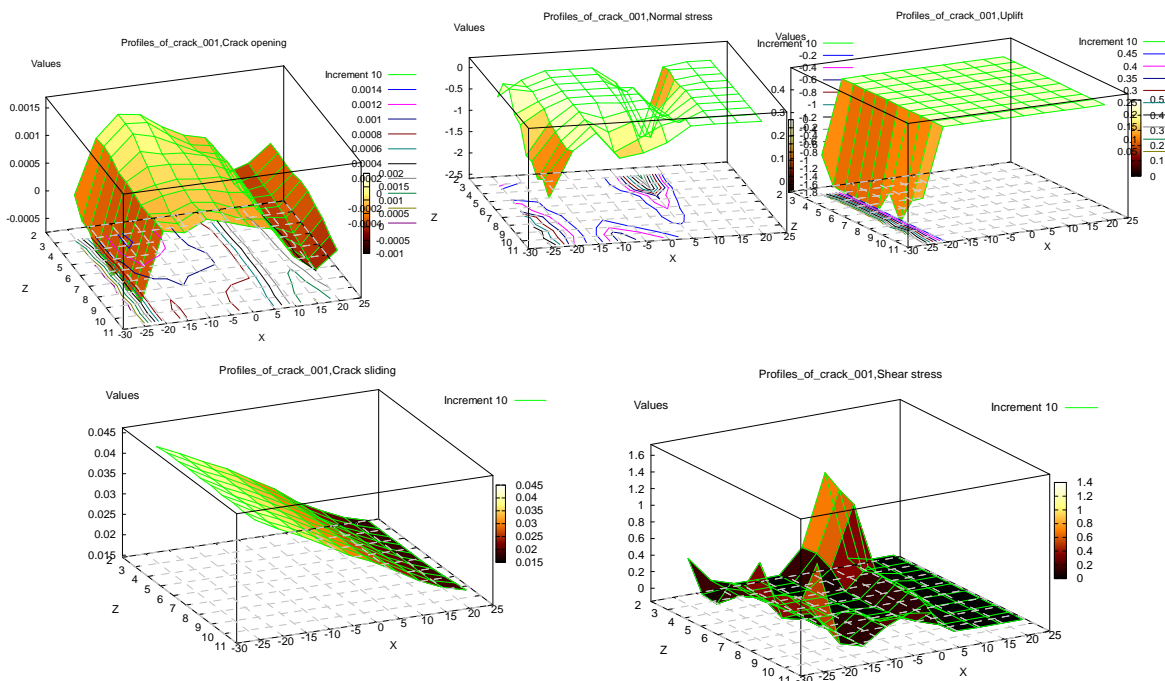
Figure 17.18: Contour plots of the main rock/concrete joint, joint opening displacements (m), normal stresses (MPa), uplift pressures (MPa), joint sliding displacements (m) and joint shear stresses (MPa)

have constrained overall sliding to such a "small" value). The shear distribution over the joint can also be visualized in this figure. According to these indications, the global safety factor relative to sliding remains below 1.

The overall AAR expansion at the end of the analysis ε^∞ was 1.65 x 10^{-3}, whereas the actual AAR expansion inside the dam was about 4 x 10^{-4}; this difference is due to the various model reduction factors.

MERLIN AAR Problems

Furthermore, this expansion is on average equivalent to 40^oC, i.e. just slightly lower than the 42^oC determined in a previous study, which did not model the interface or assume thermal expansion to be uniform.

A second analysis was conducted using the lateral faces of the dam unconstrained in the lateral (Z) direction. Figure 17.19 shows that with the lateral faces of the dam now free to expand, the vertical displacement is now reduced, in accordance with the premises of our model. The deformed shape of the dam is depicted in Figure 17.20, where the lateral swelling is quite obvious.

(a) Horizontal

(b) Vertical
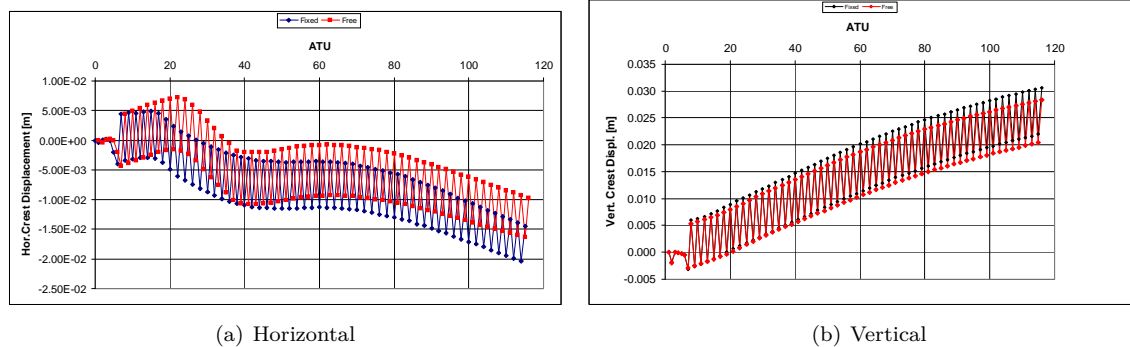
Figure 17.19: Effects of lateral constraints on AAR expansion

(a) Fixed

(b) Free
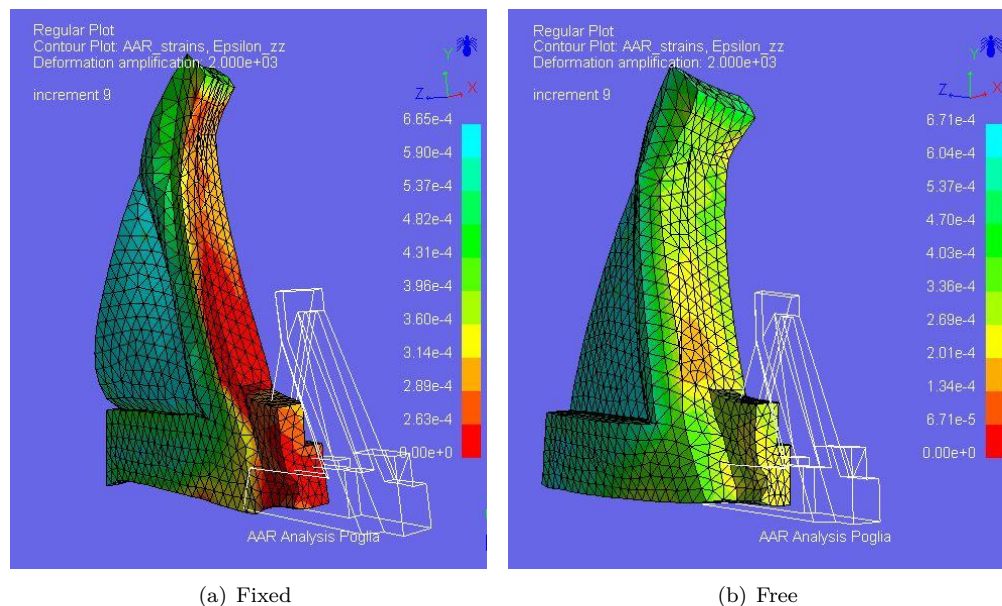
Figure 17.20: Deformed mesh and AAR strains in the lateral directions for both free and fixed boundary conditions

Despite the extensive effort for this analysis, the authors are not convinced that the structural model adopted actually reflects the current state of the dam. According to the numerical model, the dam has at the very least partially failed (though we know it is still "alive and well"). This perspective has rendered any subsequent evaluation of the failure pool elevation redundant, especially given the model's limited scope. Let's emphasize that the concern here is not the selected AAR constitutive model, but rather some of the

MERLIN AAR Problems

physical assumptions, including:

- Rock/concrete interface properties. The cohesion was specified to be 0.15 MPa by the Benchmark organizers, which is a very low value. Moreover, preliminary analysis has indicated that the dam could not even sustain the hydrostatic load, let alone AAR expansion. The cohesion and tensile strength values were thus arbitrarily increased by a factor of 10.

- The"2D" plane strain assumption may not actually reflect the complex stress state in this oddly shaped dam.

- This dam appears to be overly sensitive to thermal loads, hence an accurate long-term prediction of the dam would have required smaller time steps than what was adopted (6 months due to computational and "human" constraints).

- The benefit of a complete model is further justified by the most likely failure mechanism shown.

In light of the above assumptions and for a more accurate long-term prediction of this dam, the author would suggest that any future analysis considers the following:

1. Modeling of the entire dam, since opening of the joint connecting the dam to the lateral gravity dams may be the primary concern (Figure 17.21), which in turn could cause overall structural failure.

2. Smaller time steps for the thermal and AAR analyses, accompanied by a better grasp of the temperature boundary conditions.

3. Improved investigation of the rock/concrete interfaces through core extractions and testing, in addition to piezometer readings of the uplift pressures.

4. Possibly, but not necessarily, accelerated tests of concrete cores at either 38°C or 70°C.

5. Again possibly, but not necessarily, "calibration" of the dam response by carefully monitoring crest displacements and the internal stress state using flat jacks (an appropriate step given the relatively small thickness of the structural components) during dam drainage and impounding.

Only with these considerations can the failure pool elevation be realistically determined, as any competing approach would serve as a mere academic exercise useful for comparing models but not for performing an accurate evaluation.

(a) Initial   (b) Localized failure due to AAR expansion
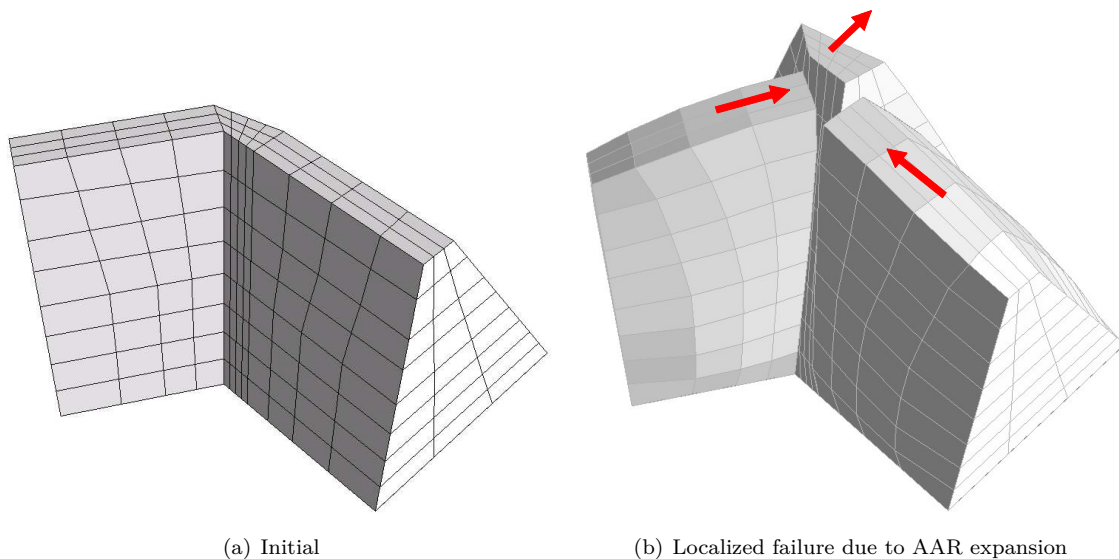
Figure 17.21: Possible failure mechanism at a joint connecting two parts of the dam

MERLIN AAR Problems

Conducting a full 3D analysis of this dam would simply offer speculation on the likely mode of failure mechanism. The sharp corner between the two dam segments constitutes, in this case, the dam's "Achilles' heel", a worrisome feature that warrants further investigation.

MERLIN AAR Problems

Bibliography

Alvaredo, A.M. and F.H. Whitman (1992). "Crack Formation Due to Hygral Gradients". In: *Third International Workshop on Behaviour of Concrete Elements Under Thermal and Hygral Gradients*. Weimar, Germany.

Army Corps of Engineers (1992). *Reliability Assessment of Navigation Structures*. ETL 1110-2-532. Washington, D.C.: Department of the Army, US Army Corps of Engineers.

— (1993). *Reliability Assessment of Navigation Structures; Stability of Existing Gravity Structures*. ETL 1110-2-321. Washington, D.C.: Department of the Army, US Army Corps of Engineers.

Bach, F., T.S. Thorsen, and M.P. Nielsen (1993). "Load-carrying capacity of structural members subjected to alkali-silica reactions". In: *Construction and Building Materials* 7.2, pp. 109 –115. ISSN: 0950-0618. DOI: http://dx.doi.org/10.1016/0950-0618(93)90040-J. URL: http://www.sciencedirect.com/science/article/pii/095006189390040J.

Barbosa, R.A. et al. (2016). "Assesment of Severely ASR Damaged Bridges: From Diagnosis to Structural Effects". In: *Proceedings of the 15th International Conference on Alkali-aggregate Reaction in Concrete (15th Icaar)*.

Bažant, Ž. and B.-H. Oh (1983). "Crack band theory for fracture of concrete". In: *Materials and Structures* 16, pp. 155–177.

Bažant, Ž., G. Zi, and C. Meyer (2000). "Fracture Mechanics of AAR in Concretes with Waste Glass Particles of Different Sizes". In: *J. of Engineering Mechanics, ASCE* 126.3, pp. 226–232.

Ben-Ftima, M., H. Sadouki, and E. Bruhwiler (2016). "Development of a computational multi-physical framework for the use of nonlinear explicit approach in the assessment of concrete structures affected by alklai-aggregate reaction". In: 9th *International Conference on Fracture Mechanics of Concrete and Concrete Structures; FraMCoS-9*. Ed. by V.E. Saouma, J. Bolander, and E. Landis. Berkeley, CA.

Benjamin, J. and C.A. Cornell (1970). *Probability, Statistics, and Decision for Civil Engineers*. New York: McGraw Hill.

Blight, G. and M. G. Alexander (2008). *Alkali-Aggregate Reaction and Structural Damage to Concrete*. Taylor & Francis.

Borst, R. de (1986). "Nonlinear Analysis of Frictional Materials". PhD thesis. Delft University of Technology, Delft.

Brühwiler, Eugen et al. (2015). "Strengthening the Chillon viaducts deck slabs with reinforced UHPFRC". In: *IABSE Symposium Report*. Vol. 105. International Association for Bridge and Structural Engineering, pp. 1–8.

Bryant, L.M., J.T. Brokaw, and P.F. Mlakar (1993). *Reliability Modeling of Concrete Overstressing*. Tech. rep. Report Submitted to U.S. Army Engineer Waterways Experiment Station. JAYCOR, Vicksburg Mississippi.

Capra, B. and J.P. Bournazel (1998). "Modeling of induced mechanical effects of alkali-aggregate reactions". In: *Cement and Concrete Research* 28.2, pp. 251–260.

Carol, I., Ž. Bažant, and P.C. Prat (1992). "Microplane Type Constitutive Models for Distributed Damage and Localized Cracking in Concrete Structures". In: *Proc. Fracture Mechanics of Concrete Structures.* Breckenridge, CO: Elsevier, pp. 299–304.

CEB (1983). *Concrete under Multiaxial States of Stress Constitutive Equations for Practical Design.* Tech. rep. Bulletin d'Information 156. Comité Euro-International du Béton.

Červenka, J. and V. Červenka (1999). "Three Dimensional Combined Fracture-Plastic Material Model for Concrete". In: *5th U.S. National Congress on Computational Mechanics.* Boulder, CO.

Cervenka, J., J.M. Chandra, and V.E. Saouma (1998). "Mixed Mode Fracture of Cementitious Bimaterial Interfaces; Part II: Numerical Simulation". In: *Engineering Fracture Mechanics* 60.1, pp. 95–107.

Cervenka, J. and V.K. Papanikolaou (2008). "Three Dimensional Combined Fracture-Plastic Material Model for Concrete". In: *International Journal of Plasticity* 24.12, pp. 2192–2220.

Červenka, V. and L. Jendele (2016). *ATENA Program Documentation Part.*

Červenka Consulting (2019). *ATENA.*

Charlwood, R. G. et al. (1992). "A Review of Alkali Aggregate Reactions in Hydroelectric Plants and Dams". In: *Proceedings of the International Conference of Alkali-Aggregate Reactions in Hydroelectric Plants and Dams.* Ed. by CEA and CANCOLD. Fredericton, Canada, pp. 1–29.

Chénier, JO et al. (2012). "An approach regarding aging management program for concrete containment structure at the gentilly-2 nuclear power plant". In: *Proceedings of 33rd Annual Conference of the Canadian Nuclear Society, TCU Place, Saskatoon, Saskatchewan, Canada.* Vol. 1013, p. 126.

Chiaramida, A. (2013). *Lab to test Seabrook's concrete problems.*

Dahlblom, O. and N. S. Ottosen (1990). "Smeared Crack Analysis Using a Generalized Fictitious Crack Model". In: *Journal of Engineering Mechanics* 116.1, pp. 55–76.

Der Kiureghian, A. and O. Ditlevsen (2009). "Aleatory or epistemic? Does it matter?" In: *Structural Safety* 31, pp. 105–112.

El Mohandes, F. and F.J. Vecchio (2013). *VecTor3: A. User's Manual; B. Sample Coupled Thermal and Structural Analysis.* Dept. of Civil Engineering, University of Toronto. Toronto, Canada.

Ellingwood, B.R. (2005). "Risk-informed condition assessment of civil infrastructure: state of practice and research issues". In: *Structure and infrastructure engineering* 1.1, pp. 7–18.

Fan, S. and J.M. Hanson (1998). "Effect of Alkali Silica Reaction Expansion and Cracking on Structural Behavior of Reinforced Concrete Beams". In: *ACI Structural Journal* 95.5, pp. 488–495.

Feenstra, P.H., R. de Borst, and J. Rots (1991). "Numerical Study On Crack Dilatancy. I: Models and Stability Analysis. II: Applications". In: *J. Eng. Mech.* 117.4, pp. 733–769.

FHWA (2010). *Report on the Diagnostis, Prognosis, and Mitigation of Alkali-Silica Reaction (ASR) in Transportation Structures.* Tech. rep. FHWA-HIF-09-004. Federal Highway Administration.

Fournier, B. et al. (2009). "Effect of environmental conditions on expansion in concrete due to alkali–silica reaction (ASR)". In: *Materials Characterization* 60.7, pp. 669–679.

Giannini, E. et al. (2013). *Non-Destructive Evaluation of In-Service Concrete Structures Affected by Alkali-Silica Reaction (ASR) or Delayed Ettringite Formation (DEF) - Final Report, Part I.* Tech. rep. 0-6491-1. Sponsoring Agency Name and Address Texas Department of Transportation Research and Technology Implementation Office P.O. Box 5080 Austin, TX 78763-5080. Center for Transportation Research The

MERLIN AAR Problems

University of Texas at Austin and Texas A&M Transportation Institute The Texas A&M University System.

Gilks, P. and D. Curtis (2003). "Dealing with the Effects of AAR on the Water Retaining Structures at Mactaquac GS". In: *Proceedings of the 21st Congress on Large Dams*. Montreal, Canada, pp. 681–703.

Goodman, R.E., R.C. Taylor, and T.C. Brekke (1968). "A Model for the Mechanics of Jointed Rocks". In: *J. of the Soil Mechanics and FOundations Division ASCE* 94, pp. 637–659.

Granger, L. (1995). "Comportement différé du béton dans les enceintes de centrales nucléaires: analyse et modélisation". PhD thesis. Ecole Nationale des Ponts et Chaussées.

Haberman, S. (2013). "Seabrook Station nuclear plant license advancing". In: *Seacoast On-Line*.

Habibi, F. et al. (2015). "Alkali Aggregate Reaction In Nuclear Concrete Structures: Part 3: Structural Shear Wall Elements". In: *Proceedings of the 23rd Conference on Structural Mechanics in Reactor Technology (SMiRT23)*.

Hansen, E.J. and V.E. Saouma (2003). "Hybrid Models for 3D Reinforced Concrete Analysis". In: *Revue Francaise de Genie Civil* 7.5, pp. 647–658.

Hariri-Ardebili, M.A. (2018). "Risk, Reliability, Resilience (R3) and beyond in dam engineering: A state-of-the-art review". In: *International journal of disaster risk reduction* 31, pp. 806–831.

Hariri-Ardebili, M.A. and F. Pourkamali-Anaraki (2018). "Simplified reliability analysis of multi hazard risk in gravity dams via machine learning techniques". In: *Archives of Civil and Mechanical Engineering* 18.2, pp. 592–610.

Hariri-Ardebili, M.A. and V.E. Saouma (2016a). "Sensitivity and Uncertainty Quantification of the Cohesive Crack Model". In: *Engineering Fracture Mechanics* 155, pp. 18–35.

— (2016b). "Probabilistic seismic demand model and optimal intensity measure for concrete dams". In: *Structural Safety* 59, pp. 67–85.

— (2017). "Single and multi-hazard capacity functions for concrete dams". In: *Soil Dynamics and Earthquake Engineering* 101, pp. 234–249.

Hariri-Ardebili, M.A., V.E. Saouma, and C. Merz (2018). "Risk-Informed Conditional Assessment of a Bridge with Alkali Aggregate Reaction". In: *ACI Structural Journal* 115.2, pp. 475–487.

Hillerborg, A., M. Modéer, and P.E. Petersson (1976). "Analysis of Crack Formation and Crack Growth in Concrete by Means of Fracture Mechanics and Finite Elements". In: *Cement and Concrete Research* 6.6, pp. 773–782.

Hordijk, D.A. (1991). "Local approach to Fatigue of Concrete". PhD thesis. Delft University of Technology.

Huang, H. and B. Spencer (2016). "Grizzly model for fully coupled heat transfer, moisture, diffusion, alkali-silica reaction and fractureing process in concrete". In: *9th International Conference on Fracture Mechanics of Concrete and Concrete Structures; FraMCoS-9*. Ed. by V.E. Saouma, J. Bolander, and E. Landis. Berkeley, CA.

Huang, H., B. Spencer, and G. Cai (2015). *Grizzly Model of Multi-Species Reactive Diffusion, Moisture/Heat Transfer, and Alkali-Silica Reaction in Concrete*. Tech. rep. INL/EXT-15-36425. Idaho Falls, Idaho 83415: Idaho National Laboratory.

Huang, Q. et al. (2014). "Probabilistic model for steel–concrete bond behavior in bridge columns affected by alkali silica reactions". In: *Engineering Structures* 71, pp. 1–11.

Ideker, J.H. et al. (2012). "Do current laboratory test methods accurately predict alkali-silica reactivity?" In: *ACI Materials Journal* 109.4.

MERLIN AAR Problems

Iman, R. and W.J. Conover (1982). "A distribution-free approach to inducing rank correlation among input variables". In: *Communications in Statistics-Simulation and Computation* B11, pp. 311–334.

Kennedy, R. et al. (1980). "Probabilistic seismic safety study of an existing nuclear power plant". In: *Nuclear Engineering and Design* 59.2, pp. 315–338.

Kolmar, W. (1986). "Beschreibung der Kraftuebertragung ueber Risse in nichtlinearen Finite-Element-Berechnungen von Stahlbetontragwerken". PhD thesis. Darmstadt.

Kronenberg, P. et al. (2013). *A9 - Viaducs de Chillon; Diagnostic relatif à la réaction alcali-granulats du béton.* Tech. rep. TFB & Holcim & gvh.

Kupfer, BH and KH Gerstle (1973). "Behavior of Concrete under Biaxial Stresses". In: *ASCE Journal of the Engineering Mechanics Division* 99.4, pp. 853–866.

Larive, C. (1998). *Apports Combinés de l'Experimentation et de la Modélisation à la Comprehension del'Alcali-Réaction et de ses Effets Mécaniques.* Tech. rep. *In French.* Paris: *Ecole Normale des Ponts et Chaussées.*

Le Pape, Y. and Ma, Z. and Cabage, J. and Lenarduzzi, R. (2014). *Design of a large-scale concrete mockup to study the effects of alkali-silica reaction on expansion, damage and shear fracture propagation in stress-confined safety related structures.* Tech. rep. Technical Report M3LW-14OR-0403012 - Rev. 1. Light Water Reactor Sustainability Program.

Lee, T.H. and K.M. Mosalam (2006). *Probabilistic seismic evaluation of reinforced concrete structural components and systems.* Tech. rep. 2006/04. Pacific Earthquake Engineering Research Center.

Leemann, Andreas and Christine Merz (2013). "An attempt to validate the ultra-accelerated microbar and the concrete performance test with the degree of AAR-induced damage observed in concrete structures". In: *Cement and Concrete Research* 49, pp. 29–37.

Léger, P., P. Côte, and R. Tinawi (1996). "Finite Element Analysis of Concrete Swelling Due to Alkali-Aggregate Reactions in Dams". In: *Computers & Structures* 60.4, pp. 601–611.

Li, Kefei and Olivier Coussy (2002). "Concrete ASR degradation: from material modeling to structure assessment". In: *Concrete Science and Engineering* 4.13, pp. 35–46.

Lindgård, Jan et al. (2010). "The EU "PARTNER" Project-European standard tests to prevent alkali reactions in aggregates: final results and recommendations". In: *Cement and Concrete Research* 40.4, pp. 611–635.

Lindgård, Jan et al. (2012). "Alkali–silica reactions (ASR): literature review on parameters influencing laboratory performance testing". In: *Cement and Concrete Research* 42.2, pp. 223–243.

Lotfi, H.R. (1992). "Finite Element Analysis of Fracture of Concrete and Masonry Structures". PhD thesis. University of Colorado, Boulder.

Lukschová, Šárka, Richard Přikryl, and Zdeněk Pertold (2009). "Petrographic identification of alkali–silica reactive aggregates in concrete from 20th century bridges". In: *Construction and building materials* 23.2, pp. 734–741.

Malla, S. and M. Wieland (1999). "Analysis of an arch-gravity dam with a horizontal crack". In: *Computers & Structures* 72.1, pp. 267–278.

Marquié, C. (2016). *IRSN R&D on Concrete Pathologies Issues: The ODOBA Project.* URL: \url{https://www.nrc.gov/public-involve/conference-symposia/ric/past/2016/docs/abstracts/marquiec-t7-hv.pdf}.

Menétrey, P. and K. Willam (1995). "Triaxial failure Criterion for Concrete and its Generalization". In: *ACI Structural Journal* 92.3, pp. 311–318.

MERLIN AAR Problems

Merz, C. (2013). "Assessment of the residual expansion potential of concrete from structures damaged by AAR". In: *Cement and Concrete Research* 52, pp. 182–189.

Mier, J.G.M. van (1986). "Multi-axial Strain Softening of Concrete; Part I: Fracture". In: *Materials and Structures, RILEM* 19.111.

Mirzabozorg, H. (2013). Personal Communication.

Miyagawa, T. (2013). "Fracture of Reinforcing Steel in Concrete Damaged by ASR". In: *Construction and Building Materials* 39, pp. 105–112.

Miyagawa, T. et al. (2006). "Fracture of reinforcing steels in concrete structures damaged by alkali-silica reaction-field survey, mechanism and maintenance". In: *Journal of Advanced Concrete Technology* 4.3, pp. 339–355.

Mohammed, T.U., H. Hamada, and T. Yamaji (2003). "Alkali-Silica Reaction-Induced Strains over Concrete Surface and Steel Bars in Concrete". In: *ACI Materials* 100.2, pp. 133–142.

Montez, C. and Stokes III, W.E. (2009). *6th Street Viaduct Seismic Improvement Project; Environmental Impact Report.* Tech. rep. INL/EXT-15-36425. Idaho Falls, Idaho 83415: City of Los Angeles and State of California Department of Transportation.

Mood, A., F.A. Graybill, and D.C. Boes (1974). *Introduction to the theory of statistics 3rd ed.* McGraw-Hill.

Multon, S. (2004). "Evaluation expérimentale et théorique des effets mécaniques de l'alcali-réaction sur des structures modèles". PhD thesis. Université de Marne la Vallée, France.

Multon, S., J.F. Seignol, and F. Toutlemonde (2005). "Structural behavior of concrete beams affected by alkali-silica reaction". In: *ACI Materials Journal* 102.2, p. 67.

Multon, S. and F. Toutlemonde (2006). "Effect of Applied Stresses on Alkali-Silica Reaction Induced Expansions". In: *Cement and Concrete Research* 36.5, pp. 912–920.

Nakamura, E., H. Watanabe, and H. Koga (2008). "Shear resisting Mechanism in RC Beams with Stirrups Fracture due to ASR Expansion". In: *Proceedings of the 13th International Conference on Alkali-Aggregate Reaction in Concrete.*

Nevander, O. and N. Orbovic (2017). *ASCET Phase II - Summary, Conclusions and Recommendation.* Tech. rep. Draft final report. OECD Nuclear Energy Agency (NEA).

NextEra-ML121160422 (2012). *Impact of Alkali Silica Reaction on Seabrook Concrete Structure.*

NOAA (2013). *Satellite and Information Servis (NESDIS).*

NRC-CU Grant (2014). *Experimental and Numerical Investigation of Alkali Silica Reaction in Nuclear Reactors.* Tech. rep. Grant and Cooperative Agreement NRC-HQ-60-14-G-0010.

NRC-NIST Project (2014). *Structural Performance of Nuclear Power Plant (NPP) Concrete Structures Affected by Alkali-Silica Reaction (ASR).* Tech. rep. Interagency Agreement No. NRC-HQ-60-14-I-0004.

NUREG/CR-6706 (2001). *NUREG/CR-6706: Capacity of Steel and Concrete Containment Vessels With Corrosion Damage.*

Omikrine, M. et al. (2016). "A new model for the analysis of the structural/mechanical performance of concrete structures affected by DEF–Case study of an existing viaduct". In: *Structural Concrete.*

Orbovic, N. et al. (2015). "Alkali Aggregate Reaction in Nuclear Concrete Structures: Part 1: A Holistic Approach". In: *Proceedings of the 23rd Conference on Structural Mechanics in Reactor Technology (SMiRT23).*

Pan, J. et al. (2013). "Numerical prediction of swelling in concrete arch dams affected by alkaliaggregate reaction". In: *European Journal of Environmental and Civil Engineering* 17.4, pp. 231–247.

MERLIN AAR Problems

Pan, Jianwen et al. (2014). "A unified approach for long-term behavior and seismic response of AAR-affected concrete dams". In: *Soil Dynamics and Earthquake Engineering* 63, pp. 193–202.

Piguet SA, Bureau Technique (1971). "The viaducts of Chillon (Switzerland)". In: *La Technique des Travaux* 47, pp. 47–60.

Plum, N. M. (1961). *Tentative Recommendations for the Prevention of Alkali Aggregate Reactions.* Danish Building Research Institute.

Poole, A.B. (1992). "Introduction to Alkali-Aggregate Reaction in Concrete". In: *The Alkali-silica Reaction in Concrete.* Ed. by R.N. Swamy. Van Nostrand Reinhold, New York, pp. 1–28.

Reich, R.W. (1993). "On the Marriage of Mixed Finite Element Methods and Fracture Mechanics: An Application to Concrete Dams". PhD thesis. University of Colorado, Boulder.

Rivard, P. and F. Ballivy (2000). "Quantitative assessment of concrete damage due to alkali-silica reactions(ASR) by petrographic analysis". In: *11th international conference on alkali aggregate reaction*, pp. 889–898.

Rodriguez, J. et al. (2011). "Contribution to Theme A of the Benchmark Workshop: Effect of Concrete Swelling on the Equilibrium and Displacements of an Arch Dam". In: *Proceedings of the XI ICOLD Benchmark Workshop on Numerical Analysis of Dams.* Valencia, Spain.

Rots, J. G. and J. Blaauwendraad (1989). "Crack Models for Concrete: Discrete or Smeared? Fixed, Multi-directional or Rotating?" In: *HERON* 34.1, pp. 1512–1533.

Saouma, V.E. (2005). "Reliability Based Nonlinear Fracture Mechanics Analysis of a Dam". In: *Dam Engineering* 16.3, pp. 219–241.

— (2009). *KumoNoSu, a 3D Interactive Graphics Mesh Generator for MERLIN; User's Manual.* URL: \url{http://civil.colorado.edu/~saouma/pdf/kumo.pdf}.

— (2013). *Numerical Modeling of Alkali Aggregate Reaction.* 320 pages. CRC Press.

— (2017). *Effect of AAR on Shear Strength Panels.* Tech. rep. Final Report to NRC, Grant No. NRC-HQ-60-14-G-0010, Task 1-C. University of Colorado, Boulder.

Saouma, V.E., M.A. Hariri-Ardebili, and Y. Le Pape (2015). *Effect of Alkali-Silica Reaction on Shear Strength of Reinforced Concrete Structural Members.* Tech. rep. ORNL/TM-2015/588. Oak Ridge, TN 37831: Oak Ridge National Laboratory.

Saouma, V.E. and L. Perotti (2004). *2D AAR Parametric Investigation of a Dam.* Tech. rep. Bienne, Switzerland: Report No. 4, Submitted to the Swiss Federal Agency of Water and Geology.

— (2006). "Constitutive Model for Alkali Aggregate Reactions". In: *ACI Materials Journal* 103.3, pp. 194–202.

Saouma, V.E., L. Perotti, and Y. Uchita (2005). "AAR Analysis of Poglia Dam with Merlin". In: *8th ICOLD Benchmark Workshop on Numerical Analysis of Dams.* Wuhan, China.

Saouma, V.E., J. Červenka, and R.W. Reich (2010). *Merlin Finite Element User's Manual.*

Saouma, V.E. et al. (1994). "Mixed mode fracture of rock-concrete interfaces". In: *US-Europe Workshop on Fracture and Damage of Quasi-Brittle Materials: Experiment, Modeling and Computer Analysis.* Ed. by Ž. Bažant. Prague, Czech Republic.

Saouma, V.E et al. (2016). "Effect of alkali–silica reaction on the shear strength of reinforced concrete structural members. A numerical and statistical study". In: *Nuclear Engineering and Design* 310, pp. 295–310.

Saouma, V.E. et al. (2017). *Benchmark Problems for AAR FEA Code Validation.* URL: \url{http://www.rilem.org/global/gene/doc_link.php?doc=2016161048_rilem-tc-259-isr-wg2-benchmark.pdf}.

MERLIN AAR Problems

Saouma, V.E. (2014). *Numerical Modeling of AAR*. 324 pages. CRC Press.

Saouma, V.E. and Hariri-Ardebili, M.A. and Puatatsananon, W. and Le Pape, Y. (2014). *Preliminary Results on the Structural Significance of Alkali-Silica Reaction in Massive Reinforced Concrete Structures*. Tech. rep. ORNL/TM-2014/489. Oak Ridge, TN 37831: Oak Ridge National Laboratory.

Schmidt, J. W. et al. (2014a). "Novel shear capacity testing of ASR damaged full scale concrete bridge". In: *Engineering Structures* 79, pp. 365–374.

Schmidt, J.W. et al. (2014b). "Novel shear capacity testing of ASR damaged full scale concrete bridge". In: *Engineering Structures* 79, pp. 365–374.

Scrivener (2003). Personal Communication.

— (2005). Personal Communication.

Sellier, A. et al. (2009). "Combination of structural monitoring and laboratory tests for assessment of alkali-aggregate reaction swelling: application to gate structure dam". In: *ACI materials journal* 106.3, pp. 281–290.

Shayan, A, A Xu, et al. (2015). "Implications of alkali-aggregate reaction for three concrete bridges". In: *Concrete Institute of Australia Conference, 27th, 2015, Melbourne, Victoria, Australia.*

Sheikh, S. (2017). Personal Communication, March 10, 2017.

Shimizu, H. et al. (2005). "Study on Material Properties in Order to Apply for Structural Analysis of Turbine Generator Foundation Affected by Alkali-Silica Reaction". In: *18th International Conference on Structural Mechanics in Reactor Technology (SMIRT 18)*. SMIRT18-H03-5. Beijing, China, pp. 2055–2060.

Stankowski, T. (1990). "Numerical Simulation of Progressive Failure in Particle Composites". PhD thesis. University of Colorado, Boulder.

Struble, L. and S. Diamond (1981). "Swelling Properties of Synthetic Alkali Silica Gels". In: *Journal of the American Ceramic Society* 64.11, pp. 652–655.

Takatura, T. et al. (2005). "Investigation of the expanded value of turbine generator foundation affected by alkali-silica reaction". In: *18th International Conference on Structural Mechanics in Reactor Technology (SMIRT 18)*. SMIRT18-H03-7. Beijing, China, pp. 2061–2068.

Tcherner, J. and T. Aziz (2009). "Effects of AAR on Seismic Assessment of Nuclear Power Plants for Life Extensions". In: *20th International Conference on Structural Mechanics in Reactor Technology (SMIRT 20)*. SMIRT20-Division 7 Paper 1789. Espoo, Finland.

Thonstad, T. et al. (2021). *Structural Performance of Nuclear Power Plant Concrete Structures Affected by Alkali-Silica Reaction (ASR); Task 2: Assessing Bond and Anchorage of Reinforcing Bars in ASR-Affected Concrete*. NIST Technical Note 2127. US Department of Commerce, National Bureau of Standards.

Touma, W.E. (2000). *Alkali-Silica Reaction in Portland Cement Concrete: Testing Methods and Mitigation Alternatives*. Tech. rep. International Center for Aggregate Research.

Uijl, J. den and N. Kaptijn (2003). "Shear Tests on Beams Cut from ASR-Affected Bridge Decks". In: *ACI Special Publication* 211.SP211-06, pp. 115–133.

Uijl, J.A. den and N. Kaptijn (2002). "Structural Consequenses of ASR: an Example on Shear Capacity". In: *HERON* 47.2. Special Issue on ASR, pp. 125–139.

Ulm, F. et al. (2000). "Thermo-Chemo-Mechanics of ASR Expansion in Concrete Structures". In: *ASCE J. of Engineering Mechanics* 126.3, pp. 233–242.

Wang, J. and H. Morikawa (2012). "Study on shear beahavior of deteriorated RC beams due to Alkali-Silica reaction". In: *37th Conference on Our World in Concrete and Structures*. Singpore.

MERLIN AAR Problems

West, G. (1996). *Alkali-aggregate reaction in concrete roads and bridges*. Thomas telford.

Whitman, F.H. et al. (1988). "Fracture Energy and Strain Softening of Concrete as Determined by Means of Compact Tension Specimens". In: *Materials and Structures* 21, pp. 21–32.

Wilkins, M.L. (1964). "Calculation of Elasto-plastic Flow". In: *Methods of Computational Physics* 3, pp. 211–263.

Wojslaw, K. and M. Wisniewski (2014). "Nonlinear and Time Dependent Analysis of a Concrete Bridge Suffering from Alkali-Silica Reaction: A Case Study of the Elgeseter Bridge in Trondheim." MA thesis. Norwegian University of Science and Technology, Institutt for konstruksjonsteknikk.

Xu, X. and L. Graham-Brady (2005). "A stochastic computational method for evaluation of global and local behavior of random elastic media". In: *Computer methods in applied mechanics and engineering* 194.42, pp. 4362–4385.

MERLIN AAR Problems

Appendix A

Mathematical and Statistical Support

A.1 Multiple Linear Regression Analysis

Multiple linear regression (MLR) is the extension of simple linear regression (SLR) to the case of multiple *explanatory variables* (which may or may not be truly independent). Hence, rather than modeling the mean response as a straight line, as in simple regression, it is now modeled as a function of several explanatory variables.

Multiple explanatory variables are required when scientific knowledge and experience tells us they are likely to be useful. In the problem at hand, this may be the depth of the beam, the maximum ASR expansion or others.

Simply put the model is:

$$y = \beta_0 + \sum_{i=1}^{n} \beta_i x_i + \varepsilon \tag{A.1}$$

where y is the response variable (such as shear strength variation), β_0 the intercept, β_i is the slope coefficient of explanatory variable i, and ε is the remaining unexplained noise in the date (the error), x_i are all the constituents of the 18 variables listed in Table 13.5, and the β_i coefficients are to be determined.

Given the normalized approach taken by R, a higher β coefficient is indicative of a higher "participation factor" or relevant parameter in the shear strength change.

This equation will be solved by minimizing the error between data points and the estimated one (ˆ):

$$\hat{y} = \operatorname{argmin}(y - \hat{y})^2 \tag{A.2}$$

A.11 Dummy Variables

A *categorical variable* is one which is not continuous, yet it can take a value that is one of several possible categories.

In the statistical analysis of the results, none of the variables is continuous (such as load), but are rather *dichotomous* (such as depth of 24" or 48"), or (multiple) *categorical variable*, such as Boundary Conditions (U, R, or FR), or type of structure (B, TB or P). Yet internally statistical programs use numbers in all of their calculations, not words. So, even if one did not code dichotomous or multi-categorical variables using numbers, they will be converted by the program into numbers.

We can have R automatically do dummy variable coding, using a "factor" declaration.

A.12 Hypothesis Tests for Multiple Regression

The single most important hypothesis test for MLR is the F test for comparing any two nested models. Let model "s" be the "simpler" MLR model

$$y_s = \beta_0 + \beta_1 x_1 + \beta_2 x_2 + \cdots + \beta_k x_k + \varepsilon_s \qquad (A.3)$$

It has $k + 1$ parameters including the intercept, with degrees of freedom (dfs) of $n - (k + 1)$. Again, the degrees of freedom equals the number of observation minus the number of parameters estimated, as in SLR. Its sum of squared errors is SSE_s.

Let model "c" be the more complex regression model

$$y_s = \beta_0 + \beta_1 x_1 + \beta_2 x_2 + \cdots + \beta_k x_k + \beta_{k+1} x_{k+1} + \cdots + \beta_m x_m + \varepsilon_s \qquad (A.4)$$

It has $m + 1$ parameters and residual degrees of freedom (dfc) of $n - (m + 1)$. Its sum of squared errors is SSE_c.

The test of interest is whether the more complex model provides a sufficiently better explanation of the variation in y than does the simpler model. In other words, do the extra explanatory variables x_{k+1} to x_m add any new explanatory power to the equation? The models are "nested" because all of the k explanatory variables in the simpler model are also present in the complex model, and thus the simpler model is nested within the more complex model. The null hypothesis is

$$H_0 \quad : \quad \beta_{k+1} = \beta_{k+2} = \cdots = \beta_m = 0 \qquad \text{versus the alternative} \qquad (A.5)$$

$$H_1 \quad : \quad \text{at least one of these } m - k \text{ coefficients is not equal to zero.} \qquad (A.6)$$

If the slope coefficients for the additional explanatory variables are all not significantly different from zero, the variables are not adding any explanatory power in comparison to the cost of adding them to the model. This cost is measured by the loss in the degrees of freedom $= m - k$, the number of additional variables in the more complex equation.

The test statistic is

$$F = \frac{(SSE_s - SSE_c)(df_s - df_c)}{(SSE_c/df_c)} \qquad (A.7)$$

where $(df_s\text{-}df_c) = m - k$.

If F exceeds the tabulated value of the F distribution with $(df_s\text{-}df_c)$ and df_c degrees of freedom for the selected α (say $\alpha=0.05$), then H_0 is rejected. Rejection indicates that the more complex model should be chosen in preference to the simpler model. If F is small, the additional variables are adding little to the model, and the simpler model would be chosen over the more complex.

A.13 Variable Selections: Akaike and Bayesian Models

How can we decide what variables to include? Following Ockham's razor (or in Latin *ex parsimoniae*) "Among competing hypotheses that predict equally well, the one with the fewest assumptions should be selected". In the context of MLR this means that a model with fewer parameters is to be preferred to one with more. However, this needs to be weighed against the ability of the model to actually predict anything.

Or one can say that the cost of adding additional variables is that the degrees of freedom decreases, making

MERLIN AAR Problems

it more difficult to find significance in hypothesis tests and increasing the width of confidence intervals. Hence, a "good" model should explain as much of the variance of y as possible with a small number of explanatory variables.

Two particular statistical models are considered:

Akaike Information Criterion (AIC) is one of the most common model selection for model selection procedure that is available in most statistical software packages. It is based on maximum likelihood and a penalty for each parameter, (**akaike74**). For each model, compute

$$AIC = n\ln(\text{SSE}) - n\ln(n) + 2p \tag{A.8}$$

where SSE is the usual residual sum of squares from that model, p is the number of parameters in the current model, and n is the sample size. After doing this for all possible models, the "best" model is the one with the smallest AIC.

Note that the AIC is formed from three terms: The first is a measure of fit, since $n\ln(\text{SSE})$ is essentially the sum of squared residuals. The second term, $n\ln(n)$ is a constant, and really plays no role in selecting the model. The third term, $2p$ is a "penalty" term for adding more terms to the model. This is because the first term always decreases as more terms are added into the model, so this is needed for "balance".

Schwartz's Bayesian information criterion (BIC) is similar to AIC, but penalizes additional parameters more. For each model, calculate:

$$BIC = n\ln(\text{SSE}) - n\ln(n) + \ln(n)p \tag{A.9}$$

Where SSE is the usual residual sum of squares from that model, p is the number of parameters in the current model, and n is the sample size. After doing this for all possible models, the "best" model is the one with the smallest BIC. Note the similarity between AIC and BIC, only the last term changes.

A.14   R Listing and Output

The command in R used for linear fitting is "lm". It can be used to carry out regression, single stratum analysis of variance and analysis of covariance. The following short and elegant sample code is at the heart of the procedure.

The results of the linear model fitting are provided in a table including the β_i coefficients for the most relevant sub-variables, their standard deviation, t and $Pr(>|t|)$ (previously defined) are also reported.

Estimated Coefficient: is the value of slope calculated by the regression. It might seem a little confusing that the Intercept also has a value, but should be interpreted as a slope that is always multiplied by 1. This number will obviously vary based on the magnitude of the variable which is going to be an input into the regression, but it is always good practice to spot check this number to evaluate its reasonableness.

Standard Error of the Coefficient Estimate : Measure of the variability in the estimate for the coefficient. Lower means better but this number is relative to the value of the coefficient. As a rule of thumb, this value should to be at least an order of magnitude less than the coefficient estimate.

t: Score that measures whether or not the coefficient for this variable is meaningful for the model.

$Pr(>|t|)$: A predictor that has a low p-value is likely to be a meaningful addition to model because changes in the predictor's value are related to changes in the response variable A large p-value suggests that

changes in the predictor are not associated with changes in the response. Hence this number should
be as small as possible.

Significance Stars : The stars are shorthand for significance levels, with the number of asterisks displayed
according to the p-value computed. $***$ for high significance and $*$ for low significance.

A.2   Taylor's Series-Finite Difference Estimation

The concept behind the sensitivity analysis is rooted in the so-called Taylor's series finite difference estimation
of the mean μ in terms of all the random variables individual means μ_i is the mean for all random variables
Bryant, Brokaw, and Mlakar, 1993. Hence, for an independent random variables, the variance is given by

$$\mu_F = F(\mu_i) \tag{A.10}$$

where

$$Var(F) = \sigma_F^2 \quad = \quad \sum \left(\frac{\partial F}{\partial x_i} \sigma_i \right)^2 \tag{A.11}$$

$$\frac{\partial F}{\partial x_i} \quad \approx \quad \frac{F_i^+ - F_i^-}{2\sigma_i} \tag{A.12}$$

$$F_i^+ \quad = \quad F(\mu_1, \cdots, \mu_i + \sigma_i, \cdots, \mu_n) \tag{A.13}$$

$$F_i^- \quad = \quad F(\mu_1, \cdots, \mu_i - \sigma_i, \cdots, \mu_n) \tag{A.14}$$

where σ_i are the standard deviations of the variables. Hence,

$$\sigma_F = \sum \left(\frac{F_i^+ - F_i^-}{2} \right) \tag{A.15}$$

The procedure can be summarized as follows:

1. Perform an initial analysis in which all variables are set equal to their mean value. This analysis
   provides the mean μ.
2. Perform $2n$ analysis, in which all variables are set equal to their mean values, except variable i, which
   assumes a value equal to $\mu_i + \sigma_i$, and then $\mu_i - \sigma_i$.
3. For each pair of analysis in which variable x_i is modified, determine the standard deviation component
   associated with the specific variable i, which will provide an indication of the *sensitivity* of the results
   to variation of this particular variable. $\left(\frac{F_i^+ - F_i^-}{2} \right)$.
4. The standard deviation of the entire structure is then determined by simply adding all the $\left(\frac{F_i^+ - F_i^-}{2} \right)$
   terms.
5. Sort the results in an descending order and form the so-called "Tornado diagram".

This simplified method has been first reported by Benjamin and Cornell (1970) in the context of structural
engineering, and then used in (Army Corps of Engineers, 1992) (Army Corps of Engineers, 1993) and
(Saouma, 2005)..

MERLIN AAR Problems